Christopher Moswitzer, BSc

Calibration of computer simulations using reference measurements of granular flow in a rotating drum

DIPLOMA THESIS

For obtaining the academic degree

Diplom-Ingenieur

Master Programme of

Technical Physics

Graz University of Technology

Supervisor:

Univ.-Prof. Dipl.-Phys. Dr.rer.nat. Wolfgang von der Linden,

Institute of theoretical and computational physics

Graz,10.02.2014

/Entre o sono e sonho, //

Entre mim e o que em mim //

É o quem eu me suponho //

Corre um rio sem fim.

(Fernando Pessoa)

Table of Contents

List of Figures

List of Tables

1 Acknowledgement

I would like to express my special appreciation and thanks to my advisor *Univ.-Prof. Dipl.-Phys. Dr.rer.nat. Wolfgang von der Linden*.

I wish to express my sincere thanks to *Dipl.Ing. Gregor Toschkoff* for providing me with all the necessary facilities. I would like to thank you for encouraging my research and for allowing me to grow as a research scientist. Your advices have been priceless.

A special thanks to my parents, who made this possible in the first place. This work will be dedicated to you.

I would also like to thank all of my friends who supported me in writing, and incented me to strive towards my goal.

This work was funded through the Austrian COMET Program by the Austrian Federal Ministry of Transport, Innovation and Technology (BMVIT), the Austrian Federal Ministry of Economy, Family and Youth (BMWFJ) and by the State of Styria (Styrian Funding Agency SFG).

2 Abstract

In a lot of engineering processes, such as mixing, milling, coating, granulation and agglomeration, compression, transport and storage, knowledge of the flow behavior of the particles in these systems is essential. With this knowledge, it is possible to optimize the processes to make it more reliable, increase product quality, and reduce cost. Many aspects of the particle flow are still not well understood, and the target of current research. One new and powerful possibility is the use of computational methods to simulate complex systems of particles. One of the most common techniques nowadays is the discrete element method (DEM). It has proven to be a reliable tool, and can provide a detailed understanding of underlying mechanics.

However, when using simulations, the choice of the correct model parameters is always a challenging task. It has shown that using material properties from direct measurements is unreliable. Therefore, the established method now is to create a model setup for (indirect) calibration.

In this work, experiments of granular flow in a rotating cylinder are performed. Based on this, DEM simulations are validated. An established commercial software (EDEM 2.5, DEM Solutions Ltd, UK) is used. Glass spheres, biconvex tablets (coated Thrombo ASS 100mg) and self pressed tablets are prepared in a transparent, rotating cylinder. The properties of the flow are investigated under different conditions (number of particles, rotational speed, tablet shape and surface roughness). As the main characteristic of such systems, the angle of repose and the center of area are measured, which directly correlates to the static friction properties (both particle-particle and particle-wall friction), and the boundary conditions. Measurements will be done using an imaging system. The obtained data both in the experiment and simulation is investigated using a self-written MATLAB algorithm in order to get quick and reliable statistical information about the angle of repose and the center of area. The same setup as in the experiment is then investigated by DEM simulations. In this way, results of experiment and simulation can be compared directly. It is then sought to find those parameters settings for the friction properties that give best agreement. This will be done with the concept of statistical DoE (Design of Experiments), where the fitted model can be shown as a contour plot, where on the axis the factors are plotted and the contour lines are the responses. In the current work the factors have been the rotation speed, the static coefficient of friction between wall-particle and the static coefficient of friction between particle-particle. With comparison to the experimental result these friction coefficient at a certain rotation speed can be predicted. As particles Silibead glass spheres, biconvex Thrombo ASS 100mg and self pressed tablets under the surface roughness conditions of Plexiglas and steel have been investigated. One main result of the current work was the irrelevance of the choice of the static coefficient of friction between the drum wall and the particles. The reason is that no slipping between the particles and wall appear, because the tangential contact force cannot overcome the sliding friction. The values (or at least the possible value range) of the static friction coefficient between the particles with each other depending on the rotation speed, surface roughness, particle type and number of particles are determined.

In vielen technischen Prozessen wie Mischen, Mahlen, Beschichten, Granulieren und Agglomerieren, Verdichten, Transport und Lagerung, Kenntnis des Strömungsverhaltens der betrachteten Teilchen in diesen Systemen sind notwendig. Mit diesem Wissen ist es möglich, die Prozesse zu optimieren, um, die Produktqualität steigern und die Kosten zu reduzieren. Da viele Aspekte des Strömungsverhaltens von Partikeln noch nicht gut verstanden, sind sie nachwievor das Ziel aktueller Forschungen. Eine neue und leistungsfähige Möglichkeit ist die Verwendung von Computersimulationsverfahren um komplexe Systeme von Teilchen zu simulieren. Eines der am häufigsten verwendeten Techniken heutzutage ist die diskrete Elemente-Methode (DEM). Es hat sich als ein zuverlässiges Untersuchungsinstrument herausgestellt, und kann ein detailliertes Verständnis der zugrunde liegenden Strömungsmechanik liefern. Bei der Verwendung von Simulationen ist jedoch die Wahl der richtigen Modellparameter immer eine anspruchsvolle Aufgabe. Es hat sich gezeigt, dass die Materialeigenschaften von direkten Messungen unzuverlässig sind. Daher stellt sich die Aufgabe, ein Modellsetup für (indirekte) Kalibrierung zu erstellen.

In dieser Arbeit werden Experimente von körniger Strömung in einen rotierenden Zylinder durchgeführt. Auf dieser Basis werden DEM Simulationen validiert. Dafür wird eine etablierte kommerzielle Software (EDEM 2.5, DM Solutions Ltd , UK) verwendet. Glaskugeln, bikonvexe Tabletten (beschichtete Thrombo ASS 100mg) und selbst gepresste Tabletten werden in einem transparenten, rotierenden Zylinder präpariert. Die Eigenschaften der Strömung unter verschiedenen Bedingungen (Füllstand, Drehzahl, Tablettenform und der Oberflächenrauhigkeit) werden untersucht. Als Hauptmerkmal dieser Systeme werden der Böschungswinkelwinkel und der Massenschwerpunkt untersucht, welche in direktem Zusammenhang zu den statischen Reibungseigenschaften (sowohl zwischen Teilchen-Teilchen als auch zwischen Teilchen-Wand) und den Randbedingungen stehen. Die Messungen werden mit einer Spiegelreflexkamera durchgeführt. Die erhaltenen Daten sowohl im Experiment als auch in der Simulation werden mit Hilfe eines selbst geschriebenen MATLAB-Algorithmus ausgewertet, um einen effizienten und zuverlässigen Zugriff auf den Böschungswinkel und des Massenschwerpunktes der Bilder zu gewährleisten. Der gleiche Aufbau wie in dem Experiment wird in DEM-Simulationen herstellt. Auf diese Weise können die Ergebnisse von Experiment und Simulation direkt verglichen werden. Es wird dann versucht, die Parameter-Einstellungen für die Reibungseigenschaften in EDEM, in bester Übereinstimmung mit dem Experiment zu finden. Dies wird mit dem Konzept des statistischen DoE (Design of Experiments), in welchem das gefittete Modell als Konturplot ausgegeben werden kann, in welchem auf den Achsen die Faktoren aufgetragen werden und die Konturlinien repräsentieren den Böschungswinkel und den Massenschwerpunkt. In der vorliegenden Arbeit wurden als Faktoren, die Drehzahl, der statische Reibungskoeffizient zwischen Teilchen-Wand und der statische Reibungskoeffizient zwischen Teilchen-Teilchen ausgewählt. Mit dem Vergleich des experimentellen Ergebnisses können diese Reibungskoeffizienten bei einer bestimmten Rotationsgeschwindigkeit, Partikeltypus, Füllgrad und Oberflächenrauhigkeit der Trommel vorhergesagt werden. Als Teilchen wurden Silibead Glaskugeln, bikonvexe Thrombo ASS 100mg Tabletten und selbst gepresste Tabletten unter den Bedingungen unterschiedlicher Oberflächenrauheit (Plexiglas und Stahl) untersucht. Ein Hauptergebnis dieser Arbeit war die Irrelevanz der Wahl des statischen Reibungskoeffizienten zwischen Wand und Teilchen. Der Grund ist, dass es kein Rutschen zwischen den Teilchen und Wand gibt, weil die tangentiale Kontaktkraft die Rutschreibung nicht überwinden kann. Die Werte des statischen Reibungskoeffizienten der Partikel untereinader (abhängig vom Füllgrad, Oberflächenrauhigkeit, Partikeltypus und Umdrehungsgeschwindigkeit) wurden ermitteln

3 Introduction

> *"Particle science and technology is a rapidly developing interdisciplinary research area with its core being the understanding of the relationships between micro- and macroscopic properties of particulate/granular matter – a state of matter that is widely encountered but poorly understood"[1]*

During the manufacturing process, pharmaceutical tablets often are spray-coated with a cosmetic or functional film. This film provides different benefits. Cosmetic coatings are needed to improve taste masking [2], tablet elegance [3], dose differentiation [4], to change the color [5], the taste or the odor [2] of the tablets. Functional coatings for example provide an additional active pharmaceutical ingredient (API) in the coating, or modify the release rate of the API from the tablet [6], often enabling a controlled release application of this drug. One application is that the considered drug could be protected from gastric environment of the stomach by using an acid-resistant enteric coating.

To optimize the coating process, it is necessary to study the flow behavior of the considered tablets. Although the behavior of particle flow in general has been studied for more than hundred years, a lot of appearing effects are still not clearly understood. The flow properties are essential not only for coating, but also in processes including mixing [7–16], drying [17–25], milling [26–29], compression [30–39], granulation [40–45], agglomeration [46–50], transport and storage [51–60], and others. During these processes it is crucial to know the boundary conditions, that is, to know in detail the device in which the particle flow event takes place (chutes, hoppers[51–53], [61], [62], rotating drums [8–10], [63–68], fluidized beds [49], [50], [69], and similar).

With increasing speed and memory of available computers over the years it became common practice in industry to use numerical simulations. In general they are in many cases much faster and less expensive; in some cases simulations may even be the only feasible alternative to investigate certain properties of the concerned physical system. In order to study the flow behavior of granular materials via computer simulations, an efficient numerical method suitable for the physical system in consideration is needed. To treat macroscopic behavior of particle matter, it is necessary to understand the microscopic mechanism of the system by investigating the appearing interactions between individual particles. This can be achieved by particle-scale research utilizing the detailed microdynamic information. Therefore discrete modeling techniques such as Monte Carlo methods, cellular automata and discrete element methods are custom-made for treatment of particulate systems. In recent years, it has been seen that the discrete element method (DEM) is a valuable tool for the simulation of these particulate processes.

3.1 Discrete element method (DEM)

"At the heart of a DEM simulation is a particle interaction model."[70]

Mathematically speaking, the discrete element method (DEM) is an explicit finite difference numerical method for predicting the motion of individual independently moving objects. It can be applied when a (large) number of particles interact and the physical principles that govern the interaction and motion of each particle are fully understood (or at least appropriate models can be formulated). DEM is similar to molecular dynamics simulations (MDS), which investigate the dynamics of molecular liquids and solids [71–75]. The DEM is an expansion of MDS, as it may also include non-central and non-linear interactions between the particles due to asymmetric structure and friction, respectively.

The aim of the DEM is to determine the trajectory of each particle in the system. Within the DEM simulation, the particles are mainly influenced by forces such as friction, electrostatic -, magnetic -, gravitational - and cohesive forces. The forces can be divided into two groups: body forces such as gravity, electromagnetic, centrifugal or coriolis forces act on the particles, and interaction forces (such as collision forces).

In order to describe particle-particle interactions or particle-boundary interactions, a contact force model is required. In further consequence, these forces are used to calculate the accelerations of every particle in the system by applying Newton's second law of motion:

$$\boldsymbol{F} = \mathrm{m_i}\boldsymbol{a_i} = \mathrm{m_i}\,\frac{\mathrm{d}^2\boldsymbol{x_i}}{\mathrm{dt}^2} = \sum_{\mathrm{j}} \boldsymbol{F}_{\mathrm{ij}}^{\mathrm{c}} + \sum_{\mathrm{k}} \boldsymbol{F}_{\mathrm{ik}}^{\mathrm{nc}} + \boldsymbol{F}_{\mathrm{i}}^{\mathrm{f}} + \boldsymbol{F}_{\mathrm{i}}^{\mathrm{g}}, \tag{1}$$

$$\mathrm{I_i}\frac{\mathrm{d}\boldsymbol{\omega}_{\mathrm{i}}}{\mathrm{d}t} = \sum_{\mathrm{j}} \boldsymbol{M}_{\mathrm{ij}}. \tag{2}$$

$\boldsymbol{F}_{\mathrm{ij}}^{\mathrm{c}}$	Contact force on particle i by particle j or wall
$\boldsymbol{F}_{\mathrm{i}}^{\mathrm{f}}$	Particle-fluid interaction force on particle i
$\boldsymbol{F}_{\mathrm{i}}^{\mathrm{g}}$	Gravitational force on particle i
$\boldsymbol{M}_{\mathrm{ij}}$	Torque acting on particle i by particle j or wall
$\boldsymbol{F}_{\mathrm{ik}}^{\mathrm{nc}}$	Non-contact force acting on particle i by particle k or other sources
$\mathrm{m_i}$	Mass of particle i
$\mathrm{I_i}$	Moment of inertia of particle i

$\boldsymbol{\omega}_{\mathrm{i}}$ Angular velocity of particle i

$\boldsymbol{x}_i$ Position of particle i

$\boldsymbol{a}_i$ Acceleration of particle i

The forces and torques in equation (1) and (2) are used to predict the particles future locations and velocities after a small time increment (time step). This means that to get the updated particle velocities $\boldsymbol{v}$ and positions $\boldsymbol{x}$, equation (1) and (2) have to be integrated over time within the chosen time step. This process is repeated for every particle in the system for each time step. To justify the assumption that the accelerations and velocities are constant during one calculation step, the time step has to be sufficiently small. Additionally, the time step has to be small enough such that the change in positions of particles from one step to the other is not too large, as this may introduce additional problems (see chapter 3.3)

If one considers a simple formulation of equation (1), where the vector field of the force just depends on the location of the particle [76],

$$\ddot{q} = f(q), \tag{3}$$

the easiest way to handle this differential equation is by using the central second-order difference quotient [76]:

$$q_{n+1} - 2q_n + q_{n-1} = (\Delta t)^2 f(q_n). \tag{4}$$

In equation (3) and (4), q is a generalized coordinate; the principle applies to any problem where the related differential equation has this form. The basic method in equation (4) is used in different areas of physics, but is named different [77–80]:

- Störmer method in astronomy
- Verlet-method in molecular dynamics
- Modified Leap-frog method in partial differential equations

If f(q) is the acceleration $\boldsymbol{a}$ divided by the mass m and q is the position of the particle $\boldsymbol{x}$, equation (4) describes Newton's equation as formulated in equation (1). The whole classic Verlet algorithm in terms of discrete values of location $\boldsymbol{x}$, velocity $\boldsymbol{v}$ and acceleration $\boldsymbol{a}$ is:

$$\boldsymbol{x}_{n+1} + \boldsymbol{x}_{n-1} = 2\boldsymbol{x}_n + \boldsymbol{a}_n(\Delta t)^2 + \mathcal{O}((\Delta t)^4),$$
$$\boldsymbol{v}_n = \frac{\boldsymbol{x}_{n+1} - \boldsymbol{x}_{n-1}}{2\Delta t}. \qquad (5)$$

In equation (**5**), $\boldsymbol{a}_n$ is known by dividing the total force acting on the particle by the mass ($\boldsymbol{a} = \boldsymbol{F} / m$). Note that the contact force models are discussed in the following chapters.

For the first loop, $\boldsymbol{x}_{n-1}$ is undefined. Because the classic Verlet algorithm is not self-starting and has a substantial roundoff error [81], an equivalent algorithm, called Velocity-Verlet method, is used, which avoids the problems mentioned:

$$\boldsymbol{x}_{n+1} = \boldsymbol{x}_n + \boldsymbol{v}_n \Delta t + \frac{1}{2}\boldsymbol{a}_n(\Delta t)^2,$$
$$\boldsymbol{v}_{n+1} = \boldsymbol{v}_n + \frac{1}{2}(\boldsymbol{a}_{n+1} + \boldsymbol{a}_n)\Delta t. \qquad (6)$$

The local error of the above discussed algorithm schemes are $\mathcal{O}(\Delta t^4)$ for the position and $\mathcal{O}(\Delta t^2)$ for the velocity. The global error for the position and the velocity is $\mathcal{O}(\Delta t^2)$ [82]. The concept is explained graphically for a simple explicit forward Euler scheme in Figure 1 and Figure 2.

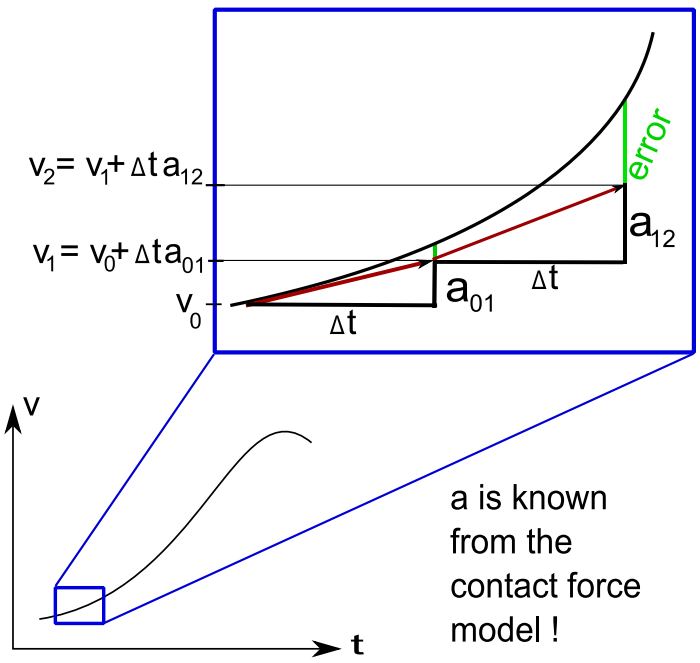

Figure 1: Illustration of a simple explicit forward Euler method. After every time step of length Δt the new value of the velocity v_{n+1} is calculated from the known acceleration a_n.

Another sufficient algorithm based on the classical Verlet-algorithm, but avoiding the appearing roundoff error, is the Beeman method [83], [84]. It has a better energy conservation behavior, but it is not self-starting. The global error for the position and velocity is $\mathcal{O}(\Delta t^3)$. Due to that, it is more precise than the classic Verlet-algorithm. The scheme is given below:

$$\boldsymbol{x}_{n+1} = \boldsymbol{x}_n + \boldsymbol{v}_n \Delta t + \frac{1}{6}(4\boldsymbol{a}_n - \boldsymbol{a}_{n-1})(\Delta t)^2,$$
$$\boldsymbol{v}_{n+1} = \boldsymbol{v}_n + \frac{1}{6}(2\boldsymbol{a}_{n+1} + 5\boldsymbol{a}_n - \boldsymbol{a}_{n-1})\Delta t. \quad (7)$$

In some cases, where a Hamiltonian of the system can be derived, the DEM uses a symplectic integrator as an integration scheme [85].

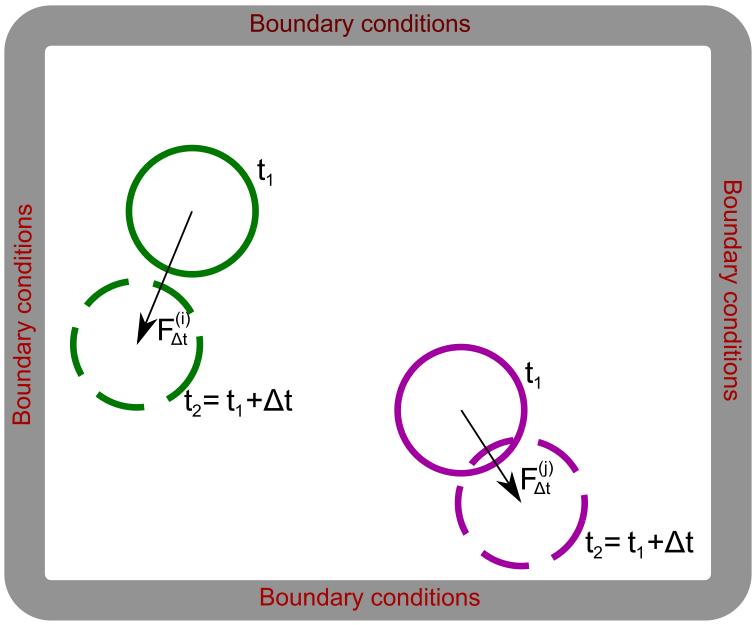

Figure 2: Illustration of the DEM principle. Within the time step Δt, all the forces $F_{\Delta t}^{(i)}$ on the particle i are determined; from this, the motion of the particles can be predicted.

3.2 Hard- and soft particle models

There are two types of approaches for granular materials as part of DEM simulations: the hard particle and the soft particle approach. Within the hard particle model [86–92] the particles are assumed to be rigid, the forces between the particles are repulsive and the collisions are instantaneous and binary [70]. The hard-particle approach can be computational efficient if the

time between collisions is large [70]. In reality, the particle contact takes place over a finite time, depending on the deformation properties of particles. Therefore, in the soft-particle model, the collisions are treated as a continuous process [93]. In this form, this was first formulated by Cundall and Strack [94]. Within the model, particle properties such as the Poisson ratio, Young's Modulus, and coefficient of restitution are taken into account. The soft particle approach is more computationally reliable and can predict more physical information about structure and dynamics behavior than the hard-particle approach. It is the starting point of the force contact models used in the current work.

3.3 Noncontact interactions

Among the noncontact forces, the most important are capillary cohesion, van der Waals interactions, and electrostatics, which are of increased importance in systems with small-sized particles. Seville et al. [95] provide an overview of these forces. Zhu et al. [1] presented the implementation of noncontact forces in the DEM. Cohesive forces affect processes where they are large compared to the body forces, such as the flowability of powders [96] or fluidization processes [97], and can be often neglected. Simple models for cohesive forces could be based on a modified linear spring approach [98], [99], a constant related to the particle weight [100–102], a square-well potential [103–105], a pendular liquid bridge specified by the Young-Laplace equation [106], [107] or a constant proportional to the contact area [108]. The van der Waals force describes the interactions between molecules and atoms, where the interactions energy E_{vdW} between them decreases inversely proportional to the sixth power of the distance:

$$E_{vdW} \sim \frac{1}{r^6} \tag{7}$$

Although the van de Waals force is always present, it is often negligible because it is weak compared to the other appearing forces. To include the van der Waals force in DEM, the Hamaker theory, which describes the interaction between two spheres and a sphere and a wall, can be used [109]. However, the appearing equation has a singularity at zero distance between the two considered particles. This problem is solved by defining a cutoff distance for the van der Waals force [110–113]. The electrostatic force appears only between charged particles and is categorized into three types: Coulomb force, image-charge forces and space charge forces [112]. Compared to the

other forces described above, it is a long-range interaction; its implementation in the collision-based DEM is therefore difficult and accompanied with a significant increase in simulation time.

3.4 Contact interactions

During the movement of a particle, it may interact with its neighboring particles or walls. Strictly speaking, the contact between two particles is not just a single point but over an area due to particle deformation. This particle deformation is not directly included in standard DEM simulations. To still model this behavior, it is assumed that the two particles are rigid, but are allowed to overlap. From the magnitude of the overlap, a repulsive force is calculated, following a certain contact model [1]. Unfortunately it is hard to accurately describe this contact traction distribution over this area and thus to find a proper description of the total force and torque acting on the particles. In general, it is reasonable to subdivide the force between two particles into a normal component and a tangential component.

3.4.1 Treatment of normal force

Different models are commonly used for the normal force. One is the Linear Spring Dashpot (LSD) model by Cundall et al [94], [114], [115], which uses a spring to include a repulsive force and a dashpot to consider energy dissipation caused by plastic deformation. An advantage of this model is that it gives an analytical expression for the coefficient of restitution, contact time and the maximum overlap. It should be mentioned that within this model, the coefficient of restitution does not depend on the impact velocity. Schwager and Poeschel found out that the analytical solution for two isolated particles given in literature is even qualitatively incorrect, because of the wrong definition of the duration of the collision [116].

In a modified version of the LSD method, a nonlinear spring is used for the repulsive force, following the Hertzian theory [117], [118]. Due to this modification, the coefficient of restitution becomes dependent on the impact velocity, but it only shows agreement with experimental data on the coefficient of restitution [119] if it is considered that the material is viscoelastic instead of elastic [120], [121]. Viscoelastic materials show a combination of the characteristics of both viscous and elastic materials. They show the following properties: a hysteresis loop in the stress-strain curve occurs, with the area of the loop equals the dissipated energy; additionally stress relaxation and creep occurs; constant strain steps causes decreasing stress and constant stress steps causes increasing strain, respectively [122].

Walton and Braun [123] introduced a partial spring model, where a linear spring is used to describe the repulsive force, but a distinction is made between the spring during the loading and

the unloading process. Effectively, different plastic stiffnesses for loading and unloading are used. Because no viscous damping coefficient appears within the model of Walton and Braun for the normal force, many researchers used this model [124–127].

Thornton and Yin [128–130] propose a model treating interactions for spherical elastic particles for both the adhesive and the non-adhesive case. This model uses a different sliding criterion.

In the work of Oda et al [131] a rolling resistance is added to the conventional linear spring-dashpot model.

3.4.2 Treatment of tangential force

A simple model to treat the tangential force was given by Cundall and Strack [94]. They used a linear spring to simulate the tangential force, where the displacement is related to the relative velocity at the contact point. The model is limited by the Coulomb or Rankine criterion, which connects the maximum friction force with the normal force via the coefficient of friction as a proportional constant. Therefore, this model is relatively easy to implement. Additionally, there is reasonable agreement with experimental data [132].

Mindlin and Deresiewicz [133] introduced a more complex model for the tangential force, where the displacement depends on the loading history and the variation of the normal force. Several researchers used this model [123], [125–127].

In the Hertz-Midlin-Deresiewicz model considered in chapter 0, the sliding friction coefficient is one of the key parameter. Based on this, Yanjie Li et al [134] constructed a simple setup to measure the sliding friction between spherical particles by determining the friction coefficient between a particle and a wall of the same material. According to classical friction theory the friction effect between two particles can be considered as a point-point contact. Because of the small contact area between particle and wall it is sufficient to measure the friction between the particle and a plane wall of the same material to extrapolate to the particle-particle sliding friction. The received experimental values were in good agreement with the DEM simulation with the same parameters.

3.5 Contact force models

In section 3.4 above, an overview of different contact interactions was given. In this section, most common models and considerations used in the DEM framework are described in detail. This includes the different collision models, friction considerations, particle-fluid interaction, contact detection and particle orientation description.

3.5.1 **Linear Spring-Dashpot model LSD**

In this contact model, the normal force $\boldsymbol{F}_{\mathrm{n}}$ is calculated as

$$\boldsymbol{F}_{\mathrm{n}} = (\mathrm{k}_{\mathrm{n}}\delta_{\mathrm{n}} + \beta_{\mathrm{n}}\dot{\delta}_n)\mathbf{n}_{\mathrm{c}}, \tag{8}$$

where δ_n is the overlap, $\dot{\delta}_n$ is the overlap velocity, β_n is the normal damping coefficient, $\mathbf{n}_{\mathrm{c}}$ is the normal contact vector and k_n is the normal spring constant. Navarro et al [135] derived a analytical expression of the normal spring constant of the linear model through numerical parameters of the non-linear Hertz-Midlin-Deresiewicz model, see chapter 0 [135]. But in general, the spring and damping coefficients can only be determined experimentally or via numerical calibration with experimental reference measurements.

The tangential component of the contact force is given as ([94], [129])

$$\boldsymbol{F}_{\mathrm{t}} = \mathrm{k}_{\mathrm{t}} \left| \int_{\mathrm{t}_{\mathrm{c},0}}^{\mathrm{t}} |\Delta\boldsymbol{v}_{\mathrm{t}}(\tau)| \mathrm{d}\tau \right| \mathbf{n}_{\mathrm{t}} + \beta_{\mathrm{t}}\Delta\boldsymbol{v}_{\mathrm{t}}, \tag{9}$$

where k_{t} is the tangential spring constant, $\mathrm{t}_{\mathrm{c},0}$ is the time where the contact between the particles started, $\Delta\boldsymbol{v}_{\mathrm{t}}$ is the relative tangential velocity, $\boldsymbol{n}_{\mathrm{t}}$ is the contact point tangential vector and β_{t} is tangential damping coefficient.

The LSD model has the advantage of a relatively simple analytical solution for the overlap and the simple relationships between k_{n} and β_{n} [135].

The derivation of the analytical expression for the overlap δ_n, the collision time t_c and the coefficient of restitution ε_d in the LSD model can be found in the appendix 7.1.

3.5.2 **Hertz-Midlin-Deresiewicz model**

In order to describe interactions between two dry spherical particles with radii R_1 and R_2 without adhesion, one has to consider both normal force and tangential force. Within the Hertzian theory the normal force is determined as

$$\boldsymbol{F}_{\mathrm{n}} = \frac{4}{3}\mathrm{E}^*\sqrt{\mathrm{R}^*}\delta_{\mathrm{n}}^{\frac{3}{2}}\mathbf{n}_{\mathrm{c}}, \tag{10}$$

where δ_{n}, R^* and E^* are defined as

$$\delta_{\mathrm{n}} = \mathrm{R}_1 + \mathrm{R}_2 - \sqrt{(x_2 - x_1)^2 + (y_2 - y_1)^2 + (z_2 - z_1)^2} \quad (11)$$

$$\frac{1}{\mathrm{R}^*} = \frac{1}{\mathrm{R}_1} + \frac{1}{\mathrm{R}_2} \quad (12)$$

$$\frac{1}{\mathrm{E}^*} = \frac{1 - \nu_1{}^2}{\mathrm{E}_1} + \frac{1 - \nu_2{}^2}{\mathrm{E}_2} \quad (13)$$

ν_1, ν_2 are the Poisson ratios of the two spheres. δ_n is the normal overlap of the two spheres, E^* is the equivalent Young's Modulus and $\mathbf{n}_{\mathrm{c}}$ is the unit vector at contact. The Hertz-Mindlin-Deresiewicz model is illustrated in Figure 3.

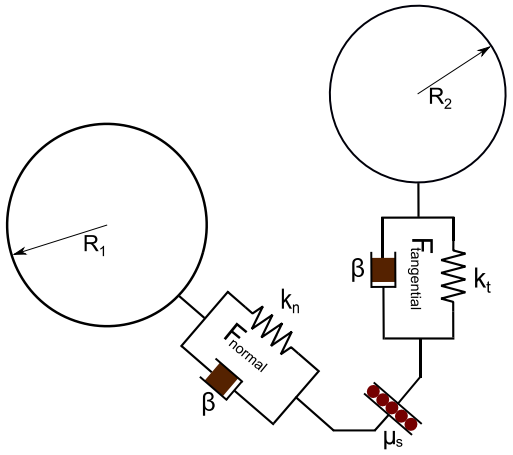

Figure 3: Illustration of the Hertz-Mindlin model. The contact between two *spheres R_1, R_2 is modeled by connecting them with springs (tangential spring constant k_t, normal spring constant k_n) and dashpots β. μ_s describes the sliding* friction.

There are different approaches to treat the damping effects [136–139]. In this work, the following equation is used to determine the damping force [1]:

$$\boldsymbol{F}_{\mathrm{n}}^{\mathrm{d}} = -2\sqrt{\frac{5}{6}}\,\beta\sqrt{\mathrm{k_n m^*}}\,\boldsymbol{v}_{\mathrm{n}}^{\mathrm{rel}} \quad (14)$$

Where m^*, β, k_n, $\boldsymbol{v}_{\mathrm{n}}^{\mathrm{rel}}$ are the equivalent mass, the damping coefficient, the normal spring constant and the normal component of the relative velocity, respectively.

$$\frac{1}{\mathrm{m}^*} = \frac{1}{\mathrm{m}_1} + \frac{1}{\mathrm{m}_2} \quad (15)$$

$$\beta = \frac{\ln(CoR)}{\sqrt{\ln^2(CoR) + \pi^2}} \quad (16)$$

$$k_n = 2E^*\sqrt{R^*\delta_n}, \quad (17)$$

where CoR is the coefficient of restitution [135], which is the ratio between the speed after and before an impact according along the line of impact. The value of the CoR describes how elastic or inelastic a collision is:

CoR = 1:	elastic collision;
CoR < 1:	inelastic collision;
CoR = 0:	object stops at the collision, no bouncing;
CoR > 1:	collision that creates kinetic energy.

For the sake of completeness, the Poisson ratio ν and the Young's modulus E are given:

$$E = \frac{\text{tensile stress}}{\text{tensile strain}} = \frac{\sigma}{\varepsilon}, \quad (18)$$

$$\nu = -\frac{d\varepsilon_{trans}}{d\varepsilon_{axial}}, \quad (19)$$

The tangential force depends on the loading status and on the normal force, given by the following formula taken from Thornton [140]:

$$\Delta T = 8Ga\Theta_k\Delta\delta + (-1)^k\mu\Delta F_n(1-\Theta_k), \quad (20)$$

where ΔT is the incremental tangential force, $\Delta\delta$ is the incremental displacement and μ is the sliding friction coefficient.

θ_k depens on the loading status:

$$\theta_k = \begin{cases} \sqrt[3]{1 - \frac{T + \mu\Delta F_n}{\mu N}}, & k = 0 \text{ (loading)} \\ \sqrt[3]{1 - \frac{(-1)^k(T - T_k) + 2\mu\Delta F_n}{2\mu}}, & k = 1,2 \text{ (un- and reloading)} \end{cases} \quad (21)$$

where G is the particle shear modulus, defined as

$$\frac{1}{\mathrm{G}} = \frac{2-\nu_1}{\mathrm{G}_1} + \frac{2-\nu_2}{\mathrm{G}_2}. \qquad (22)$$

In sum, there are eleven different loading/unloading possibilities [70], but for DEM simulation only those three above are taken into account.

3.5.3 Braun-Walton model

The Braun-Walton model is a plastic-elastic contact model which is applied to include plastic deformation due to collisions. The deformation of the particles and the impact energy associated with it leads to dissipation. The normal force differs if the contact is loading or unloading:

$$\boldsymbol{F}_{\mathrm{n}} = \begin{cases} -\mathrm{K}_1 \delta \mathbf{n}_{\mathrm{c}}, & \text{loading} \\ -\mathrm{K}_2(\delta - \delta_{\mathrm{def}})\mathbf{n}_{\mathrm{c}}, & \text{unloading} \end{cases} \qquad (23)$$

$$\begin{aligned} \mathrm{K}_1 &= 1.6\pi \mathrm{R}\mathrm{Y}_0, \\ \mathrm{Y}_0 &= \mathrm{E}\vartheta, \\ \mathrm{K}_2 &= \frac{1}{\mathrm{E}_{\mathrm{f}}}\mathrm{K}_1, \\ \delta_{\mathrm{def}} &= \delta_{\max}(1-\mathrm{E}_{\mathrm{f}}). \end{aligned} \qquad (24)$$

Here, E is the Young's modulus defined in equation (18), δ is the contact overlap and $\delta_{\max}$ the maximum overlap reached during loading. *R* is the ration of the new contact radii, ϑ and E_{f} are user-defined parameters, describing the onset of plastic deformation and the amount of energy recovering during loading, respectively.

The tangential displacement consists of two parts, one parallel ($\Delta s^{\parallel}$) and one perpendicular ($\Delta s^{\perp}$) to the current friction force. The preliminary tangential force can be calculated:

$$\overline{\boldsymbol{F}_{\mathrm{t}}} = k^{\parallel}\Delta s^{\parallel}\mathbf{t}^{\parallel} + \mathrm{k}_0\Delta s^{\perp}\mathbf{t}^{\perp}, \qquad (25)$$

where $\mathbf{t}^{\parallel}$, $\mathbf{t}^{\perp}$ are the unit vectors in the tangential plane parallel and perpendicular to the current tangential force. $\mathrm{k}^{\parallel}$ is different whether the magnitude of the tangential force increases (softer stiffness) or decreases (harder stiffness) [141]:

$$k^{\parallel} = \begin{cases} \mathrm{K}_0^{\mathrm{t}} \left(1 - \dfrac{|\boldsymbol{F}_{\mathrm{t}}| - F^*}{\mu |\boldsymbol{F}_{\mathrm{n}}| - F^*}\right)^{\gamma}, & |\boldsymbol{F}_{\mathrm{t}}| \nearrow \\ \mathrm{K}_0^{\mathrm{t}} \left(1 + \dfrac{|\boldsymbol{F}_{\mathrm{t}}| - F^*}{\mu |\boldsymbol{F}_{\mathrm{n}}| + F^*}\right)^{\gamma}, & |\boldsymbol{F}_{\mathrm{t}}| \searrow \end{cases} \quad (26)$$

where $\mathrm{K}_0^{\mathrm{t}}$ is the initial tangential stiffness, γ is a fixed parameter and μ is the coefficient of inter-particle friction. F^* is initially zero and is set to the magnitude of $\boldsymbol{F}_{\mathrm{t}}$, whenever the time derivative of $\Delta s^{\parallel}$ reverses its direction.

The total tangential force considers the Coulomb-like friction law, where sliding appears when the friction limit $\mu_s |\boldsymbol{F}_{\mathrm{n}}|$ is achieved:

$$\boldsymbol{F}_{\mathrm{t}} = \begin{cases} \boldsymbol{F}_{\mathrm{t}}, & \boldsymbol{F}_{\mathrm{t}} < \mu_s |\boldsymbol{F}_n| \\ \dfrac{\mu_s |\boldsymbol{F}_{\mathrm{n}}|}{|\boldsymbol{F}_{\mathrm{t}}|} \boldsymbol{F}_{\mathrm{t}}, & \text{otherwise} \end{cases} \quad (27)$$

3.5.4 **Sliding friction** [142], [143]

Since the coefficient of friction is the core of interest in this work, it is worthwhile to give friction in general a closer look. Friction is a force that tries to resist the relative motion of two objects

which are in contact to each other. A non-exhaustive overview is given in Figure 4.

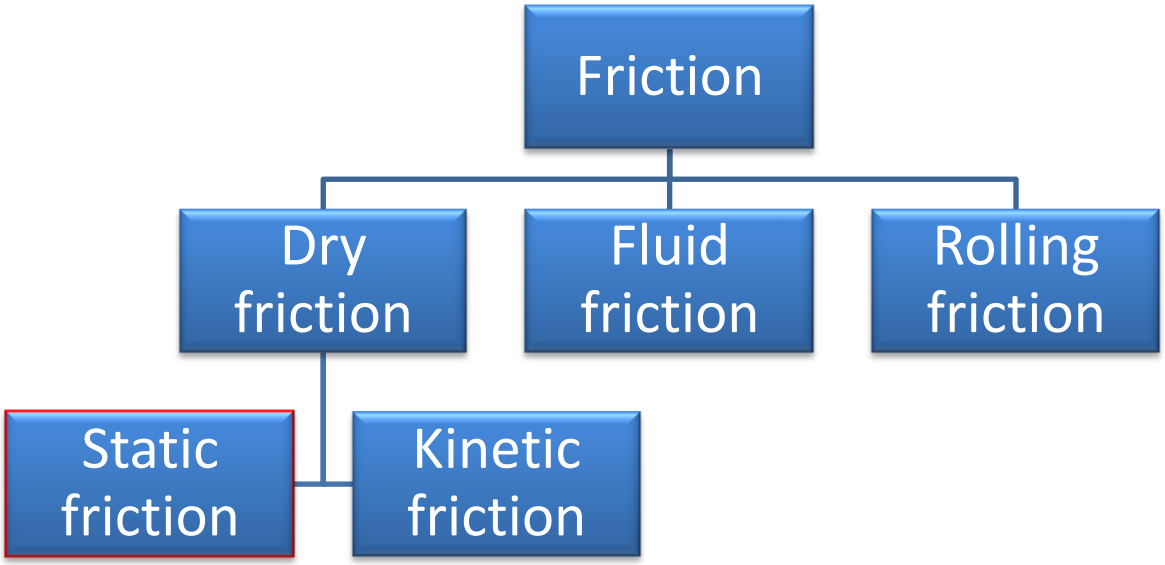

Figure 4: Short overview of the different classes of friction.

The rolling friction will be explained in chapter 3.5.5. Fluid friction occurs in fluids, where layers are moving relatively to each other and the internal resistance is described by viscosity. The dry friction force or Coulomb friction can be modeled as

$$F_f \leq \mu F_n. \qquad (28)$$

As can be seen in equation (28) the Coulomb friction can have any value from zero to μF_n.

There are two possible situations: either the objects are moving relative to each other or not. Depending on this, different coefficients of friction are defined: the coefficient of static friction μ_s when the objects are at rest and coefficient of kinetic friction μ_k when the objects are moving. The expressions kinetic friction, dynamic friction and sliding friction are equivalent. Static friction describes how much force is required to put an object of a given material that is in contact with another object into motion. μ_s is usually larger than μ_k, because irregularities on each surface do not get time to interlock when the objects are moved. Overall, the coefficient of friction is not only a material property as often assumed, it is in fact a system property. Within the theory of contact forces the coefficient of friction is responsible for shear interaction and a second spring-dashpot response to tangential or rolling friction interaction (taken from EDEM Technical Overview).

3.5.5 **Rolling friction**

> *"Two technical terms, rolling and rotation, must be carefully distinguished. The former denotes a micromechanism of deformation taking place at contacts, while the latter denotes pure rotation with respect to a reference axis."* *[144]*

The particles considered in DEM simulations are not point-like and thus it has to be taken into account that the interaction forces act at the contact point between particles rather than at the centre of mass of a particle. This generates a torque, resulting in a particle rotation. The torque is mainly governed by the tangential and asymmetrical normal traction distribution [1]. The determination of this distributions is difficult and still an active research area [145–148]. The torque M_i acting on a particle with radius R_i due to the tangential contact force $F_{t,ij}$ at contact point is

$$M_i = \mathrm{R_i} \times F_{t,ij}. \qquad (29)$$

Because this principle is fundamental of understanding the rolling resistance, it is elaborated in more detail. If two equal viscoelastic cylinders are pressed together, the contact surface is flat and (apart from surface friction) the contact stresses are perpendicular to the contact surface. If one would record the vertical deformation going through a horizontal line parallel to the contact surface, he or she would see that at the beginning, as the vertical deformation increases (resisted by the hysteresis effect), additional pressure is generated in order to avoid interpenetration of the two surfaces and at one point as vertical deformation decreases the pressure decreases. This leads to an asymmetric pressure distribution within the contact surface, which is illustrated in Figure 5. Because the line of action of the vertical forces does not pass through the center of the cylinder any more, the two bodies get a momentum and start to rotate. The direction in which the cylinders are spinning depends on the asymmetric pressure distribution. The bigger the hysteresis effect, the bigger the rolling resistance.

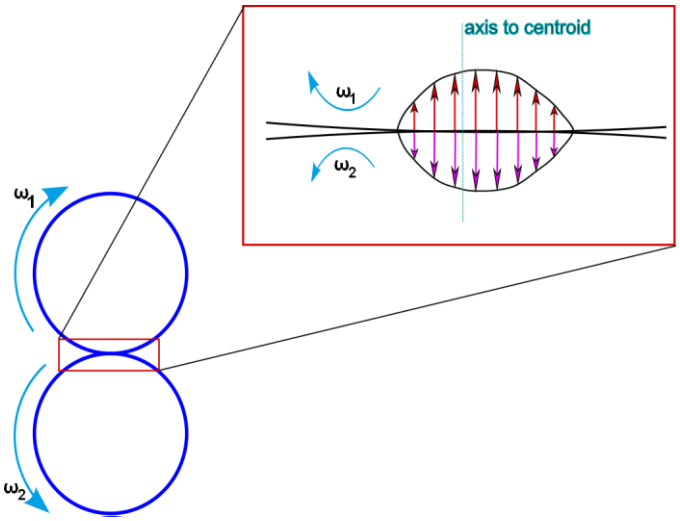

Figure 5: Illustration of the asymmetric pressure distribution (arrows above) in the contact area when two viscoelastic steadily rolling balls collide.

The torque plays a significant role especially in cases with a transition between static and dynamic states, such as heaping [149] or formation of shear bands [144], [150].

Both numerical studies [144], [151], [152] and physical experiments [153–156] on granular flow behavior have been shown the significant importance of the rotational inertia and the associated energy loss in rotation of particles.

A granular system can be in a dynamic flow state (such as in cases of avalanching, discharge from containers, stockpile formation, rotating drum, pneumatic flow, screw auger transportation) , in a pseudo-static state (such as shear bands, confined compression, penetration), or also in a mixed state where the two states coexist [157]. In investigating dynamic flow states or pseudo-static states, researchers commonly use the term rolling friction or rolling resistance, respectively [144], [149], [158], [159]. Although the two terms are describing different states, the framework of the models is the same, because both are expressed as a pair of torques at the contact.

Rolling resistance can have several sources at the contact between two particles or between a particle and wall, which may include [157]:

- *Micro-slip and friction on the contact surface* [118], [160–164]*:*
  Micro-slip may occur at the interface, if the two bodies have different curvatures at the contact, different coefficients of slipping friction μ_s or dissimilar elastic constants [146].
- Plastic deformation [146], [165–168]:
  It is a major source of energy dissipation, where the energy is not usually dissipated at the interface, but within the solid at a point where the maximum shear stress appears.

- Viscous hysteresis [147], [165], [169–174]:
  Viscous hysteresis is another important dissipation mechanism appearing for viscoelastic particles, which depends both on temperature and deformation rate [170], [173].
- Surface adhesion [175–180]:
  If the adhesive bond at the separation point between particles breaks during rolling motion, energy is dissipated.
- Shape effect [159], [181]:
  Non-spherical or non-circular particle shape may lead to a rolling resistance effect. This lack of sphericity is present in all real particles, either a priori or due to deformations of the particles.

It should be noted that rolling resistance does not only arise from sources around the contact points but also can occur from other factors such as air drag in a multiphase problem [157] electrostatic interaction or surface defects [118], [149]. Further, the propagation of disturbance waves of particles and fluids far away from the considered particles plays a significant role [149].

It is important to implement a rolling friction model to avoid arbitrary treatments and unnecessary assumption [149]. Thus, a short introduction into torque acting models including rolling friction should be given. Over the years a lot of researchers concerned themselves with rolling resistance and developed several rolling resistance models [111], [144], [147], [149–151], [158], [159], [164], [181–199]. In appendix 7.2 it is shown that existing models, especially according to rolling torque models, do not always obey the physical requirements of the considered system. Those models should be modified or even refused; however, finding a new model for complex systems may be a very challenging task.

Figure 6, lists some important works on the implementation of rolling resistance model into the DEM. It has to be mentioned that while a large number of researchers tried to find an appropriate generalized model to treat assemblies of granular material, to date no such generalized model has been proposed. Between the existing models, there are in some cases a lot of similarity, in other cases the models are completely different. At this point Ai et al [157] said: “ Given this diversity, it is naturally quite possible that a rolling resistance model may work well for some problems but not for others.”

One of the model that got much attention was the MDEM proposed by Iwashita and Oda [144], where they describe the rolling resistance as an elastic rotational spring, a dash pot, a non-tension joint and a slider. A number of researchers felt inspired by their work and proposed a series of rolling resistance models. Jiang et al [159] pointed out that the MDEM has several limitations.

Within the model, three artificial parameter appear, which only can be chosen separately by trial-and-error.

In most of the commercial DEM software available, either the rolling friction model of Iwashita and Oda [144], [181]

$$M_r = -\mathrm{k_r}\theta_r - \mathrm{C_r}\frac{d\theta}{dt}, \tag{30}$$

or the modified model of Zhou et al [149] and Zhu et al [200]

$$M_r = -\,min\{\mu_\mathrm{r}|F_n|, \mu_\mathrm{r}'|\omega_n|\}\frac{\omega_n}{|\omega_n|}, \tag{31}$$

are used. $\mathrm{k_r}$ is the rolling stiffness, $\mathrm{C_r}$ is the viscous coefficient, μ_r' is the rotational stiffness and ω_n is the component of the relative angular velocity in contact plane.

The influence of the magnitude of rolling resistance is not investigated in the current work. Although it is one of the unknown input parameter in the DEM simulations, it was set to 0.01 for every system configuration. It was assumed that its relative influence can be neglected, based on the plausible observation that it requires much less force to roll a wheel than to slide it [143].

Figure 6: Brief summary of the first historical steps of implementing rolling resistance into the DEM. The implementation of rolling resistance is a 'young' research area and still under construction. The corresponding papers are: [144], [149], [151], [158], [159], [201].

3.5.6 Particle-fluid-interaction

In systems with relatively large particles (typically greater than 500 µm), the effects of interstitial fluids can normally be neglected [202]. To include those effects, in most of the cases an Eulerian CFD (computational fluid dynamics) model coupled with a Lagrangian DEM model is used [1], [203]. For more information on coupled CFD-DEM simulation, refer to [204–209] and [210], [211],[212].

3.5.7 Methods of contact detection

In the DEM, it is important to know after every time step which particles are in contact with each other. For typical system sizes, a large number of contacts occur. Thus, an efficient detection algorithm is needed. A simple method is to sort the particles into appropriate cells and only to test contacts of particles in neighboring cells. A detailed description is given in [71], [72], [213].

3.5.8 Orientation with quaternions

In classical mechanics, the rotation of a rigid body is typically described by the Euler angles. A rotation matrix is used to switch between global and local coordinates [71], [214]. But if the angle around the y-axes reaches the angle $\pm\frac{\pi}{2}$, the determinant of the rotation matrix becomes zero and the inverse does not exist. Evans [214] solved the problem of this singularity by using quaternions. The quaternions are implemented in the rotation matrix such that the singularity disappears. The big advantage of using quaternions is that the simultaneous rotation about x, y, and z axes of the rigid body can be described by using just one rotation axis [93], [215].

The concept of quaternions is used in the DEM simulations for describing both the rotation of the drum and the torque movement of the particles. For the sake of completeness, the main formulas should be noted down:

$$\begin{gathered} Q = Q_r + Q_i i + Q_j j + Q_k k, \\ \theta = 2\cos^{-1} Q_r \\ Q_r = \sin^{-1}\sqrt{{Q_i}^2 + {Q_j}^2 + {Q_k}^2}, \\ (\eta_x, \eta_y, \eta_z) = \frac{1}{\sin 0.5\theta}(Q_i, Q_j, Q_k), \end{gathered} \tag{32}$$

$$\begin{pmatrix} \sin\theta + {\eta_x}^2(1-\sin\theta) & \eta_x\eta_y(1-\sin\theta) - \eta_z\cos\theta & \eta_x\eta_z(1-\sin\theta) + \eta_y\cos\theta \\ \eta_x\eta_y(1-\sin\theta) + \eta_z\cos\theta & \sin\theta + {\eta_y}^2(1-\sin\theta) & \eta_z\eta_y(1-\sin\theta) - \eta_x\cos\theta \\ \eta_z\eta_x(1-\sin\theta) - \eta_y\cos\theta & \eta_z\eta_y(1-\sin\theta) + \eta_x\cos\theta & \sin\theta + {\eta_z}^2(1-\sin\theta) \end{pmatrix}. \tag{33}$$

As can be seen, the rotation of a body can be described by the definition of three quaternions in equation (32 **)** and the rotation matrix in equation (33).

3.6 Particle shape

In a number of studies, the particles in the system are approximated to be spherical. However, in many applications this simplification cannot be justified. Comparisons of studies between spherical and non-spherical particles show that they have a different angle of repose [216], [217] and a reduced strength [218], [219]. Therefore, models to implement the non-spherical objects into the DEM simulation were introduced. A commonly used model is to approximate non-spherical particles by a number of spheres that do not move relative to each other (glued sphere approach) [7], [220–224]. Another widely used method is the concept of mathematical dilation to create spherocylinders [202], [225–229]. An important particle shape (that is also part of the investigations in this work) is that of round bi-convex tablets [93], [230], which is can be mathematically defined by intersection of one small sphere that represents the tablet band and two larger spheres that represents each of the convex sides, Figure 7. Due to the easy mathematically formation using only spheres, this is computationally efficient.

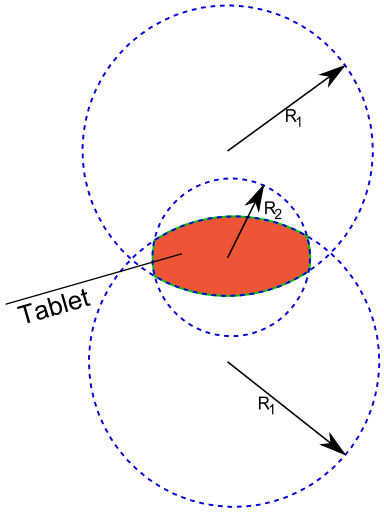

Figure 7: Construction of a biconvex tablet via the composition of two bigger spheres with radii R_1 and one small with radius R_2.

All contact possibilities between two tablets are given in Figure 8.

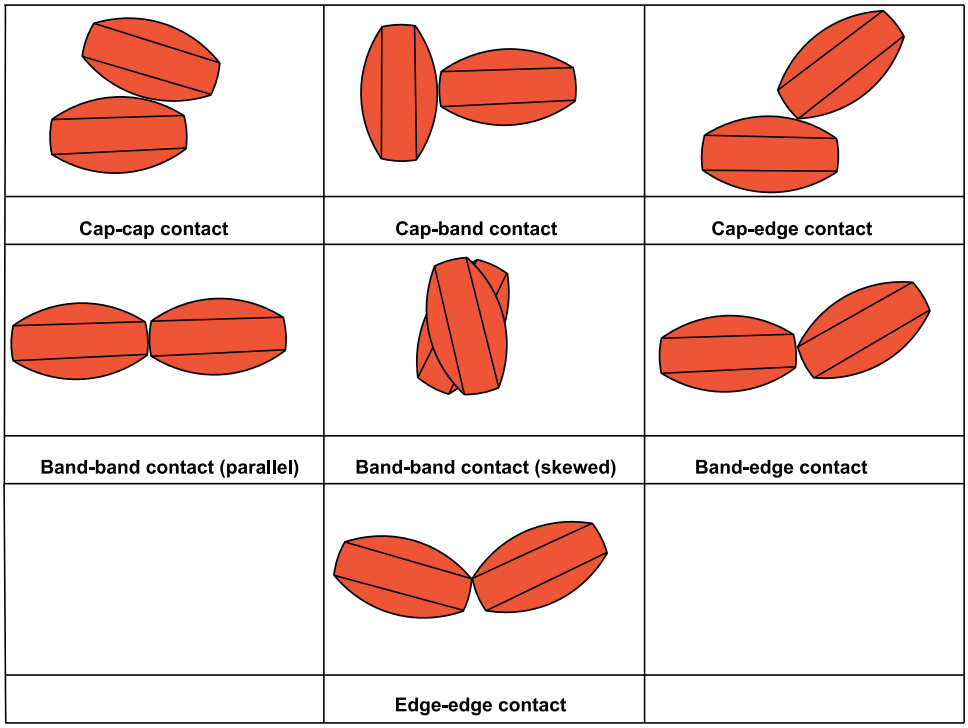

Figure 8: Illustration of all contact possibilities of two biconvex tablets.

3.7 Experimental methods to study particulate flow

3.7.1 PEPT

PEPT (Positron Emission Particle Tracking) measurements are able to look into the depths of a particulate system to study the kinematics and dynamics of the flow of the considered particles. A single particle (tracer) is marked with a radionuclide. The measurement is based on positron annihilation. After a beta-plus decay in the tracer, an electron and a positron disperse into two gamma rays radiated in opposite directions. PEP-detectors are positioned in an array to detect the gamma rays. From the location of multiple detection points, the position of the tracer can be calculated. By detecting the position continuously, the trajectory of the tracer is followed. This makes it ideal to study granular materials [14], [231–234].

3.7.2 MRI

Magnetic resonance imaging uses the principle of nuclear magnetic resonance based on the Lamour precession motion of the nuclear spin after a disturbance of a radio frequency magnetic pulse perpendicular to the applied constant magnetic field. When the constant field is superimposed by an additional gradient magnetic field, the Lamour-frequency changes by changing the position of the particle with the nuclei spins inside [235–238]. It is obvious that the particles to be tracked have to have a non-zero nuclear spin.

3.7.3 Video-imaging techniques

Typically, a CCD camera is installed in the area where the particle movement is measured. The movement of the particle of interest, mostly tagged with color, is tracked via machine vision. Several researchers used this technique in their investigation of particle movements [239–242]. In the current work, imaging techniques will be used to investigate the particle arrangement in a transparent rotating drum made of Plexiglas, see chapter 4.2 and 4.3.

3.7.4 PIV

Particle Image Velocimetry is a commonly used technique to measure the velocity field of particles in a test medium. The particles of interest are added to the fluid (or in some cases to a granular medium with similar density) and a pulsed, extended laser is shining on the system. Two pictures in small time intervals are made. The reflected light of the laser pulses is recorded by a CCD camera. The velocity-field is then determined by cross-correlation of the two images [243].

3.7.5 Photometry

A photometric method to discover the velocity field of particle movement is to measure the duration of emission of a luminous tablet with a photomultiplier [244].

3.8 DEM simulations in a rotating drum

The granular flow in a rotating (cylindrical) drum is a common study object, as it is relatively easy to set up, but still captures the underlying mechanics. In literature, approaches of different complexity are seen. Baumann et al [245], [246] developed a computationally efficient numerical model [247], [248], called bottom to top restructuring (BTR) to simulate a granular system for monodisperse and bidisperse disks in a two dimensional rotating drum. They found that for every ratio of the particle radii except 1, segregation occurs. In their work they also tagged a particle and showed ergodicity. Dury and Ristow [64] investigated the same system as Bauman et al [246] but used DEM with linear contact forces. They examined carefully the dependence of the segregation process due to the angular velocity of the drum and saw that the segregation decreases with increasing angular velocity.

Kwapinska et al [9] worked out the number of revolution required for uniform mixing of the solids in a two-dimensional rotating drum. Cleary et al [65] compared DEM simulations and experiments for a mixing processes in a rotating drum; they came to the conclusion that the flow pattern matches qualitatively.

Yang et al [10] investigated the particle flow of mono-sized spheres (3mm diameter) in a rotating drum using DEM and validated the method with PEPT measurement by comparing the angle of repose and the spatial velocity field taken from [249], with good agreement. They found a strong influence of the rotational speed of the drum on the relative collision velocity and collision frequency. Additionally, they made a microdynamic analysis by following the path of one particle by taking the dynamic information of the DEM simulation into account. Their study is a good example on the advantages of DEM analysis, because in regular experimental measurements, no prediction of e.g. the coordination number or the normal contact forces on a particle would be possible.

Wightman et al [8] used DEM to investigate the bulk flow of spherical particles under conditions of a rotating and rocking drum. They found out that the rocking motion of the drum leads to a significant perturbation compared to the purely rotational motion of the drum, but it enhances the mixing of the particles.

In the current work, glass spheres moving in a rotating drum were investigated. For comparison,Table 1 gives an overview of some experiments done with glass spheres in a rotating drum and the used parameters for the DEM simulation.

Reference	Investigation	Drum parameter [mm]	Particle parameter	External conditions	Parameters
Yang et al [10]	Experiment DEM	D = 100;	d = 3mm;	ω = (10-65)rpm; NP = 2000 Periodic boundary conditions	μ_s= 0.5; μ_r= 0.01; β_n= 2*$10^{-5}s^{-1}$; CoE = 0.73 Y = 10^7; ν = 0.29
Wightman et al [8]	Experiment DEM	D = 126 (experiment), 106(DEM)	d = 3.78mm	ω=15rpm; NP = 10000-25000;solid rotating boundaries	μ_p=0.4; μ_w=0.4; CoR = 0.85;
Liu et al[250]	Experiment	D = 200,300,500	d =3,5	ω<1; f = 0.2-0.4; Inner wall glued with sandpaper	--
Yang et al [251]	Experiment DEM	D = 100;	d = 3; ρ = 2.5×10^3kg m^{-3}	ω = (0.1-300)rpm, f = 35%	μ_s= 0.5; μ_r= 0.002; β_n = $10^{-6}s^{-1}$; Y = 10^7Nm^{-2}; υ = 0.29

Table 1: Experiments done with glass spheres in a rotating drum. D is the diameter of the drum, d is the diameter of the sphere, Y is the Young modulus, ν is the Poisson ratio, ρ is the density of the sphere, ω is the angular velocity, NP is the number of particles, f the filling degree, μ_s is the coefficient of static friction, μ_r is the coefficient of rolling friction, μ_p is the coefficient of static friction between particle and particle, μ_w is the coefficient of static friction between particle and wall, β_n is the normal damping coefficient and CoR is the coefficient of restitution

3.8.1 Flow regimes in a rotating drum

In general there are different flow regimes describing the particle motion in a rotating drum. Henein [252] identified the following six regimes: slipping, slumping, rolling, cascading, cataracting and centrifugal. Mellman [253] and Henein [252] showed how the different regimes depend on the Froude number, defined as [254]:

$$Fr = \frac{\omega^2 \mathrm{R}_D}{\mathrm{g}}, \qquad (34)$$

where g is the gravitational constant, R_D is the radius of the drum and ω is the angular speed of the drum.

In the presence of a fluid the Froude number has to be modified [255]:

$$\mathrm{Fr} = \frac{\omega^2 R}{g}\left(\frac{\sin\beta_s\sqrt{1-f}}{1-\frac{\rho_f}{\rho_p}}\right), \qquad (35)$$

where β_s is the material angle of repose, f is the fill factor, ρ_f the density of the fluid and ρ_p is the density of the particles.

A useful overview of the regimes with the corresponding Froude number are given in Table 2 taken from [253].

Basic form	Slipping motion		Cascading ("tumbling") motion			Cataracting motion	
Subtype	Sliding	Surging	Slumping	Rolling	Cascading	Cataracting	Centrifuging
Schematic	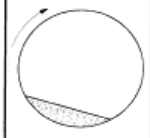			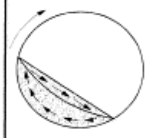	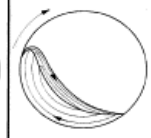	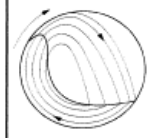	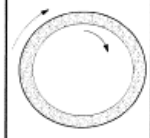
Physical process	Slipping		Mixing			Crushing	Centrifuging
Froude number Fr [-]	$0 < \mathrm{Fr} < 10^{-4}$		$10^{-5} < \mathrm{Fr} < 10^{-3}$	$10^{-4} < \mathrm{Fr} < 10^{-2}$	$10^{-3} < \mathrm{Fr} < 10^{-1}$	$0.1 < \mathrm{Fr} < 1$	$Fr \geq 1$
Filling degree f [-]	$f < 0.1$	$f > 0.1$	$f < 0.1$	$f > 0.1$		$f > 0.2$	
Wall friction coeff. μ_w [-]	$\mu_w < \mu_{w,c}$	$\mu_w \geq \mu_{w,c}$	$\mu_w > \mu_{w,c}$			$\mu_w > \mu_{w,c}$	
Application	no use		Rotary kilns and reactors; rotary dryers and coolers; mixing drums			Ball mills	no use

Table 2: An overview of the possible regimes in a rotating drum. These regimes can be predicted based on the Froud number Fr [253].

As one can see in Table 2, if the actual sliding friction coefficient is much higher than the critical sliding friction coefficient $\mu_{W,c}$ as supposed by Heinein [256] and Mellmann [253], no slipping occurs.

3.8.2 **Bulk flow behavior**

Yang et al [251] investigates the time evolution of the mean flow velocity normalized by the translational velocity of the drum wall. Accordingly, in the slumping regimes significant peaks appear as avalanches occur and in a certain range of the drum rotating speed all distributions of the normalized particle velocity v^* collapses into a single curve, described by the following formula [251]:

$$P(v^*) = a \exp\left(-b\left[\ln\left(\frac{v^*}{v_0^*}\right)\right]^2\right), \quad (36)$$

where v_0^* is the mean normalized velocity, v^* is the translation velocity of the drum wall and a, b are two parameters depending on the properties of the used drum.

Collision energy (defined via the kinetic energy at collision) is an important information in mixing, grinding and granulation processes [257]. It is difficult to measure this quantity experimentally, but it can be obtained from DEM simulations. Yang et al investigated the influence of rotation speed on the collision energy [251]. At slow speed, near the transition from slumping to sliding, most of the particles at the bottom are closely packed with few collisions. By increasing the rotation speed, the number of collisions increases near the wall, but in the centre of the flow the collisions are still rare. By reaching the cascading regime, collisions in the centre of the flow are increasing, which provides good mixing behavior. The particles on the bed surface also have enough energy to fall freely inside the drum, which is very advantageous in grinding processes. The distribution of the collision energy for particle-particle interactions shifts to larger values by increasing the rotation speed. The particle-wall interaction increase much faster than the particle-particle interactions with increasing rotation speed. By normalizing the collision energy at different rotation speeds by their mean value, the distribution of the normalized particle-particle collision energy and the normalized particle-wall collision energy collapse into one curve for all investigated rotation speeds.

3.8.3 (Dynamic) angle of repose

The angle of repose (AoR) is a central quantity for the flow investigation in the presented work. In the following, some background is given. In the slumping mode (see Table 2), an upper and lower angle of repose [250] appears. The bed of the particle assemble is lifted by the wall of the rotating drum until it reaches the upper angle of repose. At that point, the particles begin to slide down. During this avalanching, the slope of the bed surface decreases until the lower angle of repose is reached. The time interval between the appearances of those two angles decrease by increasing the rotational speed until the flow is continuous (dynamic angle of repose).

The results data of Liu et al [250] are listed in Table 3. The lower and upper angles of repose are stated.

Particle size d [mm]	Drum diameter D [mm]	Filling degree f	Lower angle of repose α [°]	Upper angle of repose β[°]
3	200	0.2	27.6	30.0
		0.4	27.3	30.2
	300	0.2	27.2	28.9
		0.4	26.8	29.0
	500	0.2	26.1	27.4
		0.4	25.7	27.0
5	200	0.2	27.6	30.1
		0.4	27.9	31.1
	300	0.2	28.3	30.5
		0.4	28.2	29.7
	500	0.2	27.3	28.5
		0.4	26.9	29.0

Table 3: Experimental measurements of glass beads of the lower and upper angle of repose. Data was taken from [250].

At the dynamic angle of repose, the movement is stabilized and avalanching ceases. At this point, the rolling regime is reached. According to [253] the dynamic angle of repose is approximately the mean value of the upper and lower angle of repose:

$$\theta \approx \frac{\alpha + \beta}{2} \tag{37}$$

Additional research on the dynamic angle of repose can be found in [258–260].

Using the equation (37) and measuring the dynamic angle of repose, Liu et al [250] found out that the upper and lower angle of repose are correlated to each other with the following formula, with a maximum error of 5% [250]:

$$\alpha = 0.65\beta + 8.75°\,, \qquad \text{if } \beta > 25°. \tag{38}$$

Formula (38) can be applied to deduce the angle of repose from only one angle measurement instead of two. The Froude number at the slumping-rolling transition can be calculated by evaluating $(\beta - \alpha)^2$ [253], [256], [261], [262].

In the cascading regime, the free surface shows a distinct wavy S-shape. Thus, it is difficult to define the angle of repose, because the angles are different at the tail, middle and shoulder parts. Commonly, the angle of the middle region is taken and a straight line is fitted [263], [264]. Yang et al suggest that the reason for the appearance of this S-shape is the end cap [251].

In the present work the sliding, surging, slumping, rolling and cascading mode will appear, which makes it very difficult to create one general analysis method for the angle of repose. Especially the surging and slumping mode are recognizable in their statistical standard deviation. More information about the AoR are covered in the chapters 4.3 and 0.

3.9 Design of Experiment (DoE)[1]

"Essentially, all models are wrong. Some are useful." (George Box) [265]

Broadly speaking, design of experiment (DoE) gives a statistics-based framework for quantifying how process inputs affect process outputs using a minimum number of runs.

DoE has been developed in the twenties of the last century. The first book about it was published in 1935 by R.A. Fisher [266]. But the real breakthrough of this statistical tool in science took place after 1980; from there on it became more and more common, popular and necessary.

Nowadays, experiments are in general complex and the appearing number of parameters has a predefined pool. In contrast to an experimental design which is normally hold assessable, the interpretation of the associated results can be very difficult. Typical questions within this area are: what is the necessary sample size? How does one distinguish between real and virtual effects? What are the most important parameters and what is the optimal range for those parameters? Therefore, tailor-made designs are needed in order to use the optimal parameters during the experimental run. Due to the increasing application of computer simulations and the complexity of

[1] Most of the theory according to DoE used in the current work was taken from [267]

choosing the optimal parameters associated with it, the development of an a priori design of experiment gained even more importance.

If the process shows interactions between process inputs, the systematically and simultaneously change of the process inputs in a DoE gives defined statements on this interaction. In contrast, by changing just one factor at a time, one will not know if the currently changed factor is affected by the setting of the other factors. From a qualitative point of view, it is also important to evaluate random variability which enables the experimenter to distinguish between real effects and noise. From a time/cost perspective, DoE requires a minimum amount of resources considering the amount of information and knowledge that is built in a process development effort. This is especially true if the number of input parameter increases.

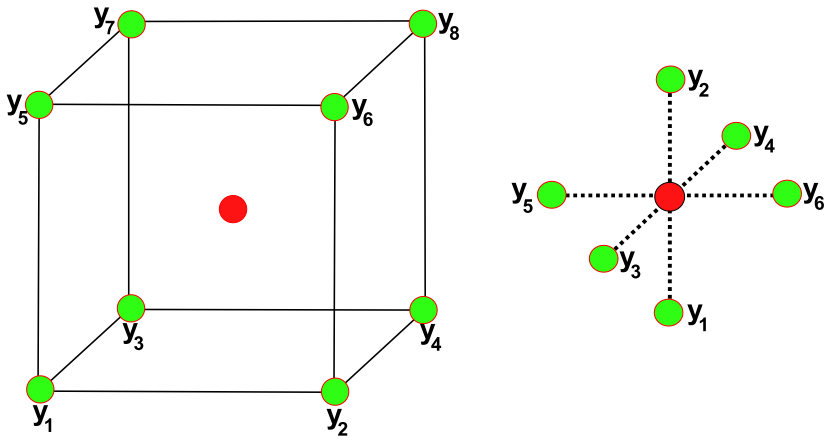

Figure 9: Illustration of using full factorial design within DoE (left hand side) and 'one factor at a time' (right hand side) in the parameter space. It can be seen that in the case of DoE the parameters are covering the whole three-dimensional parameter space.

Additionally, in typical one-factor-at-a-time designs, one point of the factor room is chosen to be the initial point and all the variations are referred to this initial point. The problem in many cases is that it is unclear what happens if another initial point is chosen. In contrast, in DoE the whole factor room is investigated and the effect of the respective factors is investigated separately. This is ensured by creating an orthogonal DoE where the columns are not correlated to each other (i.e., linearly independent).

3.9.1 Basic terminology

The first step in creating a DoE is to define the physical system and the surroundings (boundary conditions). In this, the following terms are established:

- Parameter: The sum of all inputs.
- Factor: Parameter which appear in the DoE.
- Level: Settings of the factors.

- Effect/main effect: Impact of a factor to a system. The effect characterizes the middle change of attribute response according to a level variation.
- Correlation effect: If one factor depends on the setting of the other factors.
- Response/attribute: Dependent variable for the quantification of the system. The function of a system can be quantified by one or more attributes, which have to be continuous to make an effect analysis possible.

Effect diagrams are standardized and demonstrative diagrams of the effects. On the horizontal axis the factors are plotted one by one; in each case with the investigated levels. The unit is dimensionless. The vertical axis shows the value of the responses. If there are several attributes responses, separate effect diagrams have to be drawn. The slope of the lines in the effect diagrams is characteristic for the appearing effect. Diagrams of this type can also be used to depict correlation (Figure 10 (2)). If the lines in the effect diagrams are parallel there is no or little influence of the factors to each other. Otherwise, there is an influence (correlation).

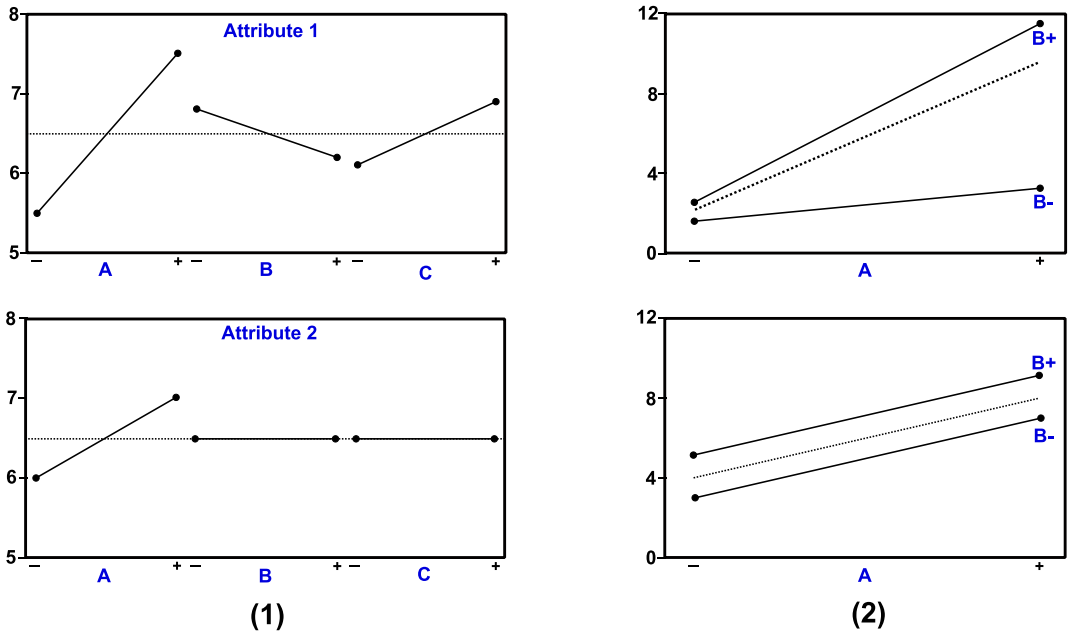

Figure 10: (1) Illustration of two effect diagrams (attribute 1 and attribute 2) with three factors and two levels. The steeper the slope the bigger the influence of the factor to the attribute. If there is no slope there is no influence of this factor to the attribute. (2) Illustration of two main effect diagrams where the influence of factor B to factor A is shown. If the lines of B are parallel to the line of A there is no influence. Otherwise there is an influence, especially when the lines are crossing.

3.9.2 DoE models

Basically a design can be interpreted as a system of linear equations, where every experiment stands for one equation. The following chapters provide a short overview over the most important model used in praxis.

Linear model

The “linear model” includes all the main effects and the correlation effects. The response obeys the following formula:

$$y = c_0 + \sum_{i=1}^{n_f} c_i x_i + \sum_{i=1}^{n_f-1} \sum_{j=i+1}^{n_f} c_{ij} x_i x_j + \varepsilon \,, \qquad (39)$$

where $c_0, c_1, \ldots . c_{n_f,} c_{12}, c_{13}, \ldots . c_{n_f-1 n_f}$ are model constants, ε is the variation, y is the response and x_i are the factors.

The linear model is not able to describe non-linear relations in a sufficient way. Nevertheless, this mode is often used and has several benefits. The non-linearity of the relations between the factors is often overestimated and the correlation effects are mostly underestimated. Due to that, the linear model can provide surprisingly good results. Besides, the linear model is descriptive and uncomplicated, which makes it easy to understanding the relations between the factors.

Screening DoEs

The strength of screening designs is the investigation of a large number of factors with a minimum of effort and information loss. Screening is mainly used for the determination of important effects. The initial point is always a full factorial design, where the number of constants are calculated as ${n_l}^{n_f}$. The full factorial design is often used by a small number of levels and factors and if the correlations between the parameters are unknown. A full factorial design for four factors and two levels is shown in Figure 11.

A	B	AB	C	AC	BC	ABC	D	AD	BD	ABD	CD	ACD	BCD	ABCD	y
-	-	+	-	+	+	-	-	+	+	-	+	-	-	+	y_1
+	-	-	-	-	+	+	-	-	+	+	+	+	-	-	y_2
-	+	-	-	+	-	+	-	+	-	+	+	-	+	-	y_3
+	+	+	-	-	-	-	-	-	-	-	+	+	+	+	y_4
-	-	+	+	-	-	+	-	+	+	-	-	+	+	-	y_5
+	-	-	+	+	-	-	-	-	+	+	-	-	+	+	y_6
-	+	-	+	-	+	-	-	+	-	+	-	+	-	+	y_7
+	+	+	+	+	+	+	-	-	-	-	-	-	-	-	y_8
-	-	+	-	+	+	-	+	-	-	+	-	+	+	-	y_9
+	-	-	-	-	+	+	+	+	-	-	-	-	+	+	y_{10}
-	+	-	-	+	-	+	+	-	+	-	-	+	-	+	y_{11}
+	+	+	-	-	-	-	+	+	+	+	-	-	-	-	y_{12}
-	-	+	+	-	-	+	+	-	-	+	+	-	-	+	y_{13}
+	-	-	+	+	-	-	+	+	-	-	+	+	-	-	y_{14}
-	+	-	+	-	+	-	+	-	+	-	+	-	+	-	y_{15}
+	+	+	+	+	+	+	+	+	+	+	+	+	+	+	y_{16}

Figure 11: Full factorial design for four factors A,B,C,D and two levels.

To reduce the number of combinations of the factors, a so called fractional factorial design can be used. The idea of fractional factorial design is to include only those columns with the main effects for the placement of the factors itself; the other combinations (columns in Figure 11) are chiefly important for the determination of the constants of higher order (see equation (39)). Based on that, an unimportant column (as described above) is declared as the placement for the next factor. This procedure is shown in Figure 12, where one can see that all the correlations between three factors are written down (A, B, AB, C, AC, BC, ABC) and then the column corresponding to the highest order (in this case ABC) is declared to be the fourth factor. The remaining correlations are treated similar (see Figure 12). The system of equations according to Figure 12 consists of 16 unknown and 8 equations. The terms of the dual correlations are inseparable connected to each other.

In sum, the price for higher efficiency in this case is the introduction of correlations. For the description of the type and amount of the correlation mixing every fraction factorial design can be assign to a resolution class. The resolution classes are listed in Table 4. Resolution below III can be seen as useless, resolution above V as wasteful [266]. It is common to label a fractional factorial design after his number of possible combinations:

$$n_l{}^{n_f - p}, \qquad (40)$$

where p is the fractional reduction number.

A BCD	B ACD	AB CD	C ABD	AC BD	BC AD	ABC D	y
-	-	+	-	+	+	-	y_1
+	-	-	-	-	+	+	y_2
-	+	-	-	+	-	+	y_3
+	+	+	-	-	-	-	y_4
-	-	+	+	-	-	+	y_5
+	-	-	+	+	-	-	y_6
-	+	-	+	-	+	-	y_7
+	+	+	+	+	+	+	y_8

Figure 12: Illustration of a fractional factorial design for four factors and two levels.

Resolution	Ability
III	Main effects are correlated with two-factor interactions
IV	Main effects are correlated with three-factor interactions and two-factor correlations are correlated to each other
V	Main effects are correlated with four-factor interactions and three-factor interactions are correlated with two-factor interactions

Table 4: Resolution according to fractional factorial DoE.

Quadratic model

If there are non-linear connections between a factor and an attribute, the linear model necessarily introduces an error. To capture nonlinear effects to some extent, quadratic terms of the main effects are added. In comparison to the linear model with interactions the number of model constants of the quadratic model is not increasing that much, as can be seen in Figure 14.

Common designs for DoEs

The Central-Composite-design CCD is based on a design with two levels. As can be seen in Figure 13(a), factor settings in a CCD consist of a "cube" like in the linear case (see Figure 9) and a "star". The "cube" has typically a resolution of IV or V. The "star" starts from the center point and spread out in every direction beyond the cube faces. In the center point all factors are set at their midpoint which means $\frac{A_{Level1}+A_{Level2}}{2}$. The realization of this kind of star is in praxis often not possible and thus the fcc-CCD as can be seen in Figure 13(b) is used, where the "star" only extends as far as the faces of the cube. The downside is that in this case the quadratic effects are correlated among each other.

If the corners of the factor space are important, the Box-Behnken-Design is applied. The middle point of every cube edge and also the center point are taken into account, as it is illustrated in

Figure 13. This implies that there is a good resolution of the interactions and the quadratic effects as well. The Box-Behnken-Design is most useful for a low number of factors [267].

Within the Monte-Carlo-Design a random generator is used to decide what factor settings should be taken. This principle is illustrated in Figure 13(d). Because the settings are chosen randomly and independently of each other, there are just weak correlation effects. The disadvantage is a large number of trial runs.

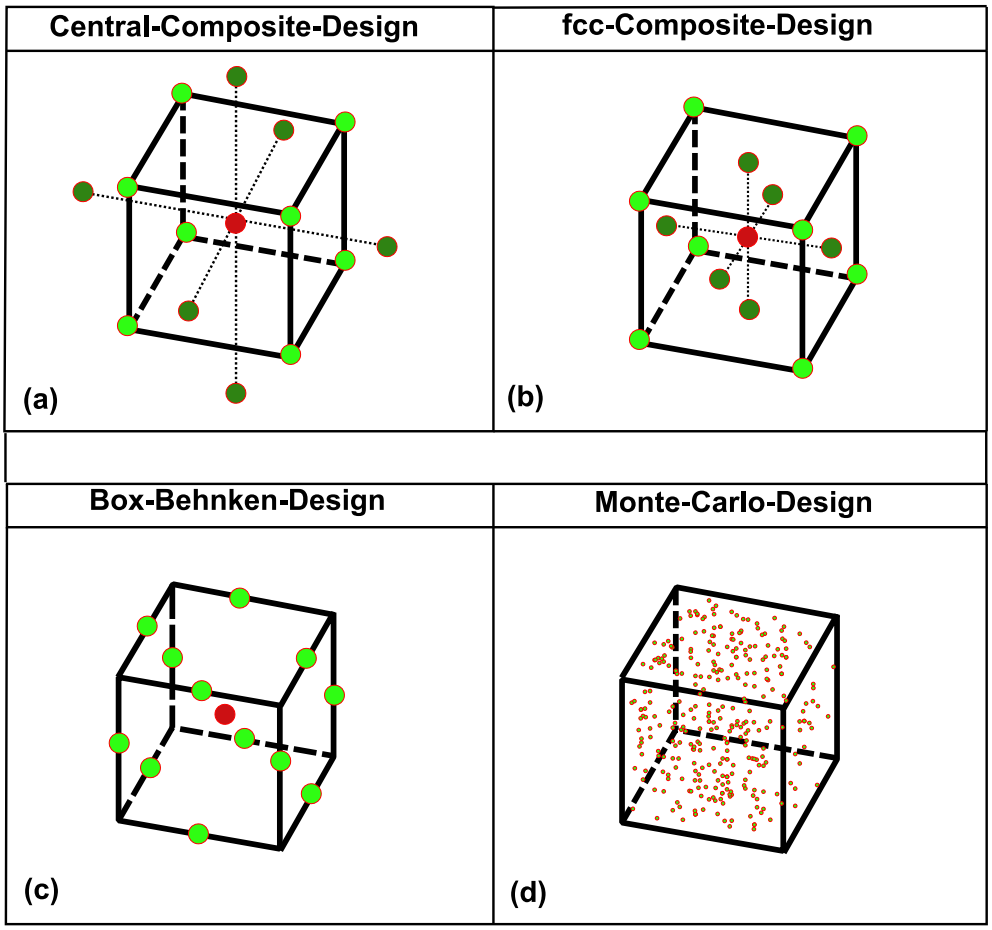

Figure 13: Different attempts to realize a DoE which includes nonlinear interactions. (a) The Central-Composite-Design is a combination of a two level experimental design (cube) and addition settings (star). (b) The Face-Centered-Central-Composite-Design is based on the same principle as the Central-Composite-Design except that the star does not leave the borders of the cube. (c) The Box-Behnken design includes the middle points of the cube edges instead of the corners. (d) In the Monte-Carlo-Design the factor settings are chosen randomly.

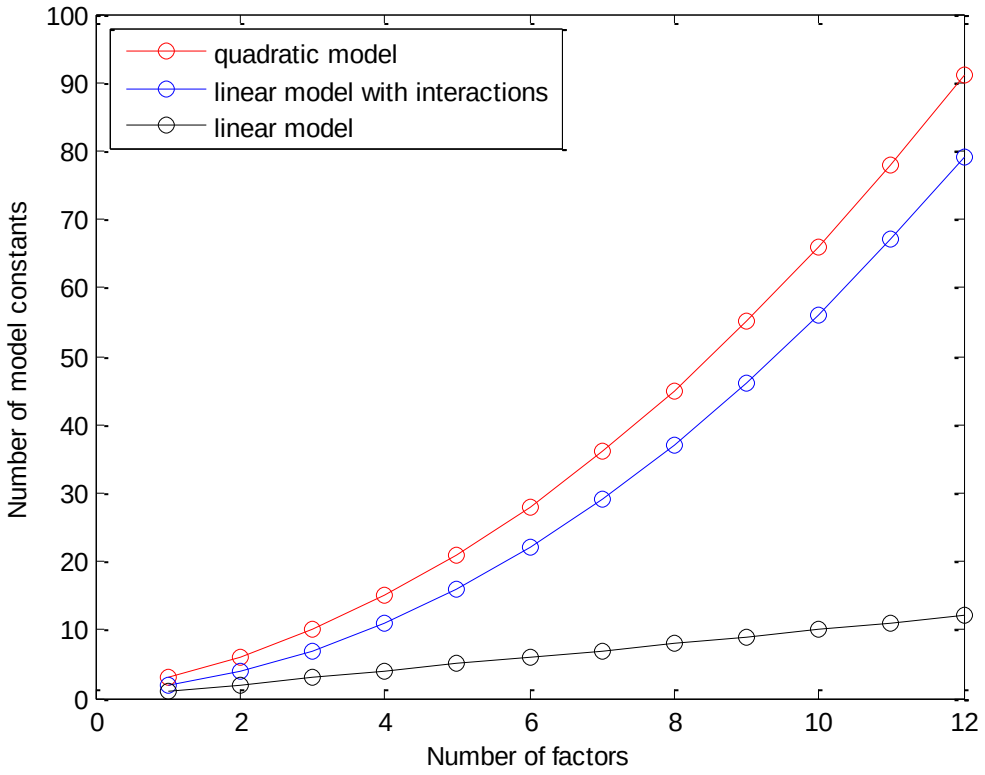

Figure 14: The increase of the number of model constants in the quadratic model ($n_m = \sum_{i=1}^{n_f+1} i$) and the linear model ($n_m = 1 + \sum_{i=1}^{n_f} i$) with interactions are in both cases progressive. The number of constants increases linear with the number of factors in the linear model without interactions.

3.9.3 Bayesian experimental design

Due to the high number of options to pick a DoE, it is natural to ask what would be the best choice. The answer of this question can be determined with the concept of Bayesian experimental design (BED). As the name already reveals, BED is based on Bayes probability theory and Bayes inference[268], [269]. It offers an excellent possibility to make an optimal decision under uncertainty and is therefore a helpful tool in designing an experimental plan with respect to maximizing the expected utility.

By using Bayes' theorem

$$p(\theta|y,\xi,\mathbb{B}) = \frac{p(y|\theta,\xi,\mathbb{B})p(\theta|\mathbb{B})}{p(y|\xi,\mathbb{B})}, \tag{41}$$

the expected utility of an experimental design ξ can be defined as

$$U(\xi) = \int p(y|\xi, \mathbb{B}) U(y, \xi) dy. \quad (42)$$

θ is the vector of the parameters, y is the observation or response, ξ is the chosen experimental design, $p(\theta|y, \xi, \mathbb{B})$ is the probability density function PDF for getting the response y by given parameter θ and the design ξ, $p(\theta|\mathbb{B})$ is the prior PDF, $p(y|\xi, \mathbb{B})$ is the marginal PDF in observation space or Likelihood function defined by:

$$p(y|\xi) = \int p(\theta|\mathbb{B}) p(y|\theta, \xi) d\theta\,, \quad (43)$$

$p(y|\theta, \xi, \mathbb{B})$ is the posterior PDF and $\mathbb{B}$ describes all the other premises. The treatment of the expression $U(y, \xi)$ in equation (42) using the Shannon entropy can be found in Appendix 7.4.

4 Material and Methods

4.1 Set-up of the rotating drum

The rotating drum equipment and the additional components to fix it are illustrated in Figure 15. Two drums were made, consisting of two Plexiglas® discs (XT transparent 0A000 GT) with a diameter of 300mm and a Plexiglas® tube (XT transparent 0A000 GT) with a diameter of 250mm and a length of 150mm. The discs and the tube are fixed together with four threaded bars and nuts. Additionally the discs are countersinked with the radius of the drum to make the fixation more stable. The front disc is removable such that it can be easily filled with particles and re-sealed particles. To generate the rotating motion a Heidolph RZR 2102 stirrer is used. The angular rotation velocity can be regulated continuously, the set value is maintained constantly even for fluctuating and relatively high torques. The drum is fixed to the stirrer via a shaft installed on one drum disc. The stirrer itself is fixed on a frame construction made of white coated wood chipboard as can be seen in Figure 15b.

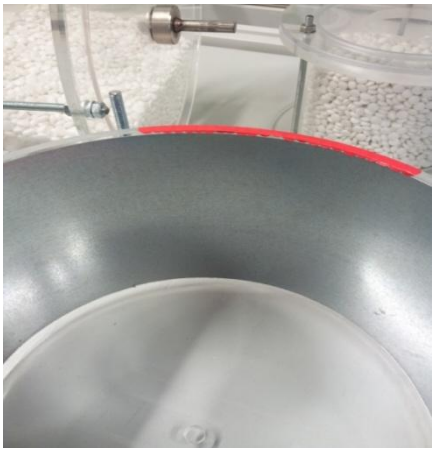

(a)

(b)

(c)

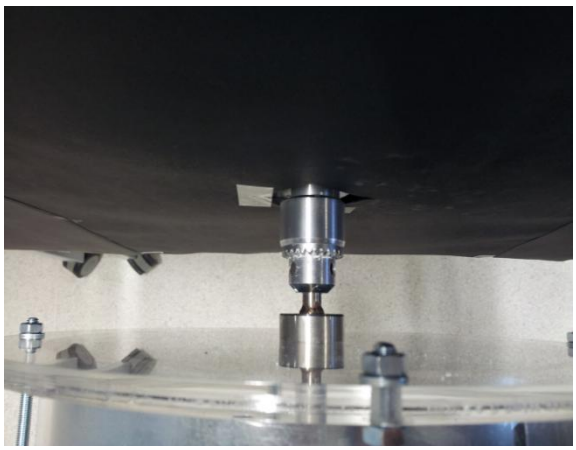

(d)

Figure 15: Pictures of the construction of the drum. (a) Fixing the red points on the edge of the drum. The steel sheet surface within the drum can also be seen here. (b) Heidolph rotary stirrer and its mounting. (c) Setting face of the rotary stirrer. (d) Mounting of the rotating drum on the rotary stirrer.

To change the surface roughness within a drum, a steel sheet was mounted along the drum circumference. Steel is chosen because it is the most common material for coating drums in the pharmaceutical industry. The parameters of these two materials can be found in Table 5.

Three types of particles have been used for the simulations:

- Silibeads 6mm Type M (Sigmund Linder GmbH, Warmensteinach, Germany)
- Thrombo ASS 100mg (G.L.Pharma, Lannach, Austria)
- Self pressed RCPE tablets(RCPE GmbH, Graz, Austria)

The particle parameter of those three particles can be found in section 4.5.1.

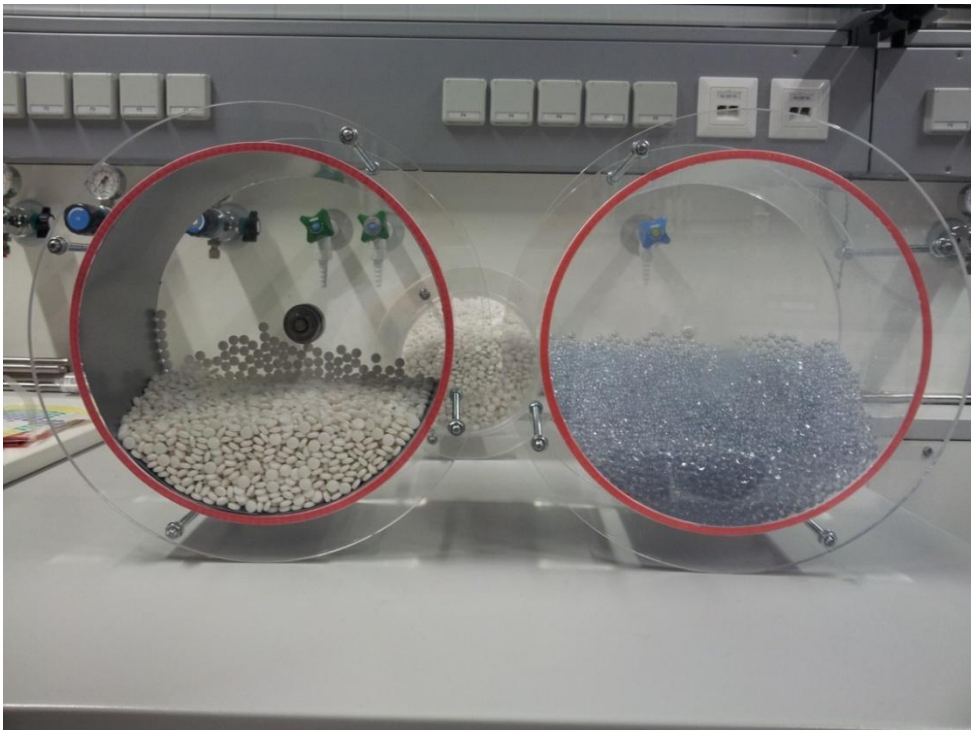

Figure 16: Pictures of the drums used for the experiment. Left hand side: Drum with steel sheet filled with the Thrombo tablets. Right hand side: Drum filled with Silibeads glass spheres.

Plexiglas® (XT transparent 0A000 GT) [270]
ρ_P = 1190 kg/m^3
Po_P = 0.37
SM_P = (1.7*10^6)Pa
Steel sheet ATSTM-A36 Grade 304 [271]
ρ_{St} = 8000 kg/m^3
Po_T = 0.265
SM_T = (8*10^{10})Pa

Table 5: Properties of the surface material used in the interior of the drum.

4.2 Image capturing

The pictures of the experiment were taken with a digital single-lens reflex camera (Nikon D-60 with lens Nikon DX AF-S NIKKOR 35mm 1:1.8 G). The three most important settings for taking the images are aperture, shutter speed or exposure time, and sensor sensitivity (ISO). A long exposure (slow shutter speed) means that a lot of light can hit the sensor. In order to get sharp pictures of moving objects, one has to set a short shutter speed. The aperture determines the amount of light that passes through the lens, and also influences the depth field.

For taking the images, shutter priority mode (termed “S”) has been used, where the shutter speed is chosen manually while the camera sets aperture accordingly for correct exposure. For all images, a constant ISO of 800 was chosen.

Slow shutter speed results in a frozen effect of the image while fast shutter speed creates the impression of movement. In Figure 17 results for different shutter times are illustrated. A blurring effect above a certain shutter speed appears. This is advantageous in the present work, as it introduces a time-averaging effect. Due to that, a shutter time between 1/2 and 3 seconds has been chosen.

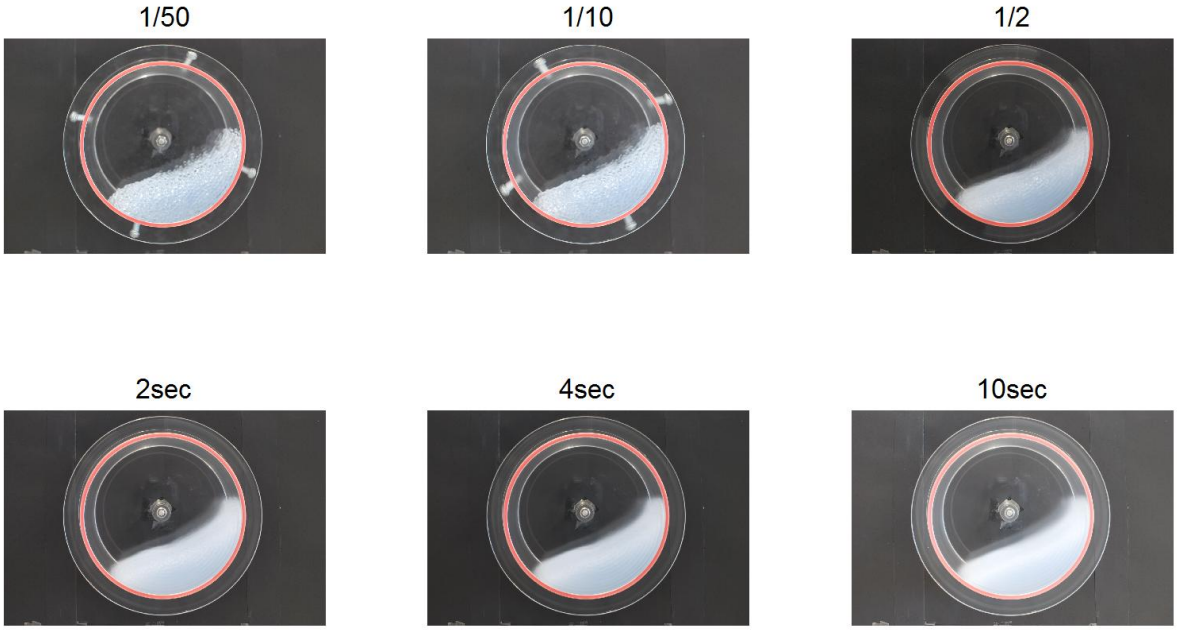

Figure 17: Illustration of the effect on different shutter speed.

To reduce disturbing reflections of the surrounding in the recorded pictures, a black construction paper sheet was fixed behind both camera and drum, see Figure 18. Together with an optimal illumination of the objects, the reflectance can be reduced to a level where provide no further problem in post-processing. Figure 19 shows the large impact of using a dark background behind the camera.

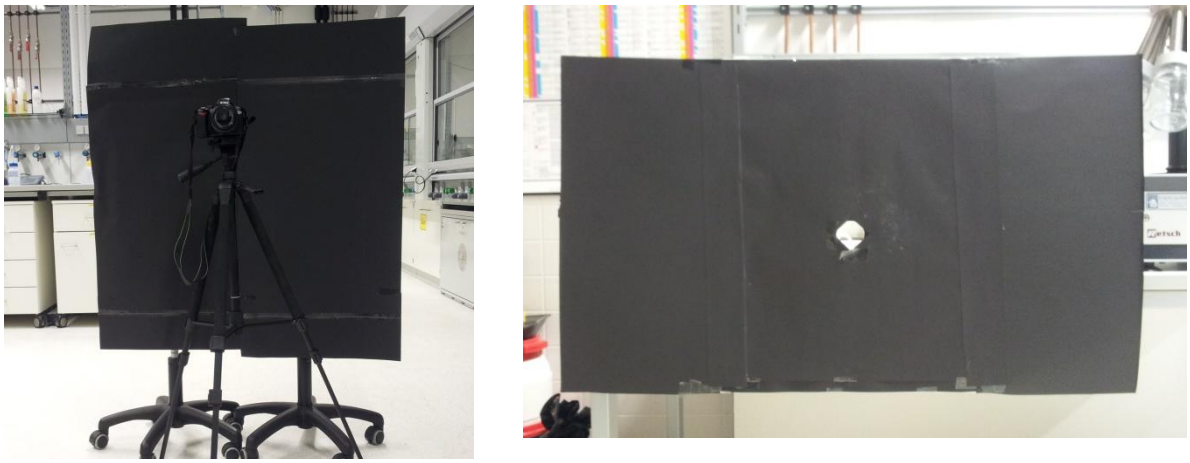

(a) (b)

Figure 18: Construction of a dark background to reduce the reflectance of Plexiglas. (a) Black construction paper mounted on chairs with wheels and set behind the camera. (b) Black construction paper fixed on the wood frame construction where the drum is fixed.

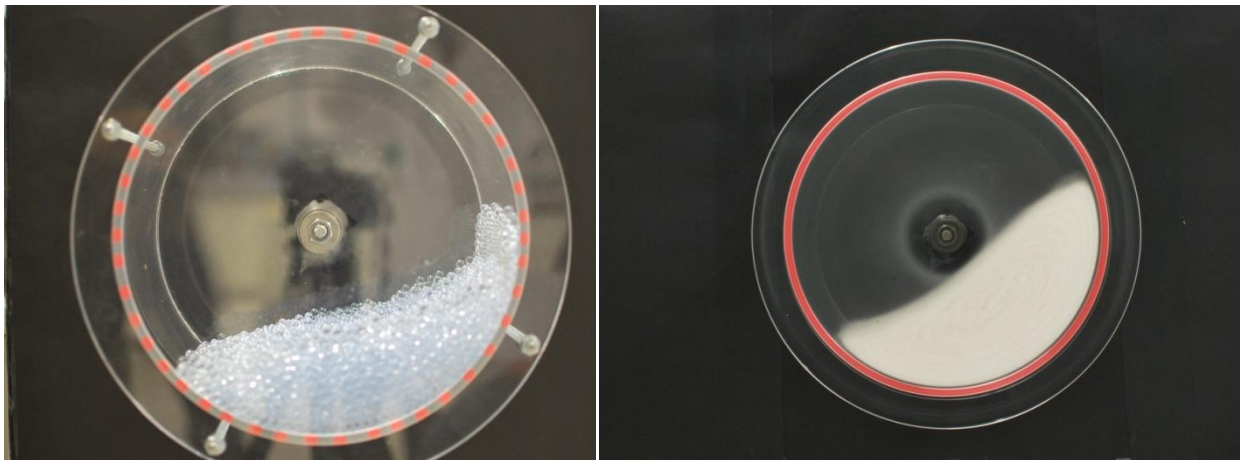

(a) (b)

Figure 19: Illustration of the difference between using no reflectance reducing construction (a) and using one (b).

4.3 Image processing in MATLAB

After making pictures of the particle arrangement in the rotating drum, the angle of repose and the center of area were measured. To do this in a reliable, fast and objective way, an automatic post-processing algorithm was developed and implemented in MATLAB v.2013b (The Mathworks Inc, Massachusetts, USA). It should be noted that for this to work, the different areas in the image have to have a sufficiently high contrast. In order to handle problematic images with low contrast and where transition between the particle arrangement and the rest are beyond recognizition, an additional algorithm needing some manual decisions has been implemented.

The idea was to convert the input-image into a binary image where just the area of interest gets the values of 1 and everything else 0. Acting on this assumption a detailed investigation of the angle of

repose and the center of area can be initiated. The whole detection algorithm can be found in the Appendix 7.5.2. (“AoR_mos_cen.m”)

The first step was to improve the contrast of an image by using the Image Processing Toolbox in Matlab. In general, a digital image is described by a three dimensional matrix. The first two dimensions describe the location of the pixels, the third dimension describes the red, blue and green component of the pixel color. Thus, the matrix has a size of [number of row pixels]-by-[number of column pixels]-by-3. For the further steps, it is easier to work with an intensity image (gray scale image). There, the image is represented by a two dimensional matrix where every entry gives the brightness of a pixel is. The values are between 0 (black) and 255 (white). (The conversion from colored image to gray scale image is done with the Matlab function “rgb2gray.m”).

One of the inputs of the function ‘AoR_mos_cen.m’ is the image file of the moving particles in the drum. The aim is to detect and extract the particle ensemble. Therefore, the image was manipulated such that until only the area of interest remains. First and foremost, reference point in the image had to be found. The idea is to find the smallest distinctive circle in the image, which here relates to the circumference of the drum, and use the center point as reference. To make this circle even more distinctive, red dots were attached, see Figure 20.

Figure 20: Illustration of an example image of the rotating drum with red fixed points on the edge of the drum in order to increase the contrast and to make the search of circles easier.

The detection itself (“imfindcircles.m”)was based on Circular Hough Transformations [272–274], which is available in the .Image Processing Toolbox in the Matlab version of 2012 and later. The algorithm was effective if the input parameters were chosen sensitive enough. In particular, one of the inputs of ‘*imfindcircle.m’* was the allowed radius range allowed for the potential circles.. This

range has to be chosen small enough to reduce computational time, and high enough to ensure the detection of the circle of interest. The radius range input had the unit of pixels. In order to estimate it in a proper way, a distance tool within the Image Processing Toolbox was used (see Figure 21):

```
imshow('test_picture.jpg');
h = imdistline(gca);
api = iptgetapi(h);
fcn = makeConstrainToRectFcn('imline',...
                             get(gca,'XLim'),get(gca,'YLim'));
api.setDragConstraintFcn(fcn);
```

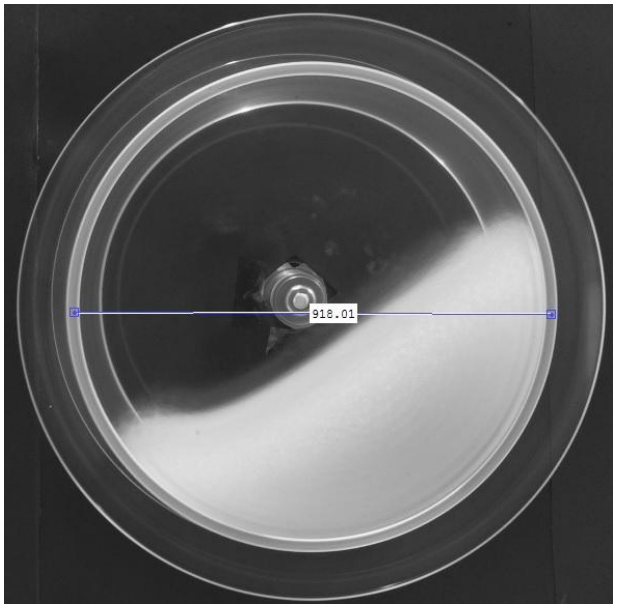

Figure 21: Manual determination of a reference in MATLAB. The line can be placed flexibly, the current value of the length in pixels is provided directly on the interface.

Under the premise that the pictures were taken in series with similar magnification, the determination of the radius range only has to be done once for the whole pool of pictures investigated for one statistical run.

Additionally the image has to have a certain quality regarding mainly well-defined edges, low random noise, and high contrast. With some input values, such as 'Sensitivity' or 'EdgeTreshold' the accurateness of the circle detection can be steered, but this increases the risk of false detections. To detect outliers, the deviation of the detected drum radii is monitored. This radius deviation should not be high if the detection works accurately. An extensive documentation of these parameters can be found in function in Appendix 7.5.2. In most cases, more than one circle will be found. In general the most correct radius is the first entry in the output vector '*radii*'. If this did not hold true, the choice is corrected manually. The detection of the red circle had a limitation: due to the fact that it is actually no circle but rather a circular ring, its finite expansion will generate an intrinsic

uncertainty in the detected radius. The deviation in radius will also influence the accurateness of the center of area, which is discussed later on.

To further increase the accuracy, knowledge of the color of the bonded points is utilized. The matrix corresponding to the red channel. Thus, to detect the red circular ring, it was searched for areas that had high intensity values in the matrix corresponding to the red color channel, and not so high intensity values in the other two matrices of the color image. After this “red color masking” filtering process, the resulting binary matrix provided information about the real extension of the circular ring. The needed intensity threshold values were chosen manually in order to create an optimal filtering. Often some random points outside the circular ring are falsely taken into account, but by applying a media filter afterwards this did not make any further problems. As Figure 22 illustrates, the implementation of the “red color masking” ensures that the found circle was located directly on the border to the particle ensemble, making the automatic circle detection more reliable.

During the analysis in the current work the variation in radius (taken over 30 images) was never above one pixel, showing that the quality and reliability of the radius detection works highly satisfying.

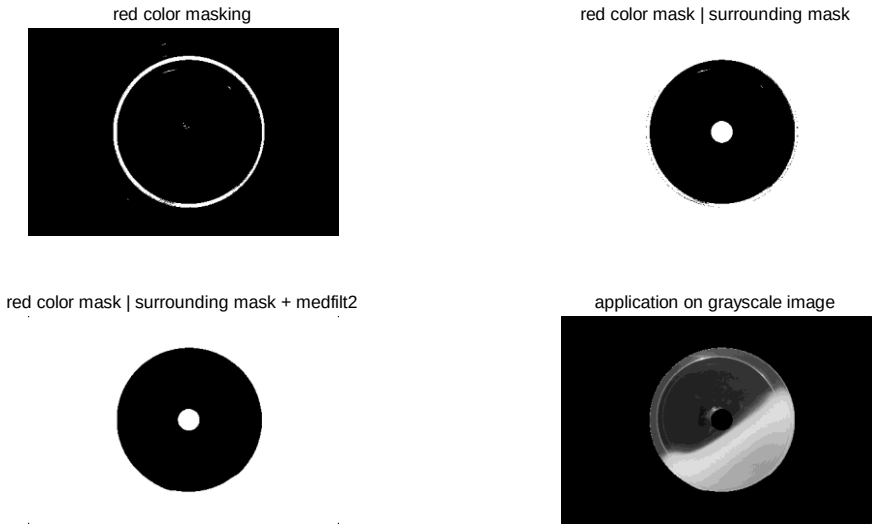

Figure 22: Illustration of the use of the ‚red color masking‘.

The output of ‘imfindcircles.m’ is the radii and the centers of the found circles. With the knowledge of the borders of the particle ensemble to the rest, one is able to eliminate unwanted areas. Such areas were everything outside the circle, and the area around the middle of the circle where axle was mounted, as can be seen in Figure 22. It has to be added that when excluding the middle area, depending on the fill level it can happen that areas of the particle ensemble are included. Such an improper choice of the nut radius was recognized and corrected.

Before and after applying the created masks to switch off unwanted areas it is advisable to improve the contrast and reduce noise. To reduce the noise of randomly occurring white and black pixels (so called 'salt and pepper noise') a median filter was used ("medfilt2.m").

This filter is known to simultaneously reduce noise and preserve edges. Alternatively the 'wiener2' filter could be used. As can be seen in Figure 23, the noise can be reduced in such a way that the transitions between dark and bright areas get accurately defined. Loosely speaking the median filter averages the pixel values of a before defined quadratic area. This kind of filtering can also be useful if in a binary image some random small areas during a masking operation still are in the wrong logical state due to unwanted effects appearing in the shooting process of the picture.

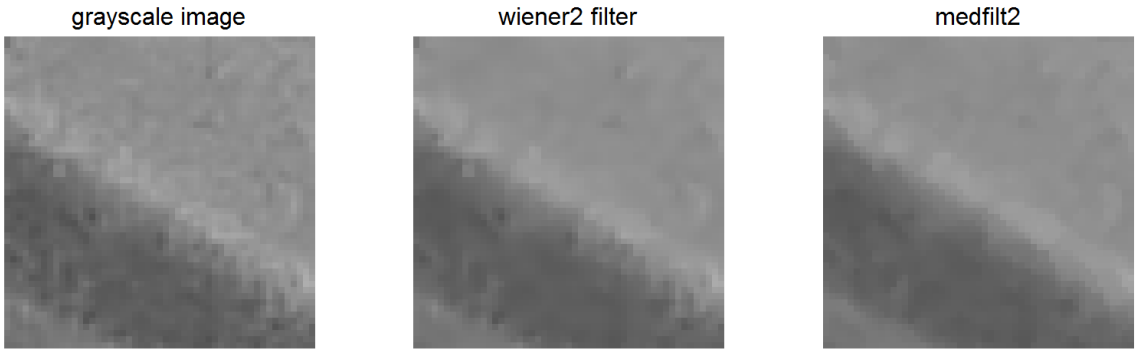

Figure 23: Application of "wiener2" and "medfilt2" filters on a gray scale image in Matlab to reduce noise. Here, the medfil2 filter gives best results.

To increase the contrast of the image the function "imadjust.m" provided in Matlab is used, where 1% of the data is saturated at low and high intensities. The application to an example picture can be seen in Figure 24.

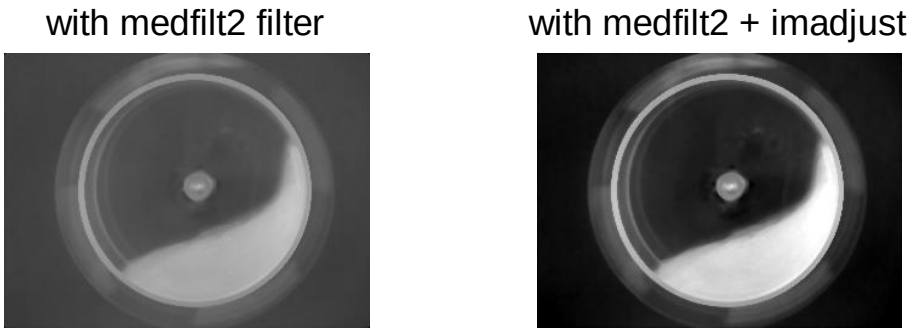

Figure 24: Illustration of 'imadjust.m' to improve the contrast of an image.

The algorithm to detect the angle of repose and the center of mass provides two options to handle certain problems. The first one (in the program termed 'handmade') is applied when artifacts may appear in the image. For more specification about those problems it is referred to chapter 4.4. The

second one (called ‘background’) is used for quite problematic input images, where contrast is hardly present and the particle ensemble merges with the environment. In the present work this found application in self-pressed tablets, which showed a high degree of abrasion. The abrasion led to a powder layer covering the drum walls, to the point where there was nearly no difference to the tablet bed. The whole problem and the solution are discussed in chapter 4.4. It has to be mentioned that only one (“handmade” or “background”) can be activated at a time.

In the next step, the image is converted into a binary (black/white) image (“im2bw”).
The principle is shown in Figure 25.

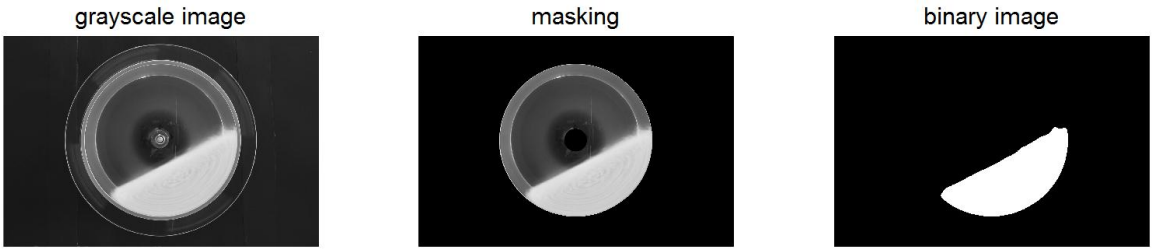

Figure 25: Illustration of the masking of unwanted areas and conversion into a binary image. A result such as on the right-hand side is well suited for the further processing.

One main goal is to extract the angle of repose. Starting from a binary image such as in Figure 24(right), the idea is to scan every column and detect the appearing black/white or 1/0 transitions. Every column was investigated separately from top to bottom. In order to detect the 0/1 transition, the Matlab function ‘diff.m’ is applied. By doing this for all columns, the bed shape of the particle arrangement can be reconstructed. To determine only the surface area, just the first appearing 0/1 transition was taken into account.

If an artifact or similar was still present in the image, there are more than two 0/1 transitions. Therefore, at four transitions, the algorithm will take the third one and at six transitions it will take the fifth one, and so on.

For further investigations, the data curve was smoothed (using either “smooth.m” or an interpolation function such as “interp1.m”. In the current work “interp1.m” had been used.
It is not strictly necessary but produces higher-quality curves later in the evaluation, while generating hardly any information loss.
When the points of the tablet bed top curve is available, it is possible to make a linear fit in different ways. In the current work, two angles of repose were used, one determined from a linear fit of the whole data points and the other determined from a linear fit just including data points located in the middle of the particle bed. The data points starting from the first quarter to the third quarter of

the whole range were taken. Both methods were based on a least square fit algorithm (using "polyfit.m")

The result of the whole algorithm and the difference between the two fitting methods are applied on the image in Figure 26. The angle of repose is calculated via the slope of the linear fit curve which is the first entry of the coefficient p_1 of the polyfit-function:

$$AoR = \tan^{-1} p_1. \qquad (44)$$

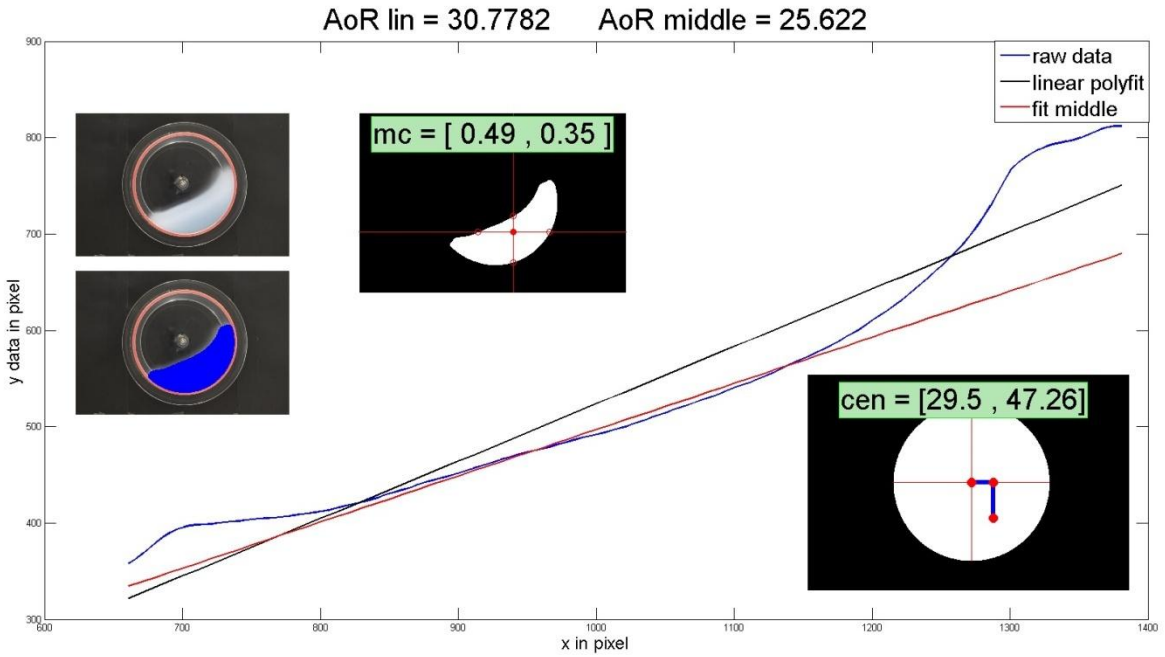

Figure 26: Illustration of the output plot of AoR_mos_cen.m where one can see the data points of the particle arrangement, the two fitted data curves (one taking the whole data points into account, the other just the data point in the middle of the particle arrangement), the grayscale example image on the left hand side on the top and beside the binary image. With the binary image one get the possibility to control if the algorithm work correct and switch off the right areas.

As one can see in the example in Figure 26 the linear fit of the data points in the middle area of the particle arrangement describes the angle of repose in a qualitatively other way. For the sake of simplicity the angle of the repose over the whole region is noted down as AoR and the angle of repose over the middle region is noted down as AoR_middle. It also has to be mentioned, that the AoR always correspond to the lowest mean square deviation according to the representation of the particle ensemble surface, because it takes all the data points into account. This fact does not automatically leads to the best quantitative judgment of the angle of repose. Especially if the system is in the cascading regime a small part of the particle will remain relatively high in the drum, which automatically increases the angle of repose in a way that could be too much. But I think this

does not matter, at least in the current work, because the main aim is to create a simulation which leads to the same behavior as in the experiment and what counts at the end is just the best match between both. By only knowing the AoR one cannot decide if the particle ensemble is in the cascading or the rolling regime (or slumping). With including the AoR_middle in the interpretation it is possible to distinguish between regimes: if AoR and AoR_middle are similar the rolling (or slumping) regime is present; if AoR_ and AoR_middle are significantly different it is likely to be in the cascading regime. By including both angles in the calculations and analysis one can provide a more trustable method according to finding the best bargain between experiment and simulation. If the standard deviation of AoR and AoR_middle within the scope of statistical analysis is relatively high it indicates that the slumping or surging mode is present. In the current work not only the angle of repose has been investigated but also the center of area. If the density distribution of the particle ensemble is isotropic this center of area is equal to the center of mass.

With the Matlab function 'regionprops.m' and by use of the Shape Measurement property 'centroid' it is possible to detect the center of area of the particle arrangement. By knowing the radius of the drum, the detected coordinates of the center of area can be normalized, so that pictures with different drum size and picture size are comparable. The principle is illustrated in Figure 27. It has to be added that for reasons of accurateness the correction due to the finite circumference of the circular ring has to be included in the calculations. The center of area can support the analysis as an additional response in the design of experiment and as a control variable.

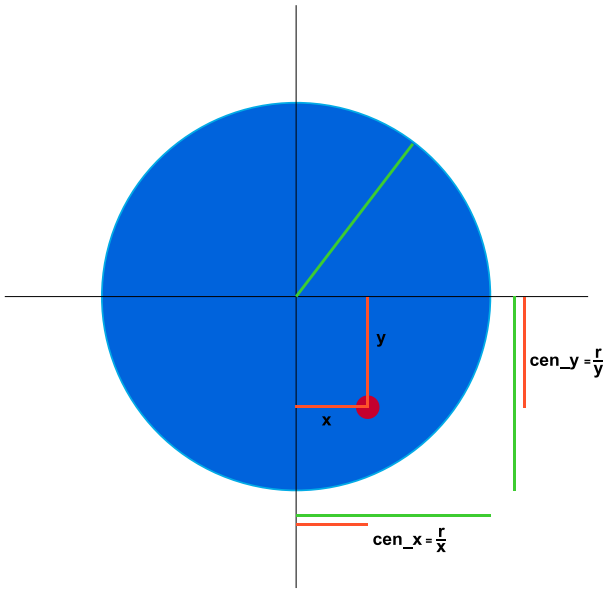

Figure 27: Illustration of the calculation of the x and y coordinate of the center of area. These coordinates are normalized to the drum radius.

Although it is possible in EDEM (commercial software used for the DEM simulations) to give out the coordinates of every single particle it have been decided to analyze the angle of repose and the

center of area via image processing, like for the images made during the experiment. The procedure is very similar as discussed above and works with the same image manipulations like Hough Transformation and filters. In the 'Analyst-mode' in EDEM every particle arrangement according to the used time step can be saved as an image. For this it is advisable to remove the legend and any other unimportant details. Additionally, the opacity of the drum should me turned back to 0, in order to see just the particles. The evaluation of the AoR also works with columns-wise black-white transitions and linear fitting bases on the least square method. The center of area can also be found with 'regionprops.m', but to guarantee coordinates relive to the radius of the drum, as is illustrated in Figure 27, a reference image of the drum has to be included in the calculation. For this one has to turn the opacity of the drum to 1, save this image and afterwards include it in the statistical analysis. It is advisable to create such a reference image for every DoE-analysis to avoid a systematical error.

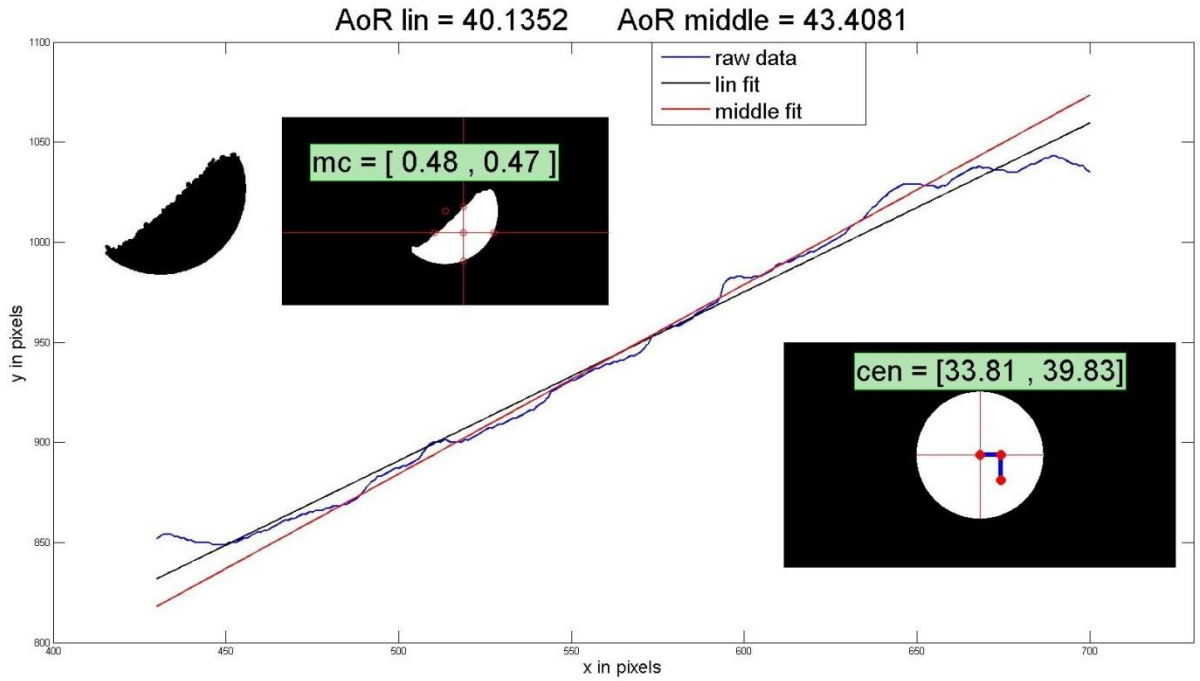

Figure 28: Illustration of the output plot of AoR_mos_centroid_EDEM.m where one can see the data points of the particle arrangement, the two fitted data curves (one taking the whole data points into account, the other just the data point in the middle of the particle arrangement), the grayscale example image on the left hand side on the top and beside the binary image.

4.4 Appearance of Difficulties

As described above a logical variable called 'handmade' was introduced, where it is possible to switch off artifacts in the image. During the image recording it could happen that some areas outside the particle ensemble which are highly reflective get relative high intensity in a grayscale

image and so the ‘im2bw.m’ function in the algorithm cannot distinguish between the particles and those areas. Any other artifacts will be eliminated with ‘medfilt2.m’. In general the drum made of Plexiglas is highly reflective. How to reduce this reflectivity is described in chapter 4.2. So a simple conversion from a grayscale image to a binary image will not work sufficient and reliable. According to that a user defined intensity value can be defined where everything below it becomes 0 and everything above it becomes 1. The allowed values are between 0 and 255. Because the investigated particles are relative bright a good default choice is 180, but it depends on the case under consideration. This problem of artifacts is very easy to recognize, as any detection of shapes is documented in a figure during the analysis of the image and is thus detected by the user immediately.

Figure 29: Illustration the advantage of the variable ‚handmade‘ by the appearance of artifacts.

In the current work self pressed tablets have been investigated and during the experimental execution they had a huge abrasion, which made the pictures difficult to handle because in some areas there was hardly any transition to recognize. Only the knowledge that there have to be a transition makes the pictures analyzable. So at some point the user have to decide where he sets the transition between the particle ensemble and the surrounding.

As can be seen in Figure 30 there are some regions where literally no transition is cognizable. No simple algorithm would be able to separate between the region of interest and the rest, only the experimenter can decide manually. For this reason the user can extract the region of interest by setting polygonal lines into the image which is illustrated in Figure 30(b).

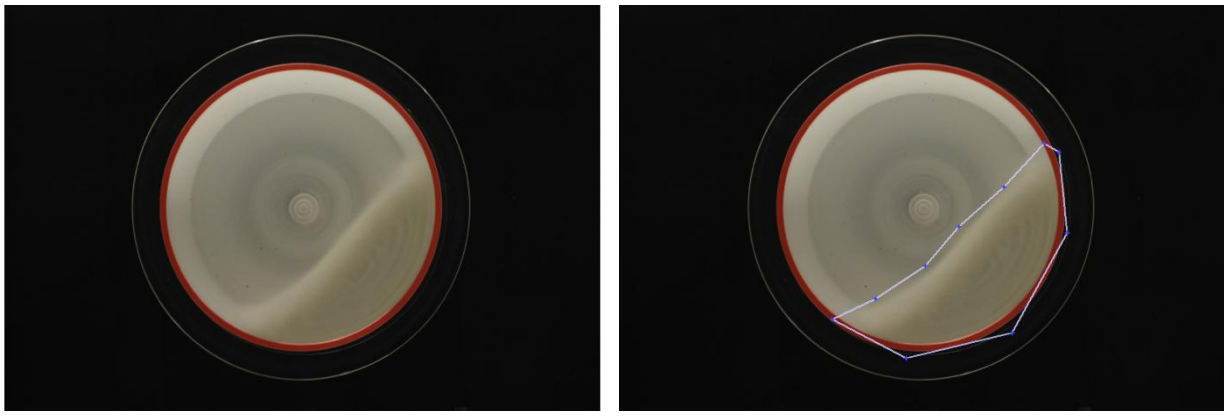

(a) (b)

Figure 30: Image of the self-pressed tablet in the rotating drum. (a) without the polygonal line and (b) with the polygonal line.

To save the data point selected in the region within the polygonal line one have to double click on this region, then the algorithm will continue. It has to be mentioned that the choice for the polygons at the bottom region of particle assemble does not have to be chosen very exactly because the masking done in the algorithm will correct overlaying areas. Afterwards the user has to manually improve the contrast in the bed region of the particles, because in some cases the contrast there is so bad that only the human eye can decide correctly. Therefore a window is opened where a grayscale histogram appears, where the user can decide what grayscale region should be taken into account in the contrast improvement. The advantage of this procedure is obvious: as can be seen in Figure 31 it seems to be that there is a white layer on the particle arrangement. The question that appears is if this layer belongs to the region of interest or not? If the experimenter knows, that it does, he can improve the contrast in a way where this layer will be part of the particle assemble. This way of treatment is illustrated in Figure 31. To save the chosen contrast improvement and to go on with the algorithm one has to close all windows.

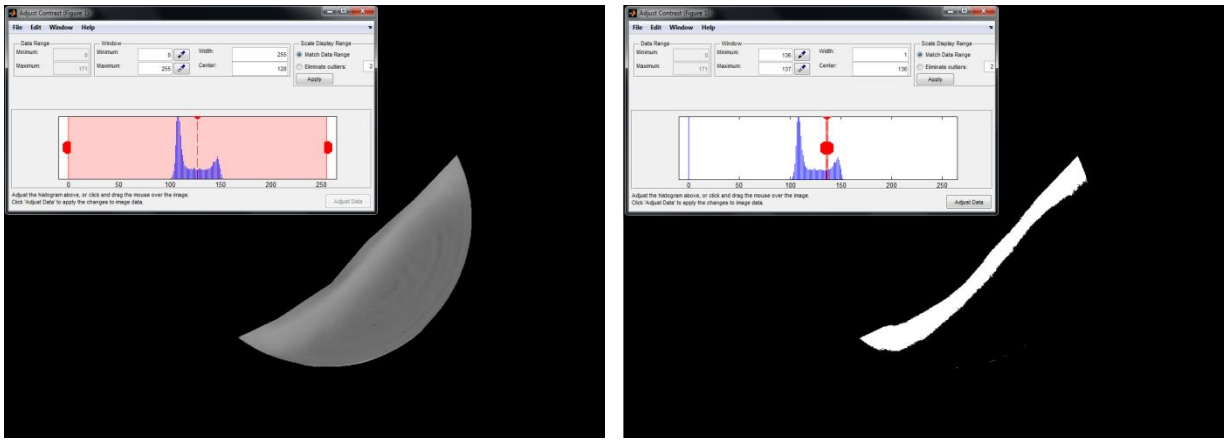

(a) (b)

Figure 31: Showing the area cut by the polynomial line (a) before and (b) after the user controllable contrast improvement.

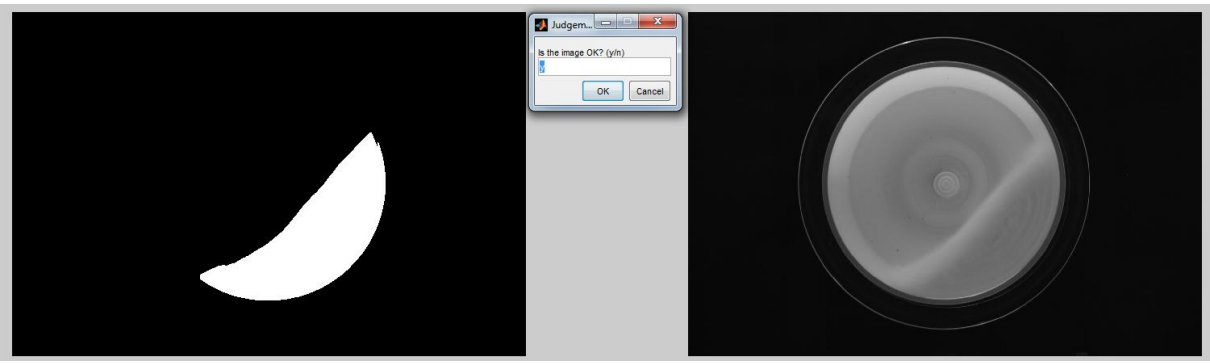

Figure 32: After the contrast improvement one will be asked if the shown binary image should be included in the statistical process.

Then the user will be asked if the manipulations he made are acceptable or not. If not the whole procedure will start again and if he is, the above discussed investigation according to angle of repose and center of area will continue.

4.5 Discrete Element Method Simulations

In the current work, an established commercial software (EDEM 2.5, DEM Solutions Ltd, UK) is used for the DEM simulations.

4.5.1 Including tablet forms in EDEM

In order to include the tablet shape in the EDEM simulations the glued sphere method as already has been mentioned in chapter 3.6 is used. There several spheres are superimposed to one resulting tablet. The possibilities to superimpose spheres are infinite depending on the number of spheres and the different radii one can chose. It is obvious that it also depend on the positions one put the center points of the spheres. In order to have a control over the result of the superimposition it is advisable to create a template of the tablet depending on its dimensions such as high, radius and additionally the crown radius for a biconvex tablet. These tablet parameters can be found in Table 6. After creating and implementing the template in EDEM the next step is to add small spheres in such a way until the superimposion of them a good match according to the template is reached. In the current work the number of spheres to superimpose was chosen to be 10 for both the Thrombo tablet and the self-pressed RCPE-tablet. In order to find the correct positions to include the spheres into interface of EDEM a Matlab code was written. It determines the Cartesian positions to superimpose spheres around a circle. The reference point of the coordinate system is both in EDEM and the Matlab code the vector (0,0,0). The algorithm can be found in Appendix 7.5.6. By trying to find a match between the volume of the template with the volume of the superimposed spheres by consideration of measured mass at the same time, one determines the density of the tablet on the one hand and on the other hand it

offers a opportunity to control the method of glued spheres according to the chosen values such as radius and number of the spheres. The result of the glued spheres method according to the tablets investigated in the current work can be seen in Figure 31. Additionally the associated templates are displayed to show the difference. It is striking that the glued tablet exceed the borders of the tablet, but for a finite number of spheres it is impossible to avoid this in consideration of the consistency of the volume. The uncertainty of the radii and the heights of the tablets arise from the statistical errors of the measurements. All other uncertainties listed in Table 6 are calculated with geometrical properties of the tablets and the Gaussian law of error propagation.

Thrombo ASS 100mg	
R_T = (4.00±0.03)mm	$V_{R,a}$ = (165.91±9.36)mm^3
h_T = (2.25±0.05)mm	$V_{T,Tem}$ = 167.15mm^3 V_T = = (167.03±0.5) mm^3
r_T = (9.64±0.47)mm	RSm_T = 0.0023m
$m_{T,Tem}$ = 0.000226kg	RS_T = 0.00187m NoS_T = 10
m_T = 0.000225kg	Po_T = 0.29
ρ_T = 1350 kg/m^3	SM_T = (2.92*10^6)Pa
RCPE tablet	
R_R = (4.00±0.01)mm	$V_{R,a}$ = (147.28±2.12)mm^3
h_R = (2.90 ±0.04)mm	$V_{T,Tem}$ = 145.60mm^3
$m_{R,Tem}$ = 0.00015kg	V_T = = (145.67±0.5) mm^3
m_R = 0.00015kg	RS_R = 0.001747m NoS_R = 10
ρ_T = 1030 kg/m^3	Po_R = 0.29 SM_R = (2.92*10^6)Pa
Silibead	
R_S = (3.0±0.3)mm	V_S = (904.77)mm^3
m_R = 0.002262kg	Po_S = 0.29
ρ_S = 2500 kg/m^3	SM_S = (2.52*10^7)Pa

Table 6: Listing of all needed tablet parameters in EDEM. Additionally the Poisson ratio and the shear modulus for the respective tablet are listed.

i = T,R,S	T = Thrombo, R = RCPE, S = Silibead
R_i	Radius of the particle i
h_R	Height of the self-pressed tablet
h_T	Height of the disc-formed part of the Thrombo tablet
r_T	Crown radius of the Thrombo tablet
$m_{i,Tem}$	Mass of the template of particle i by specification of Volume and density
$\mathrm{m_i}$	Mass of particle I determined by measuring
ρ_i	Density of particle i
$V_{i,a}$	Volume of particle by analytical calculation
$V_{i,Tem}$	Volume of the template of particle i

V_i	Volume if the glued spheres of particle i
Po_i	Poisson ratio of particle i
SM_i	Shear modulus of particle i
RSm_T	Radius of the middle sphere of the glued Thrombo tablet
RS_i	Radius of the used spheres to create the tablet form of particle i.

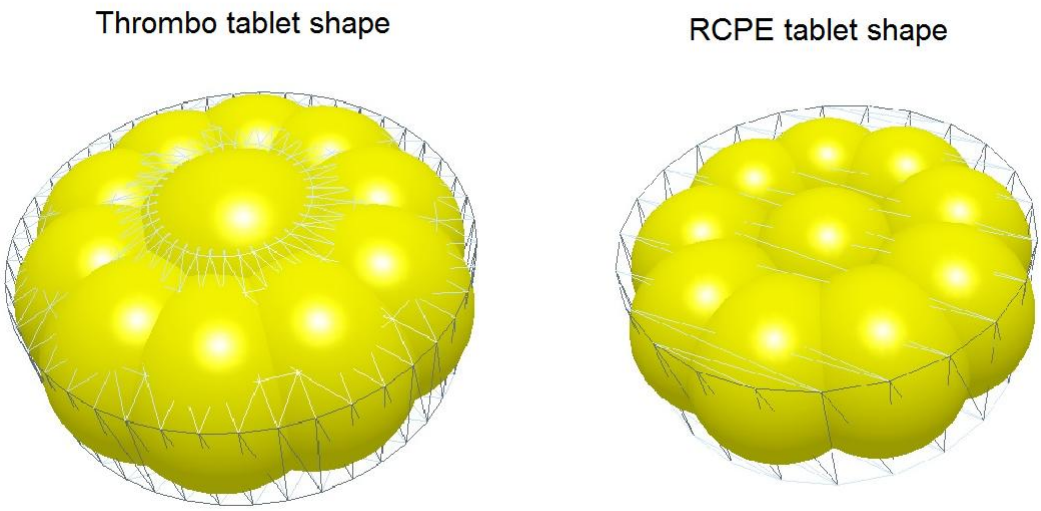

Figure 33: Illustration of the implementation of the tablet form in EDEM with the help of a template. Left hand side: superimposed Thrombo tablet with its template. Right hand side: superimposed self-pressed RCPE tablet with its template.

4.5.2 Set up: Simulation in EDEM

In the Creator interface in EDEM it is possible to construct the same drum as in the experiment. Therefore a cylinder with the parameters of the real drum is defined with a rotational axis. Additionally a particle factory has to be defined, which gets the particle, into the drum. How the drum and the implemented particle look like in EDEM is illustrated in Figure 34.

Before running the simulations in EDEM several aspects has to be discussed in the first place. These aspects especially include the coefficient of restitution, the rolling resistance and the time step. The highest time step possible can be found via trial and error. For the Thrombo and RCPE tablet a time step of $5*10^{-5}$ seconds and for the Silibeads a time step of $7*10^{-5}$ seconds has been taken. In the current work the rolling resistance is set to 0.01 for all simulations, but this is only motivated out of empirical experience that the rolling resistance is in general small. It has low influence on the particle behavior, especially for non-spherical particles. The coefficient of restitution CoR is the quotient between the velocity before and after a collision. The CoR for all tablets can be found in Table 7. The CoR for the Thrombo tablet has be measured by [275] and was found to be 0.78. The CoR for glass is taken from [276]. It was assumed that the RCPE tablet has the same values as the Thrombo tablet.

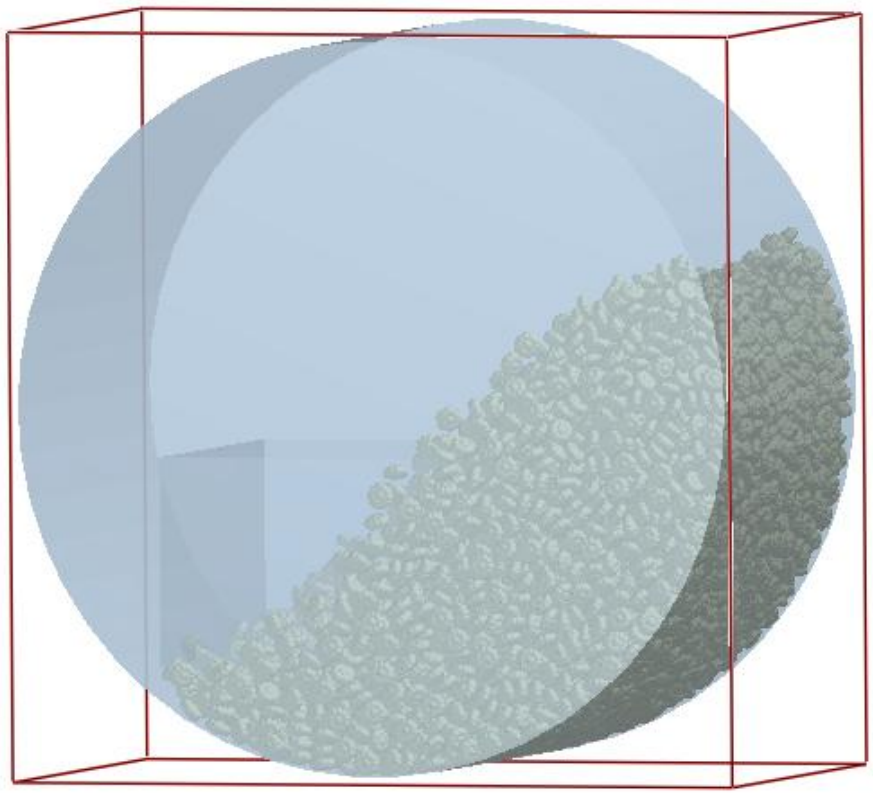

Figure 34: Illustration of the drum and the implemented Thrombo tablet in EDEM Creator.

	CoR_{PD}^{Plexi}	CoR_{PP}^{Plexi}	CoR_{PD}^{Steel}	CoR_{PP}^{Steel}
Silibeads	0.85	0.90	0.85	0.90
Thrombo	0.78	0.78	0.78	0.78
RCPE tablet	0.78	0.78	0.78	0.78

Table 7: Values for the coefficient of restitution used in the simulations.

The Poisson ration and the shear modulus used for the respective particles are listed in Table 6. The implementation parameter of the tablet shapes can be found in Table 6 as well. The statistic coefficient of friction for both wall vs. particle and particle vs. particle will be investigated in the DoE later on. In EDEM one has to decide which contact force model will be used. For example the following integrated contact models are available:

- Hertz-Mindlin (no slip)
- Hertz-Mindlin (no slip) with RVD Rolling Friction
- Hertz-Mindlin with JKR Cohesion
- Hertz-Mindlin with bonding
- Hertz-Mindlin with Heat Conduction
- Hyteretic Spring
- Linear Cohesion

- Linear Spring
- Hysteretic Spring
- Moving Plane

For brevity, explanations of these models can be found in the handbook of EDEM. In the current work the Hertz-Mindlin (no slip) model have been chosen for all simulations. The corresponding formulas can be found in chapter 0. In this model no dissipation due to slipping occurs.

4.5.3 **DoE analysis**

As discussed in chapter 3.9, for simulation experiments with lots of factors with a wide value range, a design of experiment is advisable for creating a model which is able to predict the right area in parameter space according to the related responses. In the current work MODDE 10 is used for setting up and analyzing a design of experiment. First of all a worksheet has to be created, where the factors that are investigated are defined and get their levels. In the current work three factors are chosen: the rotation speed, the static friction coefficient between particle-wall and the static friction coefficient between particle-particle. A full factorial design with center point is used. It has been decided to operate in the optimization (RSM) mode which uses a quadratic and cubic model. For the sake of completeness the whole simulation plan can be found in Table 8.

The following values for the factors are chosen:

	Low	center	High	Type of factor	Use
ω	4	17	30	Quantitative	Controlled
μ_{PD}	0.4	0.6	0.8	Quantitative	Controlled
μ_{PP}	0.1	0.5	0.9	Quantitative	Controlled

Exp No	Exp Name	Run Order	Incl/Excl	Rotation speed	Fric Tab Wall	Fric Tab Tab
1	N1	21	Incl	4	0,4	0,1
2	N2	28	Incl	17	0,4	0,1
3	N3	30	Incl	30	0,4	0,1
4	N4	4	Incl	4	0,6	0,1
5	N5	5	Incl	17	0,6	0,1
6	N6	2	Incl	30	0,6	0,1
7	N7	15	Incl	4	0,8	0,1
8	N8	24	Incl	17	0,8	0,1
9	N9	14	Incl	30	0,8	0,1
10	N10	13	Incl	4	0,4	0,5
11	N11	11	Incl	17	0,4	0,5
12	N12	10	Incl	30	0,4	0,5
13	N13	29	Incl	4	0,6	0,5
14	N14	25	Incl	17	0,6	0,5
15	N15	27	Incl	30	0,6	0,5
16	N16	18	Incl	4	0,8	0,5
17	N17	16	Incl	17	0,8	0,5
18	N18	8	Incl	30	0,8	0,5
19	N19	9	Incl	4	0,4	0,9
20	N20	7	Incl	17	0,4	0,9
21	N21	23	Incl	30	0,4	0,9
22	N22	22	Incl	4	0,6	0,9
23	N23	20	Incl	17	0,6	0,9
24	N24	3	Incl	30	0,6	0,9
25	N25	6	Incl	4	0,8	0,9
26	N26	26	Incl	17	0,8	0,9
27	N27	1	Incl	30	0,8	0,9
28	N28	12	Incl	17	0,6	0,5
29	N29	19	Incl	17	0,6	0,5

Table 8: Simulation plan according to DoE.

5 Results and discussion

After creating the simulation plan in Table 8 one has to decide which responses are included in the model fitting process. In the current work four responses are included: The angle of repose of the whole region AoR, the angle of repose of the middle region AoR_middle, the relative x and y coordinate of the center of area cen_x, cen_y, respectively. Thus, to every simulation configuration (rows in Table 8, termed N1-N29) in the simulation plan belongs four responses (AoR, AoR_middle, cen_x, cen_y). All those responses are evaluated with the self-written Matlab code 'AoR_mos_cen.m' (see chapter 4.3) and can be found in the Table 10Table 29 for all used particles and surface roughnesses, both for the experiment and computer simulation. The simulation plan was only constructed for the computer simulations in EDEM. Thus, DoE only needs the data of the computer simulations. According to the simulation plan there are 29 values for every response, which are distributed in the parameter space (rotational speed, static friction coefficient between wall-particle,

static friction coefficient between particle-particle). The idea of DoE is to fit a hypersurface into the parameter space, which can predict every response value to any parameter configuration. Therefore, MODDE used a multiple linear regression model MLR.

So for every parameter configuration a response value can be 'estimated' with the help of equation (39), In the current work only terms up to second order are included. To be more specific, the equation to fit f.i. the AoR looks like:

$$AoR_{fit} = c_0^{AoR} + c_1^{AoR} * ome + c_2^{AoR} * Fri + c_3^{AoR} * Fr2 + c_4^{AoR} * ome^2 + \\ + c_5^{AoR} * Fri^2 + c_6^{AoR} * Fr2^2 + c_7^{AoR} * ome * Fri + c_8^{AoR} * ome * Fr2 + \\ + c_9^{AoR} * Fri * Fr2. \qquad (45)$$

This has to be done for all DoEs that were done. However, it showed that the outcome is qualitatively similar in all cases. Therefore, in the following, the analysis in MODDE is shown for one representative case (Figure 35-Figure 40)

The replicate plot in Figure 35 offers a quick raw data inspection, where the green dots are the results from the simulation experiment and the blue squares are the replicates (repeated experiment).

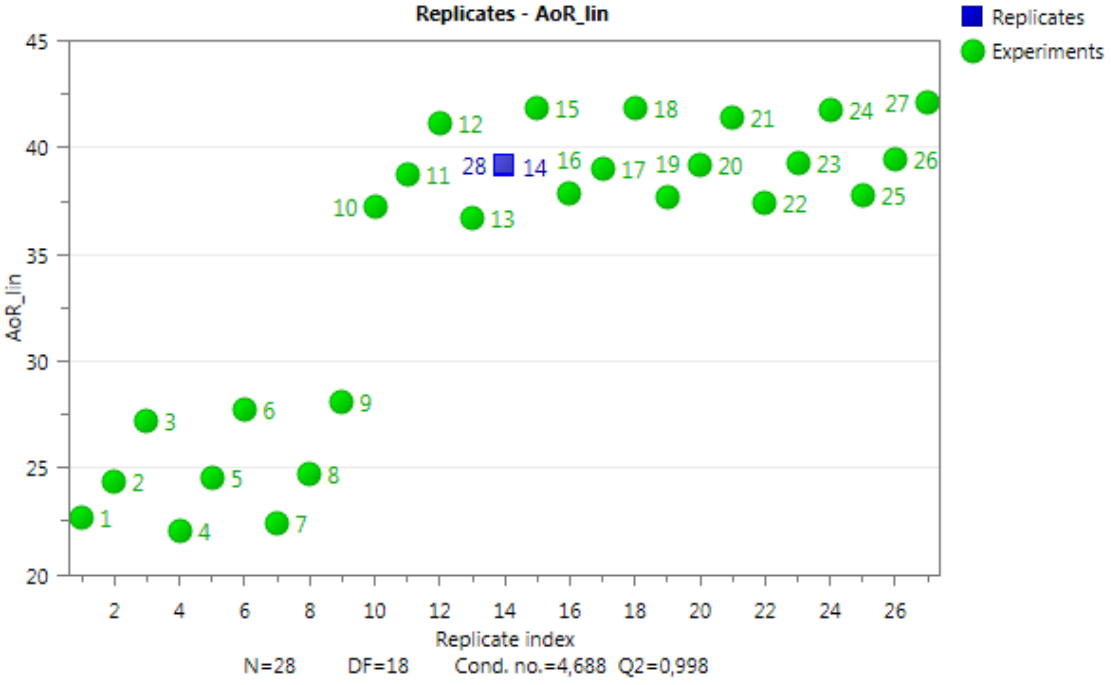

Figure 35: Illustration of the replicate plot in MODDE .

The Histogram in Figure 36 (left) shows the distribution of the response and is used to determine if a transformation is need. In general the desired contribution is a normal distribution, because it will give better model estimates and statistics. The Histogram in Figure 36 shows a typically negative

skewness and so a negative logarithmical transformation is applied.

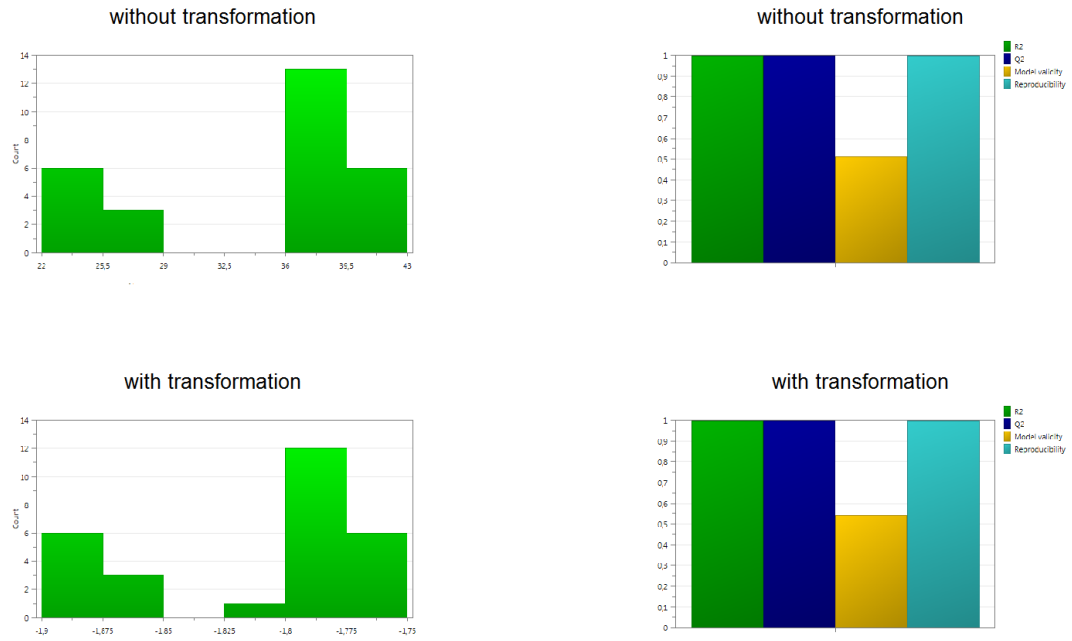

Figure 36: Exemplary illustration of the response distribution in MODDE.

The summary of fit (see Figure 36 (right)) shows four parameter, where a value of 1 would mean a perfect model. R2 shows the model fit qualtiy and Q2 corresponds with an estimate of the future prediction precision. The model validity is a test of diverse model problems and reproducibility is the variation of the replicates compared to overall variability. To see the similarity to the plots in chapter 3.9.2 (Figure 13), the design region in MODDE according to the simulation plan is illustrated in Figure 37.

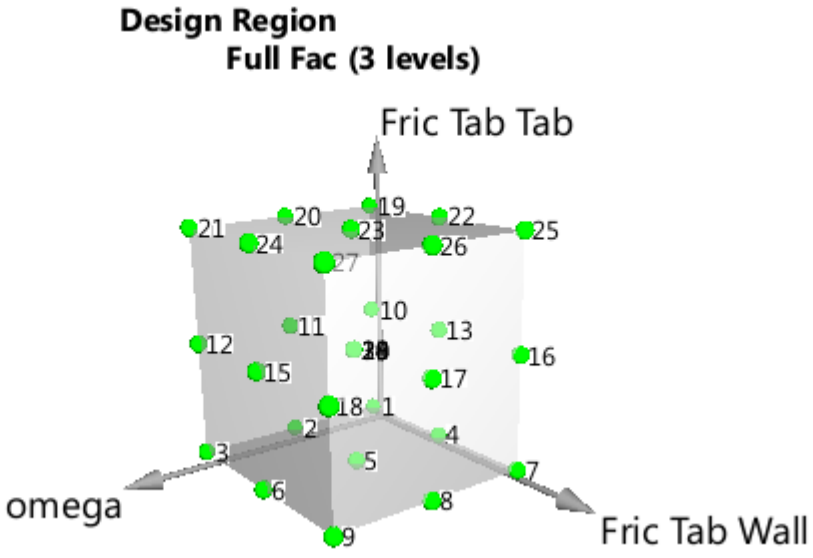

Figure 37: Illustration of the design region in MODDE.

The coefficient plot in Figure 38 is a graphical presentation of the significance of the model terms. The information in this plot is used in the backward-regression step to eliminate over-fitting: by

excluding terms with non-significant influence on the model, the nominal model quality (R2) may decrease, but its predictability is improved (Q2).

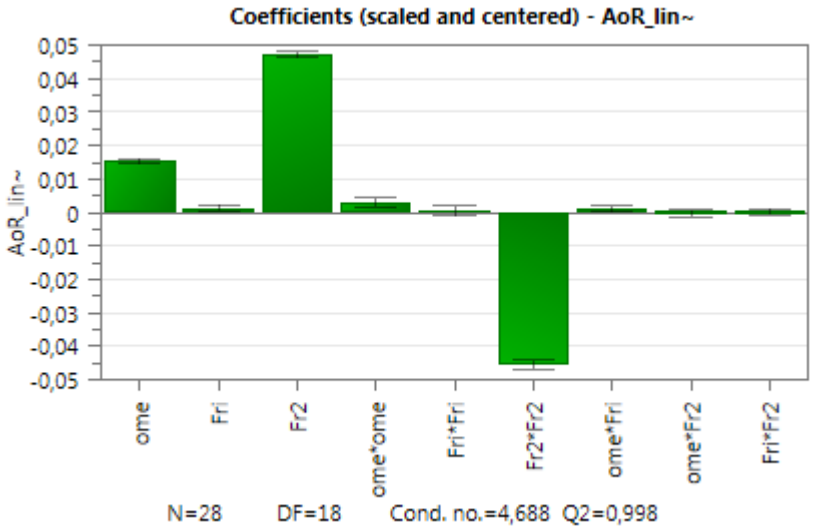

Figure 38: Illustration of the coefficient plot showing the significance of the model terms (factors).

The residual normal probability plot in Figure 39 can indicate outliers (points outside the red line) that should be checked and deleted in the worst case. In this work, no outliers were present.

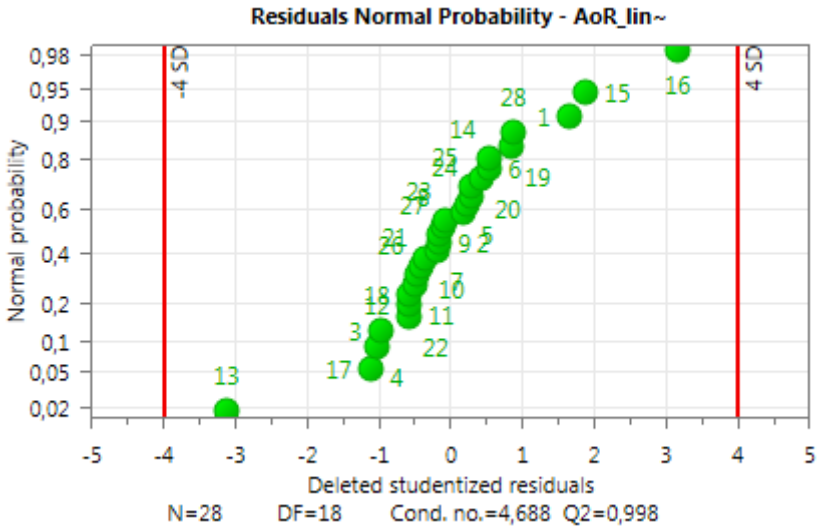

Figure 39: Illustration of the residual normal probability which indicates outliers.

Figure 40 shows the observed values vs. the predicted values. If the values are close to the median line, it is then an indicator for a strong correlation of observed vs. predicted value and therefore a good model.

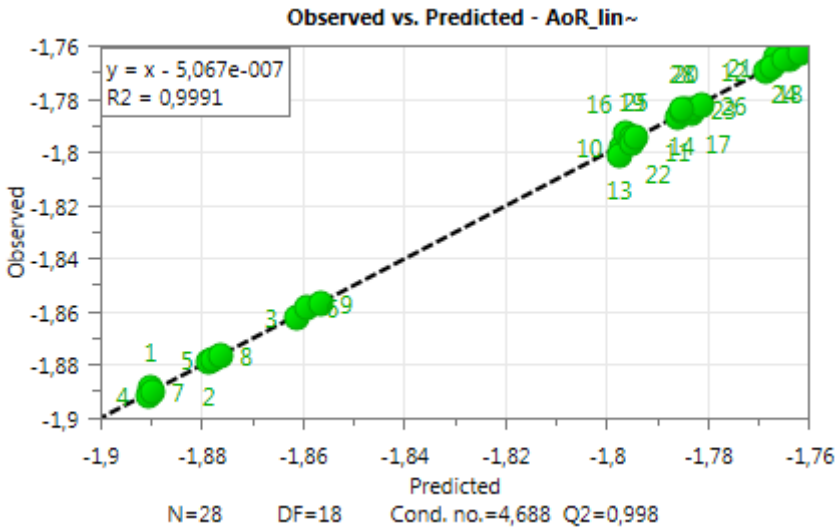

Figure 40: Illustration of the observed vs. predicted values.

5.1 Contour plot

For brevity the system configurations are named as it is shown in Table 9.

Configuation name	Particle material	Number of Particles	Surface roughness
AZ1_Plexi	Silibead	7807	Plexiglas
AZ2_Plexi	Silibead	10789	Plexiglas
AZ4_Plexi	Thrombo ASS 100mg	5997	Plexiglas
AZ5_Plexi	Thrombo ASS 100mg	7141	Plexiglas
AZ6_Plexi	RCPE tablet	4729	Plexiglas
AZ7_Plexi	RCPE tablet	5507	Plexiglas
AZ1_Steel	Silibead	7807	Steel sheet
AZ2_Steel	Silibead	10789	Steel sheet
AZ4_Steel	Thrombo ASS 100mg	5997	Steel sheet
AZ5_Steel	Thrombo ASS 100mg	7141	Steel sheet
AZ6_Steel	RCPE tablet	4729	Steel sheet
AZ7_Steel	RCPE tablet	5507	Steel sheet

Table 9: Configurations investigated in the current work according to particle material, number of particles and surface roughness.

After model building and controlling the quality criteria as described above, the most central representation of the DoE results data is generated: the contour plot. It shows the dependence of the response variable on the factors, as predicted by the model, and is as such the main goal of this work. All contour plots ($\omega = (4{,}17{,}30)$ rpm; coefficient of friction tablet-wall vs. coefficient of friction tablet-tablet) of every particle either for steel and Plexiglas are illustrated in Figure 47-Figure 90. For a representative discussion, the contour plots and the corresponding 'summary of fit' of AZ1_Plexi are shown in Figure 41 and Figure 42.

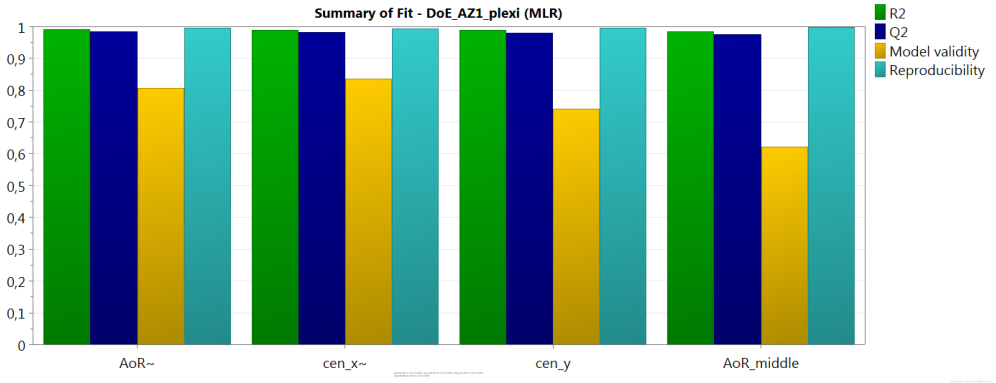

Figure 41: Representative illustration of the fitting parameter of AZ1_plexi.

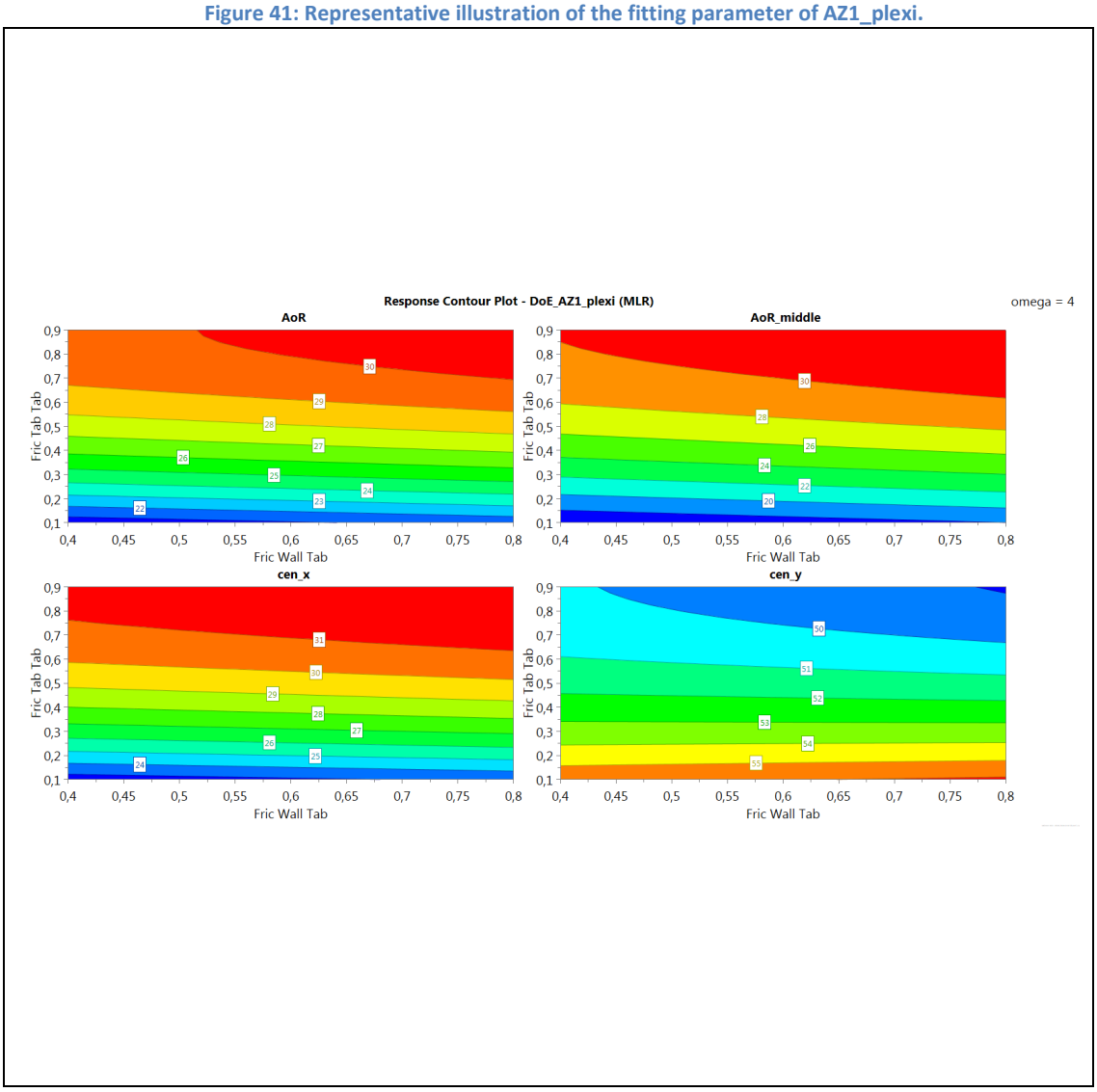

Figure 42: Contour plot of AZ1_Plexi.

It should be noted that on the contour plots, in some cases the y coordinate of the center of area does not agree with the data according to the experiment, not even within the standard deviation. The relative difference is in the range of 2-3 percent. Therefore, the filling level between simulation and experiment has been compared and the result was that in the simulation there is a higher filling level, which can be explained by different packing density. Due to that the y-coordinate of the center of area is in the simulation smaller than in the experiment. If the values of the y coordinate

are changed to the difference with respect to in the packing density, it is possible to correct the existing mismatch. Another reason of the different center of area could be the blurring effect in the S-mode at high exposure time during taking the pictures. For this reason, sometimes a shift of the detected to the real center of area could appear in the range of 2-3 percent. Because of this fact, it is legitimate to shift the response values of the DoE in order to adapt it to the experimental results in a quantitative better way.

In all contour plots for all particles it can be seen that the choice of the static coefficient of friction between particle and wall has no influence on the angle of repose or the center of mass. The reason is that no sliding between particle and wall occurs; the sticking friction between wall and particle in every case is high enough that the tangential component of the contact force does not overcome it.

By matching the contour plots in Figure 63-Figure 90 with the response out of the experiment (see Table 10-Table 21), the static friction coefficient between particle-particle μ_{PP} can be limited to a certain value range. If in further discussion the coefficient of friction is mentioned, the static coefficient of friction between the particle-particle is meant.

In general it is hard to reduce the static friction coefficient to one single value. There are different reasons for this. First, the fact that 4 responses are included in the DoE analysis makes it hard to find an exact match among them. Second, the statistical results according to the experiment naturally come with a certain standard variation (sometimes up to 2°). Third, the detection algorithm shows also a small error because of the blurring effect (due to the high exposure time) and the finite exposure of the circular ring. For those reasons, quantitative statements of the friction coefficient can only be given as a value range. It should be noted that the following deeper considerations were excluded:

- The standard deviations of the simulation data (Table 22-Table 33) are not taken into account in the DoE-fitting process.
- The standard deviations of the experimental data (Table 10-Table 21) are considered, but not methodically taken into account in the matching process.
- The model validity parameters of the responses are not taken into account (weighted according to their quantitative correctness).

Thus, a further step could be to apply a wider statistical model to the raw data of both the experiment and simulation. This should include the implementation of the standard deviation of the computer simulations into the DoE evaluations. Then, the standard deviation and the mean values of the experiment should be weighted according to their model validity parameters.. This would give a thorough quantitative statement, but is well beyond the scope of this work..

This being stated, a number of useful qualitative and quantitative assessments are possible. The contour plots of the experimental results are investigated at three rotational speeds (4rpm, 17rpm, 30rpm). In the following, an attempt is made to give both quantitative and qualitative statements.

Silibead

- Qualitative statements:
  - For the same number of particles: $\mu_{Plexi} < \mu_{Steel}$.
  - For different number of particles (AZ1, AZ2) there is a different ω-behaviour:

    Plexiglas: AZ1: increasing $\omega \rightarrow$ increasing μ

    AZ2: increasing $\omega \rightarrow$ decreasing μ

    Steel: AZ1: increasing $\omega \rightarrow$ increasing μ

    AZ2: increasing $\omega \rightarrow$ decreasing μ.
  - No statement about the behavior of μ with respect to the fill level (for same surface roughness) is possible.
- Quantitative statement:
  - AZ1_Plexi: 4rpm: $\mu = (0.25 - 0.40)$

    17rpm: $\mu = (0.25 - 0.50)$

    30rpm: $\mu = (0.30 - 0.55)$
  - AZ2_Plexi: 4rpm: $\mu = (0.30 - 0.50)$

    17rpm: $\mu = (0.30 - 0.40)$

    30rpm: $\mu = (0.28 - 0.35)$
  - AZ1_Steel: 4rpm: $\mu = (0.45 - 0.60)$

    17rpm: $\mu = (0.40 - 0.55)$

    30rpm: $\mu = (0.55 - 0.70)$
  - AZ2_Steel: 4rpm: $\mu = (0.50 - 0.65)$

    17rpm: $\mu = (0.40 - 0.65)$

    30rpm: $\mu = (0.35 - 0.55)$

Thrombo ASS 100mg:

- Qualitative statements:
  - In relation to the Silibeads, a generally lower friction coefficient is seen.
  - No clear ω-dependence.

- Plexiglass: Generally, a lower friction appears for AZ5 (AZ5 > AZ4). Such a statement is for steel not possible.
- No statement about the influence of surface roughness with respect to μ is possible.

- Quantitative statements:
  - AZ4_Plexi: 4rpm: $\mu = (0.22 - 0.30)$
    17rpm: $\mu = (0.20 - 0.40)$
    30rpm: $\mu = (0.20 - 0.45)$
  - AZ5_Plexi: 4rpm: $\mu = (0.15 - 0.20)$
    17rpm: $\mu = (0.20 - 0.30)$
    30rpm: $\mu = (0.17 - 0.30)$
  - AZ4_Steel: 4rpm: $\mu = (0.25 - 0.30)$
    17rpm: $\mu = (0.25 - 0.30)$
    30rpm: $\mu = (0.25 - 0.30)$
  - AZ5_Steel: 4rpm: $\mu = (0.25 - 0.30)$
    17rpm: $\mu = (0.25 - 0.32)$
    30rpm: $\mu = (0.28 - 0.35)$

Self-pressed tablet:

For this tablet it was difficult to make serious statements, because the standard deviation of the response values of the statistical analysis of the experiment was sometimes very high (up to 2°). The main reason for this was the high abrasion of the tablets.

- Qualitative statements:
  - No clear difference in μ in respect to the two investigated number of particles (AZ6, AZ7)
  - No statement about ω-behavior possible.

- Quantitative statements:
  - AZ6_Plexi: 4rpm: $\mu = (0.50 - 0.70)$
    17rpm: $\mu = (0.45 - 0.55)$
    30rpm: $\mu = (0.45 - 0.60)$
  - AZ7_Plexi: 4rpm: $\mu = (0.50 - 0.60)$

17rpm: $\mu = (0.54 - 0.65)$

30rpm: $\mu = (0.40 - 0.60)$

- AZ4_Steel: 4rpm: $\mu = (0.35 - 0.60)$

  17rpm: $\mu = (0.40 - 0.65)$

  30rpm: $\mu = (0.45 - 0.60)$

- AZ5_Steel: 4rpm: $\mu = (0.45 - 0.65)$

  17rpm: $\mu = (0.55 - 0.65)$

  30rpm: $\mu = (0.50 - 0.65)$

It is important to mention that the values (or in fact the value ranges) of the coefficient of friction above are very useful to get an idea and to exclude unrealistic values, but can only be seen as a general guideline. The reason for this simply is that in reality, the coefficient of friction is not a material constant that can be captured on one single number. It rather depends on different process conditions. Therefore, if the value of μ is needed for a specific process (depending on number of particles, rotational speed and surface roughness), it is recommended to look up the value in the corresponding contour plot.

In other words, there is no "true" value for the coefficient of friction. Using the presented results, rather than simply guessing a value as is commonly done, it is possible to obtain a reasonable, scientific approximation based on measurements.

Self-pressed tablet:

For this tablet it was difficult to make serious statements, because the standard deviation of the response values of the statistical analysis of the experiment was sometimes very high (up to 2°). The main reason for this was the high abrasion of the tablets.

- Qualitative statements:
  - No clear difference in μ in respect to the two investigated number of particles (AZ6, AZ7)
  - No statement about ω-behavior possible.

- Quantitative statements:
  - AZ6_Plexi: 4rpm: $\mu = (0.50 - 0.70)$

    17rpm: $\mu = (0.45 - 0.55)$

    30rpm: $\mu = (0.45 - 0.60)$
  - AZ7_Plexi: 4rpm: $\mu = (0.50 - 0.60)$

    17rpm: $\mu = (0.54 - 0.65)$

		30rpm:	$\mu = (0.40 - 0.60)$
•	AZ4_Steel:	4rpm:	$\mu = (0.35 - 0.60)$
		17rpm:	$\mu = (0.40 - 0.65)$
		30rpm:	$\mu = (0.45 - 0.60)$
•	AZ5_Steel:	4rpm:	$\mu = (0.45 - 0.65)$
		17rpm:	$\mu = (0.55 - 0.65)$
		30rpm:	$\mu = (0.50 - 0.65)$

It is really important to mention, that the values or the value-range of the coefficient of friction above are just recommended values. If the value of μ is needed (depending on number of particles, rotational speed and surface roughness), it is recommended to look in the contour plot on his own. But it has to be added that the value range given above is a good orientation and exclude a lot of other possible values.

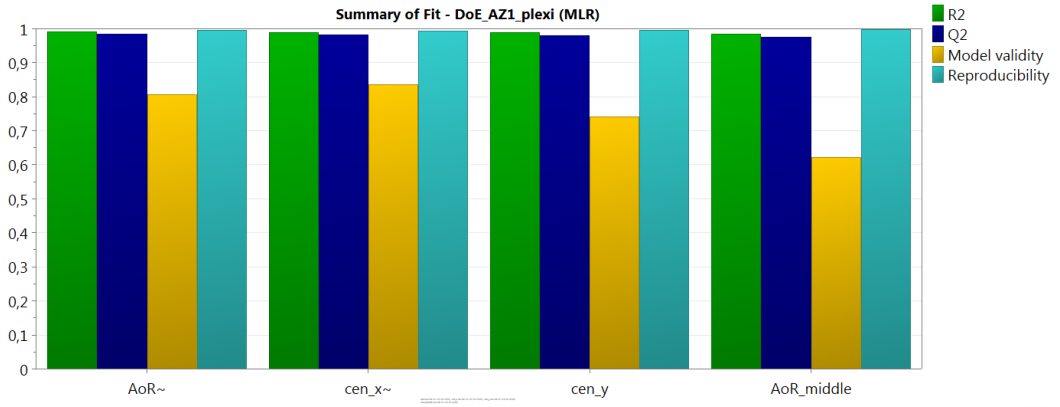

Figure 43: Illustration of the fitting parameters of AZ1_plexi.

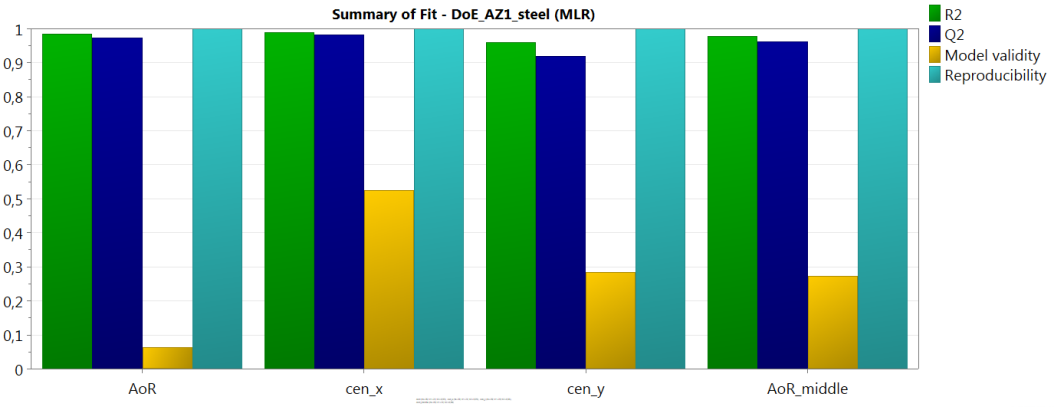

Figure 44: Illustration of the fitting parameters of AZ1_steel.

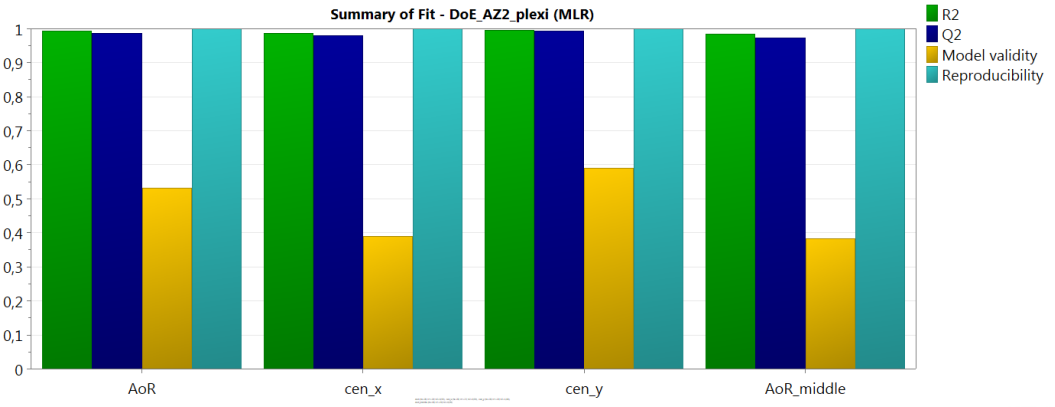

Figure 45: Illustration of the fitting parameters of AZ2_plexi.

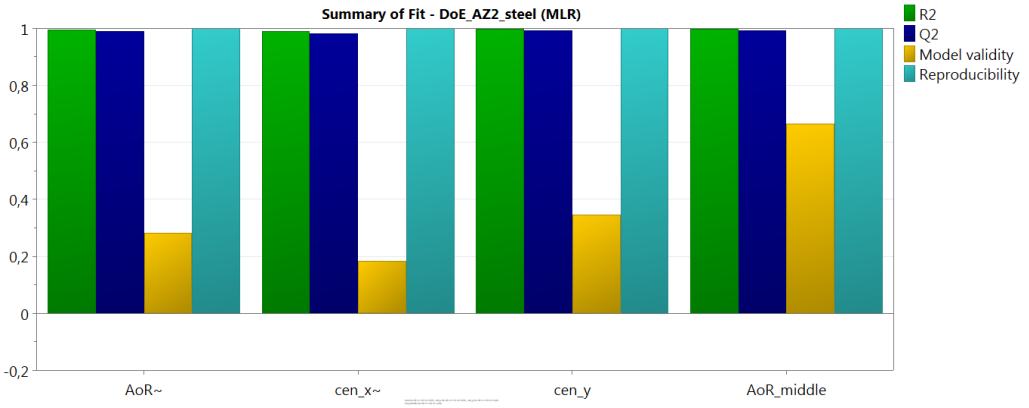

Figure 46: Illustration of the fitting parameters of AZ1_steel.

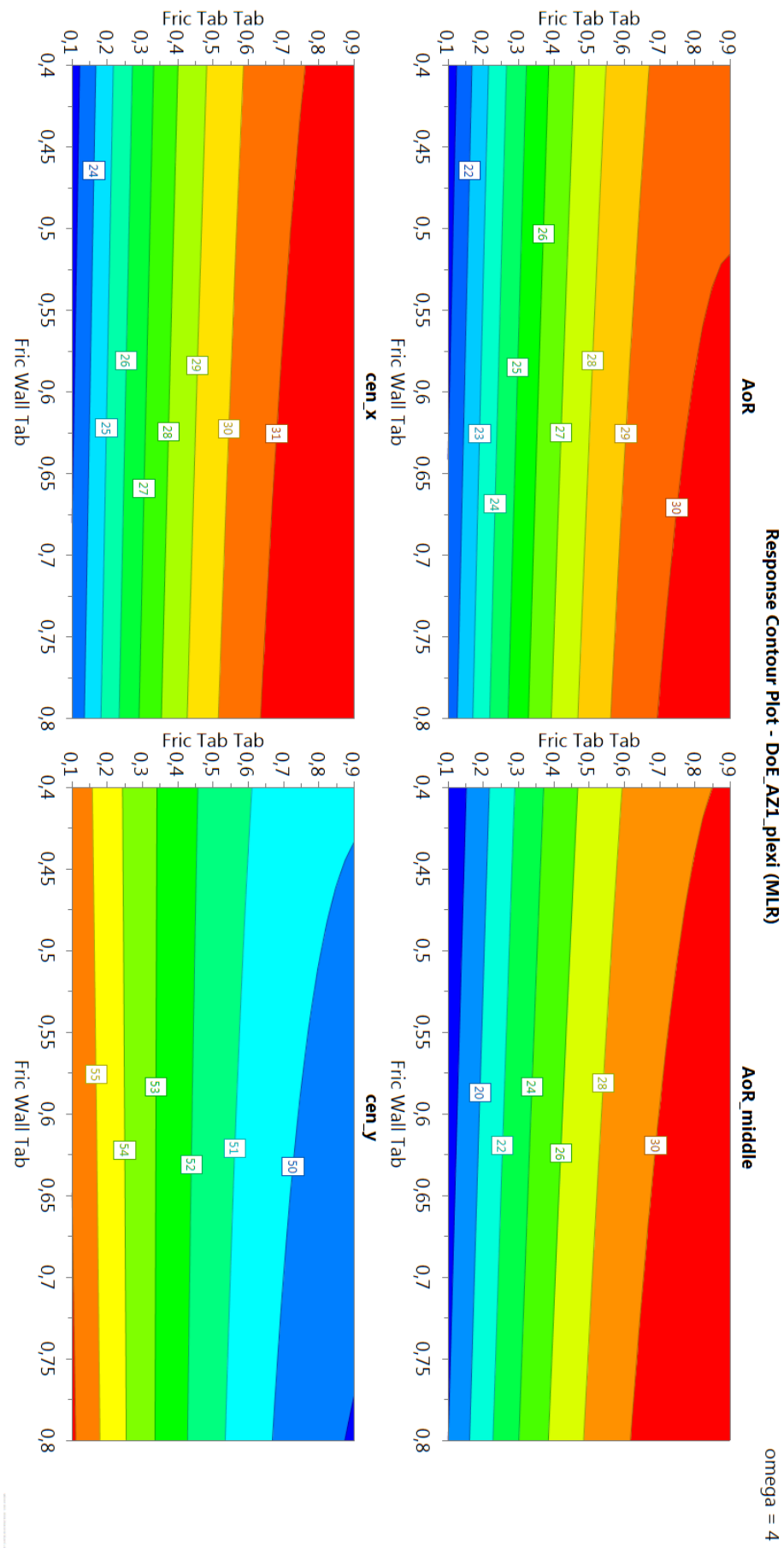

Figure 47: Contour plot of AZ1_Plexi at $\omega = 4rpm$.

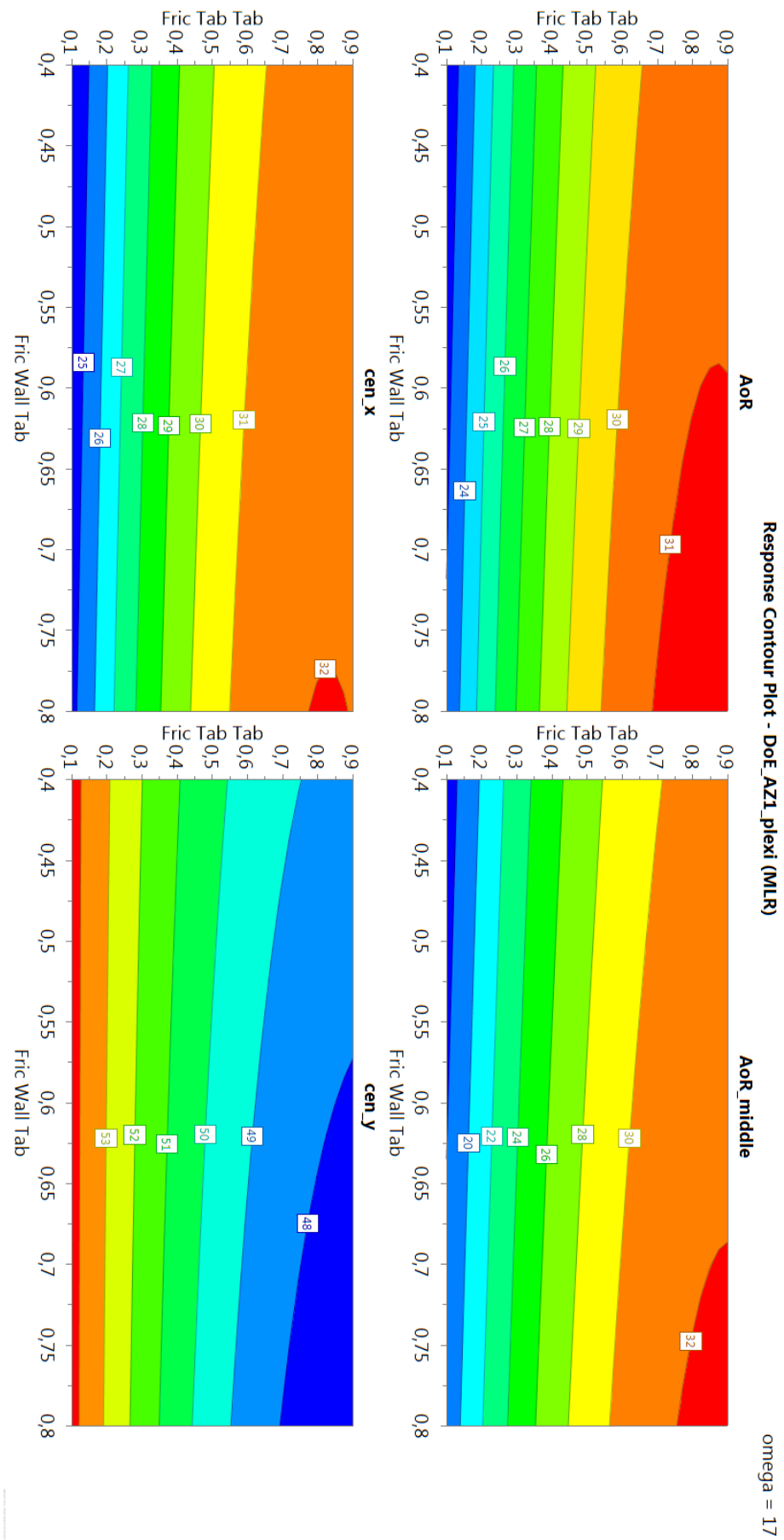

Figure 48: Contour plot of AZ1_Plexi at $\omega = 17rpm$.

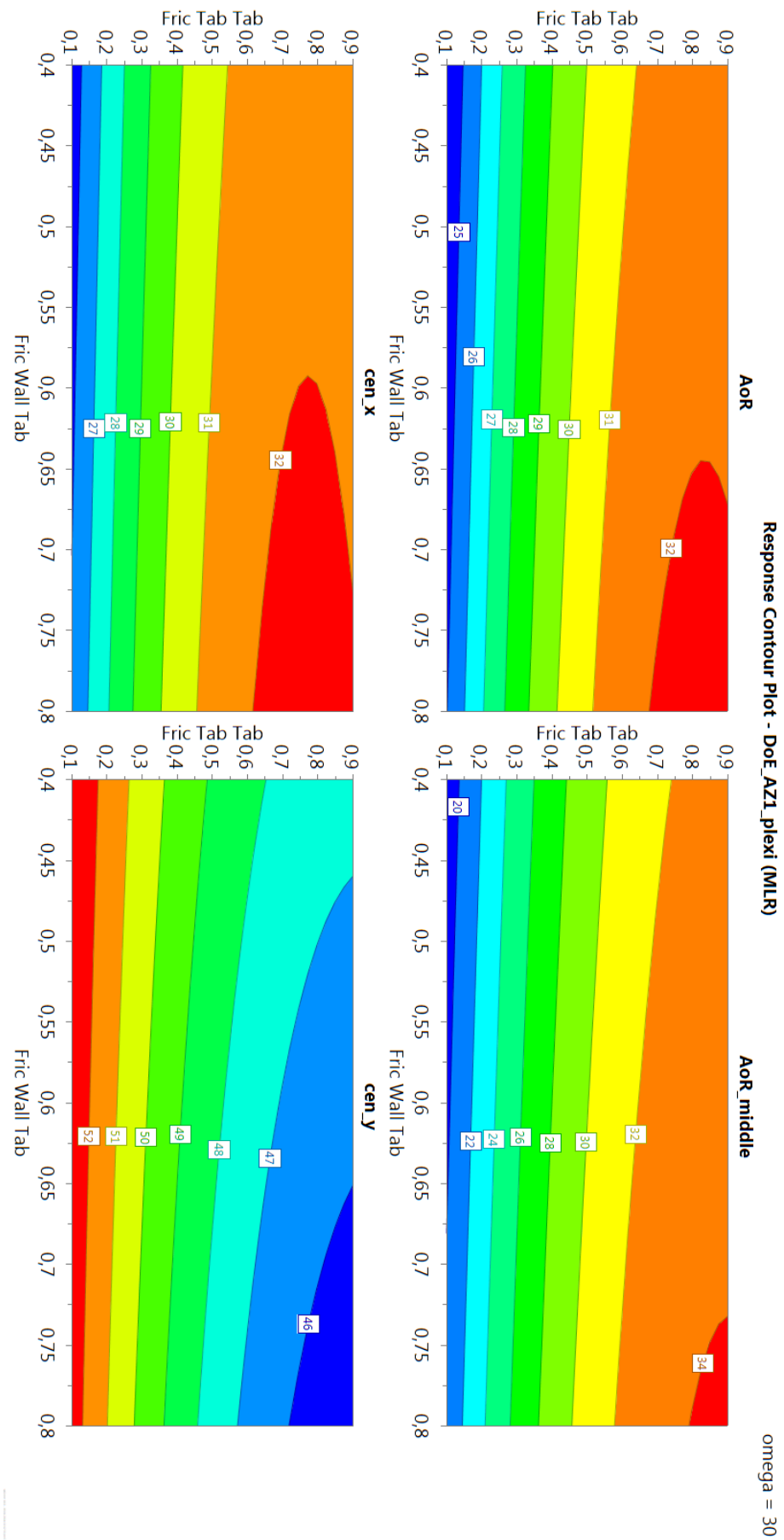

Figure 49: Contour plot of AZ1_Plexi at $\omega = 30rpm$.

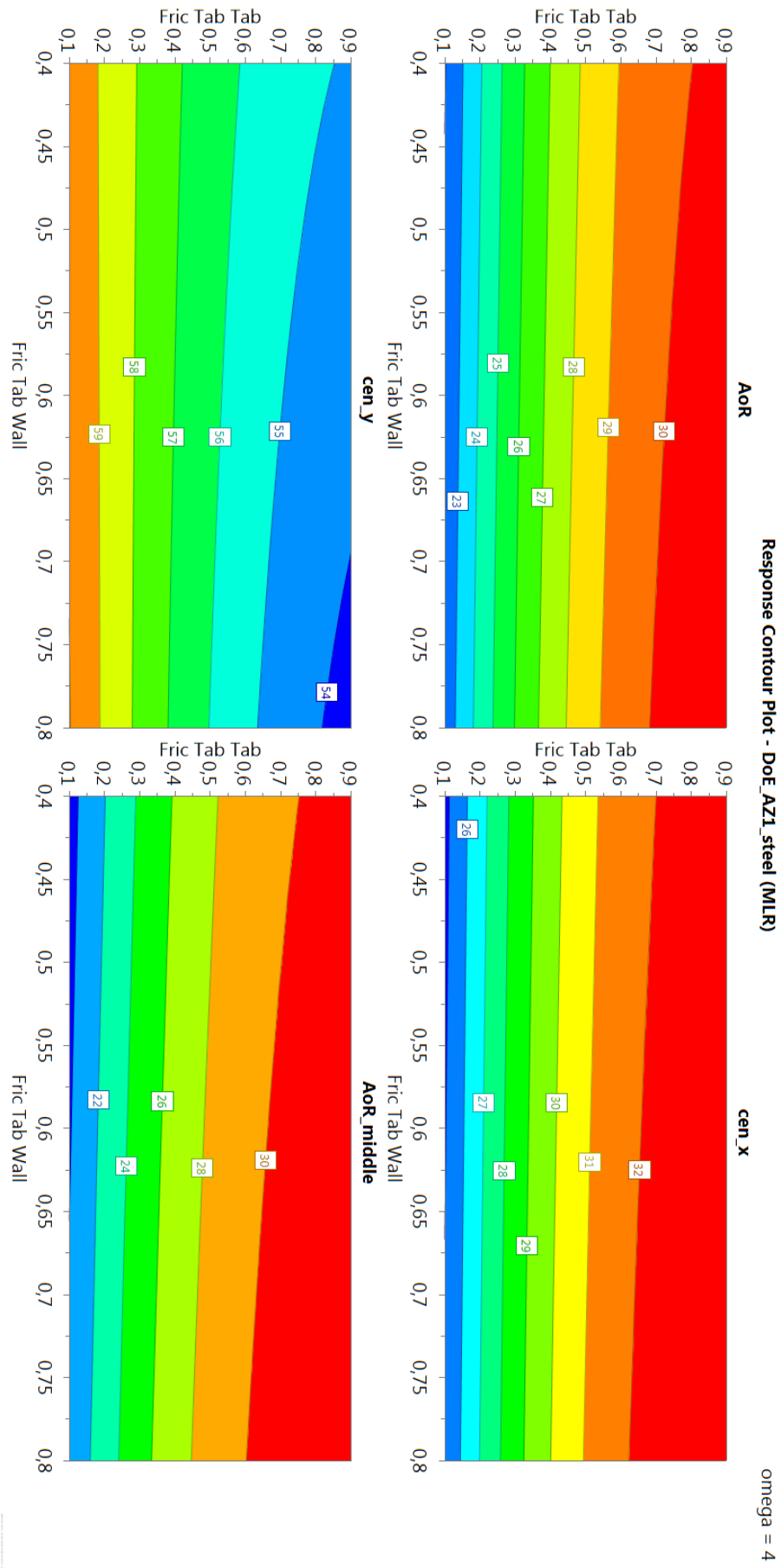

Figure 50: Contour plot of AZ1_Steel at $\omega = 4rpm$.

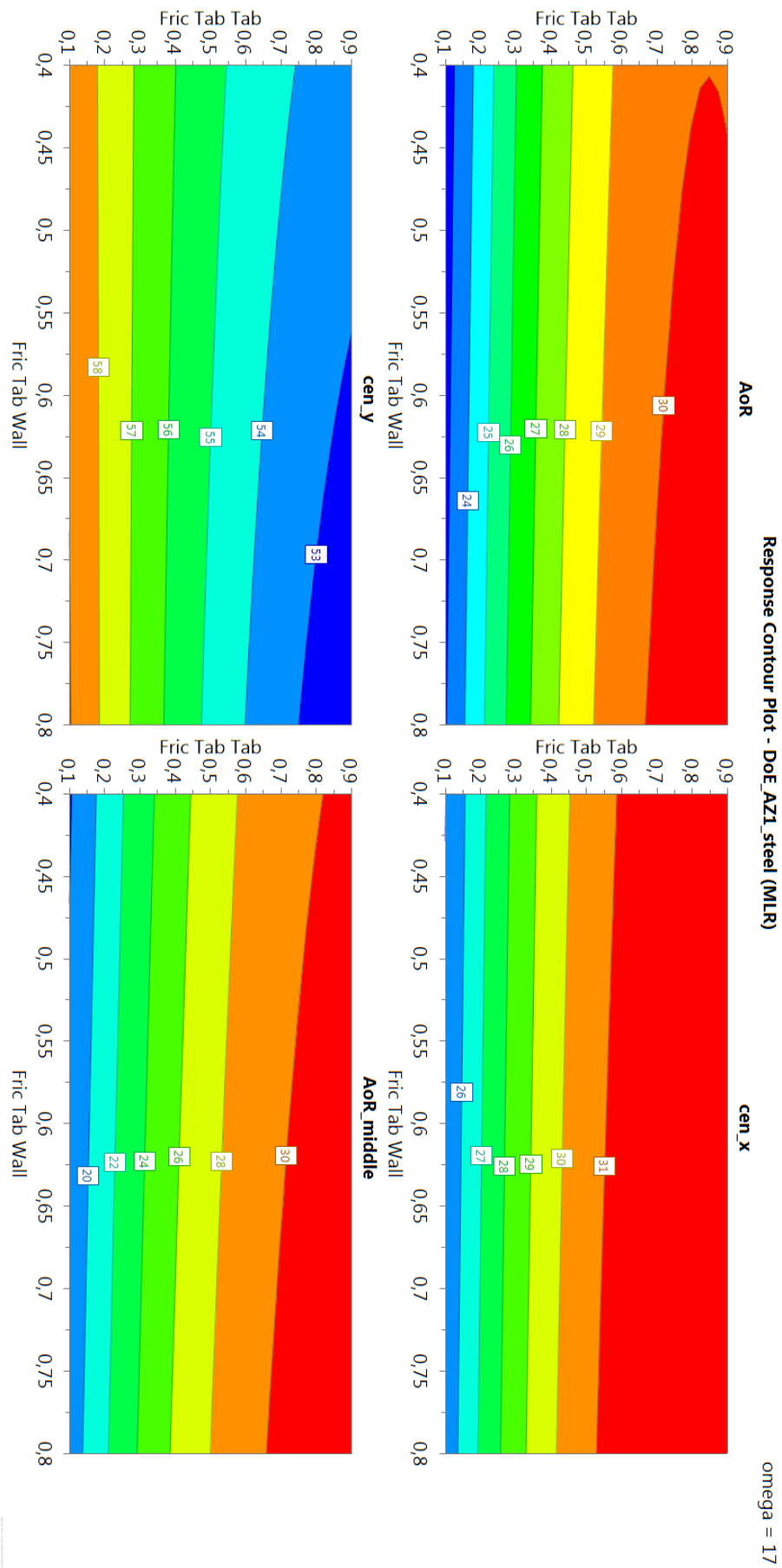

Figure 51: Contour plot of AZ1_Steel at $\omega = 17rpm$.

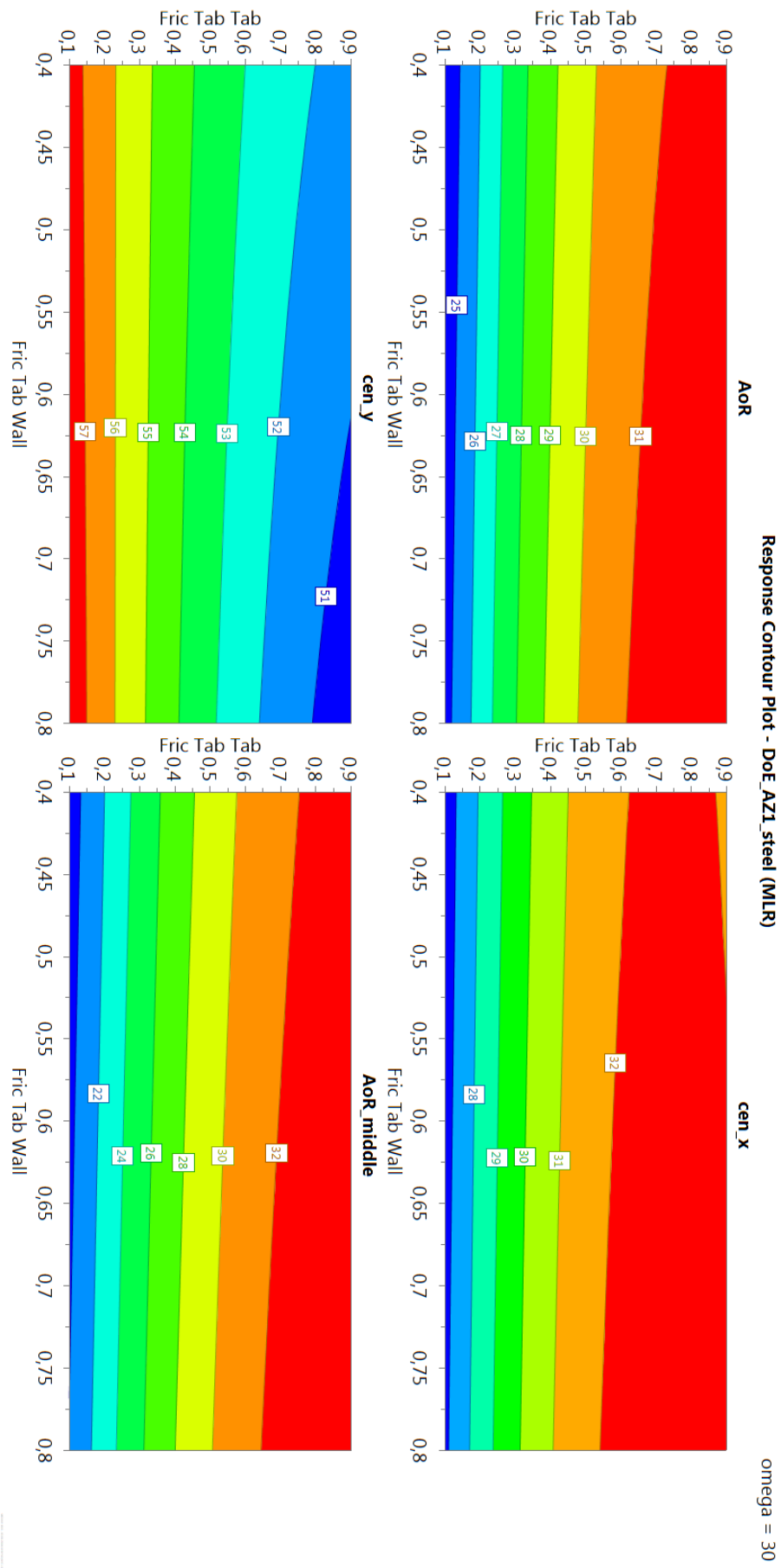

Figure 52: Contour plot of AZ1_Steel at $\omega = 30rpm$.

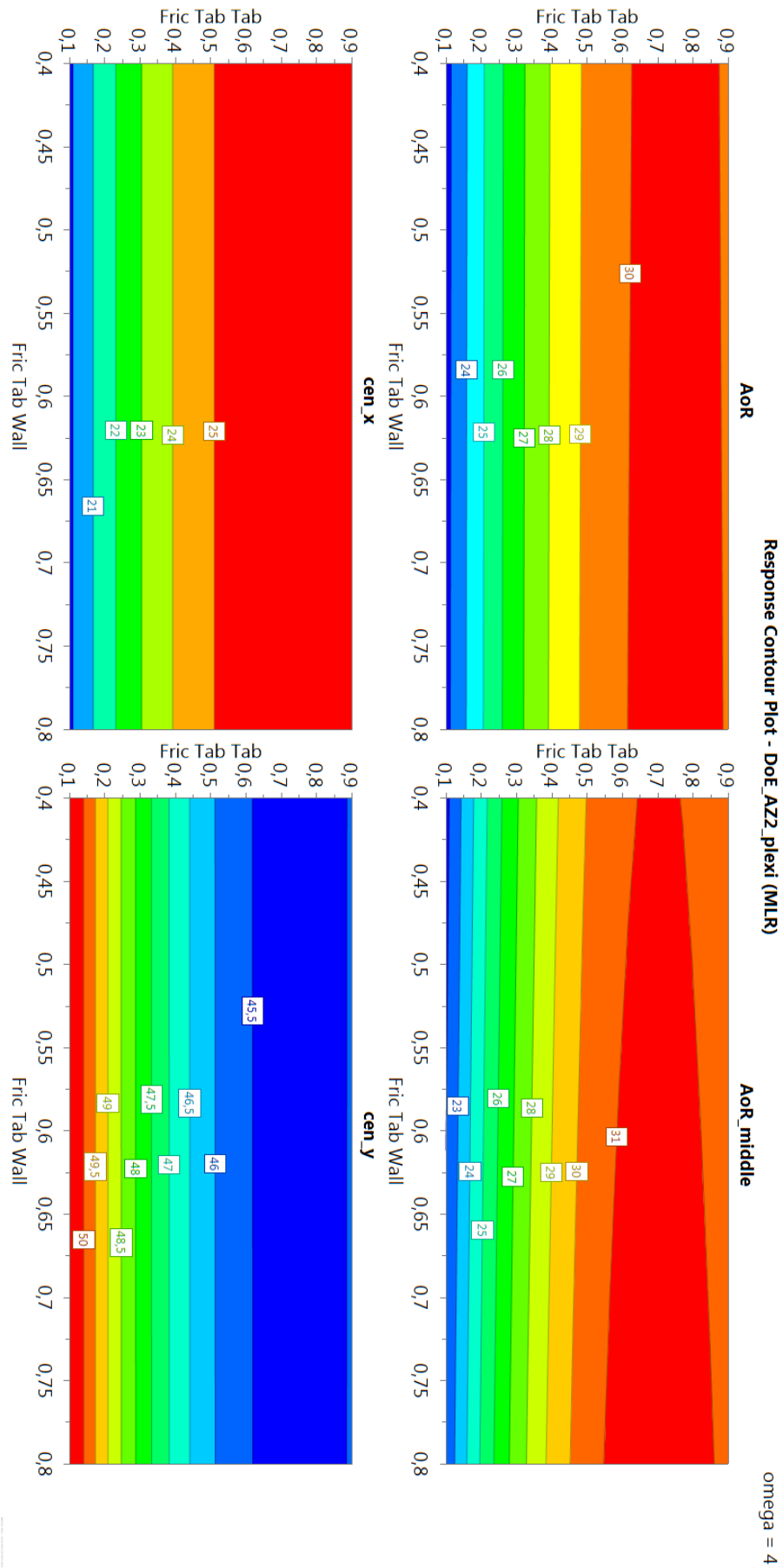

Figure 53: Contour plot of AZ2_Plexi at $\omega = 4rpm$.

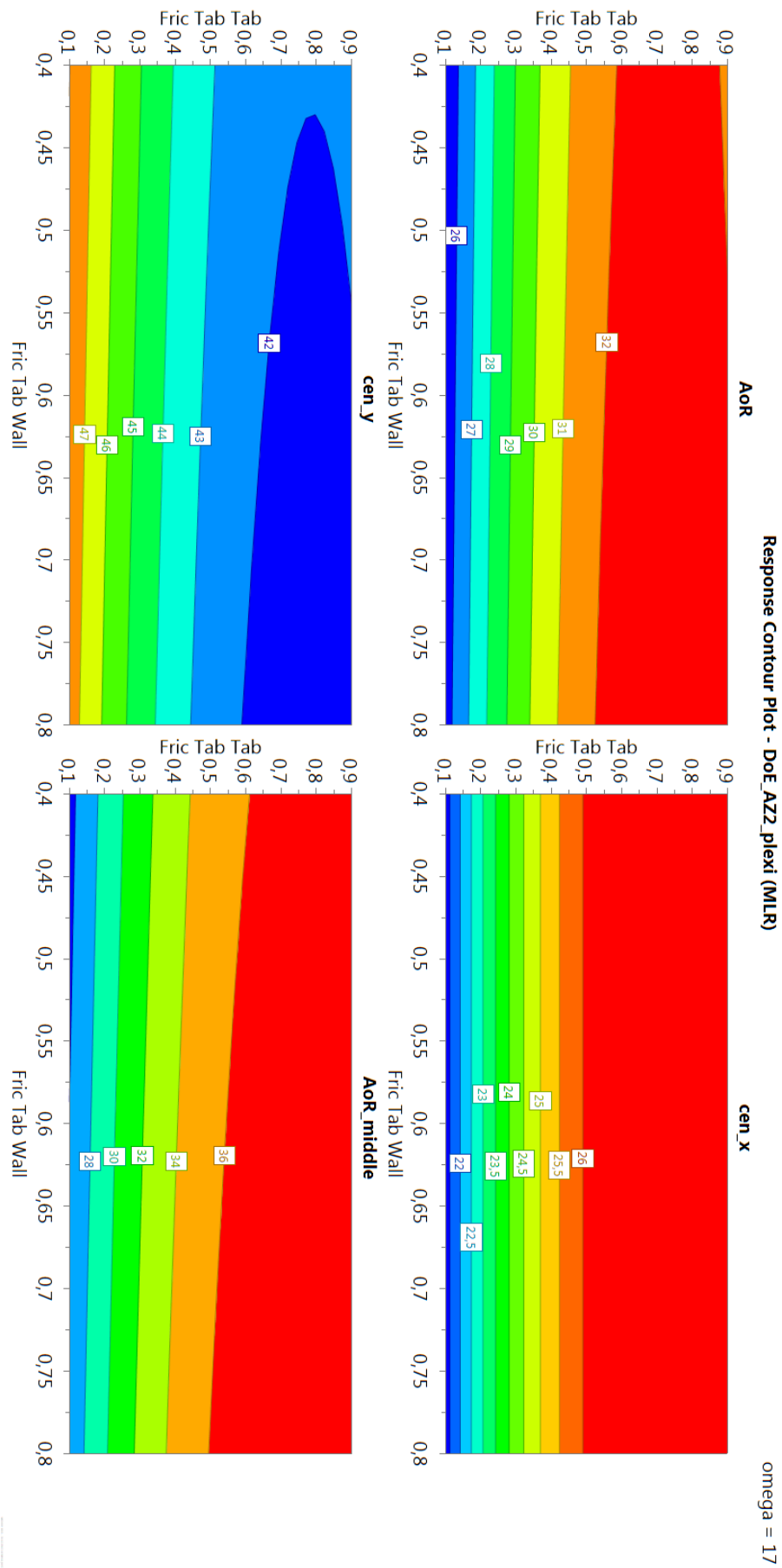

Figure 54: Contour plot of AZ2_Plexi at $\omega = 17rpm$.

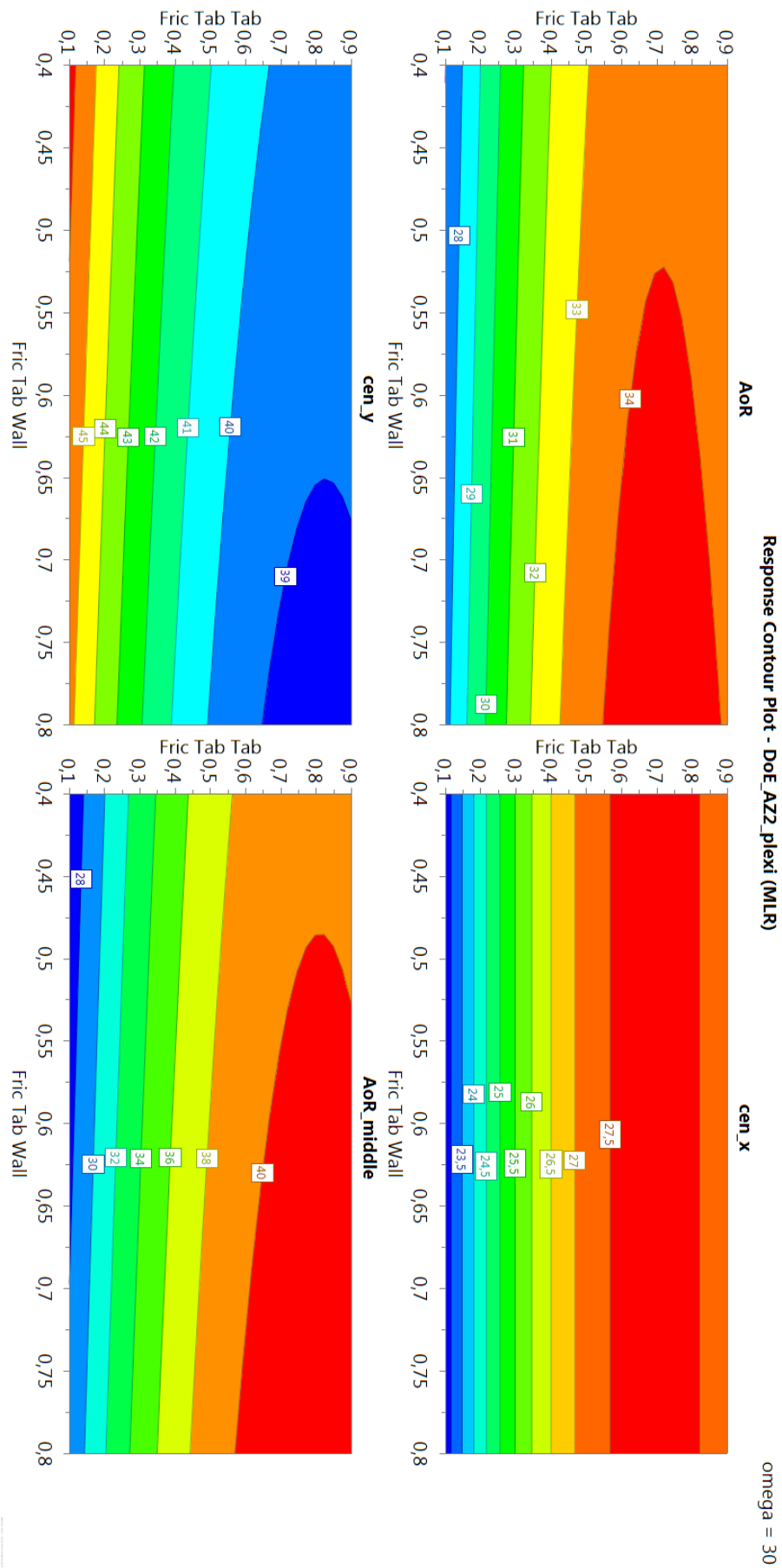

Figure 55: Contour plot of AZ2_Plexi at $\omega = 30rpm$.

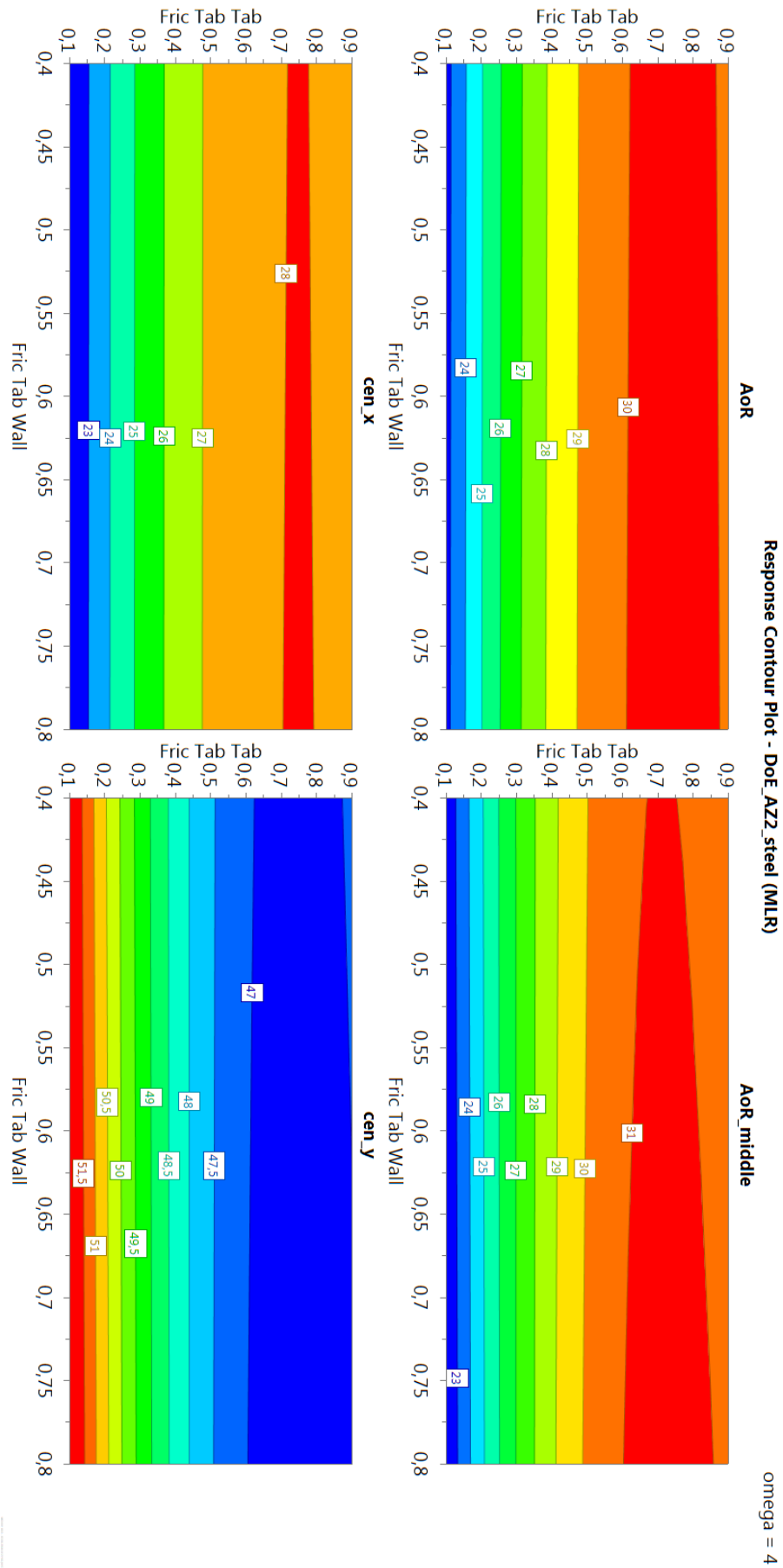

Figure 56: Contour plot of AZ2_Steel at $\omega = 4rpm$.

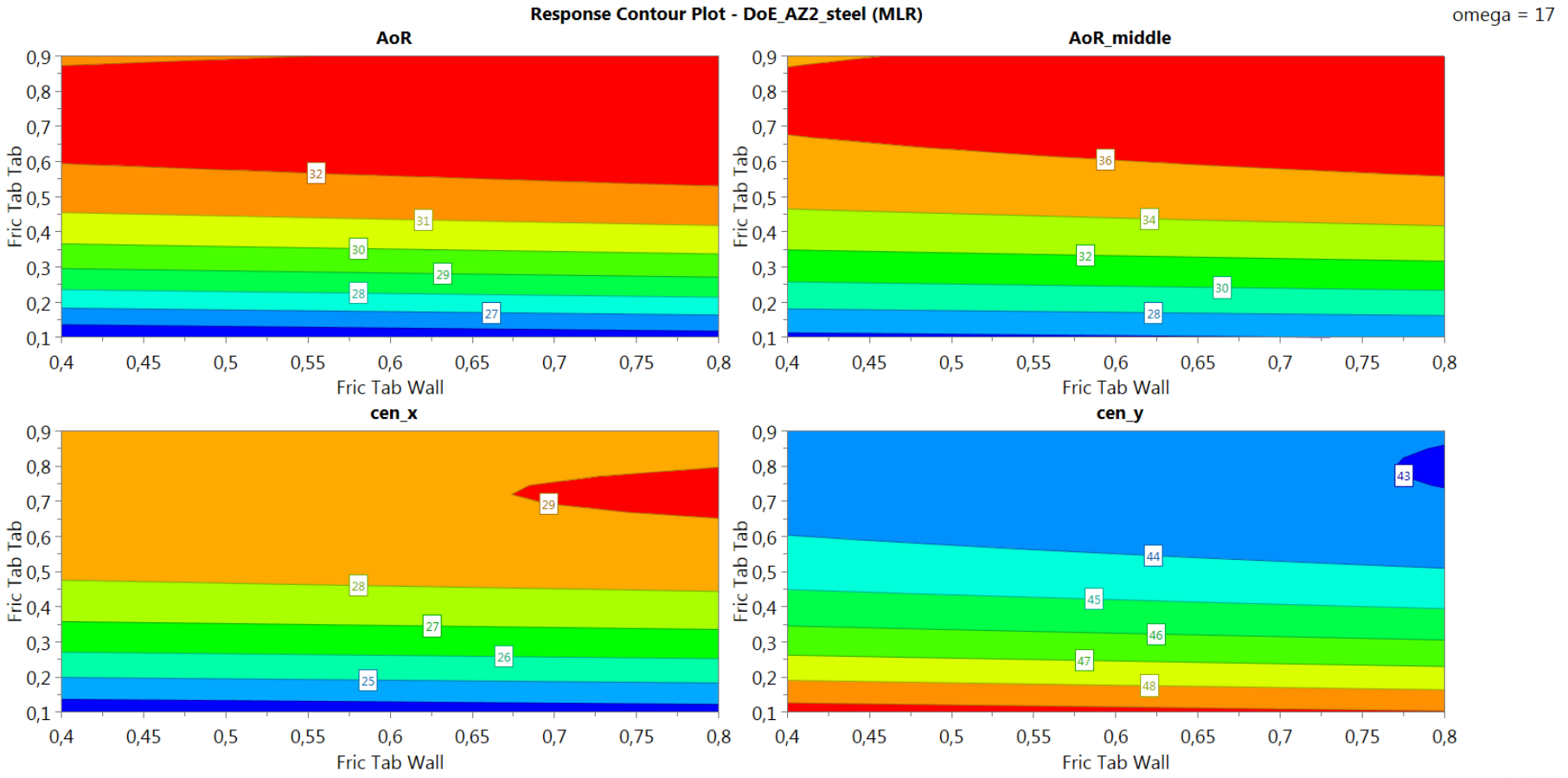

Figure 57: Contour plot of AZ2_Steel at $\omega = 17rpm$.

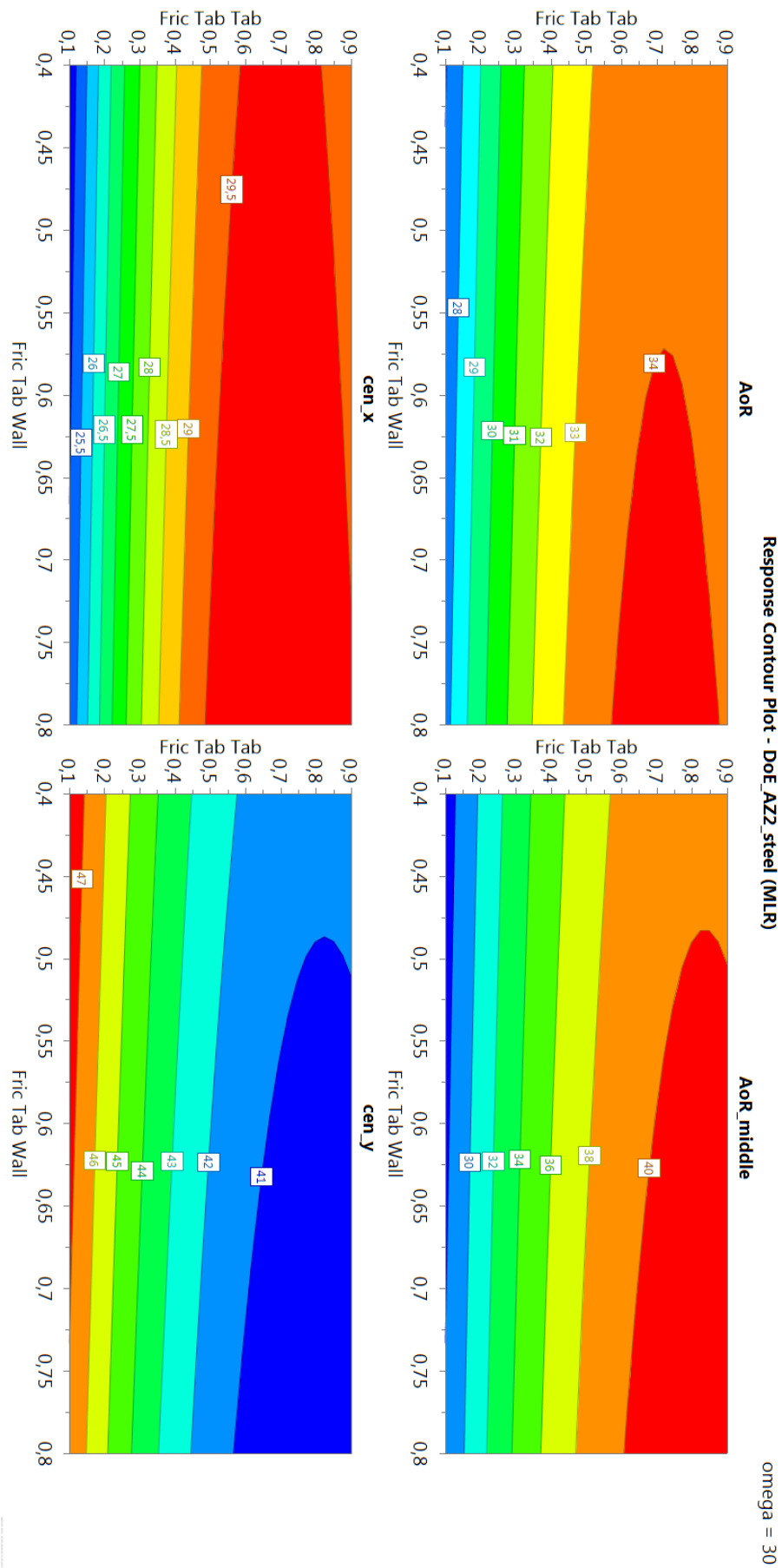

Figure 58: Contour plot of AZ2_Steel at $\omega = 30rpm$.

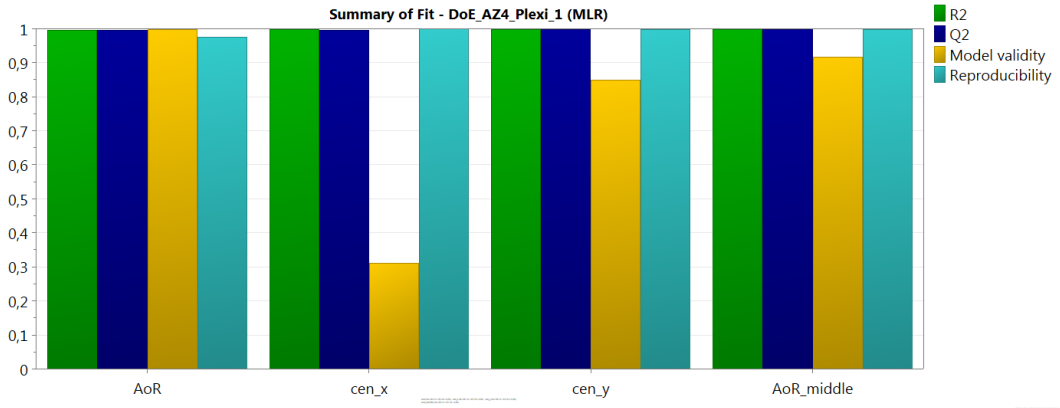

Figure 59: Illustration of the fitting parameters of AZ4_plexi.

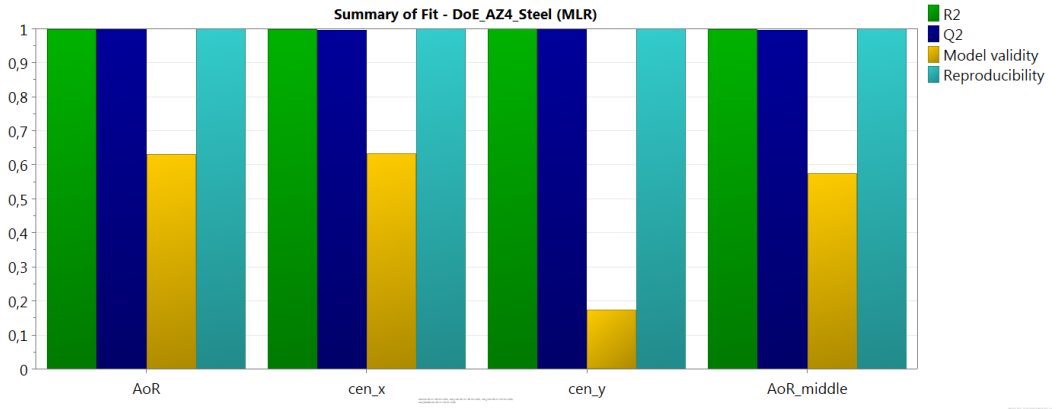

Figure 60: Illustration of the fitting parameters of AZ4_steel.

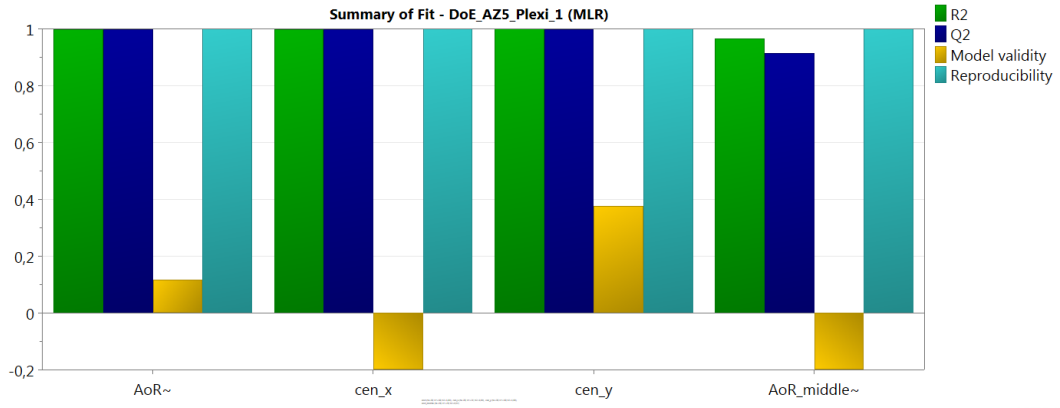

Figure 61: Illustration of the fitting parameters of AZ5_plexi.

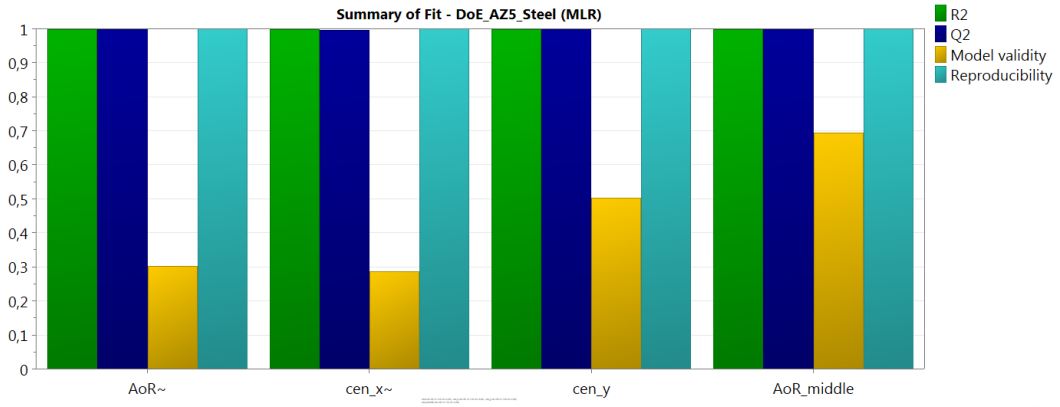

Figure 62: Illustration of the fitting parameters of AZ5_steel.

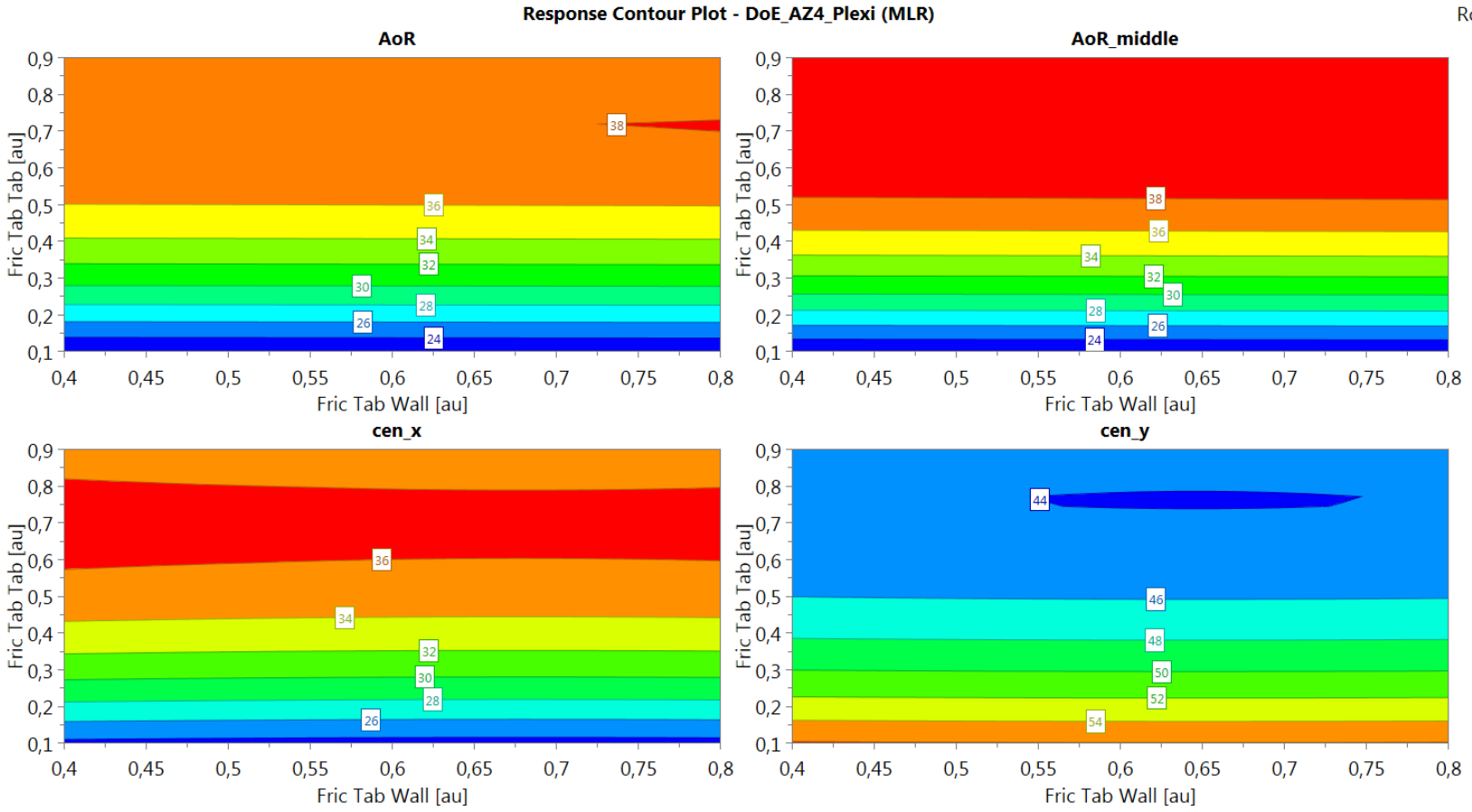

Figure 63: Contour plot of AZ4_Plexi at $\omega = 4rpm$.

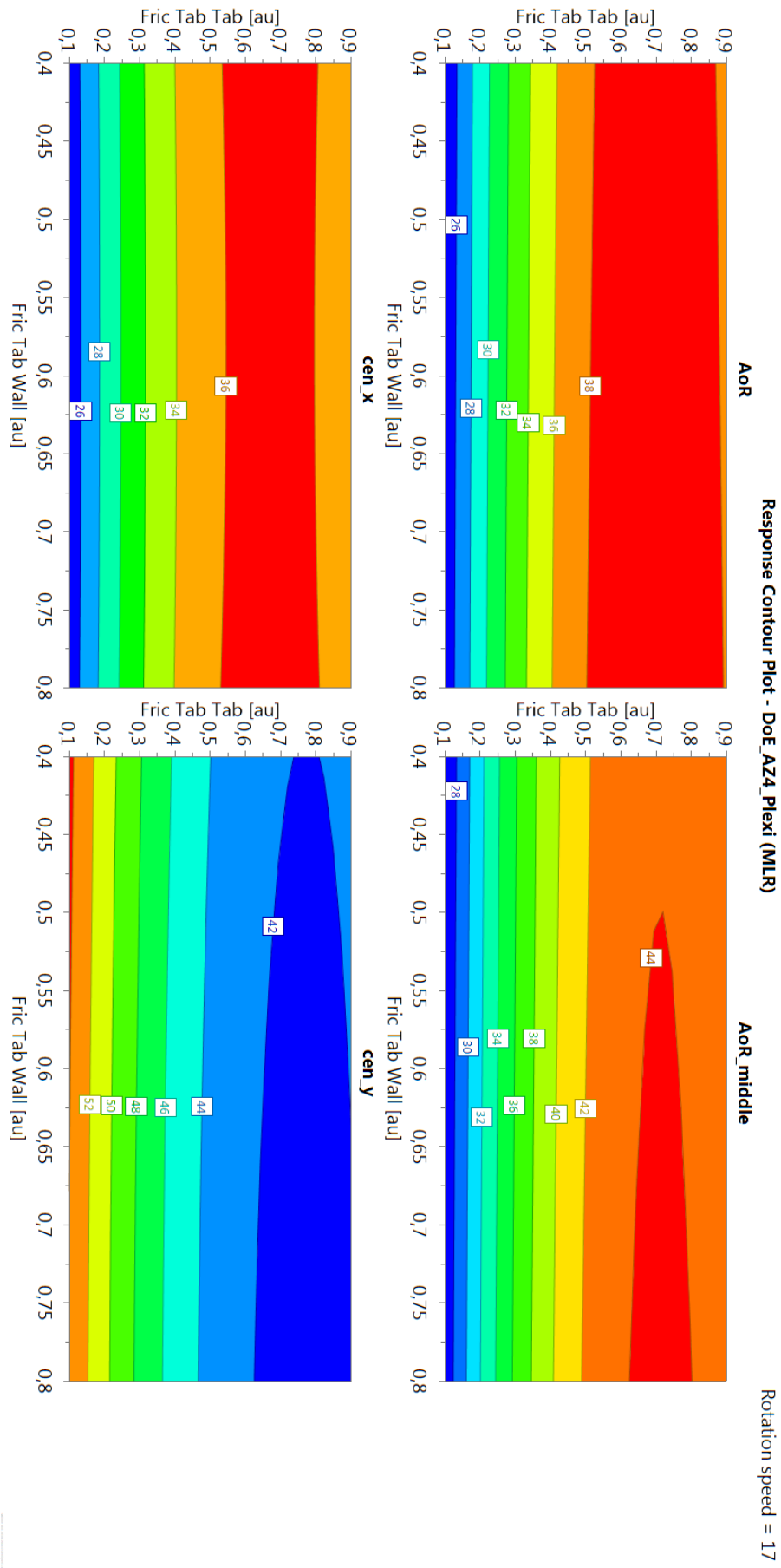

Figure 64: Contour plot of AZ4_Plexi at $\omega = 17rpm$.

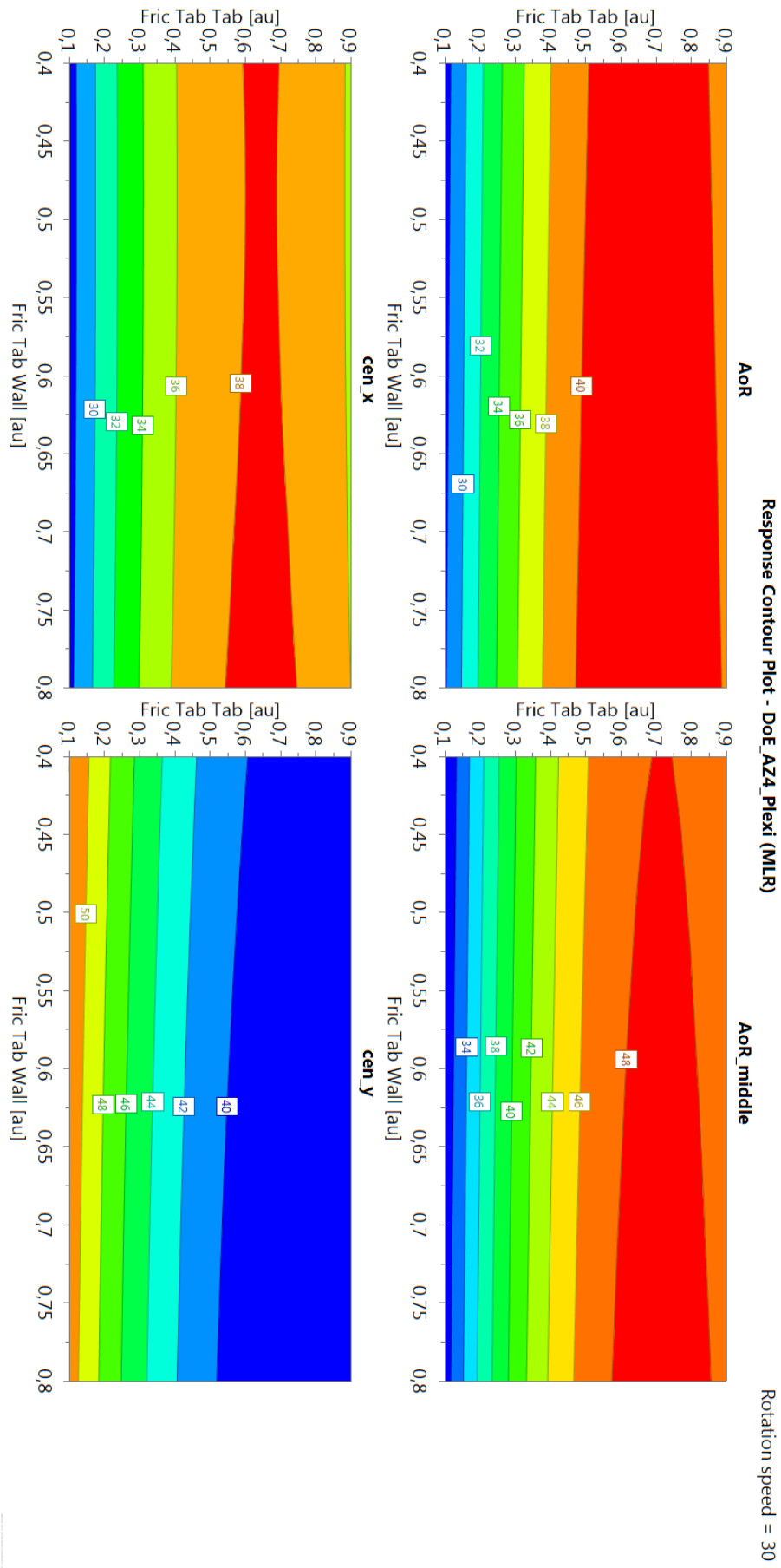

Figure 65: Contour plot of AZ4_Plexi at $\omega = 30rpm$.

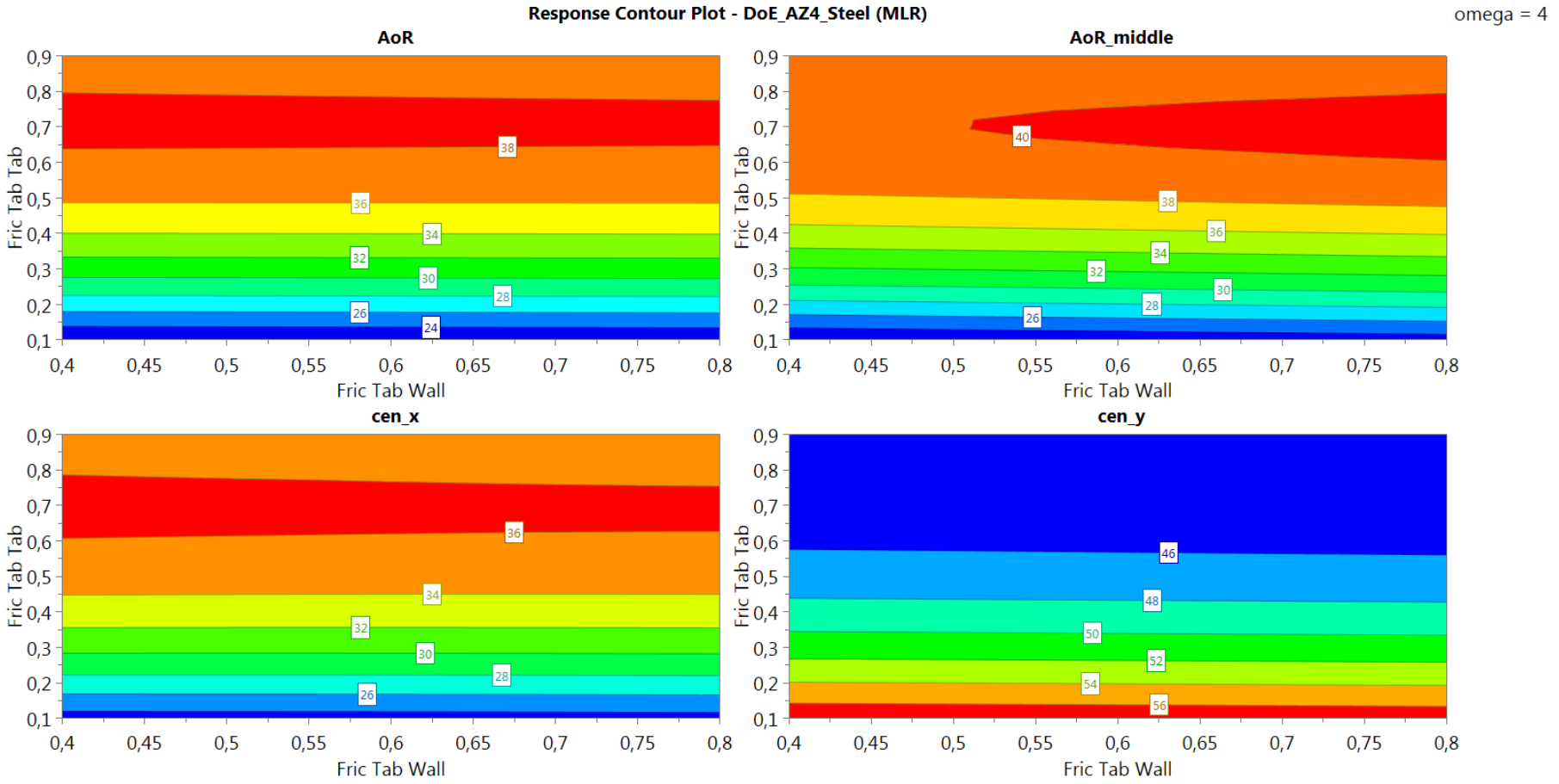

Figure 66: Contour plot of AZ4_Steel at $\omega = 4rpm$.

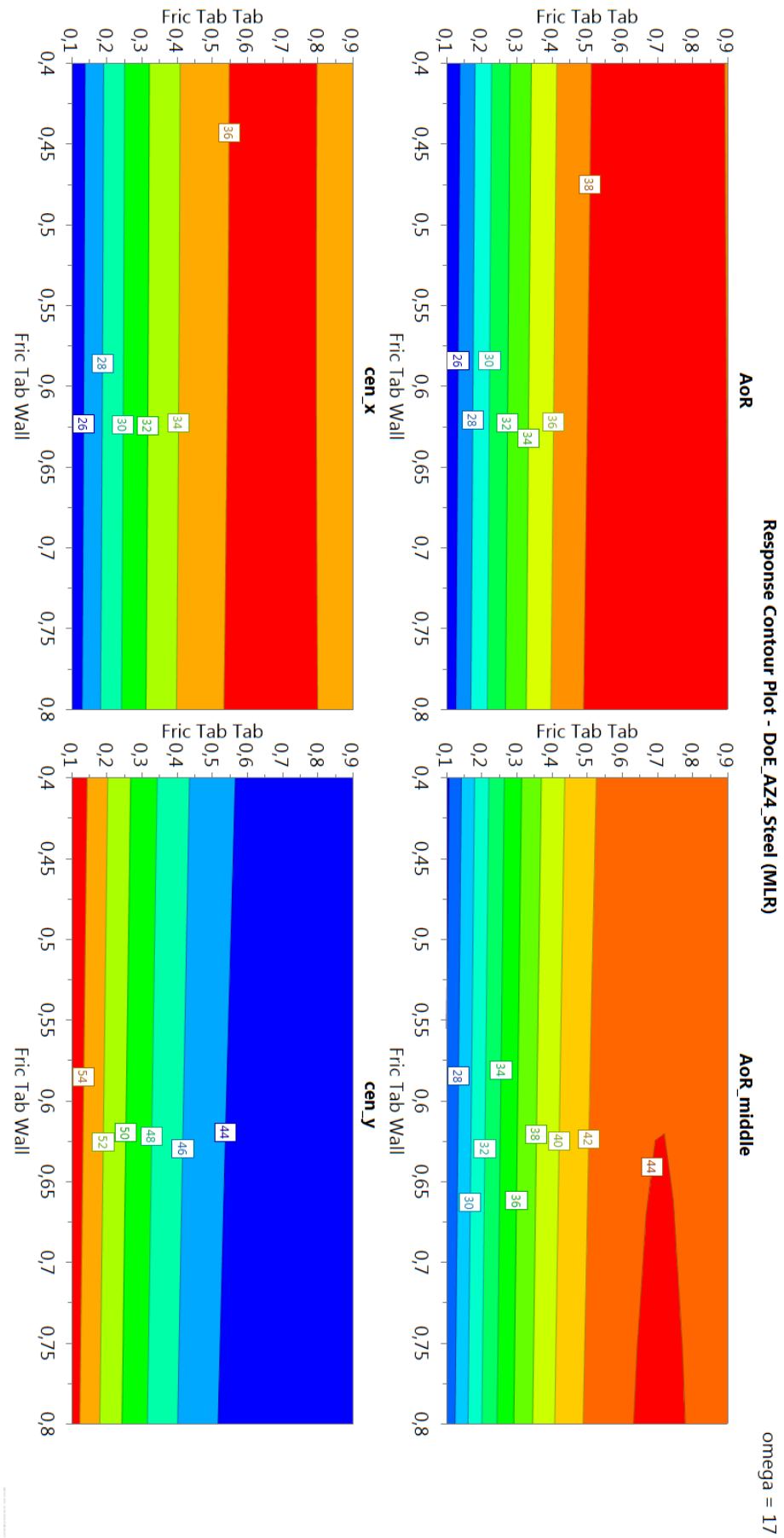

Figure 67: Contour plot of AZ4_Steel at $\omega = 17rpm$.

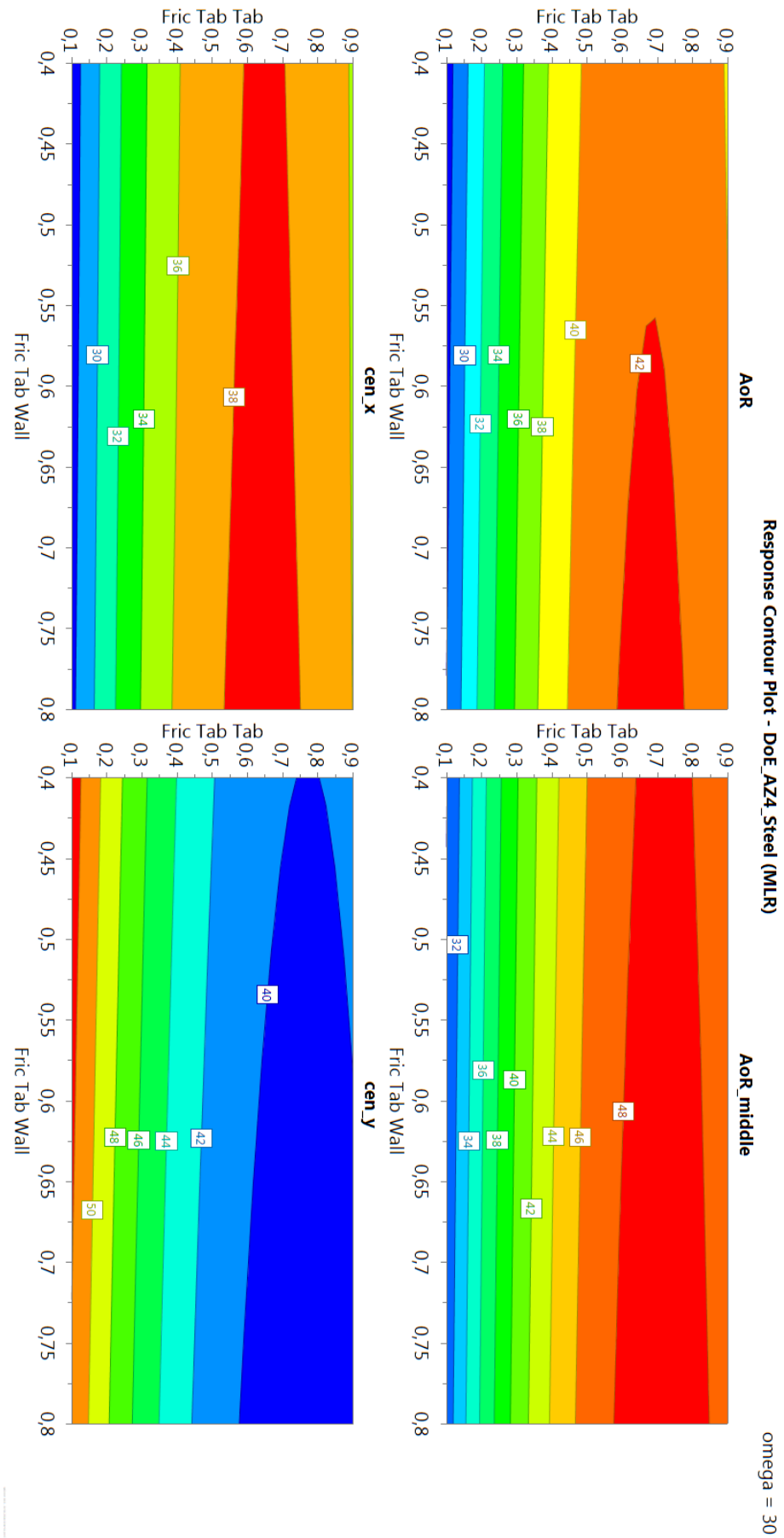

Figure 68: Contour plot of AZ4_Steel at $\omega = 30rpm$.

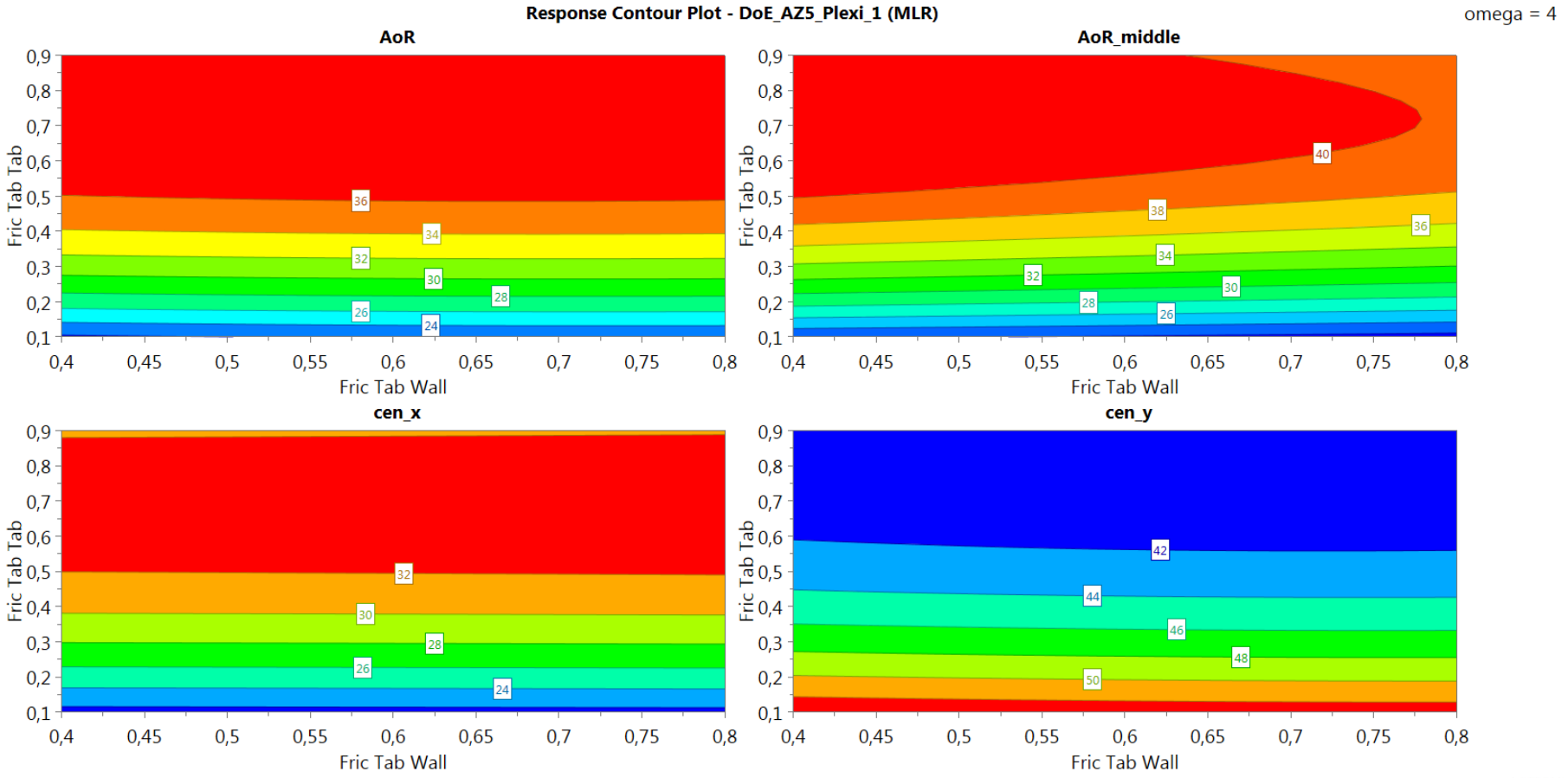

Figure 69: Contour plot of AZ5_Plexi at $\omega = 4rpm$.

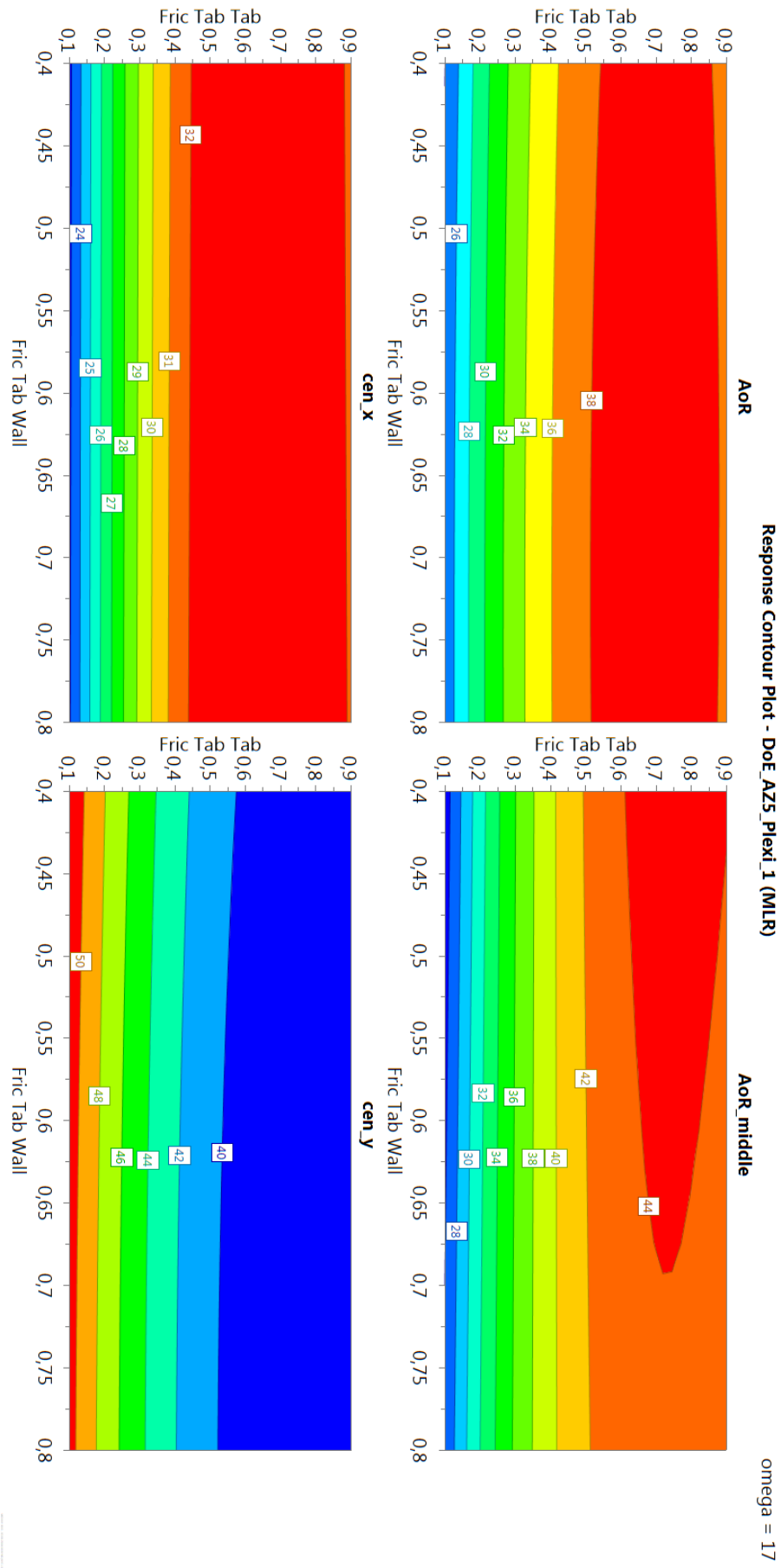

Figure 70: Contour plot of AZ5_Plexi at $\omega = 17rpm$.

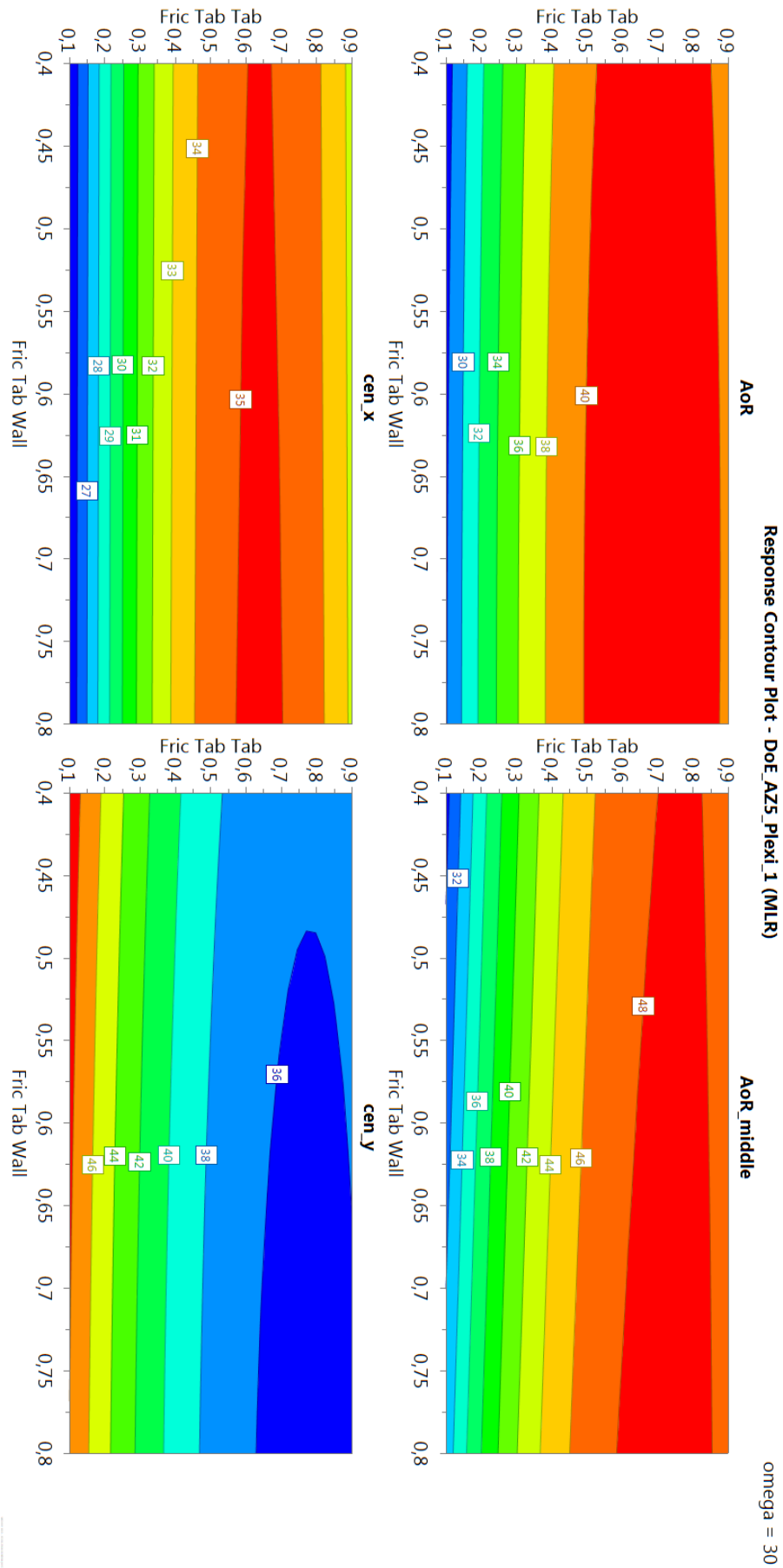

Figure 71: Contour plot of AZ5_Plexi at $\omega = 30rpm$.

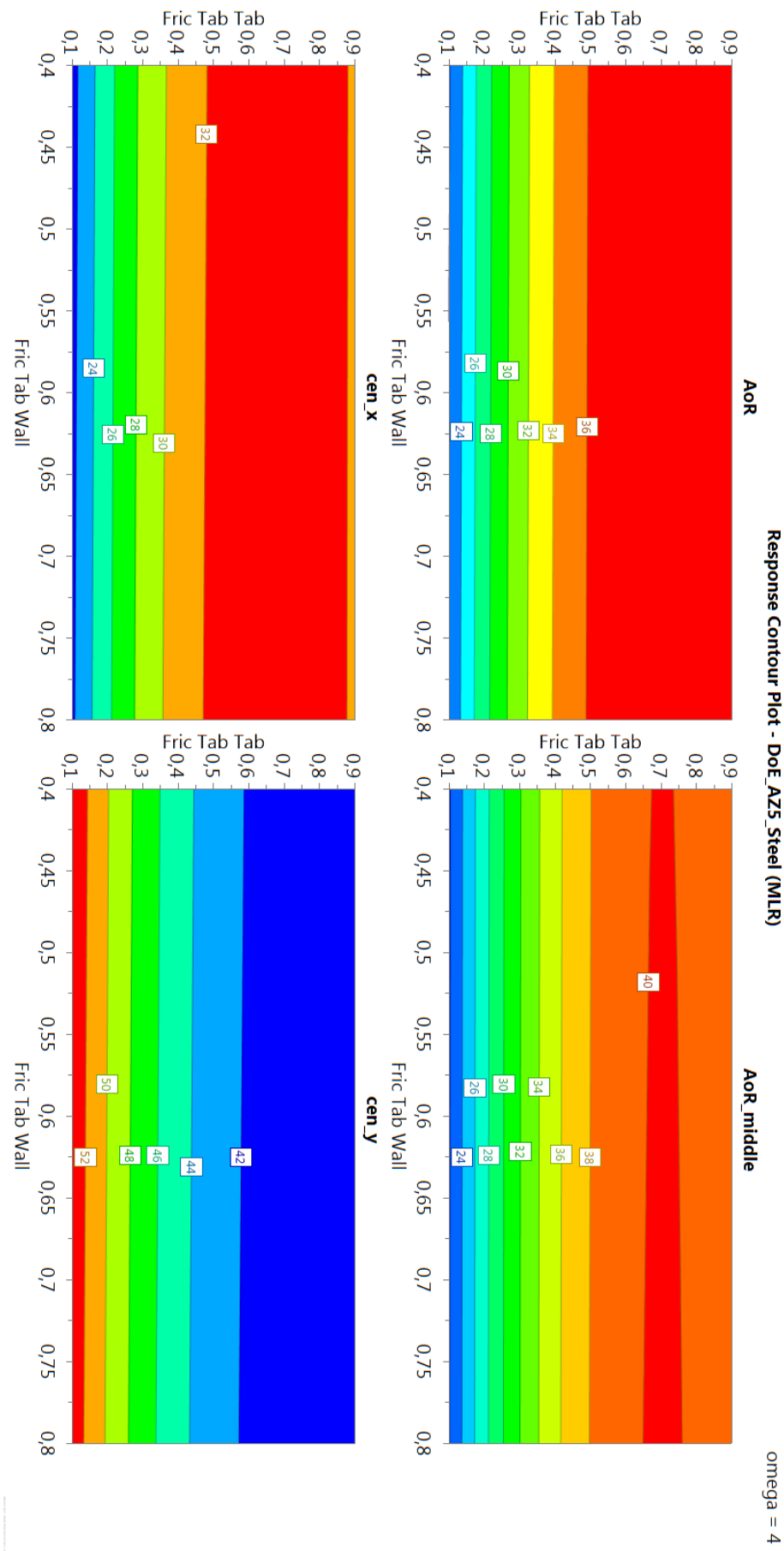

Figure 72: Contour plot of AZ5_Steel at $\omega = 4rpm$.

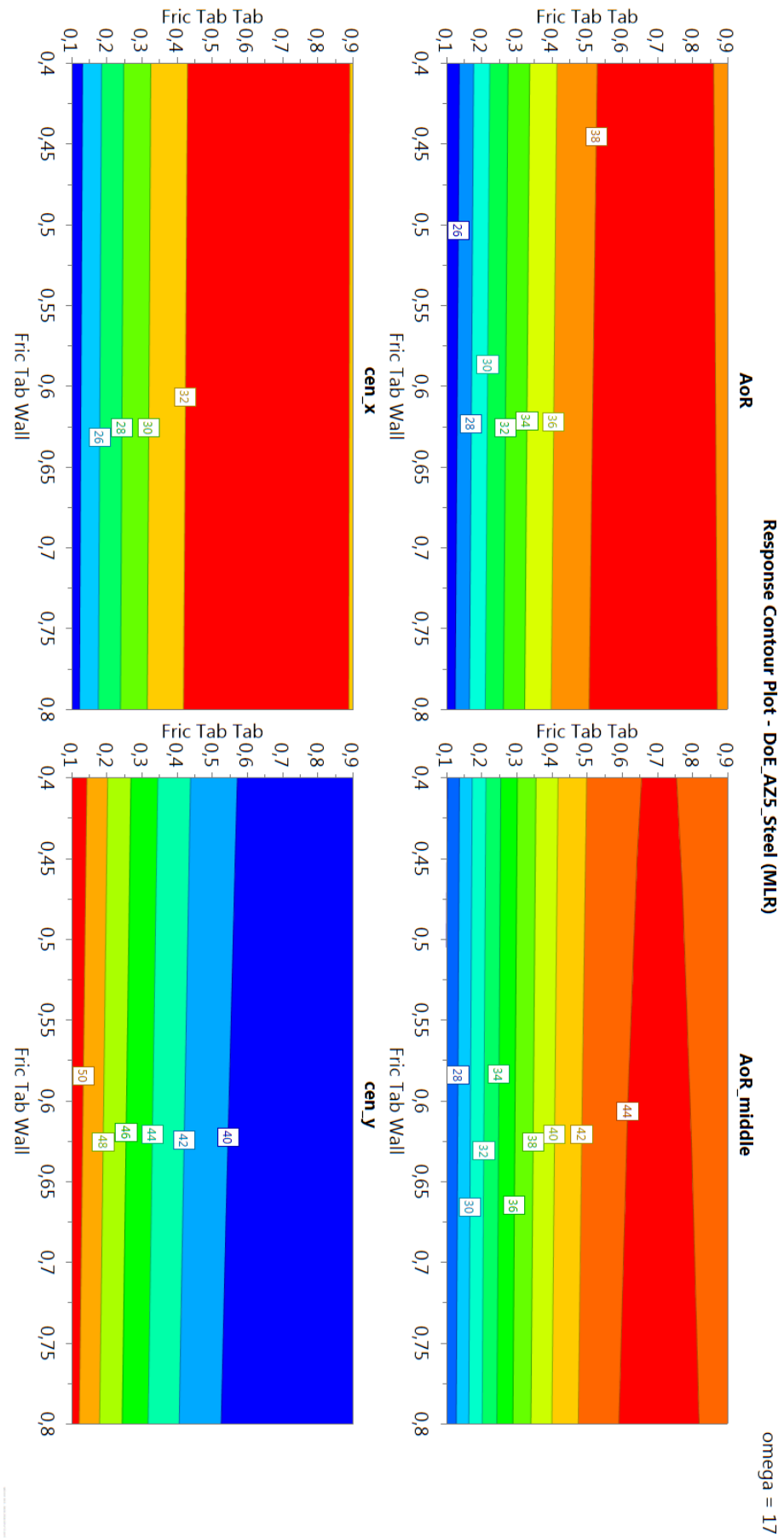

Figure 73: Contour plot of AZ5_Steel at $\omega = 17rpm$.

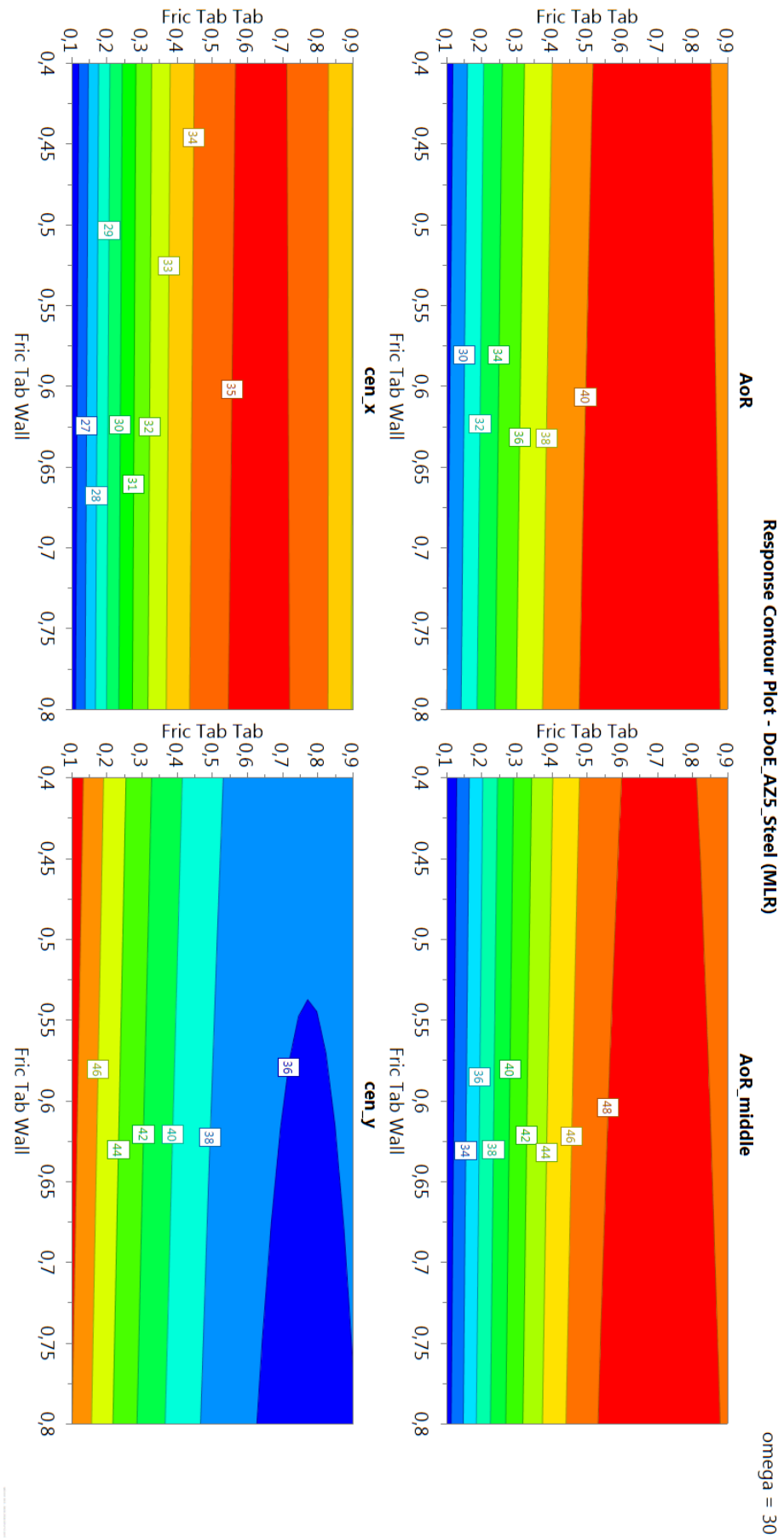

Figure 74: Contour plot of AZ5_Steel at $\omega = 30rpm$.

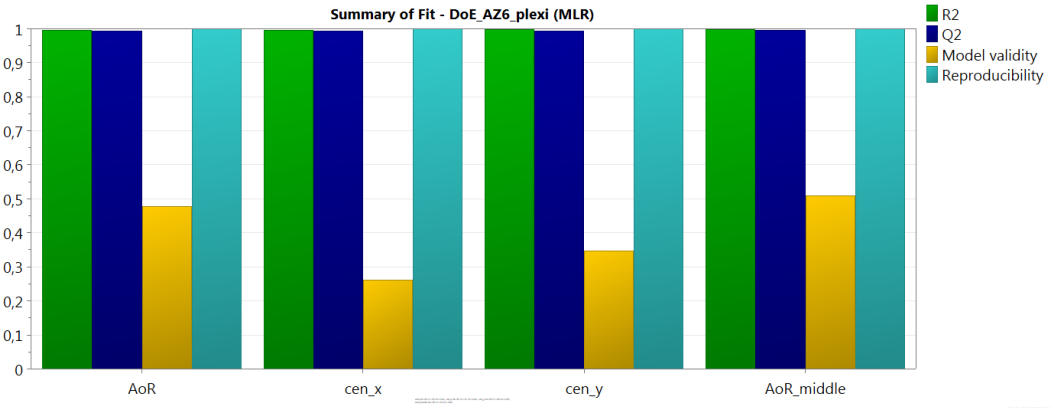

Figure 75: Illustration of the fitting parameters of AZ6_plexi.

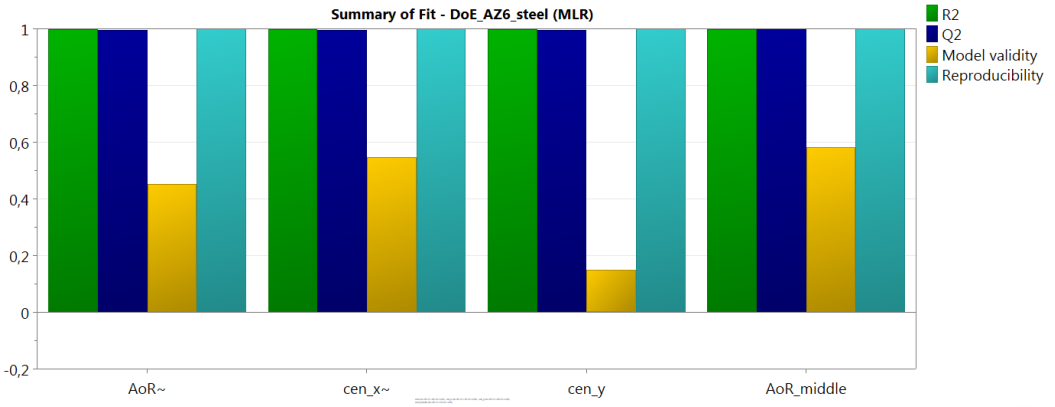

Figure 76: Illustration of the fitting parameters of AZ6_steel.

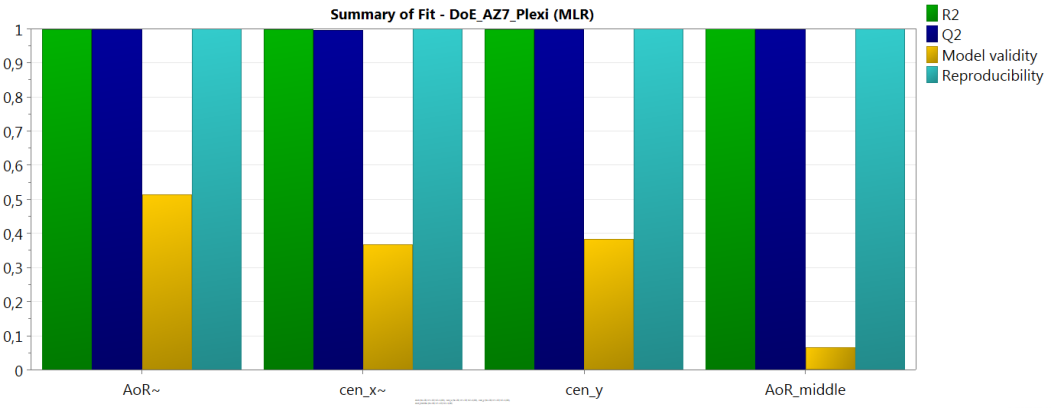

Figure 77: Illustration of the fitting parameters of AZ7_plexi

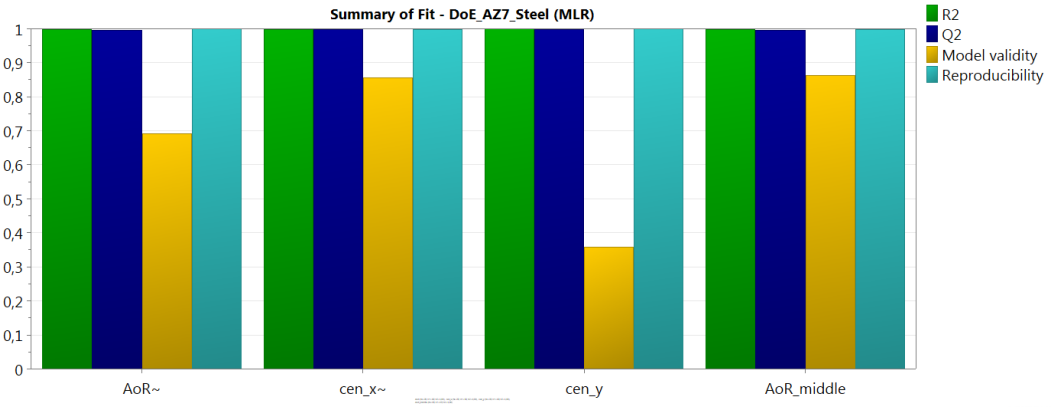

Figure 78: Illustration of the fitting parameters of AZ7_steel.

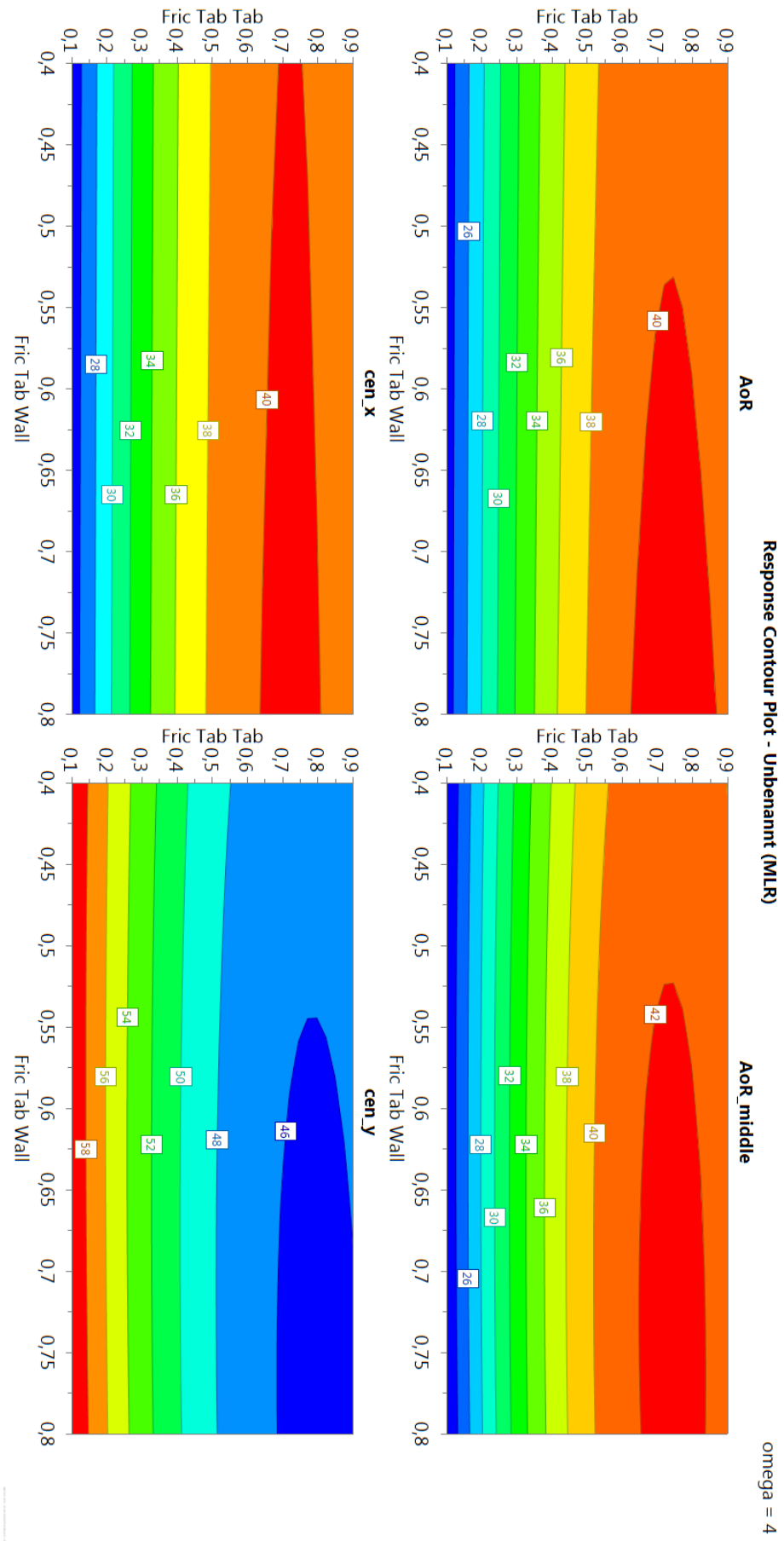

Figure 79: Contour plot of AZ6_Plexi at $\omega = 4rpm$.

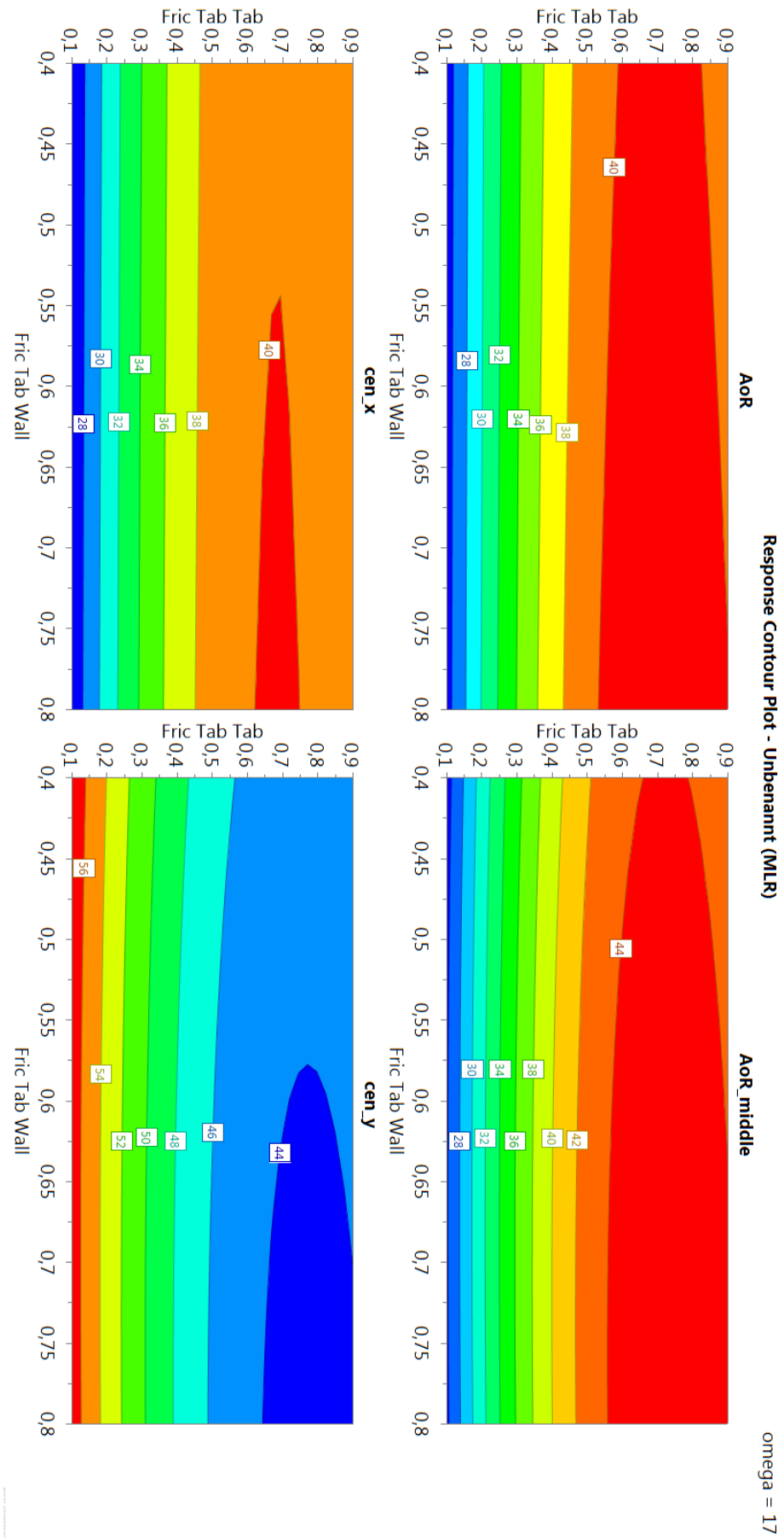

Figure 80: Contour plot of AZ6_Plexi at $\omega = 17rpm$.

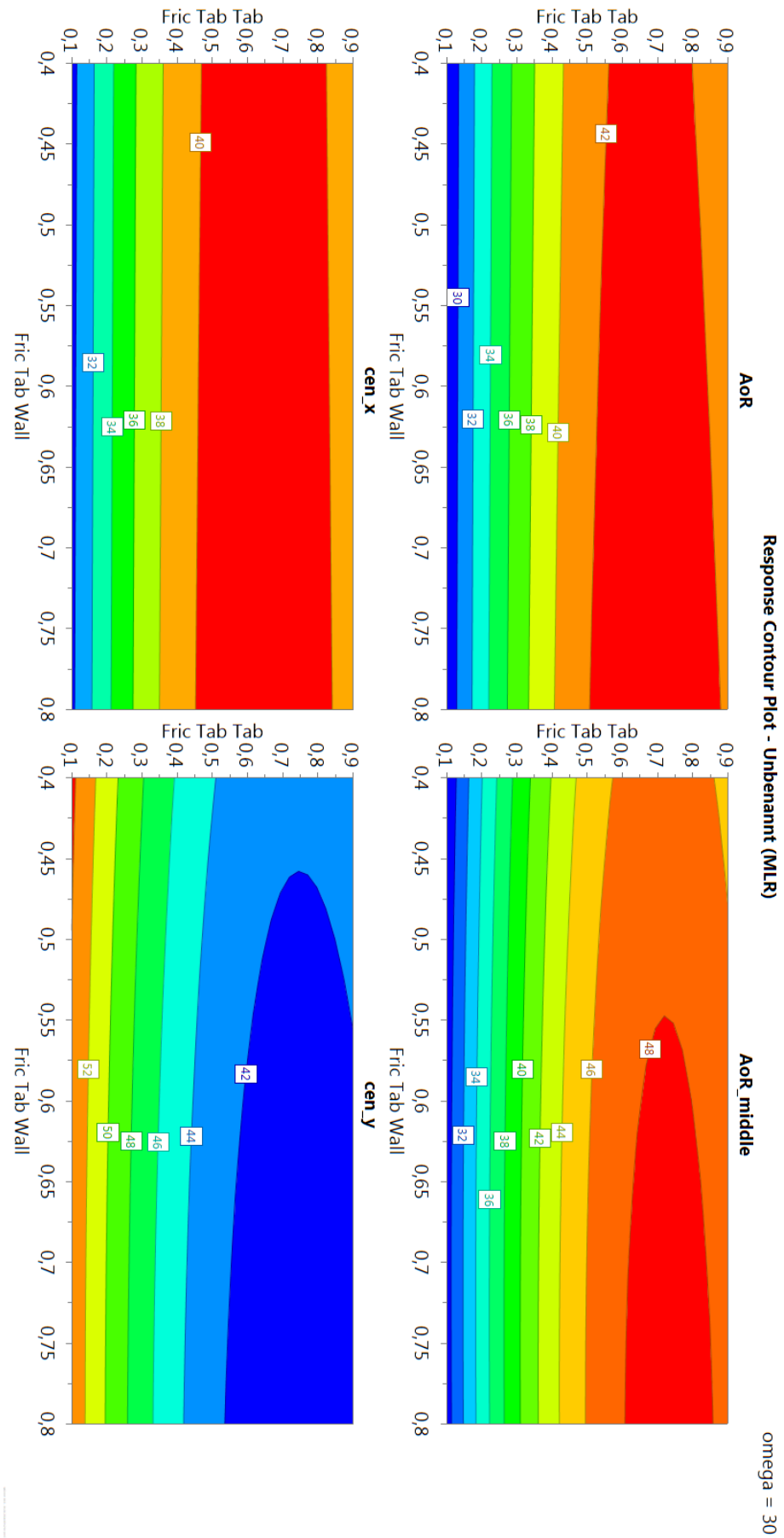

Figure 81: Contour plot of AZ6_Plexi at $\omega = 30rpm$.

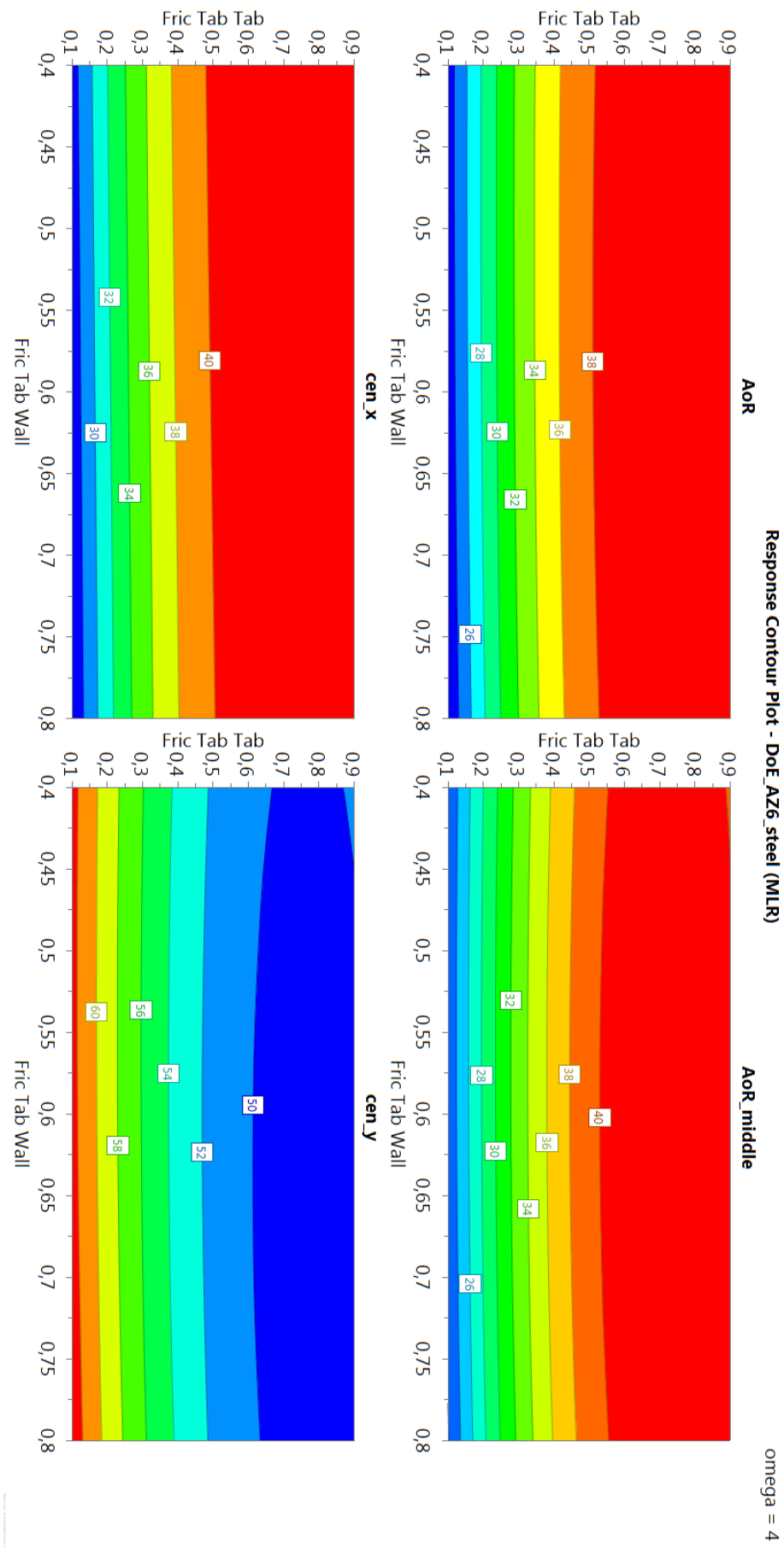

Figure 82: Contour plot of AZ6_Steel at $\omega = 4rpm$.

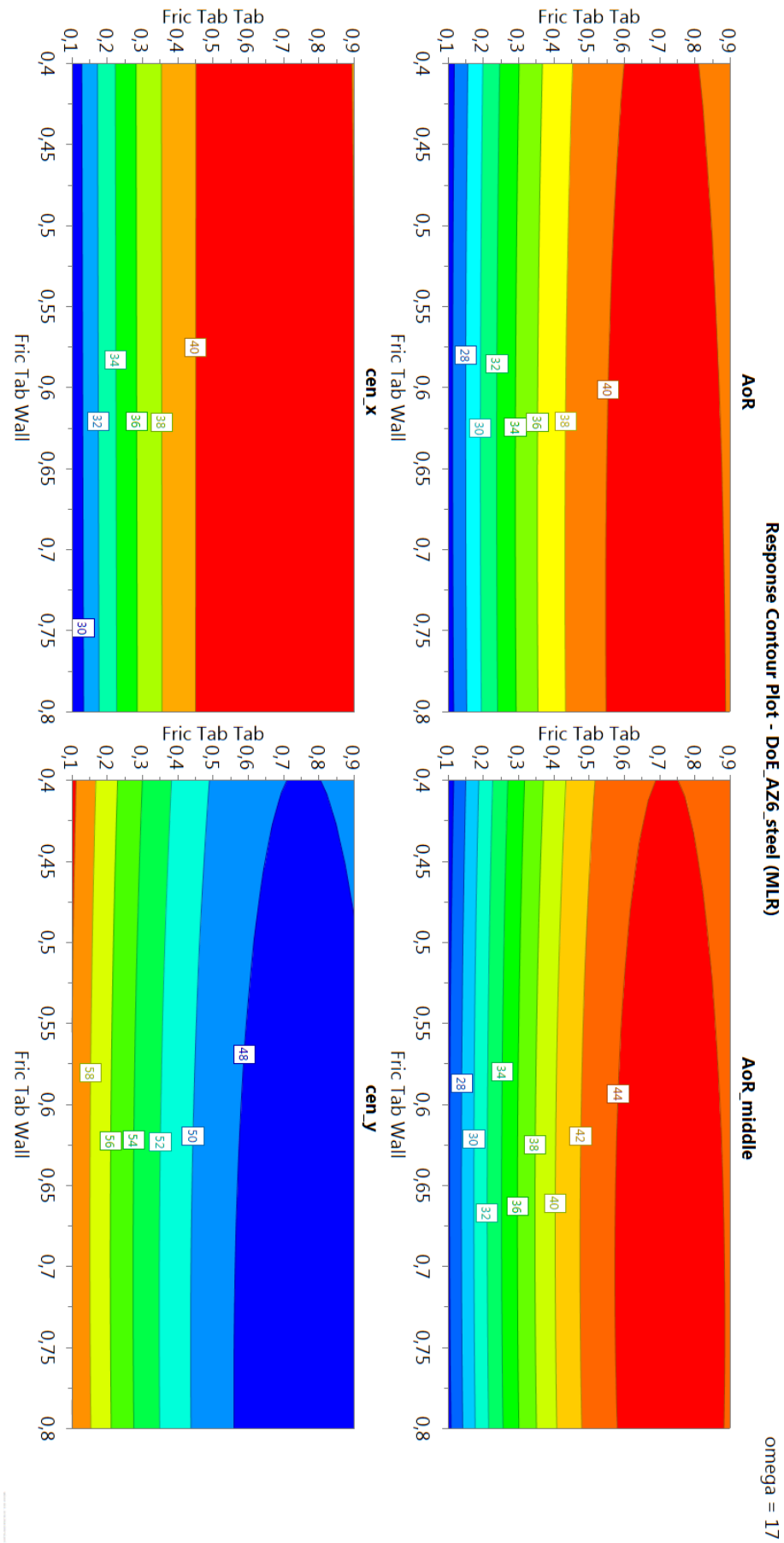

Figure 83: Contour plot of AZ6_Steel at $\omega = 17rpm$.

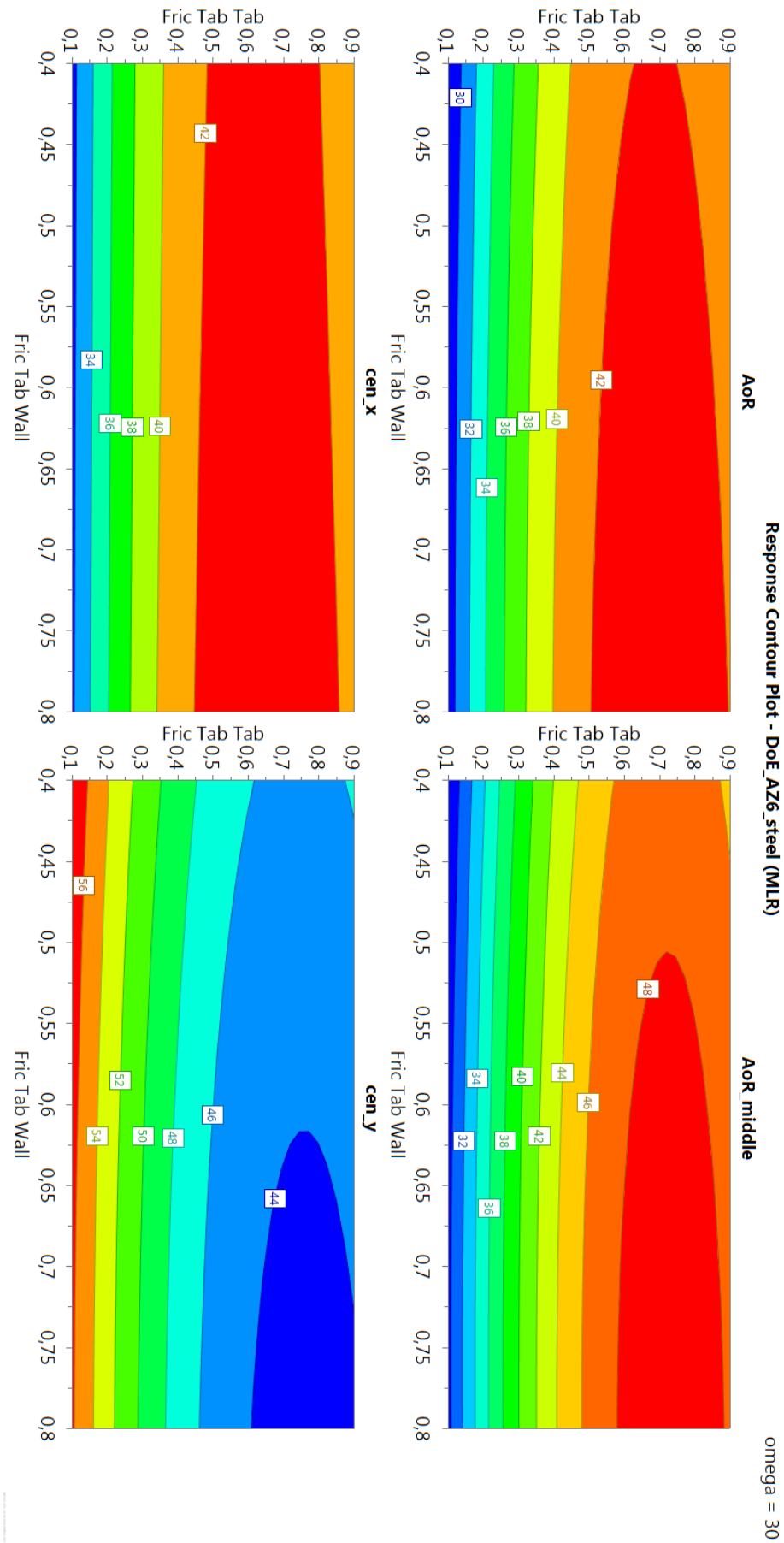

Figure 84: Contour plot of AZ6_Steel at $\omega = 30rpm$.

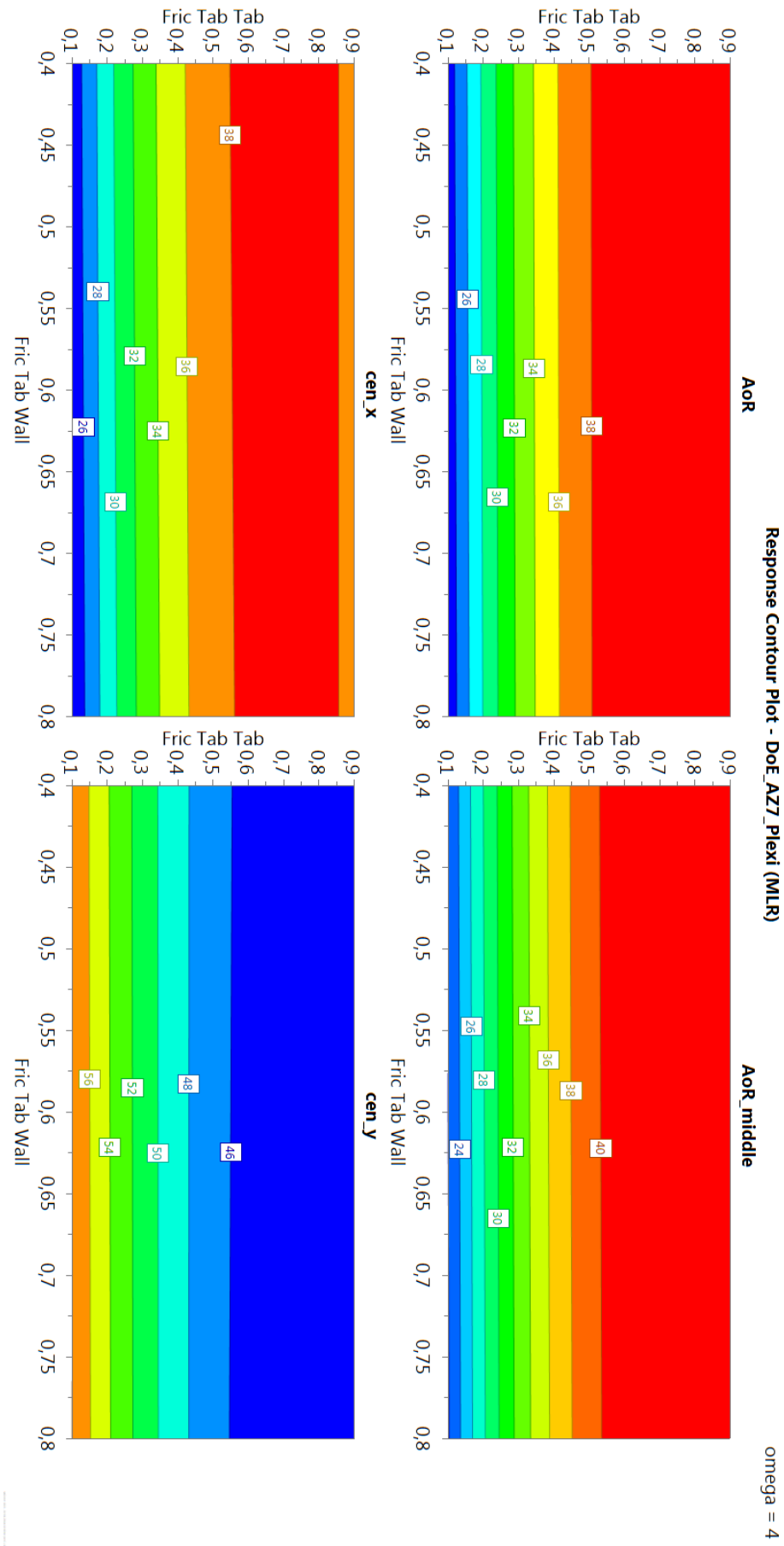

Figure 85: Contour plot of AZ7_Plexi at $\omega = 4rpm$.

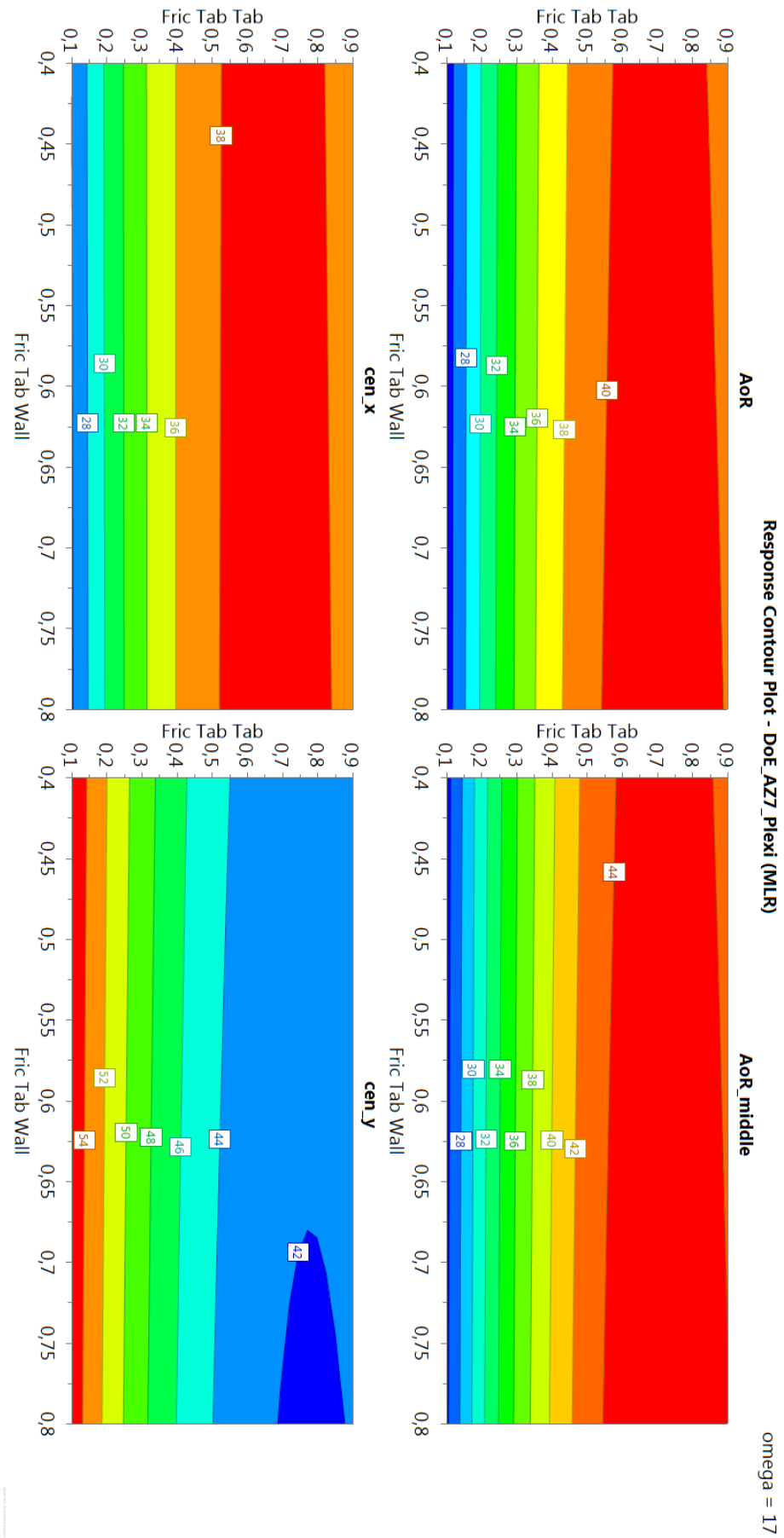

Figure 86: Contour plot of AZ7_Plexi at $\omega = 17rpm$.

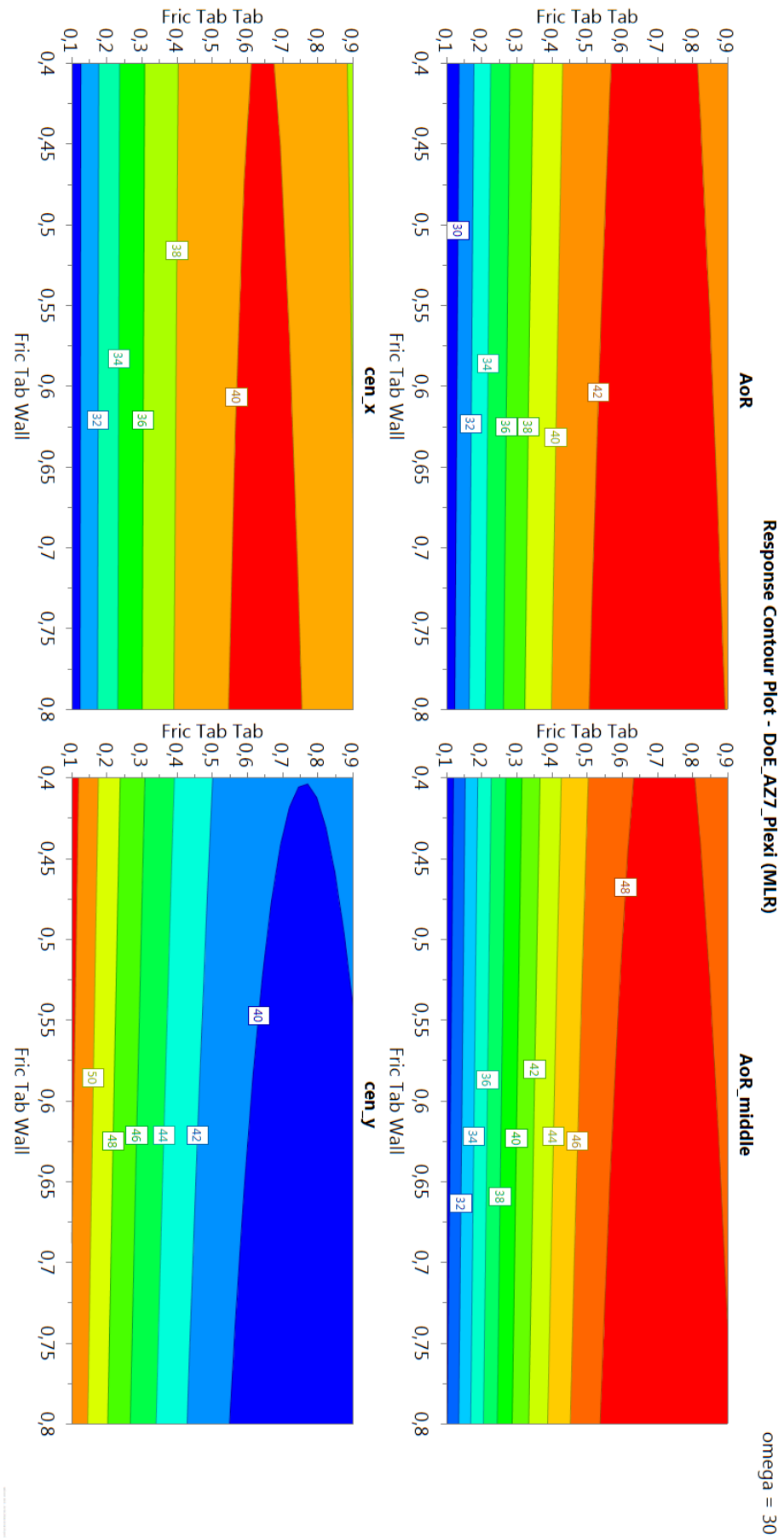

Figure 87: Contour plot of AZ7_Plexi at $\omega = 30rpm$.

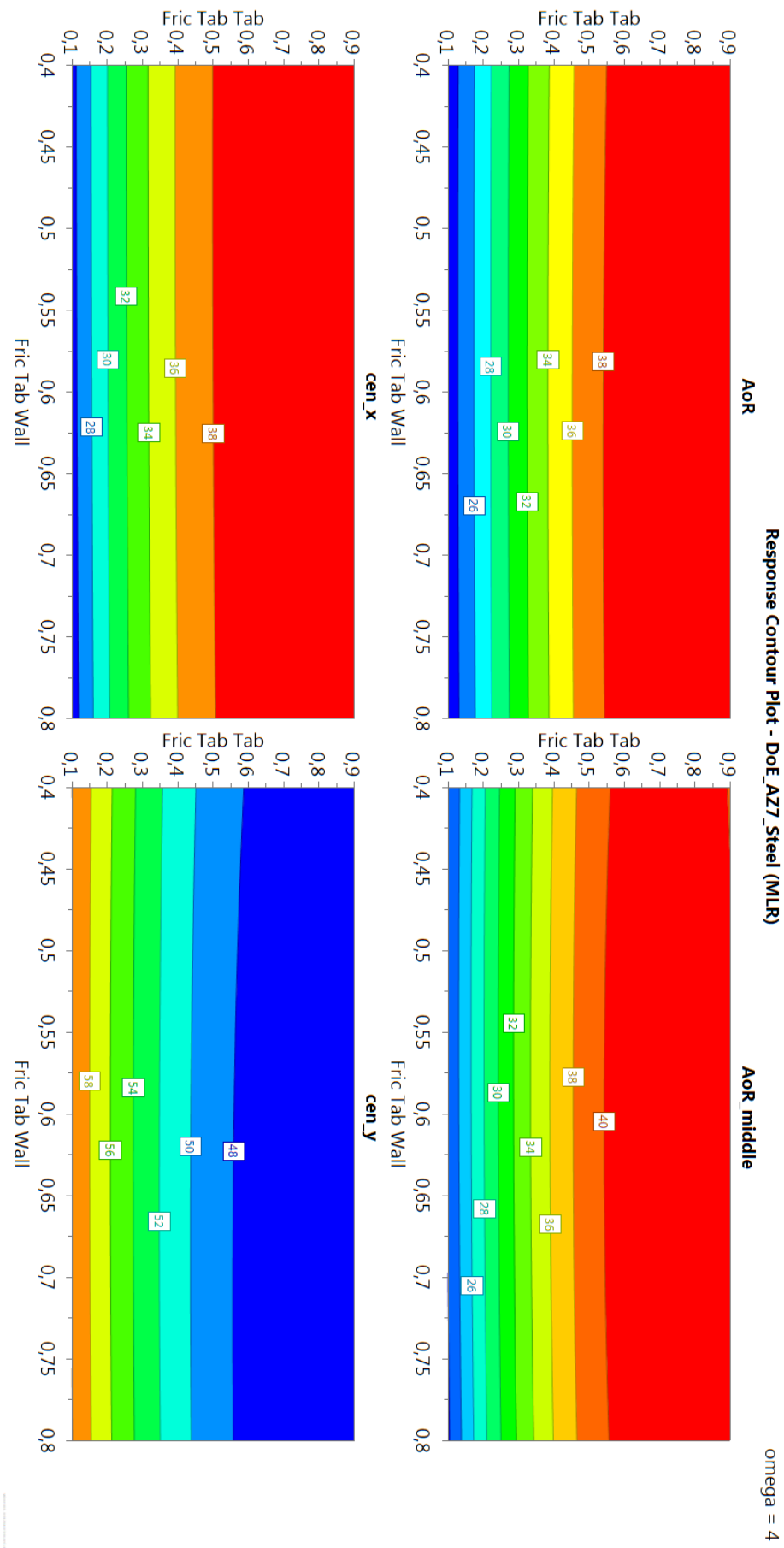

Figure 88. Contour plot of AZ7_Steel at $\omega = 4rpm$.

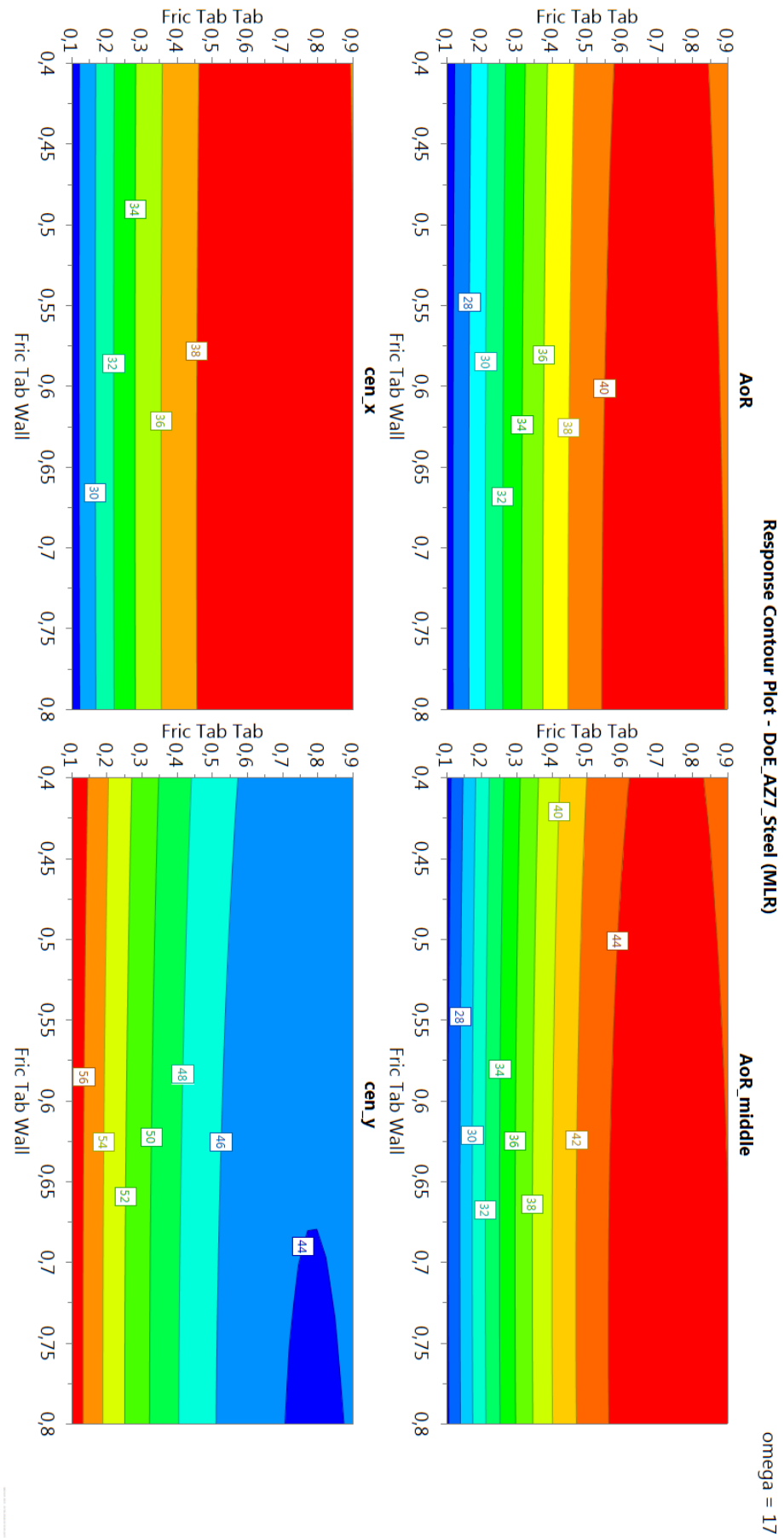

Figure 89: Contour plot of AZ7_Steel at $\omega = 17rpm$.

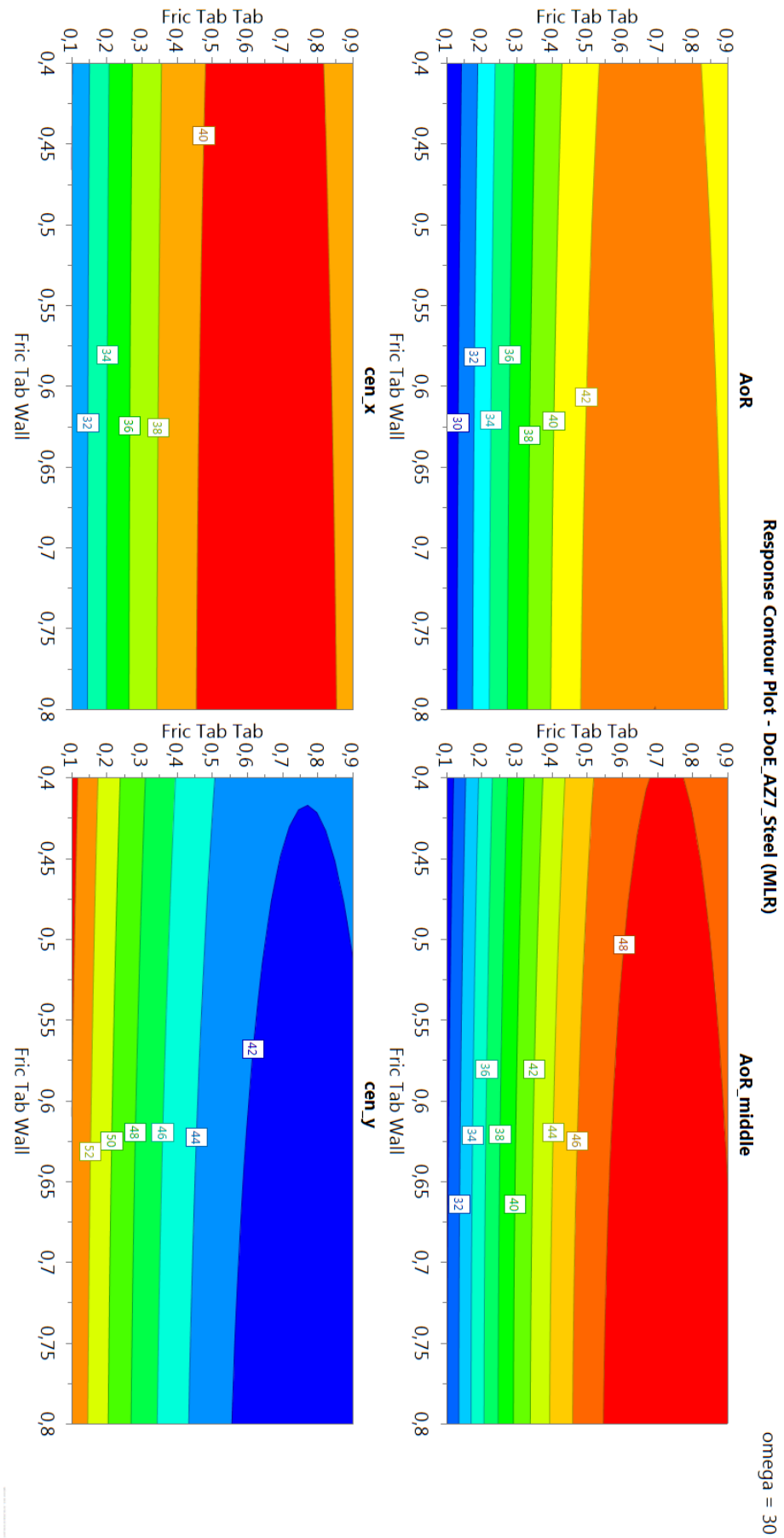

Figure 90: Contour plot of AZ7_Steel at $\omega = 30rpm$.

5.2 Results of statistical analysis

omega/[rpm]	AoR_lin/[°]	dev_lin/[°]	AoR_mid/[°]	dev_mid/[°]	cen_x/[au]	dev_x/[au]	cen_y/[au]	dev_y/[au]
4	26.71	0.57	22.99	0.78	27.37	0.58	53.46	0.54
6	27.40	0.65	23.37	0.65	27.99	0.65	52.73	0.66
8	27.44	0.83	22.86	0.83	28.00	0.69	52.75	0.72
10	27.35	0.60	23.11	0.60	27.67	0.66	52.64	0.43
12	27.87	0.79	24.31	1.04	28.11	0.81	52.77	0.55
14	28.28	0.54	24.33	0.54	28.76	0.45	52.61	0.44
16	28.80	0.33	24.27	0.48	29.06	0.27	52.13	0.32
18	29.12	0.36	24.26	0.53	29.24	0.32	51.83	0.29
20	29.29	0.28	24.31	0.36	29.22	0.29	51.56	0.28
22	29.14	0.27	24.44	0.49	28.76	0.55	51.46	0.27
24	29.11	0.25	24.43	0.55	28.52	0.27	51.21	0.23
26	29.37	0.26	24.49	0.46	28.66	0.23	50.85	0.21
28	29.57	0.20	24.58	0.55	28.73	0.25	50.60	0.16
30	29.71	0.28	24.82	0.69	28.86	0.30	50.34	0.23
32	29.94	0.21	24.85	0.57	28.92	0.25	49.97	0.21
34	30.21	0.27	25.22	0.56	29.01	0.26	49.54	0.32
36	30.38	0.24	25.31	0.56	28.99	0.26	49.45	0.23
38	30.52	0.16	25.50	0.54	29.08	0.16	49.10	0.21
40	30.57	0.28	25.43	0.37	28.99	0.36	48.83	0.34
42	30.49	0.21	25.46	0.38	28.69	0.21	48.71	0.23
44	30.67	0.17	26.02	0.81	28.72	0.14	48.37	0.14
46	30.77	0.21	26.18	0.87	28.73	0.21	48.07	0.19
48	30.91	0.12	26.39	0.91	28.69	0.16	47.64	0.20
50	31.12	0.17	26.88	0.86	28.73	0.18	47.39	0.18

Table 10: Statistical results of the experiment of configuration AZ1_Plexi.

omega/[rpm]	AoR_lin/[°]	dev_lin/[°]	AoR_mid/[°]	dev_mid/[°]	cen_x/[au]	dev_x/[au]	cen_y/[au]	dev_y/[au]
4	27.69	0.14	28.26	0.24	24.55	0.22	47.91	0.22
6	28.1	0.14	29.03	0.19	24.84	0.2	47.5	0.14
8	28.43	0.1	29.79	0.12	24.85	0.15	47.01	0.12
10	28.76	0.09	30.46	0.14	24.9	0.16	46.48	0.14
12	29.05	0.09	31.27	0.12	24.93	0.17	45.96	0.11
14	29.24	0.07	31.81	0.13	24.98	0.13	45.44	0.11
16	29.54	0.12	32.55	0.17	24.94	0.2	44.82	0.12
18	29.83	0.09	32.97	0.15	25.08	0.17	44.23	0.12
20	30.11	0.09	33.42	0.17	25.07	0.17	43.76	0.12
22	30.29	0.08	43.29	0.12	24.98	0.14	43.29	0.12
24	30.43	0.1	33.9	0.2	24.95	0.15	42.85	0.14
26	30.61	0.17	33.86	0.22	25	0.12	42.57	0.17
28	30.9	0.15	34.06	0.28	25.13	0.15	42.49	0.17
30	31.03	0.23	33.92	0.36	25.2	0.18	42.26	0.28
32	31.14	0.23	33.92	0.27	25.28	0.16	41.96	0.24
34	31.08	0.21	33.79	0.26	25.35	0.18	41.76	0.27
36	31.33	0.21	33.85	0.25	25.53	0.22	41.48	0.24
38	31.55	0.2	34.1	0.25	25.46	0.25	41.11	0.21
40	31.78	0.18	34.28	0.3	25.49	0.19	40.79	0.21
42	31.96	0.17	34.47	0.21	25.33	0.18	40.24	0.21
44	32.09	0.16	34.55	0.24	25.34	0.17	40	0.18
46	32.43	0.2	34.85	0.27	25.39	0.18	39.53	0.22
48	32.6	0.35	34.87	0.37	25.54	0.24	39.2	0.322
50	33.08	0.26	35.3	0.38	25.75	0.23	38.67	0.26

Table 11: Statistical results of the experiment of configuration AZ2_Plexi.

omega/[rpm]	AoR_lin/[°]	dev_lin/[°]	AoR_mid/[°]	dev_mid/[°]	cen_x/[au]	dev_x/[au]	cen_y/[au]	dev_y/[au]
4	29.56	1.48	30.24	1.18	28.75	1.03	50.20	1.58
6	29.13	1.10	30.47	1.20	29.13	0.89	49.61	1.01
8	31.01	0.94	30.95	1.06	29.86	0.80	48.67	1.00
10	31.69	0.73	31.21	0.68	30.41	0.65	47.64	0.80
12	32.12	0.59	31.68	0.54	30.51	0.63	47.13	0.80
14	32.55	0.42	32.18	0.56	30.83	0.44	46.67	0.65
16	32.81	0.41	32.38	0.48	31.10	0.41	46.01	0.63
18	33.67	0.41	32.74	0.46	31.87	0.33	44.79	0.51
20	33.88	0.47	33.14	0.44	31.91	0.43	44.48	0.74
22	34.05	0.44	33.46	0.43	31.97	0.36	44.34	0.59
24	34.39	0.47	33.92	0.40	31.85	0.35	44.21	0.66
26	34.74	0.40	34.37	0.38	32.06	0.34	43.68	0.61
28	35.07	0.45	34.79	0.31	32.20	0.45	43.26	0.69
30	35.55	0.32	35.16	0.47	32.53	0.25	42.79	0.47
32	36.10	0.39	35.47	0.40	33.01	0.26	42.46	0.58
34	36.54	0.44	35.80	0.45	33.14	0.38	41.75	0.66
36	36.98	0.49	35.76	0.44	33.42	0.32	40.99	0.75
38	37.46	0.60	36.09	0.35	33.73	0.41	40.47	0.79
40	37.92	0.54	35.96	0.52	33.98	0.32	39.68	0.66
42	38.24	0.60	36.32	0.49	34.18	0.40	39.38	0.83
44	38.86	0.62	36.19	0.63	34.47	0.45	38.52	0.79
46	39.24	0.57	36.37	0.59	34.71	0.32	38.32	0.71
48	39.73	0.49	36.64	0.69	34.91	0.27	37.85	0.62
50	40.14	0.57	36.86	0.72	34.87	0.28	37.47	0.79

Table 12: **Statistical results of the experiment of configuration AZ4_Plexi.**

omega/[rpm]	AoR_lin/[°]	dev_lin/[°]	AoR_mid/[°]	dev_mid/[°]	cen_x/[au]	dev_x/[au]	cen_y/[au]	dev_y/[au]
4	26.91	0.28	26.43	0.44	25.20	0.36	49.17	0.20
6	27.87	0.33	27.31	0.39	25.82	0.42	48.25	0.27
8	28.43	0.33	28.23	0.44	26.12	0.41	47.59	0.34
10	29.12	0.39	28.94	0.47	26.47	0.38	46.84	0.32
12	29.77	0.45	29.55	0.48	26.93	0.40	46.16	0.41
14	30.05	0.25	30.12	0.29	26.92	0.29	45.86	0.23
16	30.53	0.28	30.84	0.38	27.36	0.31	45.18	0.38
18	30.89	0.27	31.27	0.39	27.59	0.29	44.89	0.37
20	31.23	0.24	32.40	0.35	27.23	0.22	44.35	0.24
22	31.76	0.31	32.78	0.32	27.62	0.30	43.91	0.30
24	32.24	0.28	33.52	0.35	27.92	0.32	43.49	0.32
26	32.75	0.30	34.06	0.33	28.24	0.26	42.99	0.32
28	33.17	0.33	34.74	0.25	28.45	0.23	42.63	0.35
30	33.85	0.20	35.47	0.31	28.81	0.26	42.09	0.34
32	34.15	0.35	35.74	0.25	29.03	0.28	41.81	0.33
34	35.11	0.33	36.57	0.26	29.63	0.33	40.92	0.33
36	35.77	0.25	36.78	0.38	30.02	0.29	40.21	0.30
38	36.48	0.30	37.13	0.38	30.45	0.30	39.47	0.33
40	37.29	0.32	37.34	0.40	30.88	0.34	38.39	0.38
42	37.87	0.33	37.59	0.33	31.92	0.29	37.92	0.40
44	38.64	0.34	37.49	0.56	31.58	0.28	36.99	0.50
46	39.35	0.48	37.56	0.52	31.94	0.29	36.18	0.54
48	39.77	0.49	38.00	0.65	32.16	0.30	35.92	0.54
50	40.93	0.54	38.11	0.78	32.62	0.27	34.57	0.61

Table 13: **Statistical results of the experiment of configuration AZ5_Plexi.**

omega/[rpm]	AoR_lin/[°]	dev_lin/[°]	AoR_mid/[°]	dev_mid/[°]	cen_x/[au]	dev_x/[au]	cen_y/[au]	dev_y/[au]
4	28.48	0.50	29.08	0.99	30.31	0.41	56.01	0.49
8	28.15	0.58	28.98	0.46	29.98	0.46	55.95	0.59
12	27.99	0.46	28.01	0.77	29.93	0.42	56.06	0.42
16	28.25	0.40	27.64	0.71	30.23	0.37	55.84	0.38
17	28.41	0.33	27.75	0.43	30.31	0.28	55.68	0.26
20	29.01	0.38	28.14	0.68	30.76	0.41	55.12	0.30
24	29.56	0.38	28.56	0.86	31.07	0.34	54.65	0.33
28	30.24	0.34	29.08	0.59	31.50	0.28	54.01	0.35
30	30.74	0.34	29.68	0.67	31.74	0.28	53.43	0.42
32	31.10	0.31	30.13	0.59	32.00	0.34	53.01	0.31

Table 14: **Statistical results of the experiment of configuration AZ1_Steel.**

omega/[rpm]	AoR_lin/[°]	dev_lin/[°]	AoR_mid/[°]	dev_mid/[°]	cen_x/[au]	dev_x/[au]	cen_y/[au]	dev_y/[au]
4	30.67	0.2	31	0.27	27.58	0.31	47-81	0.29
8	31.41	0.16	32.35	0.21	27.98	0.3	46.82	0.19
12	31.74	0.1	33.51	0.19	27.99	0.24	45.93	0.24
16	32.052	0.15	34.67	0.17	27.86	0.31	45.12	0.24
17	32.27	0.09	35.07	0.16	28.04	0.18	44.89	0.17
20	32.62	0.09	35.98	0.14	28.1	0.27	44.07	0.15
24	33.02	0.13	36.96	0.18	28.04	0.28	43.18	0.35
28	33.24	0.18	37.17	0.26	28.1	0.21	42.94	0.37
30	33.39	0.19	37.37	0.28	28.1	0.18	42.69	0.44
32	33.62	0.22	37.68	0.31	28.14	0.28	42.37	0.45

Table 15: **Statistical results of the experiment of configuration AZ2_Steel**

omega/[rpm]	AoR_lin/[°]	dev_lin/[°]	AoR_mid/[°]	dev_mid/[°]	cen_x/[au]	dev_x/[au]	cen_y/[au]	dev_y/[au]
4	29.69	0.27	30.61	0.69	29.92	0.66	52.61	0.63
8	30.58	0.22	31.39	0.33	30.34	0.53	51.71	0.27
12	31.67	0.16	32.91	0.32	31.13	0.37	50.73	0.25
16	32.73	0.17	34.43	0.29	32	0.23	49.76	0.26
17	32.79	0.16	34.5	0.26	31.75	0.21	49.88	0.2
20	33.6	0.17	35.67	0.25	32.32	0.27	48.9	0.25
24	34.46	0.15	37.07	0.21	32.88	0.22	48.08	0.17
28	35.51	0.18	38.26	0.33	33.57	0.3	47.02	0.27
30	36.06	0.2	39.06	0.22	33.94	0.3	46.48	0.28
32	36.73	0.26	39.65	0.28	34.52	0.27	46.01	0.31

Table 16: **Statistical results of the experiment of configuration AZ4_Steel.**

omega/[rpm]	AoR_lin/[°]	dev_lin/[°]	AoR_mid/[°]	dev_mid/[°]	cen_x/[au]	dev_x/[au]	cen_y/[au]	dev_y/[au]
4	30.82	0.28	31.02	0.45	28.62	0.6	47.85	0.36
8	31.53	0.19	32.11	0.28	28.88	0.47	47.03	0.26
12	32.46	0.18	33.95	0.29	29.29	0.33	46.31	0.23
16	33.31	0.15	35.74	0.18	29.74	0.39	45.59	0.29
17	33.47	0.18	36.14	0.23	29.87	0.28	45.37	0.24
20	34.19	0.15	37.35	0.26	30.13	0.36	44.85	0.31
24	35.13	0.15	38.99	0.27	30.88	0.32	43.91	0.26
28	36.19	0.13	40.39	0.23	31.47	0.24	42.97	0.18
30	36.77	0.12	41.07	0.31	31.83	0.19	42.47	0.2
32	37.33	0.15	41.76	0.34	32.11	0.24	41.97	0.2

Table 17: **Statistical results of the experiment of configuration AZ5_Steel.**

omega/[rpm]	AoR_lin/[°]	dev_lin/[°]	AoR_mid/[°]	dev_mid/[°]	cen_x/[au]	dev_x/[au]	cen_y/[au]	dev_y/[au]
4	39.56	0.93	42.76	1.40	39.99	0.89	48.7	0.71
12	38.78	0.39	41.4	0.36	38.43	2.72	48.87	1.95
17	39.47	0.77	41.74	1.14	38.11	0.74	46.93	0.42
24	40.85	0.56	44..9	0.46	39.77	0.41	45.79	0.57
30	42.61	0.81	45.08	0.78	40.61	0.73	43.61	0.58

Table 18: **Statistical results of the experiment of configuration AZ6_Plexi**

omega/[rpm]	AoR_lin/[°]	dev_lin/[°]	AoR_mid/[°]	dev_mid/[°]	cen_x/[au]	dev_x/[au]	cen_y/[au]	dev_y/[au]
4	35.79	2.09	38.08	2.09	37.06	0.97	50.52	2.08
12	38.74	0.83	39.88	1.11	38.63	0.79	47.65	0.54
17	40.01	0.67	42.44	1.02	39.37	0.63	47.42	0.56
24	40.94	0.64	43.82	1.19	40.02	0.58	46.94	0.82
30	42.4	0.89	44.92	1.88	41.63	0.72	46.34	0.76

Table 19: **Statistical results of the experiment of configuration AZ6_Steel.**

omega/[rpm]	AoR_lin/[°]	dev_lin/[°]	AoR_mid/[°]	dev_mid/[°]	cen_x/[au]	dev_x/[au]	cen_y/[au]	dev_y/[au]
4	39.15	0.7	40.23	0.87	37.65	0.61	46.54	0.46
12	38.58	0.58	40.18	0.66	37.23	0.88	46.22	0.91
17	40.04	0.57	43.34	0.92	37.2	0.48	44.85	0.42
24	40.75	0.51	45.04	0.85	37.61	0.56	44.07	0.37
30	42.29	0.56	45.91	1.03	38.72	0.57	42.61	0.38

Table 20: **Statistical results of the experiment of configuration AZ7_Plexi.**

omega/[rpm]	AoR_lin/[°]	dev_lin/[°]	AoR_mid/[°]	dev_mid/[°]	cen_x/[au]	dev_x/[au]	cen_y/[au]	dev_y/[au]
4	40.4	0.75	41.79	1.11	37.92	0.7	45.1	0.66
12	40.11	0.75	43.21	1.26	37.15	0.71	44.79	0.64
17	41.69	1.15	44.11	1.59	39.19	1.13	44.67	0.77
24	43.07	0.86	46.87	1.31	40.43	0.92	43.84	0.46
30	43.42	1.07	47.02	2.07	40.81	1.03	43.34	0.96

Table 21: **Statistical results of the experiment of configuration AZ7_Steel.**

N	AoR_lin/[°]	dev_lin/[°]	AoR_mid/[°]	dev_mid/[°]	cen_x/[au]	dev_x/[au]	cen_y/[au]	dev_y/[au]
1	20.40	0.61	14.20	0.89	22.22	0.70	55.50	0.41
2	22.45	0.59	16.96	0.59	24.14	0.61	54.47	0.29
3	24.76	0.73	19.92	0.85	26.11	0.60	52.67	0.48
4	20.87	1.08	18.08	1.30	22.85	1.15	56.30	0.46
5	22.52	0.97	17.69	1.29	24.18	1.04	54.53	0.47
6	24.66	0.98	20.04	0.94	25.99	0.88	52.64	0.53
7	20.94	1.12	18.06	1.33	22.92	1,18	56.21	0.44
8	22.88	0.51	18.35	0.65	24.51	0.48	54.16	0.34
9	24.85	0.88	20.63	1.30	26.15	0.88	52.47	0.49
10	27.72	1.81	27.34	1.95	29.47	1.83	51.66	0.89
11	28.53	1.08	27.46	1.31	29.79	1.04	50.49	0.58
12	29.84	1.00	28.75	1.07	30.58	0.96	49.01	0.59
13	28.72	0.72	28.60	0.84	30.25	0.68	50.79	0.42
14	28.62	2.41	27.76	2.47	29.73	2.38	50.21	1.33
15	30.13	0.93	29.25	1.16	30.67	0.55	48.51	0.31
16	29.14	0.56	28.99	0.85	30.64	0.55	50.53	0.31
17	29.46	2.10	28.73	2.11	30.46	1.99	49.56	1.18
18	30.80	0.86	29.70	0.86	31.11	0.29	47.98	0.20
19	29.59	0.28	29.71	0.55	31.06	0.29	50.16	0.19
20	30.55	1.20	31.10	1.17	31.32	1.10	48.58	0.70
21	31.19	0.70	32.24	0.62	31.46	0.62	47.28	0.48
22	30.02	0.60	30.92	0.86	31.37	0.66	49.77	0.31
23	31.03	1.12	31.98	1.30	31.56	1.07	47.81	0.67
24	31.99	0.47	33.50	0.40	31.98	0.38	45.98	0.31
25	30.30	0.42	30.53	0.65	31.60	0.39	49.55	0.26
26	31.59	1.01	32.90	1.01	31.97	0.96	47.11	0.56
27	32.86	0.57	35.09	0.76	32.64	0.46	44.75	0.42
28	28.97	2.80	28.09	2.89	30.10	2.77	49.97	1.52

Table 22: Statistical results of the DoE in EDEM of configuration AZ1_Plexi.

N	AoR_lin/[°]	dev_lin/[°]	AoR_mid/[°]	dev_mid/[°]	cen_x/[au]	dev_x/[au]	cen_y/[au]	dev_y/[au]
1	22.48	0.54	22.32	0.64	21.49	0.49	51.71	0.26
2	25.49	0.41	25.45	0.51	23.55	0.37	48.92	0.19
3	27.12	0.55	27.29	0.57	24.58	0.42	47.04	0.33
4	22.42	0.34	21.91	0.43	21.45	0.32	51.73	0.12
5	25.79	0.27	25.99	0.45	23.75	0.24	48.59	0.16
6	27.26	0.67	27.71	0.77	24.59	0.54	46.80	0.35
7	22.45	0.35	22.31	0.42	21.68	0.32	51.68	0.17
8	25.86	0.33	25.99	0.51	23.77	0.27	48.50	0.23
9	27.41	0.65	27.71	0.69	24.71	0.57	46.55	0.39
10	29.14	0.43	29.57	0.54	26.94	0.40	47.21	0.26
11	31.44	0.44	34.63	0.72	28.02	0.35	43.97	0.31
12	32.32	0.59	36.34	0.73	28.44	0.49	42.57	0.39
13	29.26	0.43	29.67	0.67	27.05	0.41	47.13	0.22
14	31.69	0.35	35.29	0.51	28.15	0.27	43.72	0.21
15	33.39	0.50	38.28	0.76	29.13	0.43	41.34	0.42
16	29.53	0.43	30.08	0.52	27.23	0.41	46.91	0.23
17	31.73	0.32	38.96	0.55	28.16	0.25	43.59	0.18
18	33.66	0.49	38.96	0.71	29.33	0.33	40.85	0.39
19	30.04	0.36	30.52	0.39	27.61	0.36	46.49	0.25
20	31.55	0.39	35.86	0.57	27.94	0.34	43.31	0.19
21	33.40	0.32	39.49	0.55	29.09	0.30	40.80	0.21
22	29.99	0.32	30.75	0.51	27.53	0.29	46.38	0.27
23	31.76	0.38	36.27	0.53	28.06	0.27	43.06	0.19
24	33.85	0.37	40.69	0.56	29.37	0.33	39.96	0.31
25	30.01	0.33	30.83	0.51	27.57	0.25	46.56	0.28
26	31.73	0.41	36.28	0.67	28.06	0.32	43.02	0.20
27	34.14	0.43	41.36	0.52	29.65	0.28	39.48	0.27
28	31.78	0.38	35.16	0.54	28.20	0.33	43.64	0.27

Table 23: Statistical results of the DoE in EDEM of configuration AZ2_Plexi.

N	AoR_lin/[°]	dev_lin/[°]	AoR_mid/[°]	dev_mid/[°]	cen_x/[au]	dev_x/[au]	cen_y/[au]	dev_y/[au]
1	21.92	0.75	20.01	0.82	23.71	0.79	59.28	0.37
2	22.29	0.60	17.12	0.79	23.78	0.60	58.10	0.36
3	24.62	0.69	20.12	0.83	25.77	0.67	56.21	0.43
4	21.96	0.45	19.93	0.37	23.75	0.50	59.28	0.20
5	22.24	0.54	16.64	0.51	23.77	0.54	58.31	0.34
6	25.05	0.78	20.21	0.88	26.12	0.76	55.87	0.42
7	22.70	0.49	20.68	0.59	24.47	0.48	58.79	0.27
8	22.65	0.48	17.96	0.59	24.18	0.47	58.06	0.31
9	24.50	0.80	20.59	1.12	25.62	0.80	56.40	0.44
10	28.17	1.51	28.05	1.72	29.64	1.48	55.05	0.76
11	28.29	1.85	27.38	1.84	29.38	1.85	54.32	0.95
12	29.87	1.04	28.17	1.23	30.41	1.04	52.62	0.51
13	29.26	0.40	29.17	0.70	30.57	0.38	54.29	0.25
14	28.44	2.26	27.25	2.28	29.50	2.21	54.14	1.23
15	30.15	0.75	29.27	0.75	30.43	0.68	52.13	0.50
16	28.79	0.64	28.66	0.70	30.15	0.64	54.54	0.33
17	28.79	1.90	28.07	1.99	29.67	1.87	53.73	1.06
18	29.28	0.62	29.31	0.81	30.54	0.58	54.14	0.37
19	29.78	1.00	29.90	1.01	31.02	1.30	53.84	0.53
20	30.16	1.96	30.62	1.79	30.79	1.88	52.64	1.11
21	30.54	0.84	31.64	0.98	30.62	0.79	51.13	0.48
22	29.88	0.42	30.06	0.53	31.05	0.43	53.65	0.24
23	30.60	1.24	31.70	1.32	30.91	1.14	51.62	0.74
24	31.20	0.86	33.18	0.91	30.97	0.74	49.84	0.51
25	30.07	0.37	30.27	0.60	31.26	0.41	53.61	0.23
26	31.18	0.45	33.08	0.57	31.31	0.39	50.67	0.24
27	31.66	0.73	34.17	0.79	31.29	0.53	48.66	0.47
28	28.42	2.08	27.34	2.26	29.41	2.06	54.07	1.11

Table 24: Statistical results of the DoE in EDEM of configuration AZ1_Steel.

N	AoR_lin/[°]	dev_lin/[°]	AoR_mid/[°]	dev_mid/[°]	cen_x/[au]	dev_x/[au]	cen_y/[au]	dev_y/[au]
1	22.48	0.52	22.36	0.66	21.72	0.48	52.19	0.24
2	25.55	0.40	25.61	0.52	23.82	0.40	49.33	0.20
3	27.08	0.55	27.30	0.56	24.76	0.43	47.54	0.34
4	22.45	0.32	21.93	0.42	21.70	0.31	52.21	0.11
5	25.80	0.26	25.98	0.45	23.99	0.23	49.09	0.16
6	27.20	0.58	27.67	0.75	24.76	0.49	47.33	0.31
7	22.46	0.36	22.35	0.45	21.68	0.33	52.17	0.17
8	25.78	0.40	25.99	0.50	23.95	0.34	49.05	0.24
9	27.31	0.70	27.61	0.78	24.85	0.60	47.11	0.41
10	29.12	0.50	29.53	0.56	27.16	0.41	47.73	0.27
11	31.43	0.44	34.61	0.72	28.24	0.35	44.47	0.24
12	32.35	0.58	36.35	0.73	28.69	0.47	43.06	0.38
13	29.23	0.44	29.62	0.66	27.25	0.43	47.63	0.23
14	31.70	0.35	35.30	0.51	28.37	0.27	44.22	0.21
15	33.25	0.40	38.05	0.61	29.27	0.33	41.93	0.38
16	29.54	0.45	30.12	0.58	27.45	0.42	47.39	0.23
17	31.73	0.34	35.35	0.54	28.39	0.28	44.11	0.19
18	33.66	0.48	39.04	0.72	29.52	0.34	41.34	0.40
19	30.03	0.37	30.48	0.40	27.82	0.38	46.97	0.22
20	31.58	0.38	35.86	0.57	28.19	0.34	43.80	0.19
21	33.36	0.34	39.48	0.56	29.31	0.30	41.31	0.19
22	29.96	0.34	30.76	0.50	27.71	0.32	46.87	0.26
23	31.71	0.35	36.21	0.49	28.24	0.22	43.58	0.19
24	33.78	0.39	40.66	0.58	29.54	0.29	40.52	0.30
25	30.01	0.35	30.84	0.54	27.78	0.28	46.92	0.28
26	31.72	0.43	36.27	0.65	28.28	0.33	43.53	0.20
27	34.14	0.42	41.36	0.51	29.89	0.28	40.00	0.26
28	31.73	0.31	35.11	0.47	28.39	0.27	44.19	0.23

Table 25: Statistical results of the DoE in EDEM of configuration AZ2_Steel.

N	AoR_lin/[°]	dev_lin/[°]	AoR_mid/[°]	dev_mid/[°]	cen_x/[au]	dev_x/[au]	cen_y/[au]	dev_y/[au]
1	22.30	0.85	22.49	0.77	23.97	0.88	55.98	0.34
2	24.14	0.46	25.80	0.59	24.60	0.38	54.64	0.21
3	27.17	0.51	30.22	0.66	27.08	0.53	52.08	0.28
4	21.76	0.76	21.99	0.76	22.85	0.32	55.64	0.31
5	24.37	0.27	26.98	0.43	24.71	0.29	54.31	0.19
6	27.78	0.44	30.66	0.59	27.58	0.25	51.35	0.25
7	22.20	0.29	22.45	0.53	23.23	0.35	56.37	0.18
8	24.66	0.46	25.99	0.54	24.92	0.41	54.02	0.21
9	28.09	0.25	30.92	0.62	27.77	0.26	50.84	0.26
10	36.16	1.15	37.31	1.46	35.31	1.01	46.14	0.71
11	37.48	0.49	41.66	0.50	35.67	0.49	43.98	0.30
12	39.64	0.52	45.93	0.61	37.27	0.48	41.27	0.34
13	35.76	1.40	37.36	1.65	34.87	1.17	46.22	0.90
14	39.13	0.51	42.36	0.76	35.63	0.44	43.75	0.38
15	39.95	0.53	46.81	0.64	37.29	0.52	40.51	0.42
16	36.45	1.18	37.97	1.33	35.36	1.04	45.70	0.84
17	37.57	0.39	42.04	0.53	35.48	0.39	43.46	0.31
18	39.90	0.44	46.60	0.65	37.18	0.42	40.43	0.34
19	36.54	1.05	38.24	1.29	34.83	0.88	44.61	0.76
20	37.46	0.51	42.29	0.83	34.76	0.44	42.18	0.43
21	39.27	0.62	46.04	0.83	35.74	0.60	39.66	0.46
22	36.30	1.28	38.01	1.46	34.65	1.20	44.72	0.83
23	37.52	0.40	42.34	0.66	34.68	0.41	41.99	0.34
24	39.69	0.61	46.79	0.82	35.93	0.51	39.02	0.52
25	36.69	1.04	38.15	1.15	34.95	1.08	44.43	0.78
26	37.70	0.51	42.79	0.82	34.74	0.44	41.69	0.31
27	39.95	0.38	47.59	0.59	36.00	0.34	38.48	0.34
28	37.71	0.52	41.86	0.39	35.66	0.47	43.51	0.39

Table 26: Statistical results of the DoE in EDEM of configuration AZ4_Plexi.

N	AoR_lin/[°]	dev_lin/[°]	AoR_mid/[°]	dev_mid/[°]	cen_x/[au]	dev_x/[au]	cen_y/[au]	dev_y/[au]
1	21.95	0.63	21.98	0.54	21.41	0.63	53.43	0.53
2	23.97	0.38	25.72	0.48	22.69	0.34	51.53	0.15
3	27.01	0.45	30.25	0.45	24.97	0.26	49.08	0.18
4	22.02	0.34	21.87	0.70	21.31	0.29	53.20	0.15
5	24.61	0.28	26.25	0.51	23.02	0.25	51.06	0.16
6	27.72	0.36	30.93	0.54	25.45	0.27	48.41	0.22
7	22.08	0.41	22.05	0.34	21.29	0.40	53.12	0.18
8	24.55	0.24	26.07	0.50	22.91	0.22	50.50	0.12
9	27.85	0.32	30.87	0.51	25.44	0.29	48.08	0.19
10	35.56	0.65	36.72	1.95	31.85	1.54	43.41	1.03
11	37.43	0.19	41.70	0.54	32.67	0.19	41.07	0.15
12	39.61	0.43	46.33	0.54	34.16	0.35	38.49	0.35
13	36.42	1.28	37.98	1.46	32.46	1.13	42.73	0.87
14	37.84	0.35	42.47	0.63	32.88	0.33	40.47	0.19
15	39.92	0.37	47.15	0.48	34.24	0.30	37.82	0.26
16	36.25	0.94	37.80	1.16	32.31	0.85	42.79	0.66
17	38.00	0.35	42.92	0.49	32.94	0.30	40.12	0.25
18	40.07	0.34	47.48	0.47	34.27	0.25	37.50	0.26
19	36.54	2.11	47.48	0.47	31.89	1.87	41.35	1.46
20	37.53	0.33	42.32	0.66	31.77	0.27	39.23	0.30
21	39.36	0.58	46.47	0.77	32.88	0.42	36.65	0.42
22	36.43	1.30	38.41	1.31	31.61	1.15	41.23	0.86
23	37.37	0.40	42.46	0.60	31.57	0.31	39.04	0.22
24	39.73	0.33	47.26	0.53	33.01	0.28	36.05	0.27
25	36.54	1.35	38.49	1.31	31.80	1.21	41.33	0.98
26	37.37	0.32	42.58	0.42	31.52	0.25	38.91	0.23
27	39.72	0.37	47.50	0.45	32.83	0.33	35.79	0.23
28	37.85	0.45	42.45	0.71	32.88	0.34	40.45	0.38

Table 27: Statistical results of the DoE in EDEM of configuration AZ5_Plexi.

N	AoR_lin/[°]	dev_lin/[°]	AoR_mid/[°]	dev_mid/[°]	cen_x/[au]	dev_x/[au]	cen_y/[au]	dev_y/[au]
1	22.03	0.53	22.16	0.91	23.08	0.54	57.51	0.20
2	24.18	0.35	25.56	0.42	24.53	0.35	55.63	0.16
3	26.90	0.36	29.88	0.57	26.83	0.27	53.18	0.21
4	22.16	0.47	22.42	0.52	23.10	0.50	57.36	0.18
5	24.52	0.29	25.98	0.49	24.77	0.29	55.22	0.14
6	27.85	0.40	30.45	0.65	27.52	0.36	52.21	0.25
7	22.13	0.78	24.08	0.83	23.11	0.82	57.23	0.32
8	24.63	0.48	25.91	0.56	24.82	0.44	55.04	0.29
9	28.19	0.36	30.93	0.68	27.74	0.27	51.73	0.28
10	36.61	0.93	37.88	0.81	35.28	0.89	46.95	0.68
11	37.79	0.38	41.73	0.47	35.48	0.36	44.87	0.23
12	40.23	0.48	45.99	0.64	37.27	0.37	42.02	0.33
13	35.96	1.16	37.39	1.25	34.60	1.11	47.26	0.78
14	38.06	0.42	42.12	0.51	35.60	0.37	44.52	0.32
15	40.55	0.40	46.64	0.55	37.33	0.34	41.49	0.28
16	36.73	1.36	38.15	1.56	35.21	1.28	46.54	0.93
17	38.11	0.41	42.10	0.61	35.56	0.34	44.32	0.25
18	40.69	0.48	47.04	0.61	37.38	0.37	41.01	0.31
19	36.70	2.27	38.23	2.24	34.60	2.02	45.70	1.63
20	37.89	0.52	42.10	0.81	34.64	0.45	43.20	0.36
21	39.87	0.44	46.27	0.56	35.86	0.37	40.59	0.26
22	36.69	1.32	38.45	1.53	34.57	1.15	45.47	0.86
23	37.85	0.42	42.32	0.66	34.54	0.36	43.12	0.32
24	40.22	0.50	46.81	0.56	36.06	0.41	39.91	0.32
25	36.63	1.80	38.34	2.37	34.54	1.70	45.59	1.34
26	38.05	0.50	42.68	0.88	34.62	0.42	42.86	0.39
27	40.41	0.42	47.17	0.63	36.04	0.35	39.53	0.37
28	37.97	0.27	41.99	0.50	35.51	0.26	44.53	0.18

Table 28: Statistical results of the DoE in EDEM of configuration AZ4_Steel.

N	AoR_lin/[°]	dev_lin/[°]	AoR_mid/[°]	dev_mid/[°]	cen_x/[au]	dev_x/[au]	cen_y/[au]	dev_y/[au]
1	22.01	0.61	22.21	0.64	21.46	0.61	53.44	0.28
2	24.14	0.38	25.66	0.66	22.86	0.34	51.64	0.19
3	27.02	0.40	30.26	0.57	25.18	0.33	49.28	0.24
4	21.62	0.53	21.62	0.69	21.06	0.51	53.52	0.26
5	24.49	0.36	26.04	0.49	23.05	0.31	51.19	0.19
6	27.39	0.35	30.50	0.59	25.30	0.33	48.63	0.17
7	22.19	0.66	22.28	0.94	21.55	0.59	53.25	0.30
8	24.92	0.44	26.59	0.60	23.37	0.36	50.48	0.28
9	28.05	0.40	31.05	0.51	25.80	0.30	48.16	0.20
10	36.16	1.23	37.68	1.26	32.45	1.12	43.09	0.86
11	37.50	0.49	41.76	0.83	32.88	0.42	41.11	0.35
12	39.87	0.39	46.80	0.68	34.49	0.32	38.32	0.37
13	36.09	1.07	37.57	1.21	32.33	0.98	43.07	0.75
14	37.87	0.34	42.61	0.46	33.03	0.33	40.54	0.27
15	40.06	0.44	47.26	0.53	34.54	0.39	37.80	0.30
16	36.40	1.29	37.83	1.29	32.60	1.14	42.86	0.89
17	37.79	0.34	42.69	0.50	32.89	0.27	40.49	0.26
18	40.14	0.34	47.46	0.47	34.51	0.31	37.55	0.24
19	36.25	2.33	38.51	2.54	31.70	1.07	41.62	1.52
20	37.19	0.30	42.03	0.48	31.67	0.27	39.50	0.19
21	39.43	0.37	46.65	0.37	33.06	0.29	36.78	0.23
22	36.48	1.75	38.44	1.83	31.94	1.51	41.36	1.23
23	37.33	0.28	42.26	0.52	31.70	0.22	39.27	0.28
24	39.49	0.56	47.17	0.75	32.99	0.38	36.20	0.46
25	35.88	1.77	38.01	2.10	31.40	1.62	41.81	1.07
26	37.67	0.47	42.93	0.57	31.88	0.40	38.81	0.33
27	39.73	0.31	47.42	0.51	33.12	0.26	36.02	0.37
28	37.85	0.45	42.45	0.71	33.05	0.34	40.58	0.38

Table 29: Statistical results of the DoE in EDEM of configuration AZ5_Steel.

N	AoR_lin/[°]	dev_lin/[°]	AoR_mid/[°]	dev_mid/[°]	cen_x/[au]	dev_x/[au]	cen_y/[au]	dev_y/[au]
1	22.21	0.90	21.59	0.79	24.20	1.07	60.03	0.44
2	25.59	0.57	25.87	0.67	27.07	0.59	57.12	0.39
3	28.41	0.60	28.30	0.61	29.56	0.47	54.08	0.38
4	22.96	0.87	22.70	0.84	24.88	0.98	59.50	0.46
5	25.14	0.40	25.41	0.74	26.53	0.40	57.29	0.27
6	28.54	0.37	28.99	0.80	29.57	0.38	53.79	0.28
7	22.51	0.98	22.20	1.01	24.31	1.13	59.92	0.43
8	25.46	0.30	25.50	0.59	26.73	0.29	57.03	0.24
9	28.73	0.50	29.09	0.74	29.63	0.47	53.43	0.32
10	37.88	1.51	38.85	1.54	38.52	1.48	48.62	1.14
11	38.87	0.53	41.87	0.59	38.65	0.49	46.70	0.41
12	40.42	0.55	44.43	0.65	39.73	0.38	44.81	0.38
13	37.83	1.73	38.98	1.66	38.34	1.64	48.43	1.34
14	39.10	0.77	42.55	0.64	38.65	0.59	46.12	0.48
15	41.56	0.34	46.32	0.52	40.42	0.30	42.85	0.40
16	38.67	2.31	39.80	2.21	39.02	2.25	47.70	1.69
17	39.37	0.47	42.58	0.55	38.75	0.36	45.79	0.29
18	41.51	0.64	46.27	0.81	40.25	0.43	42.65	0.38
19	38.26	1.19	40.15	1.35	38.45	1.13	47.01	0.85
20	39.17	0.64	42.90	0.62	37.98	0.48	45.08	0.35
21	40.38	0.56	44.93	0.95	38.69	0.44	43.48	0.45
22	39.12	1.91	41.00	2.04	38.85	1.81	46.47	1.47
23	39.36	0.49	43.38	0.61	37.89	0.44	44.36	0.31
24	41.97	0.55	47.40	0.90	39.53	0.44	41.16	0.47
25	39.63	1.99	41.74	2.44	39.27	1.97	45.78	1.58
26	39.42	0.67	43.33	0.88	37.85	0.56	44.37	0.36
27	41.94	0.69	47.67	0.91	39.30	0.54	40.71	0.55
28	39.20	0.43	42.67	0.45	38.69	0.40	46.07	0.24

Table 30: Statistical results of the DoE in EDEM of configuration AZ6_Plexi.

N	AoR_lin/[°]	dev_lin/[°]	AoR_mid/[°]	dev_mid/[°]	cen_x/[au]	dev_x/[au]	cen_y/[au]	dev_y/[au]
1	22.76	0.73	22.18	0.85	26.86	0.84	62.78	0.41
2	25.56	0.54	25.21	0.63	29.17	0.54	60.10	0.37
3	28.27	0.54	28.35	0.65	31.43	0.51	57.24	0.39
4	22.40	0.72	22.86	0.78	26.30	0.85	62.95	0.36
5	25.32	0.46	25.53	0.78	28.70	0.45	60.13	0.25
6	28.71	0.40	29.13	0.70	31.71	0.31	56.67	0.29
7	22.21	0.53	21.69	0.62	25.98	0.59	62.99	0.29
8	25.32	0.48	25.65	0.77	28.60	0.50	60.10	0.30
9	28.72	0.47	29.28	0.75	31.61	0.45	56.42	0.34
10	37.77	1.74	38.58	1.75	40.49	1.44	51.75	1.06
11	38.75	0.48	41.65	0.61	40.58	0.44	49.86	0.32
12	40.28	0.57	44.65	0.58	41.62	0.50	48.04	0.42
13	37.86	2.44	39.11	2.42	40.44	2.36	51.44	1.75
14	39.25	0.54	42.50	0.61	40.75	0.46	49.07	0.44
15	41.69	0.49	46.43	0.66	42.43	0.40	45.80	0.33
16	37.78	2.09	38.97	1.79	40.24	1.96	51.42	1.52
17	39.29	0.50	42.67	0.59	40.74	0.42	48.82	0.29
18	42.02	0.58	46.76	0.67	42.58	0.38	45.22	0.41
19	38.64	0.89	40.36	1.11	40.48	0.86	50.05	0.66
20	38.92	0.57	42.66	0.81	39.75	0.52	48.36	0.46
21	40.48	0.56	44.99	0.77	40.69	0.45	46.39	0.45
22	38.49	1.71	40.32	1.92	40.10	1.63	49.85	1.32
23	39.33	0.65	43.29	0.89	39.88	0.58	47.52	0.51
24	41.94	0.53	47.48	0.70	41.49	0.39	44.05	0.39
25	38.71	2.73	40.27	2.92	40.35	2.63	49.68	1.95
26	39.54	0.63	43.63	0.71	39.91	0.56	47.18	0.49
27	41.83	0.55	47.39	0.72	41.27	0.37	43.93	0.58
28	39.31	0.49	42.39	0.69	40.84	0.42	49.05	0.39

Table 31: Statistical results of the DoE in EDEM of configuration AZ7_Plexi.

N	AoR_lin/[°]	dev_lin/[°]	AoR_mid/[°]	dev_mid/[°]	cen_x/[au]	dev_x/[au]	cen_y/[au]	dev_y/[au]
1	22.40	0.88	21.79	1.50	24.13	1.00	58.10	0.43
2	25.17	0.47	25.26	0.65	26.34	0.47	55.58	0.28
3	28.37	0.38	28.89	0.66	28.97	0.32	52.44	0.29
4	22.65	0.91	22.11	0.97	24.27	1.01	57.97	0.45
5	25.31	0.34	25.62	0.59	26.31	0.33	55.35	0.24
6	28.19	0.45	29.24	0.66	28.72	0.32	52.32	0.23
7	22.37	0.84	22.02	0.75	23.81	0.91	57.96	0.38
8	25.38	0.48	25.83	0.76	26.22	0.46	55.13	0.25
9	28.62	0.49	29.59	0.65	29.00	0.39	51.75	0.36
10	38.36	2.27	39.74	2.34	37.93	2.07	46.47	1.66
11	38.98	0.52	42.66	0.66	37.68	0.45	44.74	0.40
12	40.87	0.56	45.80	0.67	39.03	0.42	42.37	0.36
13	37.96	1.62	39.07	1.59	37.50	1.51	46.63	1.14
14	39.09	0.44	42.76	0.73	37.58	0.39	44.41	0.34
15	41.64	0.49	46.88	0.65	39.36	0.38	41.19	0.40
16	37.89	0.91	38.90	1.32	37.41	0.85	46.62	0.60
17	39.31	0.37	42.95	0.57	37.67	0.35	44.04	0.33
18	41.95	0.60	47.29	0.67	39.50	0.50	40.92	0.48
19	38.58	2.48	40.24	2.45	37.31	2.28	45.04	1.86
20	39.13	0.53	43.05	0.67	36.76	0.49	43.12	0.36
21	41.10	0.62	46.63	0.78	38.01	0.55	40.71	0.55
22	38.68	2.77	40.36	2.85	37.39	2.61	44.94	2.01
23	39.42	1.31	43.89	1.51	36.84	1.11	42.51	1.02
24	41.53	0.64	47.48	1.01	38.10	0.52	39.47	0.50
25	38.92	2.56	40.42	2.64	37.59	2.38	44.80	1.85
26	39.65	0.59	43.93	0.75	36.98	0.46	42.26	0.37
27	42.01	0.48	48.32	0.72	38.37	0.40	38.90	0.42
28	39.15	0.57	42.75	0.88	37.62	0.49	44.38	0.41

Table 32: Statistical results of the DoE in EDEM of configuration AZ6_Seel.

N	AoR_lin/[°]	dev_lin/[°]	AoR_mid/[°]	dev_mid/[°]	cen_x/[au]	dev_x/[au]	cen_y/[au]	dev_y/[au]
1	22.46	0.71	21.95	0.60	25.17	0.77	60.11	0.34
2	25.14	0.41	25.23	0.62	27.27	0.41	57.51	0.24
3	28.29	0.56	28.81	0.61	29.95	0.49	54.51	0.40
4	22.53	0.55	22.26	0.73	25.08	0.59	59.98	0.26
5	25.30	0.35	25.68	0.62	27.29	0.35	57.38	0.22
6	28.43	0.45	29.34	0.52	29.91	0.37	54.13	0.24
7	22.50	0.85	22.26	0.93	24.98	0.89	59.91	0.38
8	25.23	0.48	25.52	0.65	27.10	0.48	57.24	0.27
9	28.80	0.56	29.64	0.84	30.18	0.49	53.74	0.33
10	37.41	0.79	38.49	1.63	38.14	1.74	49.24	1.23
11	38.90	0.36	42.29	0.34	38.60	0.34	46.90	0.24
12	40.91	0.47	45.84	0.63	40.02	0.35	44.31	0.35
13	37.57	1.63	38.91	1.61	38.10	1.49	48.82	1.17
14	39.06	0.59	42.60	0.88	38.55	0.48	46.42	0.41
15	41.69	0.61	46.87	0.85	40.39	0.55	43.16	0.41
16	37.50	1.63	38.00	1.61	38.00	1.55	48.86	1.11
17	39.16	0.44	42.67	0.46	38.56	0.32	46.16	0.31
18	41.93	0.41	47.56	0.72	40.49	0.30	42.81	0.41
19	38.53	2.47	40.20	2.42	38.32	2.32	47.16	1.84
20	38.94	0.50	42.99	0.87	37.69	0.48	45.34	0.41
21	40.87	0.62	46.27	0.79	38.86	0.49	42.71	0.48
22	38.49	2.45	40.36	2.81	38.15	2.22	47.03	1.86
23	39.58	0.54	43.80	0.70	37.96	0.45	44.48	0.40
24	41.80	0.49	47.69	0.71	39.39	0.41	41.47	0.40
25	38.85	2.77	40.70	2.73	38.39	2.59	46.62	2.00
26	39.55	0.54	43.92	0.70	37.90	0.47	44.37	0.40
27	42.10	0.85	48.33	1.27	39.37	0.60	40.84	0.78
28	39.25	0.45	43.03	0.54	38.76	0.35	46.40	0.41

Table 33: Statistical results of the DoE in EDEM of configuration AZ7_Steel.

6 Conclusion

Over the past several years, it has become common to investigate particle behavior in diverse physical systems with DEM simulations. Experimental measurements is always needed at least for validation, but often it can provide less information about the physical properties compared to computer simulations: the deterministic theoretical model can provide access to data that is hard or impossible to determine experimentally.. Especially, in particulate processes including coating, mixing, milling, granulation, agglomeration, compression, and drying, where information about flow properties is needed, DEM simulations can be an indispensable tool.

With the increased use of DEM simulations, a new question quickly gained in importance: how does one choose the right input parameter for the simulations? Often, the represented system not investigated thoroughly enough to answer this, or the needed material or process properties are not accessible to experiment. For this reason, there is a trend towards calibration methods for DEM simulations using reference measurements.

In this work, a thorough data collection for calibration was done for an important unit system: particles in a rotating drum. The investigated particles were placed in a rotating drum, where the rotation speed and the surface roughness were changeable. The angle of repose and the center of mass were identified as characteristic properties of this arrangement and were measured. For this, an efficient, reliable and reproducible procedure was developed. Images of the rotating drum for a number of process parameter settings following a statistical design were taken. For the automatic evaluation, a Matlab algorithm was written, which can extract the angle of repose and the center of area from the images.

Then, a design of experiment with the to be examined factors was set up for the DEM simulations. The results of the simulation were investigated using the same algorithm as in the experiment.

In the current work, the investigated process parameters (the factors) have been the rotation speed, the static coefficient of friction between wall-particle and the static coefficient of friction between particle-particle. As particles Silibead glass spheres, biconvex Thrombo ASS 100mg and self pressed tablets under the surface roughness conditions of Plexiglas and steel have been investigated. One main result of the current work was the irrelevance of the choice of the static coefficient of friction. The reason is that no slipping between the particles and wall appear, because the tangential contact force cannot overcome the sliding friction.

This calibration concept of DEM simulations can be transferred to any other unknown parameter, such as rolling resistance, shear modulus, Poisson ration, coefficient of restitution or any other appearing model parameter. Other tablet forms, compositions, coatings under different surface

roughness could be core of another research. Fluids can be added or different particle could be mixed together.

7 Appendix

7.1 Analytical solutions of the LDS model

The Kelvin-Voigt model describes a viscoelastic material [277] by a parallel series of a purely viscous damper and a purely elastic spring. In the LSD-model two freely moving particles are mapped to a Kelvin-Voigt model. In order to get the analytical solution of this LSD model of two colliding balls one have to consider a one particle system, where effective coordinates are used. The following formulas are mainly taken from [116], [278]. The ball stiffness k_1,k_2 are combined to the spring stiffness k of the Kelvin-Voigt model:

$$\mathrm{k} = \frac{\mathrm{k}_1 \mathrm{k}_2}{\mathrm{k}_1 + \mathrm{k}_2} \tag{46}$$

The one particle system is described by the following differential equation:

$$\mathrm{m}_{\mathrm{eff}} \ddot{\delta} + \beta \dot{\delta} + \mathrm{k}\delta = 0, \tag{47}$$

where β is the damping coefficient, δ is the particle overlap and $\mathrm{m}_{\mathrm{eff}}$ is the effective mass of the particles. With the initial conditions

$$\begin{aligned} \delta(0) &= 0 \\ \dot{\delta}(0) &= v_0, \end{aligned} \tag{48}$$

the solution of equation (47) becomes:

$$\delta(t) = v_0 m_{eff} \left(\frac{\exp\left(-\beta + \sqrt{\beta^2 - 4km_{eff}} \right) \frac{\mathrm{t}}{2\mathrm{m}_{\mathrm{eff}}}}{\sqrt{\beta^2 - 4km_{ef}}} - \frac{\exp\left(-\beta - \sqrt{\beta^2 - 4km_{eff}} \right) \frac{\mathrm{t}}{2\mathrm{m}_{\mathrm{eff}}}}{\sqrt{\beta^2 - 4km_{ef}}} \right) \tag{49}$$

Equation (49)can be simplified as followed:

$$\delta(t) = \begin{cases} \frac{v_0}{\omega}\exp(-\tilde{\beta}t)\sin(\omega t), & if \quad damping: \tilde{\beta} < \omega_0 \\ \frac{v_0}{\Omega}\exp(-\tilde{\beta}t)\sinh(\Omega t), & if\ high\ damping\ \tilde{\beta} > \omega_0 \end{cases} \quad (50)$$

with $\tilde{\beta} = \frac{\beta}{2m_{eff}}$, $\omega = \sqrt{{\omega_0}^2 - \tilde{\beta}}$, $\Omega = \sqrt{\tilde{\beta}^2 - {\omega_0}^2}$, $\omega_0 = \sqrt{\frac{k}{m_{eff}}}$.

When the denominator in equation (50)becomes zero, the critical damping coefficient β_c is obtained and with the critical damping ratio is give as followed:

$$\alpha = \frac{\beta}{\beta_c} = \frac{\tilde{\beta}}{\omega_0}. \quad (51)$$

To give an expression for the coefficient of restitution,

$$\varepsilon = \frac{\dot{\delta}(t_c)}{\dot{\delta}(0)} \quad (52)$$

it is necessary to determine the impact duration t_c. In literature it is widely common to calculate the impact duration time out of $\delta(t_c) = 0$, which leads to the expression $t_c = \frac{\pi}{\omega}$. Schwager et al [116] had shown that this choice is wrong if one consider only repulsive interaction between granular particles, because at time t_c the interaction force becomes negative.

So the correct coefficient of restitution ε_d and the collision time t_c for granular particles with only repulsive interaction can be given analytically [116]:

$$t_c = \begin{cases} \frac{1}{\omega}\left(\pi - \tan^{-1}\left(\frac{2\tilde{\beta}}{\omega^2 - \tilde{\beta}^2}\right)\right), & \tilde{\beta} < \frac{\omega_0}{\sqrt{2}} \\ \frac{1}{\omega}\tan^{-1}\left(\frac{2\tilde{\beta}\omega}{\omega^2 - \tilde{\beta}^2}\right), & \tilde{\beta} > \frac{\omega_0}{\sqrt{2}} \end{cases} \quad (53)$$

$$\varepsilon_d = \begin{cases} \exp\left(-\frac{\tilde{\beta}}{\omega}\left(\pi - \tan^{-1}\left(\frac{2\tilde{\beta}\omega}{\omega^2 - \tilde{\beta}^2}\right)\right)\right), & \tilde{\beta} < \frac{\omega_0}{\sqrt{2}} \\ \exp\left(-\frac{\tilde{\beta}}{\omega}\tan^{-1}\left(\frac{2\tilde{\beta}\omega}{\omega^2 - \tilde{\beta}^2}\right)\right), & \tilde{\beta} \in \left[\frac{\omega_0}{\sqrt{2}}, \omega_0\right]. \\ \exp\left(-\frac{\tilde{\beta}}{\omega}\left(\ln\left(\frac{\tilde{\beta}+\Omega}{\tilde{\beta}-\Omega}\right)\right)\right), & \tilde{\beta} > \omega_0 \end{cases} \quad (54)$$

By calculation $F_{analyt} = m\ddot{\delta}(t)$ the impact force can also be given analytically,

$$F_{analyt} = \frac{m_{eff} v_0}{\omega}\left(\beta^2 e^{-\beta t}\sin(\omega t) - \omega^2 e^{-\beta t}\sin(\omega t) - 2\omega\beta e^{-\beta t}\cos(\omega t)\right) \quad (55)$$

and for high damping,

$$F_{analyt} = \frac{m_{eff} v_0}{\omega}\left(\beta^2 e^{-\beta t}\sinh(\Omega t) + \Omega^2 e^{-\beta t}\sinh(\Omega t) - 2\Omega\beta e^{-\beta t}\cosh(\Omega t)\right). \quad (56)$$

7.2 Rolling resistance between sphere and flat plate

The following formulas are mainly taken from [199].

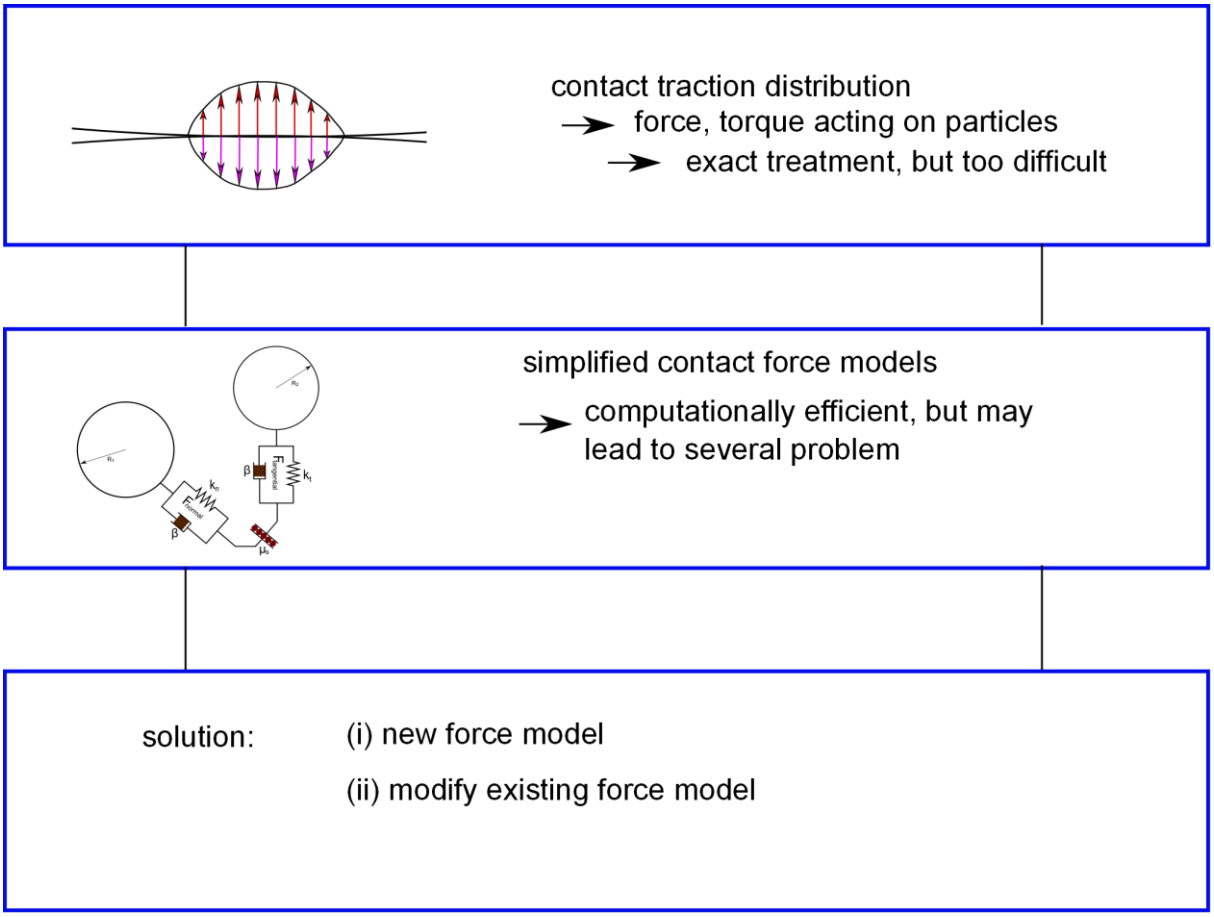

Figure 91: Illustration of what could be done if the simplified contact force model leads to problems.

Subsequently due convenience the particles are assumed to be viscoelastic moving on a hard plane demonstrated in Figure 91. The torque acting model without including rolling friction can be written as:

$$I\ddot{\Theta} = -rf(\delta) - rg(\delta)\dot{\delta}, \quad (57)$$

where Θ is the rotational coordinate, I is the moment of inertia for a sphere ($I = \frac{2}{5}mR^2$), r is the distance from the centre of the sphere to its contact area with the plane, δ is the tangential displacement of the sphere given by $\int(\dot{x} - r\dot{\theta})dt$, $f(\delta)$ and g(δ) are linear or nonlinear functions of δ and $\dot{\delta} = \dot{x} - r\dot{\theta}$.

To include rolling friction in equation (57) the following modification is done [197]:

$$I\ddot{\Theta} = -rf(\delta) - rg(\delta)\dot{\delta} - min\{k|\dot{\Theta}|, \mu_r mg\}\frac{\dot{\Theta}}{|\dot{\Theta}|}, \quad (58)$$

where the last term of the right hand side is called the rolling friction torque with μ_r as the rolling friction coefficient and k as the rotational stiffness. For the sake of completeness k can be written as $k = \mu' mg$, where $\mu' = (3\eta_2 - \eta_1)^2(1-\upsilon^2)/[3(3\eta_2+2\eta_1)Y\upsilon^2]$ [147]. Y is the Young's modulus and η_i is the dissipative constant for particle i. In another rolling friction model the rolling friction torque is independent of $\dot{\Theta}$:

$$I\ddot{\Theta} = -rf(\delta) - rg(\delta)\dot{\delta} - \mu_r mg. \quad (59)$$

In general it is very complicated to describe the contact between a sphere and a plane. The above described methods are only simplified models, which may have several theoretical problems as can be seen below. For this purpose three facts about a sphere moving on a plane were investigated by Zhu et al [199]: (1) if the sphere has no initial velocity, angular velocity and tangential displacement it will not move; (2) if the sphere has small initial velocity, angular velocity and tangential displacement, it will come to rest due to energy dissipation; (3) if the translational velocity at contact point with the plane is zero the sphere roll without slipping. Zhu et al [199] found out that there is no equilibrium state according to the model where equation (55) is used. Zhou et al pointed out that according to the models without rolling friction there exist initial translation and angular velocities and tangential displacements such that the sphere will never stop, which is not realistic. Additionally according to the models without rolling friction Zhu et al demonstrated that pure rolling just occur if both the tangential force and torque acting on the sphere are zero, which is not true because for viscoelastic spheres moving on a plane there is a non-zero rolling friction torque imposed in its pure rolling motion [147], [279].

Due to this problems Zhu et al [199] proposed a simple modification to the model described by the following equation:

$$I\ddot{\Theta} = -rf(\delta) - rg(\delta)\dot{\delta} + \frac{I}{I+mr^2}\, min\{k|\dot{\Theta}|, \mu_r mg\}\frac{\dot{\Theta}}{|\dot{\Theta}|}, \qquad (60)$$

The modified version in equation (60) obey the critical facts about the equilibrium, stability and pure rolling.

This discussion should show that by simplification of reality by using theoretical models, unphysical results can appear. There are two ways to overcome this problem; either inventing a new model or modifying the existing one. In Figure 91 this difficulty of development is illustrated.

It need to be added that in this section only a sphere moving on a hard plane was discussed und that the modification is just useful to overcome the problems with equilibrium, stability and pure rolling. For more complex systems and higher physical requirements it is not that easy to modify an existing model or even invent a new one.

7.3 Modified discrete element method

A shear band is strain localization where a narrow zone of intense shearing strain appears in dense granular soils [144]. The conventional DEM based by Cundall and Strack [94]are not able to predict this phenomena of shear bands. So Iwashita and Oda modified the DEM by including rolling friction into the model.

During a time step from t to (t+dt) two particle (radii r_1 r_2) in a two dimensional assembly make an angle $d\beta$ measured between the unit vector n which normal to the contact surface C at time t and the unit vector n' which is normal to the contact surface C'at time (t+dt), as can be seen in Figure 92.

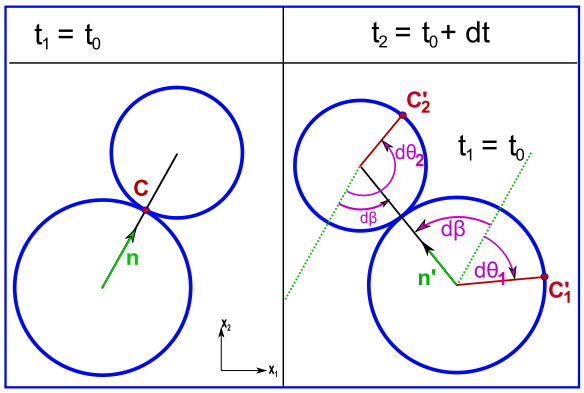

Figure 92: Kinematics at a contact, showing rolling and sliding at time t_1 and t_2.

The particles get in contact at C and after the deformation the material point at C appears at C_1' on particle 1 and at C_2' on particle 2. After the incremental rotaions of particle 1 and 2 the arc length from the contact point at time (t+dt) to the shifted material point C_1' and C_2' are given by

$$\begin{aligned} da &= r_1(d\theta_1 - d\beta) \\ db &= r_2(d\theta_2 - d\beta), \end{aligned} \tag{61}$$

According to da and db two extrema can occur at the contact during the deformation:

- $da = -db \Leftrightarrow$ pure rolling at the contact
- $da = db \quad \Leftrightarrow$ pure sliding at the contact

Usually the contacts are between those two extreme cases, thus the arc lengths can be split into a rolling $dU_r$and a sliding component dU_s:

$$\begin{aligned} da &= dU_r + dU_s \\ da &= -dU_r + dU_s \end{aligned} \tag{62}$$

7.4 Expected utility and Shannon entropy

The Shannon entropy is an information-theoretical expression which quantifies the expected value of the information of a specification of a random variable [280]. The general expression for the Shannon entropy within the information theory is:

$$S\{p_i\} = -\sum_{i=1}^{m} p_i ln(p_i) \tag{63}$$

Worth noting is that if one add the Boltzmann constant k_b multiplicative to the expression in equation (63) one get the Gibbs entropy within the theory of statistical thermodynamics.

With the concept of the Shannon entropy the expected utility of an experimental design (discussed in chapter 3.9.3) can be defined via the Shannon entropy of the prior and posterior PDF:

$$U(y,\xi) = \int ln\big(p(\theta|y,\xi,\mathbb{B})\big)p(\theta|y,\xi,\mathbb{B})d\theta - \int ln\big(p(\theta|\mathbb{B})\big)p(\theta|\mathbb{B})d\theta \tag{64}$$

Many researchers have dealt with the numerical computation of the expression in formula (64) and therefore reference is made to [281], [282].

7.5 Matlab codes

7.5.1 Circular drawing: 'circle_mos.m'

```
function [c_mask] = circle_mos(ix,iy,cx,cy,r)

% ix.....Pixel in x-direction
% iy.....Pixel in y-direction
% cx.....center of circle; x-position in pixel
% cy.....center of circle; y-position in pixel
% r......radius


[x,y] = meshgrid(-(cx-1):(ix-cx),-(cy-1):(iy-cy));
c_mask = x.^2 + y.^2 <= r.^2;

end
```

7.5.2 Detection algorithm for the experiment: 'AoR_mos_cen.m'

```
function
[data,AoR_lin,AoR_middle,rel_column,rel_row,c_mask_1,x_cm,y_cm,r,r_diff] =
AoR_mos_cen(img_name,radius_range,handmade,background);



% [data,AoR_lin,AoR_middle] = AoR_mos(img_name,radius_range)

% [data,AoR_lin,AoR_middle] = AoR_mos(img_name,radius_range) is an
% algorithm, which is adapted to problems of particle behaviour in a
% rotating drum, where the angle of repose has to be measured. This angle
% is related to the coefficient of friction. AoR_mos gives out the data
% points of the 'wavy' curve of the angle of repose. Addidionally it makes
% two different linear fits and calculates the slopes or the angles of
% those lines. Additionally a center of area of the particle ensemble is
% calculated by the algorithm

% INPUT:
% img_name..........is the image-file name; f.e. usage: img_name =
'test.jpg';
%                   possible formats: .jpeg, .jpg .bpm .cur .gif .ico .pbm
%                   .pgm .pcx .png .ppm .ras .tiff .xwd
%                   The image has to fullfil certain conditions: it should
%                   have a good contrast and low noise. Addidionally the
%                   high refelxion of the drum should be reduced as much as
%                   possible. The particles in the drum should be
%                   qualitivly high confined from the surrounding. Also
%                   the radius of the drum should be highly cognizable in
%                   order to detect furthermore this radius of the drum
% radius_range......[r_min r_max] It is an approximated radius range in
%                   units of pixels of the circles one want to detect. To
%                   make such a guess it is suggested to create a
%                   tool in the image which can measure the radius
%                   manually. Therefore the following code can be used:
%                               imshow(gim);h = imdistline(gca);
%                               api = iptgetapi(h);
%                               fcn = makeConstrainToRectFcn('imline',...
%                               get(gca,'XLim'),get(gca,'YLim'));
%                               api.setDragConstraintFcn(fcn);
```

```
%                   If the radius range is very large the computaional time
%                   is very high. So one try to make this radius range as
%                   small as possible. But attention: if it is too small,
%                   no circles will be found and the whole algorithm breaks
%                   down.
%                   possible formats: single | double | int8 | int16 |
int32 | int64 | uint8 | uint16 | uint32 | uint64
% handmade..........to use the handmade algorithm case use a logical 1, if
%                   not not use a logical 0. In some cases it is necessary
to work with the
%                   grayscale value of the particle essemble, because a
%                   simple rgb2bw-filter
%                   is not enough. by using this user-default value some
masks are defined
%                   which create a binary image where the pixels are 0 or 1
%                   depending if
%                   those pixels are above or below the handmade-value.
% background........to use the handmade algorithm case use a logical 1, if
%                   not not use a logical 0. In some special cases wher
%                   for instants the attriction of the tablets is really
%                   high, the drum itself get in the worst case scenaria
%                   the same grayscale valeus as the particle essemble. In
%                   only way to solve this problem is to reduce the area
%                   which have to be investigated. With a polygon line one
%                   can cut out a user defined area. This area is then
%                   changed in his contrast and brightness by the user via
%                   a histogramm.




% OUTPUT
% data..............It gives out the data point of the wavy curve of the
%                   angel of repose. It is a discrete function and teh x
%                   and y values are in
%                   units of pixels. The data point are smoothed and
%                   interpolated
% AoR_lin...........Is  the angle of repose calculated from a linear fit of
%                   the whole data points based on a least square method
% AoR_middle........Is the angle of repose calculated from a linear fit of
%                   the middle range of the data points based on a least
%                   square method.
% rel_column........after detecting the center of area a cross line
%                   according to this point is drawn. By taking the length
%                   to the upper and lower
%                   black/white transition and norm it to 1 you can define
a relative value
%                   counted from up to down (column) to define the place of
%                   the center of
%                   area in one diemnsion
% rel_row...........after detecting the center of area a cross line
%                   according to this point is drawn. By taking the length
%                   to the left and right black/white transition and norm
%                   it to 1 you can define a relative value
%                   counted from left to right (row) to define the place of
%                   the center of
%                   area in one dimension
% c_mask_1..........is the radius of the detected drum by
%                   usingimfindcircle, see below
% x_cm..............to compare images with different formats it is
%                   necessary to make some kind of normalization of the
%                   drum radius to make
```

```
%                   it possible to lokate the center of area. For this
%                   reason a coordnate system has to be defined. The zero
%                   point of this coordinate system ist he center of the
%                   drum.
%                   According to this a x-coordinate of the the center of
%                   area can be given.
%                   To compare it with other images with other fomats the
%                   length of x has to
%                   be devided by the drum radius in order to to have
%                   relative coordiantes.
% y_cm..............to compare images with different formats it is
%                   necessary to make some kind of normalization of the %
                    drum radius to make
%                   it possible to lokate the center of area. For this
%                   reason a coordnate system has to be defined. The zero
%                   point of this coordinate system ist he center of the
%                   drum.
%                   According to this a y-coordinate of the the center of
%                   area can be given.
%                   To compare it with other images with other fomats the
%                   length of y has to
%                   be devided by the drum radius in order to to have
%                   relative coordiantes.
% r.................Is the radius of the detected drum. it can be usful in
%                   statistical analysis, because in some cases the radii
%                   of different images
%                   can vary a lot. So r can be a good control-variable to
%                   reduce a
%                   systematical error. The standard deviation of x_cm and
%                   y_cm is highly dependent of teh standard deviation of r
%                   in an statistiacl analysis.



% possible format of img_name: all TIFF-formats
img = imread((img_name));

Red = img(:,:,1);
%mask_red = Red >= 220;
[m,n,t]=size(img);
bw=zeros(m,n);
for i=1:m
    for j=1:n
        if(img(i,j,1)>100&&img(i,j,2)<100&&img(i,j,3)<100)
            bw(i,j)=1;
        end
    end
end
mask_red = medfilt2(bw,[10,10]);

% One idea to come to the angle of repose out of the current image is to
% find the radius of the drum and isolate it from the surrounding in such a
% way that unwished gradients of contrast pixel dissappear to make sure
% that just the region where the glass spheres are, are in the region of
% detection.
% For this Matlab2012 and alter offers an image precession tool called
% 'imfindcircels'
% versions beneath 2012 do not have this function!!!


% [centers,radii] = imfindcircles(F,[Radius_range],'Sensitivity',0.99);
```

```
% F.............. input image; possible data types: single | double |
int16 | uint8 | uint16 | logical
% Radius_range.... approximate radius range as described above
% EdgeThreshold... can be very useful. For low values it detects more
%                  circular object; by incresing the value it detects fewer
%                  circles with weak edges.
% Sensitivity..... Sensitivity factor is the sensitivity for the circular
Hough transform accumulator array,
%                  specified as the comma-separated pair consisting of
'Sensitivity' and a nonnegative scalar
%                  value in the range [0,1]. As you increase the
sensitivity factor, imfindcircles detects
%                  more circular objects, including weak and partially
obscured circles. Higher sensitivity
%                  values also increase the risk of false detection.
%[centers,radii] =
imfindcircles(F,radius_range,'Sensitivity',0.99,'EdgeThreshold',0.2);

% to show the found circle;
% hcircle = viscircles(centers,radii,'EdgeColor','b');

% to implement the circle in the image and furthemore to create the mask,
which switch off the
% sourrounding not needed. Therefor a function: circle_mos was written:

% function [c_mask] = circle_mos(ix,iy,cx,cy,r)
%
% % ix.....Pixel in x-direction
% % iy.....Pixel in y-direction
% % cx.....center of circle; x-position in pixel
% % cy.....center of circle; y-position in pixel
% % r......radius
%
%
% [x,y] = meshgrid(-(cx-1):(ix-cx),-(cy-1):(iy-cy));
% c_mask = x.^2 + y.^2 <= r.^2;
%
% end

% in the command window one can see, if any circles have been found
if length(radii) == 0
    disp(['no circle found in pic',img_name]);

elseif radii > 1
    disp('more than one circle has been found');
end

[centers,radii] =
imfindcircles(mask_red,radius_range,'Sensitivity',0.99,'EdgeThreshold',0.2)
;


size_image = size(Red);
ix = size_image(2);
iy = size_image(1);



% in general the imfindcircle finds more than one circle. the smallest
```

```
% circle is choosen because according to the made pictures during this code
was developed, the nearest circle to
% the particle essemble was the smallest circle. If your images have
another
% behaviour one have to adjust the correct radius to the made pictures
r = radii(1);
centers = centers(1,:);
cx = centers(1);
cy = centers(2);
r2 = r/7;
[c_mask_1] = circle_mos(ix,iy,cx,cy,r);  % drum radius
[c_mask_2] = circle_mos(ix,iy,cx,cy,r2);

c_mask = c_mask_1 & mask_red;

c_mask_ = ~c_mask_1 | c_mask_2 | c_mask;
c_mask_ = medfilt2(c_mask_,[20 20]);

gim = rgb2gray(img);
FF = gim;
FF(c_mask_) = nan;

% It is important for further treatment to convert the realcolor_image into
% a grayscale image. NO inforamtion will get lost!!
% size(gim) = [ number of pixels along the column        number of pixels
along the row ]
% class(gim) = uint8


% Now it is essential to make the image more handable, which means that it
% is advantageous to make the pixels in the (neighbor)hood more similiar to
each
% other, to get more markant gradient point in further calculations.
% the wiener2-filter could be a good choice:
% J = wiener2(I,[m n],noise)
% [J,noise] = wiener2(I,[m n])
% wiener2 lowpass-filters a grayscale image that has been degraded by
constant power additive noise.
% wiener2 uses pixelwise adaptive Wiener method based on statistics
estimated froma local neighborhood of each pixel.
% input [m n]--> neighborhood of size m*n
% input noise--> handles the Gaussion-noise, espacially add or delete it
J = wiener2(gim,[50 50]);


% an other way to avoid annoying noise, 'cause of the hight amount of
pixels is
% to use a medianfilter over an eight-neighbourhood. It espacially reduce
% salt and pepper noise.
% B = medfilt2(A, [m n])
% B = medfilt2(A)
% B = medfilt2(A, 'indexed', ...)
% B = medfilt2(..., padopt)
% state of the art from my point of view: its more useful to work with
% medfilt2, at least for this application
% [m n ]... m-by-n neighborhood around the corresponding pixel
B = medfilt2(FF, [40 40]);

% Contrast correction can also play an important role. Therefore the
% histogrammeualized and gamma-corrected function imadjust ist used:
% J = imadjust(I)
```

```
% J = imadjust(I,[low_in; high_in],[low_out; high_out])
% J = imadjust(I,[low_in; high_in],[low_out; high_out],gamma)
% newmap = imadjust(map,[low_in; high_in],[low_out;high_out],gamma)
% RGB2 = imadjust(RGB1,...)
F = imadjust(B);

% application of the defined mask
% FF is a gray scale image with more or less sharp transitions. the
% surrounding outside the drum is black and the nut circle as well.




% if one can not adjust the parameter like sensitivity, treshholds and
% filters in order to create those images with which one can work with; one
way to make this is to define
% a value (graycolor value), where everything under it is zero and beneath
% it is 1--> so one create a handmade binary image

if handmade == 1
        mask_1 = F > 170;
        hhh = mask_1;
        hhh = medfilt2(hhh,[10 10]);
        hhh = hhh & ~c_mask_;

else
        hhh = im2bw(F) & ~c_mask_;
end



if background == 1

  cmp = 0;
    while ~cmp
        shift_r = 14;
        [c_mask_101] = circle_mos(ix,iy,cx,cy,r-shift_r);
        mask_1 = FF > 100;
        figure
        [x_BG,y_BG,BG,xi_BG,yi_BG] = roipoly(img);
        close(gcf);
        mask_BG = mask_1 & BG;
        new_img = gim;
        new_img(~mask_BG) = 0;
        new_img_ = new_img;
        new_img_(~mask_BG) = [];

    etl123 = figure;hh = imshow(new_img);
    handle_con = imcontrast(hh);

    uiwait(handle_con);

    ImageHandle = getimage;
    uiwait(etl123);
    %set(etl123, 'Visible', 'off');
    %close(etl123);
    med_img = medfilt2(ImageHandle,[10 10]);
    coa_bin = im2bw(med_img,0.2);
    %t = get(handle_con)
    %!!!!!! need of sigan processing toolbox
```

```
    %[p_value,p_min] = peakdet(count_img,0.5);
    s_mask = find(coa_bin);
    [II,JJ] = ind2sub(size(coa_bin),s_mask);
    coa_bin_2 = coa_bin;
    coa_bin_3 = coa_bin;
    for q = min(JJ):max(JJ);
        II2 = JJ == q;
        II_ind = find(II2);
        II_calc  = min(II(II_ind));
        coa_bin_2(II_calc:end,q) =(1);
        coa_bin_3(q:end,II_calc) = 1;


    end



    coa_bin_2(II_calc-20:end,q:q+100) = 1;
    hhh = coa_bin_2 & c_mask_101;
    alpagun = figure('units','normalized','outerposition',[0 0 1 1]);
    subplot(1,2,1);
    imshow(hhh);
    subplot(1,2,2);
    imshow(gim);
    %uiwait(alpagun);

    prompt = {'Is the image OK? (y/n)'};
    dlg_title = 'Judgement';
    num_lines = 1;
    def = {'y'};
    answer = inputdlg(prompt,dlg_title,num_lines,def);
    %answer = input('Sono d`accordo (y/n)?! ','s');
    cmp = strcmp(answer,'y');
    if cmp
        disp('Image OK!')
    else
        disp('Repeat the algorithm!')
    end
    close(alpagun);
    end

end


% screen every column to get to know where the transition between 1 and 0
appears
data_y = []; % pre-initialization
kk_x = [];
for k = 1:10:size(hhh,2)
% to take every 20th point is far enough
Spalt = hhh(:,k);
Spalt_diff = diff(Spalt);     % gradient determination
[uno_ind,uno]= find(Spalt_diff);   % finds the 1/0 transitions defined by
Spalt_diff

% if there are four 1/0 transition, than take the thrid entry ( counted
% from the top to the bottom) and that should be the wanted data point of

    if numel(uno) == 2
    data = uno_ind(1);
```

```
    kk = k;
     elseif numel(uno) == 4 %&& sum(Spalt) ~= sum(Spalt_vgl)
    data = uno_ind(3);
    kk = k;
    elseif numel(uno) == 6
    data = uno_ind(5);
    kk = k;
    else
        data = [];
        kk = [];
    end


%Spalt_vgl = Spalt;
data_y = [data_y,data];
kk_x = [kk_x,kk];

end

kk = regionprops(hhh, 'Centroid');
sss = cell2mat(struct2cell(kk));


siz = size(hhh);
row = hhh(ceil(sss(2)),:);
ind_row = find(row);
column = hhh(:,ceil(sss(1)));
ind_column = find(column);
row_abs = abs(ind_row(1)-ind_row(end));
column_abs = abs(ind_column(1)-ind_column(end));

rel_column = abs(ind_column(1)-sss(2))/column_abs;
rel_row = abs(ind_row(2)-sss(1))/row_abs;


% introduction of coordinate system for the circle detection, in order to
% make a connection to the center of mass

x_cm_ = abs(sss(1) - centers(1));
y_cm_ = abs(sss(2) - centers(2));
% Normalize to radius
uu = hhh(:,ceil(centers(1)));
f_uu = find(uu);
indf = max(f_uu);
ww = c_mask_1(:,ceil(centers(1)));
f_ww = find(ww);
indf_w = max(f_ww);
r_diff = abs(indf_w - indf);

x_cm = (x_cm_*100)/(r-r_diff);
y_cm = (y_cm_*100)/(r-r_diff);



% the integers from the image in y-dircetion begin from the top and go down
data_y_cor = size(hhh,1)-data_y;

% Here one cut out those values which come from the lefthandside of the
% drum, where there are no data belonging to the shape of the angle of
repose
```

```
% The idea is that where the curve is monoton falling in a whide range than
% the data point belong to the drum and not to the data points
% --> so if th change from one data point to the next is negative, lets say
% a negative default value of -5, than those data point are not needed
delta_monoton = -5;
mask_monoton = diff(data_y_cor) > delta_monoton;
data_y_out = data_y_cor(mask_monoton);
kk_x_out = kk_x(mask_monoton);

% Start to create the output figure and draw the fitting curves
%figure;
figure('units','normalized','outerposition',[0 0 1 1]);
% position of the first plot
handaxes1 = axes('position',[0.1 0.1 0.8 0.8]);
% smoothing the curve of the data points
%data_y_smooth = smooth(data_y_out);
data_y_smooth = data_y_out;
xq = kk_x_out(1):5:kk_x_out(end);
vq2 = interp1(kk_x_out,data_y_smooth,xq,'spline');

%plot(kk_x_out,data_y_smooth,'b','LineWidth',5,'LineWidth',2);
plot(xq,vq2,'b','LineWidth',5,'LineWidth',2);
hold on


% Linear fit !!!
% data that have to be fitted linearly: kk_x_out,data_y_smooth
% in order to calculate an angle, one have to fit a line with a slope,
% where this slope defines the angel of repose
% For this reason a linear polyfit is applied on teh data points

P = polyfit(xq,vq2,1); % the 1 in the input of polyfit defines the linear
fit
yfit = P(1)*kk_x_out + P(2);
plot(kk_x_out,yfit,'k','LineWidth',1.5);

% P_interp1 = interp1(data_y_smooth,kk_x_out,'nearest'); % could be a
better smooth

% Linear fit, but with special concern of the middle region of the data of
% the angle of repose
kk_middle = xq(ceil(length(xq)/4):ceil(3*length(xq)/4));
data_y_middle = vq2(ceil(length(xq)/4):ceil(3*length(xq)/4));
p_middle = polyfit(kk_middle,data_y_middle,1);
yfit_middle = p_middle(1)*kk_x_out + p_middle(2);
plot(kk_x_out,yfit_middle,'r','LineWidth',1.5);

hold off
xlabel('x in pixel');
ylabel('y data in pixel');
legend('raw data','linear polyfit','fit middle');
%axis([0,1936,0,1296]);



% second plot in the main plot to show the binary image of the drum and the
% angel of repose
% axes property: 'position'--> [left bottom width height]
handaxes2 = axes('position',[0.1 0.6 0.2 0.2]);
imshow(img)
```

```
% binary image
handaxes3 = axes('position',[0.1 0.38 0.2 0.2]);
% imshow(hhh);hold on
% plot([centers(1),centers(1)],[centers(2),centers(2)+r-r_diff]);
s_mask = find(hhh);
[II,JJ] = ind2sub(size(hhh),s_mask);
imshow(img);hold on;plot(JJ,II,'bo','MarkerSize',1);hold off


handaxes3 = axes('position',[0.3 0.55 0.25 0.25]);
imshow(hhh);
hold on
plot(sss(1),sss(2),'ro','MarkerFaceColor','r');
plot(1:siz(2),ones(1,siz(2)).*sss(2),'r');
plot(ones(1,siz(1)).*sss(1),1:siz(1),'r');
plot(sss(1),ind_column(1),'ro',sss(1),ind_column(end),'ro');
plot(ind_row(1),sss(2),'ro',ind_row(end),sss(2),'ro');
plot(c_mask_1)
text(100,150,['mc = ','[ ',num2str(round(rel_row*100)/100),' ,
',num2str(round(rel_column*100)/100),' ]'],'FontSize',30,'EdgeColor',[0 1
0],'BackgroundColor',[.7 .9 .7]);

hold off

% centroid image two
handaxes4 = axes('position',[0.6 0.15 0.31 0.31]);
imshow(c_mask_1);hold on;

plot(centers(1)-r:centers(1)+r,centers(2),'r-');
plot(centers(1),centers(2)-r:centers(2)+r,'r-');
plot(linspace(centers(1),centers(1)+x_cm_,1000),centers(2)*ones(1,1000),'b-
','LineWidth',5);
plot((centers(1)+x_cm_)*ones(1,1000),linspace(centers(2),centers(2)+y_cm_,1
000),'b-','LineWidth',5);
plot(sss(1),sss(2),'ro','MarkerSize',10,'MarkerFaceColor','r');
plot(centers(1),centers(2),'ro','MarkerSize',10,'MarkerFaceColor','r');
plot(sss(1),centers(2),'ro','MarkerSize',10,'MarkerFaceColor','r');
%title(['cen = [',num2str(x_cm),',',num2str(y_cm),']']);
text(100,150,['cen = [',num2str(round(x_cm*100)/100),' ,
',num2str(round(y_cm*100)/100),']'],'FontSize',30,'EdgeColor',[0 1
0],'BackgroundColor',[.7 .9 .7]);
hold off



% calculation of the angle of repose
AoR_lin = (atan(P(1))*180)/pi
AoR_middle = (atan(p_middle(1))*180)/pi

% calculate the least square root variance
error_linfit =   sum((data_y_smooth-yfit).^2)                    % quadratic
error
error_middle =   sum((data_y_smooth-yfit_middle).^2)

title(handaxes1,['AoR lin = ',num2str(AoR_lin),'      AoR middle =
',num2str(AoR_middle)],'FontSize',30);


end
```

7.5.3 Detection algorithm for EDEM: 'AoR_mos_centroid_EDEM.m'

```
function
[data_EDEM,AoR_lin_EDEM,AoR_middle_EDEM,rel_column_EDEM,rel_row_EDEM,c_mask
_1,x_cm_EDEM,y_cm_EDEM] = AoR_mos_centroid_EDEM(img_name)

% reference circle
Alp = imread('reference_circle.jpg');
Alp_F_ = rgb2gray(Alp);
Alp_F = Alp_F_(50:end-50,100:end-100);
Alp_B = imadjust(Alp_F);

% find circle properties
radius_range = [150,250];
[centers,radii] =
imfindcircles(Alp_B,radius_range,'ObjectPolarity','dark','Sensitivity',0.99
);
center_ref = centers;
radius_ref = radii;
size_image = size(Alp_B);
ix = size_image(2);
iy = size_image(1);
centers = centers(1,:);
cx = centers(1);
cy = centers(2);
r = radii(1);
[c_mask_1] = circle_mos(ix,iy,cx,cy,r);


% image manipualtion
img = imread(img_name);
gim = rgb2gray(img);
F = gim(50:end-50,100:end-100);
F = medfilt2(F, [10 10]);
img_bin = im2bw(F);




% data evalution out of img_bin: AoR, Aor_middle, cen_x,cen_y
data_y = [];
kk_x = [];
for k = 100:1:712
    Spalt = img_bin(:,k);
    Spalt_diff = diff(Spalt);     % gradient determination
[uno_ind,uno]= find(Spalt_diff);
if numel(uno_ind) == 0
    data = [];
    kk = [];
else
    data = uno_ind(1);
    kk = k;
end


data_y = [data_y,data];
kk_x = [kk_x,kk];
end
```

```
data_y_cor = size(img,2)-data_y;
data_EDEM = data_y_cor;


hfig = figure;
scrsz = get(0,'ScreenSize');
set(hfig,'Position',[scrsz(1) scrsz(2) scrsz(3) scrsz(4)])
handaxes1 = axes('position',[0.1 0.1 0.8 0.8]);
plot(kk_x,(data_y_cor),'LineWidth',2);

hold on

% AoR_lin
P = polyfit(kk_x,data_y_cor,1); % the 1 in the input of polyfit defines the
linear fit
yfit = P(1)*kk_x + P(2);
plot(kk_x,yfit,'k','LineWidth',1.5);

AoR_lin_EDEM = (atan(P(1))*180)/pi;

% AoR_middle
data_y_middle = [];
kk_x_middle = [];
for m = ceil(kk_x(1)+(abs(kk_x(1)-kk_x(end)))/5):5:ceil(kk_x(end)-
(abs(kk_x(1)-kk_x(end)))/5)

    Spalt = img_bin(:,m);
    Spalt_diff = diff(Spalt);     % gradient determination
[uno_ind,uno]= find(Spalt_diff);
if numel(uno_ind) == 0
    data = [];
    kk = [];
else
    data = uno_ind(1);
    kk = m;
end


data_y_middle = [data_y_middle,data];
kk_x_middle = [kk_x_middle,kk];

end
data_y_cor_middle = size(img,2)-data_y_middle;



P = polyfit(kk_x_middle,data_y_cor_middle,1); % the 1 in the input of
polyfit defines the linear fit
yfit_middle = P(1)*kk_x + P(2);
plot(kk_x,yfit_middle,'r','LineWidth',1.5);


AoR_middle_EDEM = (atan(P(1))*180)/pi;
legend('raw data','lin fit','middle fit','Location','North');
hold off

%F_ = F(50:end-50,100:end-100);
F = bitcmp(F);
F = medfilt2(F,[10 10]);
```

```
kk_EDEM = regionprops(logical(im2bw(F)),'Centroid');
sss_EDEM = cell2mat(struct2cell(kk_EDEM));

siz_EDEM = size(F);

F_logical = logical(F);
row_EDEM = F_logical(ceil(sss_EDEM(2)),:);
ind_row_EDEM = find(row_EDEM);
column_EDEM = F_logical(:,ceil(sss_EDEM(1)));
ind_column_EDEM = find(column_EDEM);

row_abs_EDEM = abs(ind_row_EDEM(1)-ind_row_EDEM(end));
column_abs_EDEM = abs(ind_column_EDEM(1)-ind_column_EDEM(end));

rel_column_EDEM = abs(ind_column_EDEM(1)-sss_EDEM(2))/column_abs_EDEM;
rel_row_EDEM = abs(ind_row_EDEM(2)-sss_EDEM(1))/row_abs_EDEM;
rel_EDEM = [rel_row_EDEM,rel_column_EDEM];

x_cm_EDEM_ = abs(sss_EDEM(1) - center_ref(1));
y_cm_EDEM_ = abs(sss_EDEM(2) - center_ref(2)); %- abs(size(img,1) -
size(Alp,1));
% Normalize to radius
x_cm_EDEM = (x_cm_EDEM_*100)/r;
y_cm_EDEM = (y_cm_EDEM_*100)/r;



handaxes2 = axes('position',[0.05 0.58 0.25 0.25]);
imshow(gim(170:end-170,450:end-450));

handaxes4 = axes('position',[0.25 0.55 0.25 0.25]);
imshow(F);
hold on
plot(sss_EDEM(1),sss_EDEM(2),'ro');
plot(1:siz_EDEM(2),ones(1,siz_EDEM(2)).*sss_EDEM(2),'r');
plot(ones(1,siz_EDEM(1)).*sss_EDEM(1),1:siz_EDEM(1),'r');
plot(sss_EDEM(1),ind_column_EDEM(1),'ro',sss_EDEM(1),ind_column_EDEM(end),'
ro');
plot(ind_row_EDEM(1),sss_EDEM(2),'ro',ind_row_EDEM(end),sss_EDEM(2),'ro');
text(100,150,['mc = ','[ ',num2str(round(rel_row_EDEM*100)/100),' ,
',num2str(round(rel_column_EDEM*100)/100),'
]'],'FontSize',30,'EdgeColor',[0 1 0],'BackgroundColor',[.7 .9 .7]);
plot(centers(1),centers(2),'ro');
hold off

title(handaxes1,['AoR lin = ',num2str(AoR_lin_EDEM),'      AoR middle =
',num2str(AoR_middle_EDEM)],'FontSize',30);

handaxes5 = axes('position',[0.6 0.2 0.3 0.3]);

imshow(c_mask_1);
hold on

plot(center_ref(1)-r:center_ref(1)+r,center_ref(2),'r-');
plot(center_ref(1),center_ref(2)-r:center_ref(2)+r,'r-');
plot(linspace(center_ref(1),center_ref(1)+x_cm_EDEM_,1000),center_ref(2)*on
es(1,1000),'b-','LineWidth',5);
plot((center_ref(1)+x_cm_EDEM_)*ones(1,1000),linspace(center_ref(2),center_
ref(2)+y_cm_EDEM_,1000),'b-','LineWidth',5);
```

```
plot(center_ref(1),center_ref(2),'ro','MarkerSize',10,'MarkerFaceColor','r'
);
plot(sss_EDEM(1),sss_EDEM(2),'ro','MarkerSize',10,'MarkerFaceColor','r');
plot(sss_EDEM(1),center_ref(2),'ro','MarkerSize',10,'MarkerFaceColor','r');
text(200,80,['cen = [',num2str(round(x_cm_EDEM*100)/100),' ,
',num2str(round(y_cm_EDEM*100)/100),']'],'FontSize',30,'EdgeColor',[0 1
0],'BackgroundColor',[.7 .9 .7]);

hold off

%set(gcf,'Visible','off');

end
```

7.5.4 Evalution script: experiment

```
close all
clear all

background = 0;
handmade = 1;
numel_pic =30;
AoR_lin_array = [];
AoR_middle_array = [];
rel_row_cen = [];
rel_column_cen = [];
x_cm_array = [];
y_cm_array = [];
r_array = [];
rdiff_array = [];


for g = 1:numel_pic

% for control over the algorithm (if it works coorecct, this means if the
% binary image looks correct)--> TODO: try to make the figures within
% AoR_mos.m to subplots in a global figure


img_name = ['DSC_ (',num2str(g),')','.JPG'];
radius_range = [400 550];

[data,AoR_lin,AoR_middle,rel_column,rel_row,c_mask_1,x_cm,y_cm,r,r_diff] =
AoR_mos_cen(img_name,radius_range,handmade,background);
AoR_lin_array = [AoR_lin_array,AoR_lin];
AoR_middle_array = [AoR_middle_array,AoR_middle];
rel_row_cen = [rel_row_cen,rel_row];
rel_column_cen = [rel_column_cen,rel_column];
x_cm_array = [x_cm_array,x_cm];
y_cm_array = [y_cm_array,y_cm];
r_array = [r_array,r];
rdiff_array =[rdiff_array,r_diff];

pause(0.5)
close all
end
AoR_lin_mean = mean(AoR_lin_array)
AoR_middle_mean = mean(AoR_middle_array)
std_dev_lin = std(AoR_lin_array)
std_dev_middle = std(AoR_middle_array)
```

```
rel_row_cen_mean = mean(rel_row_cen);
rel_column_cen_mean = mean(rel_column_cen);
rel_row_cen_std = std(rel_row_cen);
rel_colum_cen_std = std(rel_column_cen);

x_cm_mean = mean(x_cm_array)
y_cm_mean = mean(y_cm_array)
x_cm_std = std(x_cm_array)
y_cm_std = std(y_cm_array)

r_mean = mean(r_array)
r_std = std(r_array)

rdiff_std = std(rdiff_array)
```

7.5.5 Evaluation script: DoE in EDEM

```
close all
clear all

numel_pic =30;
AoR_lin_array = [];
AoR_middle_array = [];
rel_row_cen = [];
rel_column_cen = [];
x_cm_array = [];
y_cm_array = [];

DoE_num = 28;
for g = 1:numel_pic
img_name = ['N',num2str(DoE_num),'_',num2str(g),'.JPG'];

[data_EDEM,AoR_lin_EDEM,AoR_middle_EDEM,rel_column_EDEM,rel_row_EDEM,c_mask
_1,x_cm_EDEM,y_cm_EDEM] = AoR_mos_centroid_EDEM_2(img_name);
AoR_lin_array = [AoR_lin_array,AoR_lin_EDEM];
AoR_middle_array = [AoR_middle_array,AoR_middle_EDEM];
rel_row_cen = [rel_row_cen,rel_row_EDEM];
rel_column_cen = [rel_column_cen,rel_column_EDEM];
x_cm_array = [x_cm_array,x_cm_EDEM];
y_cm_array = [y_cm_array,y_cm_EDEM];



end
AoR_lin_mean = mean(AoR_lin_array)
AoR_middle_mean = mean(AoR_middle_array)
std_dev_lin = std(AoR_lin_array)
std_dev_middle = std(AoR_middle_array)

rel_row_cen_mean = mean(rel_row_cen);
rel_column_cen_mean = mean(rel_column_cen);
rel_row_cen_std = std(rel_row_cen);
rel_colum_cen_std = std(rel_column_cen);

x_cm_mean = mean(x_cm_array)
y_cm_mean = mean(y_cm_array)
x_cm_std = std(x_cm_array)
y_cm_std = std(y_cm_array)
```

7.5.6 Tablet implementation position data

```
clear all
%Radius_tablet rcpe = 0.00421
Radius_tablet = 0.0042;

Numb_circles = 9;

r_fit = 0.0017;

phi_ = 360/Numb_circles;
phi = phi_*pi/180;



r_second = Radius_tablet - r_fit;

figure
axis equal


hold on

viscircles([0,0],Radius_tablet-r_fit);



viscircles([Radius_tablet-r_fit,0],r_fit);

x_data = [];
y_data = [];

for k = 1:Numb_circles

phis = k*phi_;
phi = phis*pi/180;;

y=sin(phi)*r_second;
x=cos(phi)*r_second;
x_data = [x_data,x]
y_data = [y_data,y]
viscircles([x,y],r_fit,'EdgeColor',[0 0 1]);
end

viscircles([0,0],Radius_tablet,'LineWidth',2);
```

8 References

[1] H. P. P. Zhu, Z. Y. Y. Zhou, R. Y. Y. Yang, and a. B. B. Yu, “Discrete particle simulation of particulate systems: Theoretical developments,” *Chemical Engineering Science*, vol. 62, no. 13, pp. 3378–3396, Jul. 2007.

[2] Y. Fu, S. Yang, S. H. Jeong, S. Kimura, and K. Park, “Orally Fast Disintegrating Tablets: Developments, Technologies, Taste-Masking and Clinical Studies,” *Critical Reviews in Therapeutic Drug Carrier Systems*, vol. 21, no. 6, pp. 433–476, 2004.

[3] C. F. Vesey, K. A. Fegely, N. P. Development, and C. W. Point, “Determination of critical parameters on the application of an aqueous, high gloss film coating system.”

[4] K. V. Allam and G. P. Kumar, “COLORANTS THE COSMETICS FOR THE PHARMACEUTICAL DOSAGE FORMS,” vol. 3, 2011.

[5] J.Teckoe, “A coat of many clours,” *Manufacturing Chemist*, vol. 77, no. 3, pp. 28–30, 2006.

[6] T. C. Dahl and I. I. Sue, “Mechanisms to control drug release from pellets coated with a silicone elastomer aqueous dispersion.,” *Pharmaceutical research*, vol. 9, no. 3, pp. 398–405, Mar. 1992.

[7] K. Yamane, M. Nakagawa, S. A. Altobelli, T. Tanaka, and Y. Tsuji, “Steady particulate flows in a horizontal rotating cylinder,” *Physics of Fluids*, vol. 10, no. 6, p. 1419, Jun. 1998.

[8] C. Wightman, M. Moakher, F. J. Muzzio, and O. Walton, “Simulation of flow and mixing of particles in a rotating and rocking cylinder,” *AIChE Journal*, vol. 44, no. 6, pp. 1266–1276, Jun. 1998.

[9] M. Kwapinska, G. Saage, and E. Tsotsas, “Mixing of particles in rotary drums: A comparison of discrete element simulations with experimental results and penetration models for thermal processes,” *Powder Technology*, vol. 161, no. 1, pp. 69–78, Jan. 2006.

[10] R. Y. Yang, R. P. Zou, and a. B. Yu, “Microdynamic analysis of particle flow in a horizontal rotating drum,” *Powder Technology*, vol. 130, no. 1–3, pp. 138–146, Feb. 2003.

[11] N. Taberlet, P. Richard, and E. John Hinch, “S shape of a granular pile in a rotating drum,” *Physical Review E*, vol. 73, no. 5, p. 050301, May 2006.

[12] M. Lemieux, G. Léonard, J. Doucet, L.-A. Leclaire, F. Viens, J. Chaouki, and F. Bertrand, “Large-scale numerical investigation of solids mixing in a V-blender using the discrete element method,” *Powder Technology*, vol. 181, no. 2, pp. 205–216, Feb. 2008.

[13] M. Lemieux, F. Bertrand, J. Chaouki, and P. Gosselin, “Comparative study of the mixing of free-flowing particles in a V-blender and a bin-blender,” *Chemical Engineering Science*, vol. 62, no. 6, pp. 1783–1802, Mar. 2007.

[14] H. P. Kuo, P. C. Knight, D. J. Parker, Y. Tsuji, M. J. Adams, and J. P. K. Seville, “The influence of DEM simulation parameters on the particle behaviour in a V-mixer,” *Chemical Engineering Science*, vol. 57, no. 17, pp. 3621–3638, Sep. 2002.

[15] F. Bertrand, L.-A. Leclaire, and G. Levecque, “DEM-based models for the mixing of granular materials,” *Chemical Engineering Science*, vol. 60, no. 8–9, pp. 2517–2531, Apr. 2005.

[16] M. Moakher, T. Shinbrot, and F. J. Muzzio, “Experimentally validated computations of flow, mixing and segregation of non-cohesive grains in 3D tumbling blenders,” *Powder Technology*, vol. 109, no. 1–3, pp. 58–71, Apr. 2000.

[17] G. N. Tiwari, A. K. Singh, and P. S. Bhatia, “Experimental simulation of a grain drying system,” *Energy Conversion and Management*, vol. 35, no. 5, pp. 453–458, May 1994.

[18] N. Wei, “Municipal Sewage Sludge Drying treament by an Composite Modifier,” *Mathematical Problems in Engineering*, 2012.

[19] X.-K. Yi, W.-F. Wu, Y.-Q. Zhang, J.-X. Li, and H.-P. Luo, “Thin-Layer Drying Characteristics and Modeling of Chinese Jujubes,” *Mathematical Problems ind Engineering*, 2012.

[20] L. Liu, G. Yang, and M. Yu, “Simulation for Sludge Flocculation I: Brownian Dynamic Simulation for Perikinetic Flocculation of Charged Particle,” *Mathematical Problems in Engineering*, Mar. 2012.

[21] Y. Guo and X. Wang, “Experimental Study on Forecasting Mathematical Model of Drying Shrinkage of Recycled Aggregate Concrete,” 2012.

[22] Y. Bolea, A. Grau, and A. Miranda, “SDSim: A Novel Simulator for Solar Drying Processes,” *Mathematical Problems in Engineering*, vol. 2012, pp. 1–25, 2012.

[23] C. Cogné, P. U. Nguyen, J. L. Lanoisellé, E. Van Hecke, and D. Clausse, “Modeling heat and mass transfer during vacuum freezing of puree droplet,” *International Journal of Refrigeration*, vol. 36, no. 4, pp. 1319–1326, Jun. 2013.

[24] S. Zhang and J. Liu, “Distribution of Vapor Pressure in the Vacuum Freeze-Drying Equipment,” *Mathematical Problems in Engineering*, vol. 2012, pp. 1–10, 2012.

[25] Z. Zhang and N. Kong, “Nonequilibrium Thermal Dynamic Modeling of Porous Medium Vacuum Drying Process,” 2012.

[26] Z. Ning and M. Ghadiri, “Distinct element analysis of attrition of granular solids under shear deformation,” *Chemical Engineering Science*, vol. 61, no. 18, pp. 5991–6001, Sep. 2006.

[27] T. HAN, H. KALMAN, and A. LEVY, “DEM Simulation of Particle Comminutionin Jet Milling,” *Particulate Science and Technology*, vol. 20, no. 4, pp. 325–340, Oct. 2002.

[28] D. I. Hoyer, “The discrete element method for fine grinding scale-up in Hicom mills,” *Powder Technology*, vol. 105, no. 1–3, pp. 250–256, Nov. 1999.

[29] A. V. Potapov and C. S. Campbell, “Computer simulation of shear-induced particle attrition,” *Powder Technology*, vol. 94, no. 2, pp. 109–122, Dec. 1997.

[30] R. W. Lewis, D. T. Gethin, X. S. Yang, and R. C. Rowe, “A combined finite-discrete element method for simulating pharmaceutical powder tableting,” *International Journal for Numerical Methods in Engineering*, vol. 62, no. 7, pp. 853–869, Feb. 2005.

[31] J. Lian and S. Shima, “Powder assembly simulation by particle dynamics method,” *International Journal for Numerical Methods in Engineering*, vol. 37, no. 5, pp. 763–775, Mar. 1994.

[32] R. . Ransing, D. . Gethin, A. . Khoei, P. Mosbah, and R. . Lewis, “Powder compaction modelling via the discrete and finite element method,” *Materials & Design*, vol. 21, no. 4, pp. 263–269, Aug. 2000.

[33] D. . Gethin, R. . Ransing, R. . Lewis, M. Dutko, and A. J. . Crook, “Numerical comparison of a deformable discrete element model and an equivalent continuum analysis for the compaction of ductile porous material,” *Computers & Structures*, vol. 79, no. 13, pp. 1287–1294, May 2001.

[34] A. Zavaliangos, “A multiparticle simulation of powder compaction using finite element discretization of individual particles,” in *MODELING AND NUMERICAL SIMULATION OF MATERIALS BEHAVIOR AND EVOLUTION*, 2002, vol. 731, pp. 169–175.

[35] H. Hashimoto, Z. M. Sun, Y. H. Park, and T. Abe, “Model simulation of powder compaction by complex mold based on deformation behavior of free particles measured by compression test,” in *GRANULAR MATERIAL-BASED TECHNOLOGIES*, 2003, vol. 759, pp. 41–45.

[36] R. S. Ransing, R. W. Lewis, and D. T. Gethin, “Using a deformable discrete-element technique to model the compaction behaviour of mixed ductile and brittle particulate systems.,” *Philosophical transactions. Series A, Mathematical, physical, and engineering sciences*, vol. 362, no. 1822, pp. 1867–84, Sep. 2004.

[37] C. L. Martin and D. Bouvard, “Study of the cold compaction of composite powders by the discrete element method,” *Acta Materialia*, vol. 51, no. 2, pp. 373–386, Jan. 2003.

[38] O. Skrinjar and P.-L. Larsson, “Cold compaction of composite powders with size ratio,” *Acta Materialia*, vol. 52, no. 7, pp. 1871–1884, Apr. 2004.

[39] Y. Sheng, C. J. Lawrence, B. J. Briscoe, and C. Thornton, “Numerical studies of uniaxial powder compaction process by 3D DEM,” *Engineering Computations*, vol. 21, no. 2/3/4, pp. 304–317, Jan. 2004.

[40] Y. C. Zhou, A. B. Yu, R. L. Stewart, and J. Bridgwater, “Microdynamic analysis of the particle flow in a cylindrical bladed mixer,” *Chemical Engineering Science*, vol. 59, no. 6, pp. 1343–1364, Mar. 2004.

[41] I. T. Cameron, F. Y. Wang, C. D. Immanuel, and F. Stepanek, “Process systems modelling and applications in granulation: A review,” *Chemical Engineering Science*, vol. 60, no. 14, pp. 3723–3750, Jul. 2005.

[42] J. A. Gantt and E. P. Gatzke, “High-shear granulation modeling using a discrete element simulation approach,” *Powder Technology*, vol. 156, no. 2–3, pp. 195–212, Aug. 2005.

[43] D. Verkoeijen, G. A. Pouw, G. M. H. Meesters, and B. Scarlett, “Population balances for particulate processes—a volume approach,” *Chemical Engineering Science*, vol. 57, no. 12, pp. 2287–2303, Jun. 2002.

[44] J. A. Gantt, I. T. Cameron, J. D. Litster, and E. P. Gatzke, “Determination of coalescence kernels for high-shear granulation using DEM simulations,” *Powder Technology*, vol. 170, no. 2, pp. 53–63, Dec. 2006.

[45] I. Talu, G. I. Tardos, and M. I. Khan, “Computer simulation of wet granulation,” *Powder Technology*, vol. 110, no. 1–2, pp. 59–75, May 2000.

[46] G. I. Tardos, M. I. Khan, and P. R. Mort, “Critical parameters and limiting conditions in binder granulation of fine powders,” *Powder Technology*, vol. 94, no. 3, pp. 245–258, Dec. 1997.

[47] R. Moreno-Atanasio and M. Ghadiri, “Mechanistic analysis and computer simulation of impact breakage of agglomerates: Effect of surface energy,” *Chemical Engineering Science*. 01-Apr-2006.

[48] G. Lian, C. Thornton, and M. J. Adams, “Discrete particle simulation of agglomerate impact coalescence,” *Chemical Engineering Science*, vol. 53, no. 19, pp. 3381–3391, Oct. 1998.

[49] M. J. . Goldschmidt, G. G. . Weijers, R. Boerefijn, and J. A. . Kuipers, “Discrete element modelling of fluidised bed spray granulation,” *Powder Technology*, vol. 138, no. 1, pp. 39–45, Nov. 2003.

[50] Z. Mansourpour, N. Mostoufi, and R. Sotudeh-Gharebagh, “A mechanistic study of agglomeration in fluidised beds at elevated pressures,” *The Canadian Journal of Chemical Engineering*, vol. 91, no. 3, pp. 560–569, Mar. 2013.

[51] P. A. Langston, U. Tüzün, and D. M. Heyes, “Continuous potential discrete particle simulations of stress and velocity fields in hoppers: transition from fluid to granular flow,” *Chemical Engineering Science*, vol. 49, no. 8, pp. 1259–1275, Apr. 1994.

[52] P. A. Langston, U. Tüzün, and D. M. Heyes, “Discrete element simulation of granular flow in 2D and 3D hoppers: Dependence of discharge rate and wall stress on particle interactions,” *Chemical Engineering Science*, vol. 50, no. 6, pp. 967–987, Mar. 1995.

[53] J. Kano, F. Saito, A. Shimosaka, and J. Hidaka, “Simulation of mass flow rate of particles discharged from hopper by Particle Element Method,” *JOURNAL OF CHEMICAL ENGINEERING OF JAPAN*, vol. 31, no. 6, pp. 936–940, 1998.

[54] J. Li and D. . Mason, “A computational investigation of transient heat transfer in pneumatic transport of granular particles,” *Powder Technology*, vol. 112, no. 3, pp. 273–282, Oct. 2000.

[55] T. Han, A. Levy, and H. Kalman, “DEM simulation for attrition of salt during dilute-phase pneumatic conveying,” *Powder Technology*, vol. 129, no. 1–3, pp. 92–100, Jan. 2003.

[56] E. W. C. Lim, Y. Zhang, and C.-H. Wang, “Effects of an electrostatic field in pneumatic conveying of granular materials through inclined and vertical pipes,” *Chemical Engineering Science*, vol. 61, no. 24, pp. 7889–7908, Dec. 2006.

[57] S. Watano, “Mechanism and control of electrification in pneumatic conveying of powders,” *Chemical Engineering Science*, vol. 61, no. 7, pp. 2271–2278, Apr. 2006.

[58] Y. Tsuji, T. Tanaka, and T. Ishida, “Lagrangian numerical simulation of plug flow of cohesionless particles in a horizontal pipe,” *Powder Technology*, vol. 71, no. 3, pp. 239–250, Sep. 1992.

[59] E. Wee Chuan Lim, C.-H. Wang, and A.-B. Yu, “Discrete element simulation for pneumatic conveying of granular material,” *AIChE Journal*, vol. 52, no. 2, pp. 496–509, Feb. 2006.

[60] Y. Zhang, E. W. C. Lim, and C.-H. Wang, “Pneumatic Transport of Granular Materials in an Inclined Conveying Pipe: Comparison of Computational Fluid Dynamics−Discrete Element Method (CFD−DEM), Electrical Capacitance Tomography (ECT), and Particle Image Velocimetry (PIV) Results,” *Industrial & Engineering Chemistry Research*, vol. 46, no. 19, pp. 6066–6083, 2007.

[61] S. Masson and J. Martinez, “Effect of particle mechanical properties on silo flow and stresses from distinct element simulations,” *Powder Technology*, vol. 109, no. 1–3, pp. 164–178, Apr. 2000.

[62] M. L. Hunt, R. C. Weathers, A. T. Lee, C. E. Brennen, and C. R. Wassgren, “Effects of horizontal vibration on hopper flows of granular materials.” 1999.

[63] J. J. McCarthy, D. V Khakhar, and J. M. Ottino, “Computational studies of granular mixing,” *Powder Technology*, vol. 109, no. 1–3, pp. 72–82, Apr. 2000.

[64] C. M. Dury and G. H. Ristow, “Radial Segregation in a Two-Dimensional Rotating Drum,” *Journal de Physique I*, vol. 7, no. 5, pp. 737–745, May 1997.

[65] P. W. Cleary, G. Metcalfe, and K. Liffman, “How well do discrete element granular flow models capture the essentials of mixing processes?,” *Applied Mathematical Modelling*, vol. 22, no. 12, pp. 995–1008, Dec. 1998.

[66] H. Li and J. J. McCarthy, “Phase diagrams for cohesive particle mixing and segregation.,” *Physical review. E, Statistical, nonlinear, and soft matter physics*, vol. 71, no. 2 Pt 1, p. 021305, Feb. 2005.

[67] K. Yamane, “Discrete-element method application to mixing and segregation model in industrial blending system,” *Journal of Materials Research*, vol. 19, no. 02, pp. 623–627, Mar. 2011.

[68] J. J. McCarthy, “Micro-modeling of cohesive mixing processes,” *Powder Technology*, vol. 138, no. 1, pp. 63–67, Nov. 2003.

[69] J. M. Link, W. Godlieb, N. G. Deen, and J. A. M. Kuipers, “Discrete element study of granulation in a spout-fluidized bed,” *Chemical Engineering Science*. Pergamon Press, 01-Dec-2007.

[70] W. R. Ketterhagen, M. T. A. M. Am Ende, and B. C. Hancock, “Process Modeling in the Pharmaceutical Industry using the Discrete Element Method,” vol. 98, no. 2, pp. 442–470, 2009.

[71] M. P. Allen and D. J. Tildesley, *Computer Simulation of Liquids*. Oxford University Press, USA, 1989, p. 408.

[72] R. . Hockney and J. . Eastwood, *Computer Simulation Using Particles*. Taylor & Francis, 1988, p. 540.

[73] A. Bródka and T. W. Zerda, “Dynamics of liquid acetone: Computer simulation,” *The Journal of Chemical Physics*, vol. 104, no. 16, p. 6313, Apr. 1996.

[74] P. M. Rodger, A. J. Stone, and D. J. Tildesley, “The intermolecular potential of chlorine,” *Molecular Physics*, vol. 63, no. 2, pp. 173–188, Feb. 1988.

[75] W. Swope and H. Andersen, “106-particle molecular-dynamics study of homogeneous nucleation of crystals in a supercooled atomic liquid,” *Physical Review B*, vol. 41, no. 10, pp. 7042–7054, Apr. 1990.

[76] E. Hairer, C. Lubich, and G. Wanner, *Geometric Numerical Integration: Structure-Preserving Algorithms for Ordinary Differential Equations (Springer Series in Computational Mathematics)*. Springer, 2010, p. 664.

[77] P. J. van der Houwen, E. Messina, and J. J. B. de Swart, “Parallel Störmer–Cowell methods for high-precision orbit computations,” *Applied Numerical Mathematics*, vol. 31, no. 3, pp. 353–374, Nov. 1999.

[78] L. Verlet, “Computer ‘Experiments’ on Classical Fluids. I. Thermodynamical Properties of Lennard-Jones Molecules,” *Physical Review*, vol. 159, no. 1, pp. 98–103, Jul. 1967.

[79] C. L. Ernst Hairer, “Geometric numerical integration illustrated by the Störmer/Verlet method,” *Acta Numerica*, 2003.

[80] C. K. Birdsall and A. . Langdon, *Plasma Physics via Computer Simulation (Series in Plasma Physics)*. Taylor & Francis, 2004, p. 504.

[81] F. Vesely, *Computational Physics: An Introduction (Google eBook)*. Springer, 2001, p. 259.

[82] C. Andersen, “Rattle : A ‘ Velocity ’ Molecular Version of the Shake Dynamics Calculations for,” pp. 24–34, 1983.

[83] D. Beeman, “Some multistep methods for use in molecular dynamics calculations,” *Journal of Computational Physics*, vol. 20, no. 2, pp. 130–139, Feb. 1976.

[84] P. Schofield, “Computer simulation studies of the liquid state,” *Computer Physics Communications*, vol. 5, no. 1, pp. 17–23, Jan. 1973.

[85] L. Monasse and C. Mariotti, “An energy-preserving Discrete Element Method for elastodynamics∗,” *ESAIM: Mathematical Modelling and Numerical Analysis*, vol. 46, no. 6, pp. 1527–1553, 2010.

[86] C. S. Campbell and C. E. Brennen, “Computer simulation of granular shear flows,” *Journal of Fluid Mechanics*, vol. 151, no. -1, p. 167, Apr. 2006.

[87] C. S. Campbell and A. Gong, “The stress tensor in a two-dimensional granular shear flow,” *Journal of Fluid Mechanics*, vol. 164, no. -1, p. 107, Apr. 2006.

[88] E. D. Liss and B. J. Glasser, “The influence of clusters on the stress in a sheared granular material,” *POWDER TECHNOLOGY*, vol. 116, no. 2–3, SI, pp. 116–132, 2001.

[89] M. E. Lasinski, J. S. Curtis, and J. F. Pekny, “Effect of system size on particle-phase stress and microstructure formation,” *Physics of Fluids*, vol. 16, no. 2, p. 265, Dec. 2004.

[90] Y. Wang and M. T. Mason, “Two-Dimensional Rigid-Body Collisions With Friction,” *Journal of Applied Mechanics*, vol. 59, no. 3, p. 635, Sep. 1992.

[91] C. Hogue and D. Newland, “Efficient computer simulation of moving granular particles,” *Powder Technology*, vol. 78, no. 1, pp. 51–66, Jan. 1994.

[92] B. P. B. Hoomans, J. A. M. Kuipers, W. J. Briels, and W. P. M. van Swaaij, “Discrete particle simulation of bubble and slug formation in a two-dimensional gas-fluidised bed: A hard-sphere approach,” *Chemical Engineering Science*, vol. 51, no. 1, pp. 99–118, Jan. 1996.

[93] Y. Song and W. Virginia, “Study of the Dynamic Behavior of Tablet Movement in a Rotating Drum Using Discrete Element Modeling (DEM) Method,” 2006.

[94] O. D. L. S. P.A.Cundall, “DISCRETE NUMERICAL-MODEL FOR GRANULAR ASSEMBLIES,” *Geotechnique*, vol. 29, pp. 47–65, 1979.

[95] J. P. K. Seville, C. D. Willett, and P. C. Knight, “Interparticle forces in fluidisation: a review,” *Powder Technology*, vol. 113, no. 3, pp. 261–268, Dec. 2000.

[96] J. Baxter, H. Abou-Chakra, U. TüZün, and B. Mills Lamptey, “A DEM Simulation and Experimental Strategy for Solving Fine Powder Flow Problems,” *Chemical Engineering Research and Design*, vol. 78, no. 7, pp. 1019–1025, Oct. 2000.

[97] T. Mikami, H. Kamiya, and M. Horio, “Numerical simulation of cohesive powder behavior in a fluidized bed,” *Chemical Engineering Science*, vol. 53, no. 10, pp. 1927–1940, May 1998.

[98] B. N. Asmar, P. A. Langston, A. J. Matchett, and J. K. Walters, “Energy monitoring in distinct element models of particle systems,” *Advanced Powder Technology*, vol. 14, no. 1, pp. 43–69, Feb. 2003.

[99] B. N. Asmar, P. A. Langston, A. J. Matchett, and J. K. Walters, “Validation tests on a distinct element model of vibrating cohesive particle systems,” *Computers & Chemical Engineering*, vol. 26, no. 6, pp. 785–802, Jun. 2002.

[100] M. . Rhodes, X. . Wang, M. Nguyen, P. Stewart, and K. Liffman, “Onset of cohesive behaviour in gas fluidized beds: a numerical study using DEM simulation,” *Chemical Engineering Science*, vol. 56, no. 14, pp. 4433–4438, Jul. 2001.

[101] J. Kant Pandit, X. S. Wang, and M. J. Rhodes, “A DEM study of bubble formation in Group B fluidized beds with and without cohesive inter-particle forces,” *Chemical Engineering Science*, vol. 62, no. 1–2, pp. 159–166, Jan. 2007.

[102] J. K. Pandit, X. S. Wang, and M. J. Rhodes, “On Geldart Group A behaviour in fluidized beds with and without cohesive interparticle forces: A DEM study,” *Powder Technology*, vol. 164, no. 3, pp. 130–138, Jun. 2006.

[103] W. MW, H. DK, and H. CM, “Discrete-particle simulations of cohesive granular flow using a square-well potential,” *Granul Mateer*, no. 6, pp. 239–254, 2004.

[104] A. W. Alexander, B. Chaudhuri, A. Faqih, F. J. Muzzio, C. Davies, and M. S. Tomassone, “Avalanching flow of cohesive powders,” *Powder Technology*, vol. 164, no. 1, pp. 13–21, May 2006.

[105] M. W. Weber and C. M. Hrenya, “Square-well model for cohesion in fluidized beds,” *Chemical Engineering Science*, vol. 61, no. 14, pp. 4511–4527, Jul. 2006.

[106] R. A. Fisher, “On the capillary forces in an ideal soil; correction of formulae given by W. B. Haines,” *The Journal of Agricultural Science*, vol. 16, no. 03, pp. 492–505, Jul. 1926.

[107] G. Lian, C. Thornton, and M. J. Adams, “A Theoretical Study of the Liquid Bridge Forces between Two Rigid Spherical Bodies,” *Journal of Colloid and Interface Science*, vol. 161, no. 1, pp. 138–147, Nov. 1993.

[108] H. Matuttis and A. Schinner, “PARTICLE SIMULATION OF COHESIVE GRANULAR MATERIALS,” *International Journal of Modern Physics C*, vol. 12, no. 07, pp. 1011–1021, Sep. 2001.

[109] H. C. Hamaker, “The London—van der Waals attraction between spherical particles,” *Physica*, vol. 4, no. 10, pp. 1058–1072, Oct. 1937.

[110] K. Z. Y. Yen and T. K. Chaki, “A dynamic simulation of particle rearrangement in powder packings with realistic interactions,” *Journal of Applied Physics*, vol. 71, no. 7, p. 3164, Apr. 1992.

[111] R. Yang, R. Zou, and A. Yu, “Computer simulation of the packing of fine particles,” *Physical Review E*, vol. 62, no. 3, pp. 3900–3908, Sep. 2000.

[112] H. Krupp, “Particle adhesion theory and experiment,” *Advances in Colloid and Interface Science*, vol. 1, no. 2, pp. 111–239, May 1967.

[113] J. N. Israelachvili, *Intermolecular and Surface Forces*. 2010.

[114] H.J.Herrmann and S.Luding, “Modeling granular media on the computer,” *Continuum Mechanics and Thermodynamics*, 1997.

[115] S.Luding, “Collisions and contacts between two particles,” *Physics of dry granular media 1st edition*, 1998.

[116] T. Schwager and T. Poeschel, “Coefficient of restitution and linear dashpot model revisited,” pp. 2–5, 2008.

[117] H. Hertz, “Über die Berührung fester elastischer körper,” *Journal für reine und angewandte Mathematik*, pp. 156–171, 1882.

[118] K. L. Johnson, *Contact Mechanics*. 1987.

[119] Y. Taguchi, “POWDER TURBULENCE - DIRECT ONSET OF TURBULENT-FLOW,” *J Phys France II*, pp. 2103–2114, 1992.

[120] G. Kuwabara and K. Kono, “Restitution Coefficient in a Collision between Two Spheres,” *Japanese Journal of Applied Physics*, vol. 26, no. Part 1, No. 8, pp. 1230–1233, Aug. 1987.

[121] N. V Brilliantov, F. Spahn, J. M. Hertzsch, and P. Thorsten, “A model for collisions in granular gases,” vol. 53, 1996.

[122] M. A. Meyers and K. K. Chawla, *Mechanical Behavior of Materials*. Cambridge University Press, 2008.

[123] O. R. Walton, “Viscosity, granular-temperature, and stress calculations for shearing assemblies of inelastic, frictional disks,” *Journal of Rheology*, vol. 30, no. 5, p. 949, 1986.

[124] W. R. Ketterhagen, J. S. Curtis, and C. R. Wassgren, “Stress results from two-dimensional granular shear flow simulations using various collision models.,” *Physical review. E, Statistical, nonlinear, and soft matter physics*, vol. 71, no. 6 Pt 1, p. 061307, Jun. 2005.

[125] M. JJ and O. JM, “Particle dynamics simulation: A hybrid technique applied to granular mixing,” *Powder Technol*, no. 97, pp. 91–99, 1998.

[126] G. G. JOSEPH, E. GEFFROY, B. MENA, O. R. WALTON, and R. R. HUILGOL, “SIMULATION OF FILLING AND EMPTYING IN A HEXAGONAL-SHAPE SOLAR GRAIN SILO,” *Particulate Science and Technology*, vol. 18, no. 4, pp. 309–327, Oct. 2000.

[127] M. Moakher, T. Shinbrot, and F. J. Muzzio, “Experimentally validated computations of flow , mixing and segregation of non-cohesive grains in 3D tumbling blenders,” pp. 58–71, 2000.

[128] C. Thornton, “Coefficient of Restitution for Collinear Collisions of Elastic-Perfectly Plastic Spheres,” *Journal of Applied Mechanics*, vol. 64, no. 2, p. 383, Jun. 1997.

[129] Y. Zhou, “A theoretical model of collision between soft-spheres with Hertz elastic loading and nonlinear plastic unloading,” *Theoretical and Applied Mechanics Letters*, vol. 1, no. 4, p. 041006, Jul. 2011.

[130] C. Thornton and K. K. Yin, “Impact of elastic spheres with and without adhesion,” *Powder Technology*, vol. 65, no. 1–3, pp. 153–166, Mar. 1991.

[131] M.Oda, K.Iwashita, and T.Kakiuchi, “Importance of particle rotation in the mechanics of granular materials,” *Pwder and Grains 97*, pp. 207–214, 1997.

[132] S. J, D. S, and Wolf, “Force schemes in simulations of granular materials,” *Journal Phys I France*, pp. 5–20, 1996.

[133] R. D. M. H.Deresiewicz, “ELASTIC SPHERES IN CONTACT UNDER VARYING OBLIQUE FORCES,” 1952.

[134] Y. Li, Y. Xu, and C. Thornton, “A comparison of discrete element simulations and experiments for ‘sandpiles’ composed of spherical particles,” *Powder Technology*, vol. 160, no. 3, pp. 219–228, Dec. 2005.

[135] H. a. Navarro and M. P. de Souza Braun, “Determination of the normal spring stiffness coefficient in the linear spring-dashpot contact model of discrete element method,” *Powder Technology*, vol. 246, pp. 707–722, Jun. 2013.

[136] K. Mao, M. Y. Wang, Z. Xu, and T. Chen, “DEM simulation of particle damping,” *Powder Technology*, vol. 142, no. 2–3, pp. 154–165, Apr. 2004.

[137] B. L. Fowler, E. M. Flint, and S. E. Olson, “<title>Design methodology for particle damping</title>,” in *SPIE’s 8th Annual International Symposium on Smart Structures and Materials*, 2001, pp. 186–197.

[138] B. L. Fowler, E. M. Flint, and S. E. Olson, “<title>Effectiveness and predictability of particle damping</title>,” in *SPIE’s 7th Annual International Symposium on Smart Structures and Materials*, 2000, pp. 356–367.

[139] S. E. Olson, “An analytical particle damping model,” *Journal of Sound and Vibration*, vol. 264, no. 5, pp. 1155–1166, Jul. 2003.

[140] C. W. R. C.Thornton, “Applications of theoretical contact mechanics to solid particle system simulation,” *Micromechanics of Granular Materials*, pp. pp. 133–142, 1988.

[141] M. Moakher, “Discrete Element Simulations of Granular Flow , Mixing and Segregation inside Tumbling Blenders,” pp. 1–6, 2000.

[142] V. L. Popov, *Kontaktmechanik und Reibung: Von der Nanotribologie bis zur Erdbebendynamik (German Edition)*. Springer, 2010, p. 388.

[143] H.-J. Butt, K. Graf, and M. Kappl, *Physics and Chemistry of Interfaces*. Wiley-VCH, 2013, p. 495.

[144] K. Iwashita and M. Oda, "Rolling Resistance at Contacts in Simulation of Shear Band Development by DEM," *Journal of Engineering Mechanics*, vol. 124, no. 3, pp. 285–292, Mar. 1998.

[145] J. A. Greenwood, H. Minshall, and D. Tabor, "Hysteresis Losses in Rolling and Sliding Friction," *Proceedings of the Royal Society A: Mathematical, Physical and Engineering Sciences*, vol. 259, no. 1299, pp. 480–507, Jan. 1961.

[146] K. L. Johnson and K. K. L. Johnson, *Contact Mechanics*. 1987.

[147] N. V Brilliantov and T. Pöschel, "Rolling friction of a viscous sphere on a hard plane," *Europhysics Letters (EPL)*, vol. 42, no. 5, pp. 511–516, Jun. 1998.

[148] L. Kondic, "Dynamics of spherical particles on a surface: collision-induced sliding and other effects.," *Physical review. E, Statistical physics, plasmas, fluids, and related interdisciplinary topics*, vol. 60, no. 1, pp. 751–70, Jul. 1999.

[149] Y. C. Zhou, B. D. Wright, R. Y. Yang, B. H. Xu, and A. B. Yu, "Rolling friction in the dynamic simulation of sandpile formation," *Physica A: Statistical Mechanics and its Applications*, vol. 269, no. 2–4, pp. 536–553, Jul. 1999.

[150] K. Iwashita and M. Oda, "Micro-deformation mechanism of shear banding process based on modified distinct element method," *Powder Technology*, vol. 109, no. 1–3, pp. 192–205, Apr. 2000.

[151] Q. H. J. P. Bardet, "NUMERICAL MODELING OF MICROPOLAR EFFECTS IN IDEALIZED GRANULAR MATERIALS," *American Society of MEchanical Engeneers*, vol. 37, pp. 85–92, 1992.

[152] J. P. Bardet, "Observations on the effects of particle rotations on the failure of idealized granular materials," *Mechanics of Materials*, vol. 18, no. 2, pp. 159–182, Jul. 1994.

[153] M. Oda, J. Konishi, and S. Nemat-Nasser, "Experimental micromechanical evaluation of strength of granular materials: Effects of particle rolling," *Mechanics of Materials*, vol. 1, no. 4, pp. 269–283, Dec. 1982.

[154] F. Calvetti, G. Combe, and J. Lanier, "Experimental micromechanical analysis of a 2D granular material: relation between structure evolution and loading path," *Mechanics of Cohesive-frictional Materials*, vol. 2, no. 2, pp. 121–163, Apr. 1997.

[155] A. Misra and H. Jiang, "Measured kinematic fields in the biaxial shear of granular materials," *Computers and Geotechnics*, vol. 20, no. 3–4, pp. 267–285, Jan. 1997.

[156] J.Lanier, *Micro-mechnaism of deforamtion in granular materials: Experiments and numerical results,Continuous and Discontinuous Modelling of Cohesive-Frictional Materials*, vol. 568. Berlin, Heidelberg: Springer Berlin Heidelberg, 2001.

[157] J. Ai, J.-F. Chen, J. M. Rotter, and J. Y. Ooi, "Assessment of rolling resistance models in discrete element simulations," *Powder Technology*, vol. 206, no. 3, pp. 269–282, Jan. 2011.

[158] H. SAKAGUCHI, E. OZAKI, and T. IGARASHI, “Plugging of the Flow of Granular Materials during the Discharge from a Silo,” *International Journal of Modern Physics B*, vol. 07, no. 09n10, pp. 1949–1963, Apr. 1993.

[159] M. J. Jiang, H.-S. Yu, and D. Harris, “A novel discrete model for granular material incorporating rolling resistance,” *Computers and Geotechnics*, vol. 32, no. 5, pp. 340–357, Jul. 2005.

[160] O.Reynolds, “On rolling-friction,” *Philos T R Soc*, vol. 166, pp. 155–174, 1876.

[161] H. L. Heathcote, “The ball bearing: in the making, under test and on service,” *ARCHIVE: Proceedings of the Institution of Automobile Engineers 1906-1947 (vols 1-41)*, vol. 15, no. 1920, pp. 569–702, Jun. 1920.

[162] D. V. Konvisarov and A. A. Pokrovskaia, “Influence of radii of curvature of cylindrical bodies on their resistance to rolling under different loads,” *Proc.Sib.Phys.Tech.*, pp. 62–79, 1955.

[163] S. . Pinegin and A. V. Orlov, “Resistance to motion for certain types of free rolling,” *Mekhanika Mahinostroenie*, vol. 3, no. 91–97, 1961.

[164] J. J. Kalker, *Three-Dimensional Elastic Bodies in Rolling Contact*. 1990.

[165] D. Tabor, “The Mechanism of Rolling Friction. II. The Elastic Range,” *Proceedings of the Royal Society A: Mathematical, Physical and Engineering Sciences*, vol. 229, no. 1177, pp. 198–220, Apr. 1955.

[166] D. G. Flom, “Dynamic mechanical losses in rolling contacts,” *Rolling contact phenomena*, pp. 97–112, 1962.

[167] G. M. Hamilton, “Plastic flow in rollers loaded above the yield point,” *ARCHIVE: Proceedings of the Institution of Mechanical Engineers 1847-1982 (vols 1-196)*, vol. 177, no. 1963, pp. 667–675, Jun. 1963.

[168] K. L. Johnson, “Rolling resistance measurements at high loads,” *Mech.Sci.*, vol. 16, pp. 939–943, 1974.

[169] D. G. Flom and A. M. Bueche, “Theory of Rolling Friction for Spheres,” *Journal of Applied Physics*, vol. 30, no. 11, p. 1725, Nov. 1959.

[170] W. D. May, E. L. Morris, and D. Atack, “Rolling Friction of a Hard Cylinder over a Viscoelastic Material,” *Journal of Applied Physics*, vol. 30, no. 11, p. 1713, Nov. 1959.

[171] K. C. Ludema and D. Tabor, “The friction and visco-elastic properties of polymeric solids,” *Wear*, vol. 9, no. 5, pp. 329–348, Sep. 1966.

[172] J. T. Oden and T. L. Lin, “On the general rolling contact problem for finite deformations of a viscoelastic cylinder,” *Computer Methods in Applied Mechanics and Engineering*, vol. 57, no. 3, pp. 297–367, Sep. 1986.

[173] N. V. Brilliantov and T. Pöschel, “Rolling as a ‘continuing collision’,” *The European Physical Journal B*, vol. 12, no. 2, pp. 299–301, Nov. 1999.

[174] T. Pöschel, T. Schwager, and N. V. Brilliantov, “Rolling friction of a hard cylinder on a viscous plane,” *The European Physical Journal B*, vol. 10, no. 1, pp. 169–174, Jul. 1999.

[175] G. A. Tomlinson, “CVI. A molecular theory of friction,” *Philosophical Magazine Series 7*, vol. 7, no. 46, pp. 905–939, 1929.

[176] A. Doménech, “Introduction to the study of rolling friction,” *American Journal of Physics*, vol. 55, no. 3, p. 231, Mar. 1987.

[177] C. Dominik and A. G. G. M. Tielens, “Resistance to rolling in the adhesive contact of two elastic spheres,” *Philosophical Magazine A*, vol. 72, no. 3, pp. 783–803, Sep. 1995.

[178] J.-C. Charmet and M. Barquins, “Adhesive contact and rolling of a rigid cylinder under the pull of gravity on the underside of a smooth-surfaced sheet of rubber,” *International Journal of Adhesion and Adhesives*, vol. 16, no. 4, pp. 249–254, Jan. 1996.

[179] F. Robbe-Valloire and M. Barquins, “Adhesive contact and kinetics of adherence between a rigid cylinder and an elastomeric solid,” *International Journal of Adhesion and Adhesives*, vol. 18, no. 1, pp. 29–34, Feb. 1998.

[180] S. Hao and L. M. Keer, “Rolling Contact Between Rigid Cylinder and Semi-Infinite Elastic Body With Sliding and Adhesion,” *Journal of Tribology*, vol. 129, no. 3, p. 481, Jul. 2007.

[181] M. Oda and K. Iwashita, “Study on couple stress and shear band development in granular media based on numerical simulation analyses,” *International Journal of Engineering Science*, vol. 38, no. 15, pp. 1713–1740, Oct. 2000.

[182] A. Azarkhin, “Some History-Dependent Problems for Dissimilar Cylinders With Finite Friction,” *Journal of Applied Mechanics*, vol. 55, no. 1, p. 81, Mar. 1988.

[183] J. Morgan, “Capturing Physical Phenomena in Particle Dynamics Simulations of Granular Fault Gouge,” *Journal of Engineering Mechanics*, vol. 124, no. 3.

[184] J.F.Wang, M.Gutierrez, and J.Dove, “Effect of particle rolling resistance on interface shear behavior,” in *17th ASCE Engineering mechanics conference, University of Delaware*, 2004.

[185] A. Tordesillas and D. C. S. Walsh, “Incorporating rolling resistance and contact anisotropy in micromechanical models of granular media,” *Powder Technology*, vol. 124, no. 1–2, pp. 106–111, Apr. 2002.

[186] A. Tordesillas, J. Peters, and M. Muthuswamy, “Role of particle rotations and rolling resistance in a semi-infinite particulate solid indented by a rigid flat punch,” *ANZIAM Journal*, vol. 46. pp. C260–C275.

[187] X. Li, X. Chu, and Y. T. Feng, “A discrete particle model and numerical modeling of the failure modes of granular materials,” *Engineering Computations*, vol. 22, no. 8, pp. 894–920, Jan. 2005.

[188] A. Tordesillas, “Force chain buckling, unjamming transitions and shear banding in dense granular assemblies,” *Philosophical Magazine*, vol. 87, no. 32, pp. 4987–5016, Nov. 2007.

[189] M. Jiang, H.-S. Yu, and D. Harris, “Kinematic variables bridging discrete and continuum granular mechanics,” *Mechanics Research Communications*, vol. 33, no. 5, pp. 651–666, Sep. 2006.

[190] J. Lee and H. J. Herrmann, “Angle of Repose and Angle of Marginal Stability: Molecular Dyanmics of Granular Particles,” Nov. 1992.

[191] S. Luding, “Stress distribution in static two dimensional granular model media in the absence of friction,” Jan. 1997.

[192] T. Elperin and E. Golshtein, “Comparison of different models for tangential forces using the particle dynamics method,” *Physica A: Statistical Mechanics and its Applications*, vol. 242, no. 3–4, pp. 332–340, Aug. 1997.

[193] F. Beer, J. ,E. R. Johnston, E. Eisenberg, W. Clausen, D. Mazurek, and P. Cornwell, *Vector Mechanics for Engineers: Statics and Dynamics*. McGraw-Hill Science/Engineering/Math, 2006.

[194] Y. C. Zhou, B. H. Xu, A. B. Yu, and P. Zulli, “Numerical investigation of the angle of repose of monosized spheres.,” *Physical review. E, Statistical, nonlinear, and soft matter physics*, vol. 64, no. 2 Pt 1, p. 021301, Aug. 2001.

[195] Y. C. Zhou, B. H. Xu, A. B. Yu, and P. Zulli, “An experimental and numerical study of the angle of repose of coarse spheres,” *Powder Technology*, vol. 125, no. 1, pp. 45–54, May 2002.

[196] Y. C. Zhou, B. H. Xu, R. P. Zou, A. B. Yu, and P. Zulli, “Stress distribution in a sandpile formed on a deflected base,” *Advanced Powder Technology*, vol. 14, no. 4, pp. 401–410, Nov. 2003.

[197] H. . Zhu and A. . Yu, “The effects of wall and rolling resistance on the couple stress of granular materials in vertical flow,” *Physica A: Statistical Mechanics and its Applications*, vol. 325, no. 3–4, pp. 347–360, Jul. 2003.

[198] H. P. Zhu, G. X. Xiao, Z. Y. Zhou, A. B. Yu, and D. L. Xu, “Numerical simulation of the interaction forces between turbine meter and particles in a standpipe,” *Granular Matter*, vol. 5, no. 4, pp. 193–199, Feb. 2004.

[199] H. P. Zhu and A. B. Yu, “A theoretical analysis of the force models in discrete element method,” *Powder Technology*, vol. 161, no. 2, pp. 122–129, Jan. 2006.

[200] H. P. Zhu and A. B. Yu, “Averaging method of granular materials.,” *Physical review. E, Statistical, nonlinear, and soft matter physics*, vol. 66, no. 2 Pt 1, p. 021302, Aug. 2002.

[201] W. R. Ketterhagen, R. Bharadwaj, and B. C. Hancock, “The coefficient of rolling resistance (CoRR) of some pharmaceutical tablets.,” *International journal of pharmaceutics*, vol. 392, no. 1–2, pp. 107–10, Jun. 2010.

[202] P. A. LANGSTON, U. TÜZÜN, and D. M. HEYES, “Distinct element simulation of interstitial air effects in axially symmetric granular flows in hoppers,” *Chemical engineering science*, vol. 51, no. 6, pp. 873–891, 1996.

[203] N. G. Deen, M. Sint Annaland van, M. A. Hoef van der, and J. A. M. Kuipers, “Review of discrete particle modeling of fluidized beds,” *Chemical Engineering Science*. Elsevier, 01-Dec-2007.

[204] Y. Tsuji, T. Kawaguchi, and T. Tanaka, “Discrete particle simulation of two-dimensional fluidized bed,” *Powder Technology*, vol. 77, no. 1, pp. 79–87, Oct. 1993.

[205] B. H. Xu and A. B. Yu, “Numerical simulation of the gas-solid flow in a fluidized bed by combining discrete particle method with computational fluid dynamics,” *Chemical Engineering Science*, vol. 52, no. 16, pp. 2785–2809, Aug. 1997.

[206] T. Kawaguchi, T. Tanaka, and Y. Tsuji, “Numerical simulation of two-dimensional fluidized beds using the discrete element method (comparison between the two- and three-dimensional models),” *Powder Technology*, vol. 96, no. 2, pp. 129–138, May 1998.

[207] Y. Li, J. Zhang, and L.-S. Fan, “Numerical simulation of gas–liquid–solid fluidization systems using a combined CFD-VOF-DPM method: bubble wake behavior,” *Chemical Engineering Science*, vol. 54, no. 21, pp. 5101–5107, Nov. 1999.

[208] M. . Rhodes, X. . Wang, M. Nguyen, P. Stewart, and K. Liffman, “Study of mixing in gas-fluidized beds using a DEM model,” *Chemical Engineering Science*, vol. 56, no. 8, pp. 2859–2866, Apr. 2001.

[209] B. G. M. van Wachem, J. van der Schaaf, J. C. Schouten, R. Krishna, and C. M. van den Bleek, “Experimental validation of Lagrangian–Eulerian simulations of fluidized beds,” *Powder Technology*, vol. 116, no. 2–3, pp. 155–165, May 2001.

[210] S. Takeuchi, X. Shan Wang, and M. J. Rhodes, “Discrete element study of particle circulation in a 3-D spouted bed,” *Chemical Engineering Science*, vol. 60, no. 5, pp. 1267–1276, Mar. 2005.

[211] S. Takeuchi, S. Wang, and M. Rhodes, “Discrete element simulation of a flat-bottomed spouted bed in the 3-D cylindrical coordinate system,” *Chemical Engineering Science*, vol. 59, no. 17, pp. 3495–3504, Sep. 2004.

[212] D. E. Knuth, *Art of Computer Programming, The, Volumes 1-3 Boxed Set (3rd Edition) (Vol 1-3)*. Addison-Wesley Professional, 1998.

[213] D. J. Evans, “On the representatation of orientation space,” *Molecular Physics*, vol. 34, no. 2, pp. 317–325, Aug. 1977.

[214] B. Freireich, W. R. Ketterhagen, and C. Wassgren, “Intra-tablet coating variability for several pharmaceutical tablet shapes,” *Chemical Engineering Science*, vol. 66, no. 12, pp. 2535–2544, Jun. 2011.

[215] J. A. C. GALLAS and S. SOKOLOWSKI, “GRAIN NON-SPHERICITY EFFECTS ON THE ANGLE OF REPOSE OF GRANULAR MATERIAL,” *International Journal of Modern Physics B*, vol. 07, no. 09n10, pp. 2037–2046, Apr. 1993.

[216] J. Cordelair and P. Greil, “Discrete element modeling of solid formation during electrophoretic deposition,” *Journal of Materials Science*, vol. 39, no. 3, pp. 1017–1021, Feb. 2004.

[217] T. Pöschel and V. Buchholtz, “Static friction phenomena in granular materials: Coulomb law versus particle geometry,” *Physical Review Letters*, vol. 71, no. 24, pp. 3963–3966, Dec. 1993.

[218] R. J. Bathurst and L. Rothenburg, “Micromechanical features of granular assemblies with planar elliptical particles,” *Géotechnique*, vol. 42, no. 1, pp. 79–95, Jan. 1992.

[219] M. P. Allen and A. A. Imbierski, “A molecular dynamics study of the hard dumb-bell system,” *Molecular Physics*, vol. 60, no. 2, pp. 453–473, Feb. 1987.

[220] K. E. Evans and M. D. Ferrar, “The packing of thick fibres,” *Journal of Physics D: Applied Physics*, vol. 22, no. 2, pp. 354–360, Feb. 1989.

[221] J. F. Favier, M. H. Abbaspour-Fard, and M. Kremmer, “Modeling Nonspherical Particles Using Multisphere Discrete Elements,” *Journal of Engineering Mechanics*, vol. 127, no. 10, pp. 971–977, 2001.

[222] H. Abou-Chakra, J. Baxter, and U. Tüzün, “Three-dimensional particle shape descriptors for computer simulation of non-spherical particulate assemblies,” *Advanced Powder Technology*, vol. 15, no. 1, pp. 63–77, Jan. 2004.

[223] J. Calantoni, K. T. Holland, and T. G. Drake, “Modelling sheet-flow sediment transport in wave-bottom boundary layers using discrete-element modelling.,” *Philosophical transactions. Series A, Mathematical, physical, and engineering sciences*, vol. 362, no. 1822, pp. 1987–2001, Sep. 2004.

[224] D. W. Rebertus and K. M. Sando, “Molecular dynamics simulation of a fluid of hard spherocylinders,” *The Journal of Chemical Physics*, vol. 67, no. 6, p. 2585, Sep. 1977.

[225] A. Munjiza, J. P. Latham, and N. W. M. John, “3D dynamics of discrete element systems comprising irregular discrete elements?integration solution for finite rotations in 3D,” *International Journal for Numerical Methods in Engineering*, vol. 56, no. 1, pp. 35–55, Jan. 2003.

[226] S. R. Williams and A. P. Philipse, “Random packings of spheres and spherocylinders simulated by mechanical contraction.,” *Physical review. E, Statistical, nonlinear, and soft matter physics*, vol. 67, no. 5 Pt 1, p. 051301, May 2003.

[227] M. A. Hopkins, “Discrete element modeling with dilated particles,” *Engineering Computations*, vol. 21, no. 2/3/4, pp. 422–430, Jan. 2004.

[228] J. Li, P. A. Langston, C. Webb, and T. Dyakowski, “Flow of sphero-disc particles in rectangular hoppers—a DEM and experimental comparison in 3D,” *Chemical Engineering Science*, vol. 59, no. 24, pp. 5917–5929, Dec. 2004.

[229] Y. Song, R. Turton, and F. Kayihan, “Contact detection algorithms for DEM simulations of tablet-shaped particles,” *Powder Technology*, vol. 161, no. 1, pp. 32–40, Jan. 2006.

[230] R. L. Stewart, J. Bridgwater, Y. C. Zhou, and A. B. Yu, “Simulated and measured flow of granules in a bladed mixer—a detailed comparison,” *Chemical Engineering Science*, vol. 56, no. 19, pp. 5457–5471, Oct. 2001.

[231] C. J. Broadbent, J. Bridgwater, D. J. Parker, S. T. Keningley, and P. Knight, “A phenomenological study of a batch mixer using a positron camera,” *Powder Technology*, vol. 76, no. 3, pp. 317–329, Sep. 1993.

[232] B. P. B. Hoomans, J. A. M. Kuipers, M. Mohd Salleh, and J. P. Seville, “Experimental validation of granular dynamics simulations of gas-fluidised beds with homogeneous inflow conditions using Positron Emission Particle Tracking,” *Powder Technology*. Elsevier, 01-Mar-2001.

[233] R. D. Wildman, J. M. Huntley, and D. J. Parker, “Convection in highly fluidized three-dimensional granular beds.,” *Physical review letters*, vol. 86, no. 15, pp. 3304–7, Apr. 2001.

[234] P. S. Fennell, J. F. Davidson, J. S. Dennis, L. F. Gladden, A. N. Hayhurst, M. D. Mantle, C. R. Müller, A. C. Rees, S. A. Scott, and A. J. Sederman, “A study of the mixing of solids in gas-fluidized beds, using ultra-fast MRI,” *Chemical Engineering Science*, vol. 60, no. 7, pp. 2085–2088, Apr. 2005.

[235] R. H. H. M. PhD, W. G. B. J. M. P. FACR, and C. J. L. M. C. (ret) U. M. S, *MRI: The Basics*. Lippincott Williams & Wilkins, 2010, p. 400.

[236] Z.-P. Liang and P. C. Lauterbur, *Principles of Magnetic Resonance Imaging: A Signal Processing Perspective*. Wiley-IEEE Press, 1999.

[237] T. Kawaguchi, “MRI measurement of granular flows and fluid-particle flows,” *Advanced Powder Technology*, vol. 21, no. 3, pp. 235–241, May 2010.

[238] S. Sandadi, P. Pandey, and R. Turton, “In situ, near real-time acquisition of particle motion in rotating pan coating equipment using imaging techniques,” *Chemical Engineering Science*, vol. 59, no. 24, pp. 5807–5817, Dec. 2004.

[239] P. Pandey, “Experimental determination of surface appearance times for spherical particles in rotating drum devices with and withhout the presence of liquid spray.” Distributed by American Institute of Chemical Engineers,, [New York, N.Y. :, 2003.

[240] P. Pandey and R. Turton, “Movement of different-shaped particles in a pan-coating device using novel video-imaging techniques.,” *AAPS PharmSciTech*, vol. 6, no. 2, pp. E237–44, Jan. 2005.

[241] P. Pandey, Y. Song, F. Kayihan, and R. Turton, “Simulation of particle movement in a pan coating device using discrete element modeling and its comparison with video-imaging experiments,” *Powder Technology*, vol. 161, no. 2, pp. 79–88, Jan. 2006.

[242] N. Jain, J. M. Ottino, and R. M. Lueptow, “An experimental study of the flowing granular layer in a rotating tumbler,” *Physics of Fluids*, vol. 14, no. 2, p. 572, Feb. 2002.

[243] T. M. Leaver, H. D. Shannon, and R. C. Rowe, “A photometric analysis of tablet movement in a side-vented perforated drum (Accela-Cota).,” *The Journal of pharmacy and pharmacology*, vol. 37, no. 1, pp. 17–21, Jan. 1985.

[244] G. Baumann, M. Jánosi Imre, and E. D. Wolf, “Surface properties and flow of granular material in a two-dimensional rotating-drum model,” *Theoretical Physics*, vol. 10, 1995.

[245] G. Baumann, I. Janosi, and D. Wolf, “Particle Trajectories and Segregation in a Two-Dimensional Rotating Drum,” *Europhysics Letters*, vol. 27, no. 3, pp. 203 – 208, 1994.

[246] G. Baumann, “Computersimulationen granularer Materialien in Trommelmischern,” 1993.

[247] G. BAUMANN, E. JOBS, and D. E. WOLF, “GRANULAR COCKTAIL ROTATED AND SHAKEN,” *Fractals*, vol. 01, no. 04, pp. 767–783, Dec. 1993.

[248] D. J. Parker, a. E. Dijkstra, T. W. Martin, and J. P. K. Seville, “Positron emission particle tracking studies of spherical particle motion in rotating drums,” *Chemical Engineering Science*, vol. 52, no. 13, pp. 2011–2022, Jul. 1997.

[249] X. Y. Liu, E. Specht, and J. Mellmann, “Experimental study of the lower and upper angles of repose of granular materials in rotating drums,” *Powder Technology*, vol. 154, no. 2–3, pp. 125–131, Jul. 2005.

[250] R. Y. Yang, a. B. Yu, L. McElroy, and J. Bao, “Numerical simulation of particle dynamics in different flow regimes in a rotating drum,” *Powder Technology*, vol. 188, no. 2, pp. 170–177, Dec. 2008.

[251] H. Henein, J. K. Brimacombe, and A. P. Watkinson, “An experimental study of segregation in rotary kilns,” *Metallurgical Transactions B*, vol. 16, no. 4, pp. 763–774, Dec. 1985.

[252] J. Mellmann, “The transverse motion of solids in rotating cylinders—forms of motion and transition behavior,” *Powder Technology*, vol. 118, no. 3, pp. 251–270, Aug. 2001.

[253] J. Mellmann, E. Specht, and X. Liu, “Prediction of rolling bed motion in rotating cylinders,” *AIChE Journal*, vol. 50, no. 11, pp. 2783–2793, Nov. 2004.

[254] G. Juarez, P. Chen, and R. M. Lueptow, “Transition to centrifuging granular flow in rotating tumblers: a modified Froude number,” *New Journal of Physics*, vol. 13, no. 5, p. 053055, May 2011.

[255] H. Henein, J. K. Brimacombe, and A. P. Watkinson, “The modeling of transverse solids motion in rotary kilns,” *Metallurgical Transactions B*, vol. 14, no. 2, pp. 207–220, Jun. 1983.

[256] P. W. Cleary, “Recent advances in dem modelling of tumbling mills,” *Minerals Engineering*, vol. 14, no. 10, pp. 1295–1319, Oct. 2001.

[257] K. Hill and J. Kakalios, “Reversible axial segregation of binary mixtures of granular materials.,” *Physical review. E, Statistical physics, plasmas, fluids, and related interdisciplinary topics*, vol. 49, no. 5, pp. R3610–R3613, May 1994.

[258] A. V Orpe and D. V Khakhar, “Scaling relations for granular flow in quasi-two-dimensional rotating cylinders.,” *Physical review. E, Statistical, nonlinear, and soft matter physics*, vol. 64, no. 3 Pt 1, p. 031302, Sep. 2001.

[259] R. J. Spurling, “Granular flow in an inclined rotating cylinder: steady state and transition,” University of Cambrige, UK, 2000.

[260] X. Y. Liu, E. Specht, and J. Mellmann, “Slumping–rolling transition of granular solids in rotary kilns,” *Chemical Engineering Science*, vol. 60, no. 13, pp. 3629–3636, Jul. 2005.

[261] Y. . Ding, R. Forster, J. P. . Seville, and D. . Parker, “Granular motion in rotating drums: bed turnover time and slumping–rolling transition,” *Powder Technology*, vol. 124, no. 1–2, pp. 18–27, Apr. 2002.

[262] M. He, J. Zhang, and X. Y. Liu, “Determination of the repose angle of stuff in rotary kiln based on imaging processing,” *2009 9th International Conference on Electronic Measurement & Instruments*, pp. 4–97–4–101, Aug. 2009.

[263] J. Aldrich, “Doing Least Squares: Perspectives from Gauss and Yule,” *International Statistical Review*, vol. 66, no. 1, pp. 61–81, Apr. 1998.

[264] G. E. P. Box and N. R. Draper, *Empirical model-building and response surfaces*. 1987.

[265] S. R. A. Fisher, *The Design of Experiments*. 1951.

[266] G. E. P. Box, J. S. Hunter, and W. G. Hunter, *Statistics for Experimenters: Design, Innovation, and Discovery , 2nd Edition*. Wiley-Interscience, 2005, p. 664.

[267] K. Siebertz, D. van Bebber, and T. Hochkirchen, *Statistische Versuchsplanung: Design of Experiments (DoE) (VDI-Buch) (German Edition)*. Springer, 2010.

[268] J. A. Hartigan, *Bayes Theory (Springer Series in Statistics)*. Springer, 1983, p. 160.

[269] L. Held and D. S. Bové, *Applied Statistical Inference: Likelihood and Bayes*. Springer, 2013, p. 400.

[270] Evonik Instrustries AG, “Plexiglas® (XT transparent 0A000 GT) data sheet,” 2012.

[271] AK Steel Cooperation, “Steel Sheet 304 Stainless data sheet,” 2007.

[272] P. V. C. and Hough, “Machine Analysis Of Bubble Chamber Pictures,” *Conf.Proc.*, vol. C590914, pp. 554–558, 1959.

[273] R. C. González and R. E. Woods, *Digital image processing*. 1992.

[274] R. O. Duda and P. E. Hart, “Use of the Hough transformation to detect lines and curves in pictures,” *Communications of the ACM*, vol. 15, no. 1, pp. 11–15, Jan. 1972.

[275] S. Just, G. Toschkoff, A. Funke, D. Djuric, G. Scharrer, J. Khinast, K. Knop, and P. Kleinebudde, “Experimental analysis of tablet properties for discrete element modeling of an active coating process.,” *AAPS PharmSciTech*, vol. 14, no. 1, pp. 402–11, Mar. 2013.

[276] P. Gondret, M. Lance, and L. Petit, “Bouncing motion of spherical particles in fluids,” *Physics of Fluids*, vol. 14, no. 2, p. 643, Feb. 2002.

[277] J. D. Ferry, *Viscoelastic Properties of Polymers*. Wiley, 1980.

[278] H. Teufelsbauer, J. Hübl, and W. Wu, “A Revision of the Linear-Dashpot Model Applied in PFC,” vol. 2, no. 4, pp. 165–178, 2009.

[279] Y. Xu and K. L. Yung, “The effect of inertial normal force on the rolling friction of a soft sphere on a hard plane,” *Europhysics Letters (EPL)*, vol. 61, no. 5, pp. 620–624, Mar. 2003.

[280] M. Hazewinkel, *Encyclopaedia of mathematics*. 1990.

[281] K. J. Ryan, “Estimating Expected Information Gains for Experimental Designs With Application to the Random Fatigue-Limit Model,” *Journal of Computational and Graphical Statistics*, vol. 12, no. 3, pp. 585–603, Sep. 2003.

[282] J. van den Berg, A. Curtis, and J. Trampert, “Optimal nonlinear Bayesian experimental design: an application to amplitude versus offset experiments,” *Geophysical Journal International*, vol. 155, no. 2, pp. 411–421, Nov. 2003.